A VERSATILE DYNAMIC ROTOR AND PROPELLER MODEL FOR ELECTRIC VTOL SIMULATION APPLICATIONS

A THESIS SUBMITTED TO
THE GRADUATE SCHOOL OF NATURAL AND APPLIED SCIENCES
OF
MIDDLE EAST TECHNICAL UNIVERSITY

BY

CEREN CANSU ESMEK

IN PARTIAL FULFILLMENT OF THE REQUIREMENTS
FOR
THE DEGREE OF MASTER OF SCIENCE
IN
AEROSPACE ENGINEERING

SEPTEMBER 2022

Approval of the thesis:

A VERSATILE DYNAMIC ROTOR AND PROPELLER MODEL FOR ELECTRIC VTOL SIMULATION APPLICATIONS

submitted by **CEREN CANSU ESMEK** in partial fulfillment of the requirements for the degree of **Master of Science** i**n Aerospace Engineering, Middle East Technical University** by,

Prof. Dr. Halil Kalıpçılar
Dean, Graduate School of **Natural and Applied Sciences** _____

Prof. Dr. Serkan Özgen
Head of the Department, **Aerospace Engineering** _____

Assoc. Prof. Dr. Nilay Sezer Uzol
Supervisor, **Aerospace Engineering, METU** _____

Examining Committee Members:

Prof. Dr. Altan Kayran
Aerospace Engineering, METU _____

Assoc. Prof. Dr. Nilay Sezer Uzol
Aerospace Engineering, METU _____

Prof. Dr. Kemal Leblebicioğlu
Electrical Electronics Engineering, METU _____

Assist. Prof. Dr. Ali Türker Kutay
Aerospace Engineering, METU _____

Assist. Prof. Dr. Onur Baş
Mechanical Engineering, TEDU _____

Date: 02.09.2022

I hereby declare that all information in this document has been obtained and presented in accordance with academic rules and ethical conduct. I also declare that, as required by these rules and conduct, I have fully cited and referenced all material and results that are not original to this work.

Name Last name : Ceren Cansu Esmek

Signature :

ABSTRACT

A VERSATILE DYNAMIC ROTOR AND PROPELLER MODEL FOR ELECTRIC VTOL SIMULATION APPLICATIONS

Esmek, Ceren Cansu
Master of Science, Aerospace Engineering
Supervisor: Assoc. Prof. Dr. Nilay Sezer Uzol

September 2022, 172 pages

This thesis presents a versatile, dynamic rotor/propeller model for various all-electric and hybrid-electric vertical takeoff and landing aircraft (eVTOL) simulation applications. The goal is to reflect the transformative potential of eVTOL to carry different types of thrust sources using one generic mathematical model. The thrust sources may include propellers, articulated rotors, ducted rotors, and coaxial rotors. These rotors are modeled based on blade element theory. Rotor inflow is estimated using the uniform dynamic inflow model or Pitt-Peters dynamic inflow model. They are interchangeable based on the application's fidelity and complexity. The dynamic rotor/propeller model allows to position and orient multiple rotors and propellers in any desired configuration. This model can be used during the conceptual design phase in isolated rotor simulations, performance calculations, stability analyses, sensitivity analyses, optimization, and trade studies for eVTOL applications since it is an all-parametric and computationally robust tool. The model outputs are compared with the wind tunnel test data of the isolated rotors found in the literature. Simulation results of an example complex multi-rotor eVTOL are shown and discussed.

Keywords: eVTOL, Mathematical Modeling, Dynamic Simulation, Rotor, Propeller

ÖZ

ELEKTRİKLİ, DİKEY İNİŞ-KALKIŞ YAPABİLEN HAVA ARAÇLARININ SİMÜLASYONU İÇİN DİNAMİK ROTOR VE PERVANE MODELİ

Esmek, Ceren Cansu
Yüksek Lisans, Havacılık ve Uzay Mühendisliği
Tez Yöneticisi: Doç. Dr. Nilay Sezer Uzol

Eylül 2022, 172 sayfa

Bu tezde, elektrikli, dikey iniş-kalkış yapabilen hava araçlarının (eVTOL) simülasyonu için geliştirilmiş bir çok yönlü dinamik rotor/pervane modeli sunulmuştur. Bu kapsamlı modeli kullanarak eVTOL hava araçlarının değişik itki kaynakları taşıyarak dönüştürülebilirlik potansiyelinin yansıtılması amaçlanmaktadır. Pervane, mafsallı rotor, kanallı (örtülü, kapalı) rotor ya da eş-eksenli rotor bu itki kaynaklarındandır. Bu rotorlar Pala Elemanı Teorisi temel alınarak modellenmiştir. Eşdağılımlı dinamik iç-akış modeli veya Pitt-Peters dinamik iç-akış modeli arasında tercih yapılabilmektedir. Parametrik ve yazılım olarak gürbüz olması nedeniyle izole rotor simülasyonları, optimizasyon çalışmaları, performans, kararlılık ve hassasiyet incelemeleri için kullanılabilmektedir. Rotor modelinin doğrulaması yazılı kaynaklarda bulunun izole-rotor rüzgâr tüneli test verileri ile karşılaştırma yapılarak gerçekleştirilmiştir. Modelin çok yönlü uygulanabilirliği örnek bir çok rotorlu eVTOL tasarımının simülasyonuyla gösterilmiştir.

Anahtar Kelimeler: eVTOL, Matematik Modelleme, Dinamik Simülasyon, Rotor, Pervane

To my brother, my captain, my king

ACKNOWLEDGMENTS

I want to express my deepest gratitude to my supervisor, Assoc. Prof. Dr. Nilay Sezer Uzol for her belief in me, for her support and help. I would like to thank her for her guidance and advice in getting me through the end.

I want to extend my thanks to the dissertation committee members for their insightful comments and suggestions to improve this study further.

I thank Dr. Feyyaz Güner and Murat Şenipek for their thesis studies left behind. They were very beneficial to me during my research.

I want to thank my team in Turkish Aerospace Industries, Yusuf Onur Arslan, Ilgaz Doğa Okcu, Arda Çalışkan, Cenk Çetin, Kaan Şansal, Göktuğ Koçak, Umut Türe, Özge Kapulu, Ömer Oğuzhan Güngören, Elif Çakmak, Kağan Sarıbaş, and Ozan Ege Camcı for accepting me as a part of the team and their understanding, help, and encouragement.

I want to express my sincere appreciation to Aerotim Engineering, where I grew up technically and mentally as a freshly graduated aerospace engineer. It was an honor to work with the Aerotim Engineering team and a once-in-a-lifetime opportunity to work on such great projects. The idea behind this study comes directly from the vision I gained in Aerotim, for which I am very thankful. I also want to thank them for all the sources they provided me throughout this study. I want to thank especially my dear colleagues from Aerotim, exceptional engineers Zeynep İlkay Bostancı, Ali Karakaya, Ahmet Alp Yılmaz, and Gökay Özer, for everything I learned from them. It was a great pleasure working with them, which I will never forget. I want to thank my team leader Ali Karakaya for everything he taught me about modeling and simulation. I would also like to mention that in this thesis, I used many concepts that I learned from an admirable engineer Serdar Üşenmez, for whom I am grateful.

Besides their help in my career, I would also like to thank Zeynep İlkay Bostancı and Ali Karakaya for their assistance in my life, support, love, and friendship.

I want to thank my beloved friends, who are more like sisters and brothers, Baran Demir, Ali Alparslan, Buse Yeşim Özdemir, Elif Bişirici, Çağrı İnanç, Mehmet Safa Aysan, Ayşe Bay, Kaan Yutük, Zeynep Ünal, Tuğrul Ahtapot, Mehmet Melih Atalay, Onur Okumuş, Arın Göksan, Ahmet Alp Yılmaz, Kübra Koparan, Figen Kılıç.

I would like to thank deeply, especially Elif Değirmenci, Aybeniz Akbaba, Esra Halaçlar, Ceyda Koruk, and Rabiya Bıyıklı, who know me the best and always be there for me.

I want to thank my mother, Tamara Esmek, for her endless love and care all my life.

Last but not least, I would like to express my heartfelt gratitude to Prof. Dr. İlkay Yavrucuk, who has inspired me since the first department orientation class I took from him in 2013. He taught me everything I needed in Flight Mechanics and Control as an Aerospace Engineering undergraduate. After graduation, he continued to share his passion for helicopters in Aerotim Engineering and the department and made it grow in me too. He taught me how to keep the excitement for engineering alive and created a will to move on. He is why I started to be curious about eVTOLs; therefore, he is the architect behind this study; he even came up with the title of this thesis. He is an invaluable supervisor not only for my career but also for my life. I am very grateful for all his help and support; I was lucky to have him by me for the past decade.

TABLE OF CONTENTS

LIST OF TABLES

LIST OF FIGURES

LIST OF ABBREVIATIONS

AAM:	Advanced Air Mobility
AC:	Aerodynamic Center
AR:	Aspect Ratio
ARI:	Advanced Air Mobility Reality Index
BET:	Blade Element Theory
BL:	Butt Line
BLDC:	Brushless Direct Current Electric Motor
CCW:	Counter-clockwise
CFD:	Computational Fluid Dynamics
CG:	Center of Gravity
CW:	Clockwise
DEP:	Distributed Electric Propulsion
DOF:	Degree of Freedom
ESC:	Electronic Speed Controller
eVTOL:	Electric Vertical Take-off and Landing
FS:	Fuselage Station
IBC:	Individual Blade Coordinates
MBC:	Multi Blade Coordinates
$MTOW$:	Take-off Gross Weight
OEM:	Original Equipment Manufacturer

PWM: Pulse-width Modulation

TPP: Tip Path Plane

WL: Water Line

VFS: Vertical Flight Society

LIST OF SYMBOLS

u, v, w: Translational Velocities in Body Fixed Frame (x,y,z, respectively)

p, q, r: Angular Velocities in Body Fixed Frame (x,y,z, respectively)

$\dot{u}, \dot{v}, \dot{w}$: Translational Accelerations in Body Fixed Frame (x,y,z, respectively)

$\dot{p}, \dot{q}, \dot{r}$: Angular Accelerations in Body Fixed Frame (x,y,z, respectively)

$\bar{V}$: Translational Velocity

$\bar{a}$: Translational Acceleration

$\bar{\omega}$: Angular Velocity

$\bar{\alpha}$: Angular Acceleration

$\bar{\Omega}$: Rotational Velocity

$\dot{\bar{\Omega}}$: Rotational Acceleration

DoR: Direction of Rotation

$\bar{F}$: Total Forces

$\overline{F_{Aero}}$: Total Aerodynamic Forces

$\overline{F_{Inertial}}$: Total Inertial Forces

$\bar{M}$: Total Moments

$\overline{M_{Aero}}$: Total Aerodynamic Moments

$\overline{M_{Inertial}}$: Total Inertial Moments

C_T: Thrust Coefficient

C_L: Roll Moment Coefficient

C_M: Pitch Moment Coefficient

ϕ, θ, ψ: Euler Angles

ϕ_s, θ_s: Lateral and Longitudinal Shaft Angles

$\Delta\phi_s, \Delta\theta_s$: Delta Lateral and Delta Longitudinal Shaft Angles

$\lambda_0, \lambda_{1s}, \lambda_{1c}$: Pitt-Peters Dynamic Inflow States

λ_r: Inflow Ratio of TPP of Rotor/Propeller

μ_r: Advance Ratio of TPP of Rotor/Propeller

ν: Mean Inflow

$\bar{\nu}$: Inflow on Blade Element

B: Tip Loss Factor

κ: Inflow Correction Factor

β: Flapping Angle of Individual Blade

β_{TPP}: Sideslip Angle of TPP of Rotor/Propeller

$\dot{\bar{\beta}}$: Flapping Velocity of Individual Blade

$\ddot{\bar{\beta}}$: Flapping Acceleration of Individual Blade

$\beta_0, \beta_{1s}, \beta_{1c}$: Zeroth and First Harmonics of Flapping

β_{coning}: Coning Angle

$\beta_{precone}$: Precone Angle

θ: Pitch Angle of Individual Blade

$\theta_0, \theta_{1s}, \theta_{1c}$: Collective Angle, Pitch Cyclic Angle, Roll Cyclic Angle

θ_t: Twist Angle

δ_3: Pitch-Flap Coupling

ψ: Azimuth of Individual Blade

$\Delta\psi$: Swashplate Phase Lag

e: Hinge Offset

λ: Taper Ratio

c_t: Tip Chord

c_r: Root Chord

r_R: Root Cutout

R: Radius

R_e: Effective Radius

$\bar{r}_{Hub2CG}$: Position of Hub to Center of Gravity of eVTOL

$\bar{r}_{Hinge2Hub}$: Position of Hinge to Hub

$d_{BldCG2Hng}$: Distance from Blade Center of Gravity to Hinge

$\bar{r}_{WingAC2CG}$: Position of Aerodynamic Center of Wing to Center of Gravity of eVTOL

b: Number of Blades

m: Number of Blade Elements

m_b: Blade Mass

I_B: Flapping Inertia

$\hat{J}$: Inertia Matrix

K_β: Flapping Spring Constant

i: Incidence Angle

α: Angle of Attack of Blade Section

α_{TPP}: Angle of Attack of TPP of Rotor/Propeller

ϕ: Inflow Angle of Blade Section

ρ: Air Density

M: Mach Number

c: Speed of Sound

U_T: Tangential Velocity

U_P: Perpendicular Velocity

U_R: Radial Velocity

U: Total Velocity

C_l: Lift Coefficient of Blade Section

C_d: Drag Coefficient of Blade Section

C_{d0}: Parasite Drag Coefficient of Blade Section

C_L: Lift Coefficient of Wing

C_{L_0}: Lift Coefficient of Wing at Zero Angle of Attack

$C_{L_{MAX}}$: Maximum Lift Coefficient of Wing

$C_{L_{MIN}}$: Minimum Lift Coefficient of Wing

C_D: Drag Coefficient of Wing

C_{D_0}: Parasite Drag Coefficient of Wing

C_{L_α}: Slope of C_L vs. α Curve

C_{D_X}, C_{D_Y}, C_{D_Z}: Flat-plate Drag Area in Body-Fixed Frame

L: Lift of Blade Section

D: Drag of Blade Section

V_T: Non-Dimensional Total Average Velocity Passing the TPP of the Rotor/Propeller

$\widehat{M}$: Mass Matrix

$\widehat{V}$: Flow Parameter Matrix

$\hat{L}$: Influence Coefficient Matrix

$\bar{\tau}$: Pitt-Peters Aerodynamic Forcing Terms

H_F: Effective fan cylinder height of the ducted rotor/propeller/fan

H_M: Effective momentum cylinder height of the ducted rotor/propeller/fan

σ_d: Diffuser Expansion Ratio

A_{ref}: Reference Area

$\bar{W}$: Weight

$\bar{g}$: Gravitational Acceleration in Inertial Frame

$\vec{u}_1, \vec{u}_2, \vec{u}_3$: Unit vectors in three axes (x,y,z, respectively)

Superscripts

$(\,)^{Body}, (\,)^{Hub}, (\,)^{Blade}, (\,)^{TPP}, (\,)^{Precone}, (\,)^{Wind}$: Reference Frames

$(\,)^{t}$: Sample Time of the States

Subscripts

$(\,)_{CG}, (\,)_{Hub}, (\,)_{Hinge}, (\,)_{Shroud}, (\,)_{Wing}, (\,)_{Body}$: Entities at which calculations are done

$(\,)_{k}$: Rotor/Propeller Identification Number

$( )_i$: Individual Blade Identification Number

$( )_n$: Blade Element Identification Number

$( )_u$, $( )_l$: Upper Rotor and Lower Rotor for Coaxial Rotor Model

Accents

$\overline{( )}$: Column Matrix

$\widehat{( )}$: Matrix

$\overrightarrow{( )}$: Vector

$\dot{( )}$: $\frac{d}{dx}$

$\ddot{( )}$: $\frac{d^2}{dx^2}$

CHAPTER 1

INTRODUCTION

Aircraft focusing on electric-powered VTOL aircraft large enough to carry passengers without conventional helicopter flight controls are called all-electric and hybrid-electric powered vertical takeoff and landing (eVTOL) aircraft [1]. Although electric helicopters (eHelos) and electric Gyrocopters (eGyros) have conventional flight controls, they are also included in electric VTOL aircraft. The term "eVTOL" for electric VTOLs was first used in late 2016 and has been used to describe these types of aircraft since then [2].

The transformative potential of eVTOL provided by its degree of freedom in propulsion systems leads to many possible solutions with unconventional concepts with multiple rotors and propellers that may best fit the trade-in: the safest, quietest, cleanest, and cheapest.

Table 1.1 shows the Advanced Air Mobility Reality Index (ARI), established by SMG Consulting. The ARI is based on the funding received by the company, the team that leads the company, the technology readiness of the eVTOL design, the certification progress of the eVTOL, and production readiness towards full-scale manufacturing [3]. Therefore, it evaluates the applicability and survivability of the eVTOL concepts in this vibrant market. According to ARI calculated in June 2022, the highest-ranked eVTOL among more than 700 eVTOL designs still has 8.7 points out of 10, indicating that in the long run, the eVTOL revolution requires work to be done to find the best concept to become "real."

Table 1.1. Advanced Air Mobility Reality Index [3]

OEM (stock ticker)	ARI	Funding ($M)	Use Case	Vehicle Type	Propulsion	Operation	Vehicle	First Flight	Country
Joby Aviation (NYSE: JOBY)	8.7	$1,844.60	Air Taxi	Vectored Thrust	Electric	Piloted	-	2018	USA
Volocopter	8.4	$579.00	Air Taxi	Multicopter / Lift + Cruise	Electric	Piloted	VoloCity / VoloConnect	2021 / 2022	Germany
Beta Technologies	8	$796.0*	Cargo, Air Taxi	Lift + Cruise	Electric	Piloted	Alia S250c / S250	2020	USA
Eve Holding (NYSE: EVEX)	7.7	$362.40	Air Taxi	Lift + Cruise	Electric	Piloted	Eve	2022	Brazil
Lilium (NASDAQ: LILM)	7.7	$938.00	Regional, Cargo, Biz Av	Vectored Thrust	Electric	Piloted	Jet	-	Germany
Wisk	7.5	$775.00	Air Taxi	Lift + Cruise	Electric	Autonomous	Cora	2018	USA
Archer (NYSE: ACHR)	7.4	$856.30	Air Taxi	Vectored Thrust	Electric	Piloted	Maker	2021	USA
Ehang (NASDAQ: EH)	7.4	$132.00	Air Taxi, Tourism	Multicopter / Lift + Cruise	Electric	Autonomous	EH-216S / VT-30	2018 / 2021	China
Elroy Air	7.4	$50.00	Cargo	Lift + Cruise	Hybrid	Autonomous	Chaparral C1	2022	USA
Kitty Hawk	7.3	Privately funded	Air Taxi	Vectored Thrust	Electric	Autonomous	Heaviside	2018	USA
Pipistrel (Textron)	7.2	Corporate backed	Cargo	Lift + Cruise	Hybrid	Autonomous	Nuuva V300	2022	USA
Vertical Aerospace (NYSE: EVTL)	7.2	$337.30	Air Taxi, Cargo, EMS	Vectored Thrust	Electric	Piloted	VX4	2022	UK
Airbus	7	Corporate backed	EMS, Tourism, Air Taxi	Multicopter	Electric	Piloted	CityAirbus NextGen	2023	France
Supernal	7	Corporate backed	Air Taxi	Vectored Thrust	Electric	Piloted	S-A1	2023	South Korea
Overair	6.2	$170.00	Air Taxi	Vectored Thrust	Electric	Piloted	Butterfly	2023	USA
Honda Motor Company	6	Corporate backed	Air Taxi	Lift + Cruise	Hybrid	Piloted	-	2023	Japan
eAviation (Textron)	5.9	Corporate backed	Air Taxi	Vectored Thrust	Electric	Piloted	Nexus	-	USA
Eviation	5.9	$200.00	Regional, Cargo, Biz Av	Conventional	Electric	Piloted	Alice	2022	USA
REGENT	5.9	$27.00	Regional	Augmented Lift	Electric	Piloted	Viceroy	2023	USA
AutoFlight	5.8	$200.00	Air Taxi	Lift + Cruise	Electric	Piloted	Prosperity I	2022	China
Ascendance Flight Technologies	5.4	$11.90	Regional, Cargo	Lift + Cruise	Hybrid	Piloted	Atea	2023	France
Dufour Aerospace	5.2	$11.00	EMS, Regional	Vectored Thrust	Hybrid	Piloted	Aero3	2022	Switzerland
Electra	5.2	$49.00	Cargo, Regional	Augmented Lift	Hybrid	Piloted	-	2022	USA
Jaunt Air Mobility	4.4	$3.10	Air Taxi	Lift + Cruise	Electric	Piloted	Journey	2023	USA
Volkswagen	3.4	Corporate backed	Air Taxi	Lift + Cruise	Electric	Autonomous	V.MO	2022	Germany

As the eVTOL industry has been born yet, challenges to improving the designs still exist to meet the requirements in the market. Designing a safe, reliable, cost-efficient

eVTOL is one of the critical challenges in the industry. Therefore, trade studies between all possible concepts are necessary for the best operation of the mission. Considering the necessity of these trade studies, the engineering models' requirement to predict the aircraft's performance arises to conduct them. Since, in the beginning, the primary determinant component that changes the concept is the rotor for eVTOL aircraft, a mathematical rotor model for each configuration is needed in the conceptual design phase.

This thesis presents a versatile, dynamic rotor model to reduce the workload of creating different mathematical models reflecting different rotor configurations: articulated rotor, ducted propeller, coaxial propeller, and propeller. It aims to combine the dynamics of varying rotor configurations with critical aerodynamic phenomena in one mathematical model having desirable fidelity. It is an all-parametric and computationally robust tool for isolated rotor simulations, performance calculations, stability analyses, sensitivity analyses, and optimization.

1.1 Introduction to Electric VTOL Aircraft

Most improvements in military and commercial aircraft capabilities can be attributed to advanced aircraft engine technology. The eVTOL revolution is led by innovations in electric propulsion systems [4]. In Figure 1.1, the historical trend in VTOL development can be seen. After 2010, the exponential growth in VTOL development resulted from the progress mainly in distributed electric propulsion (DEP) systems technologies.

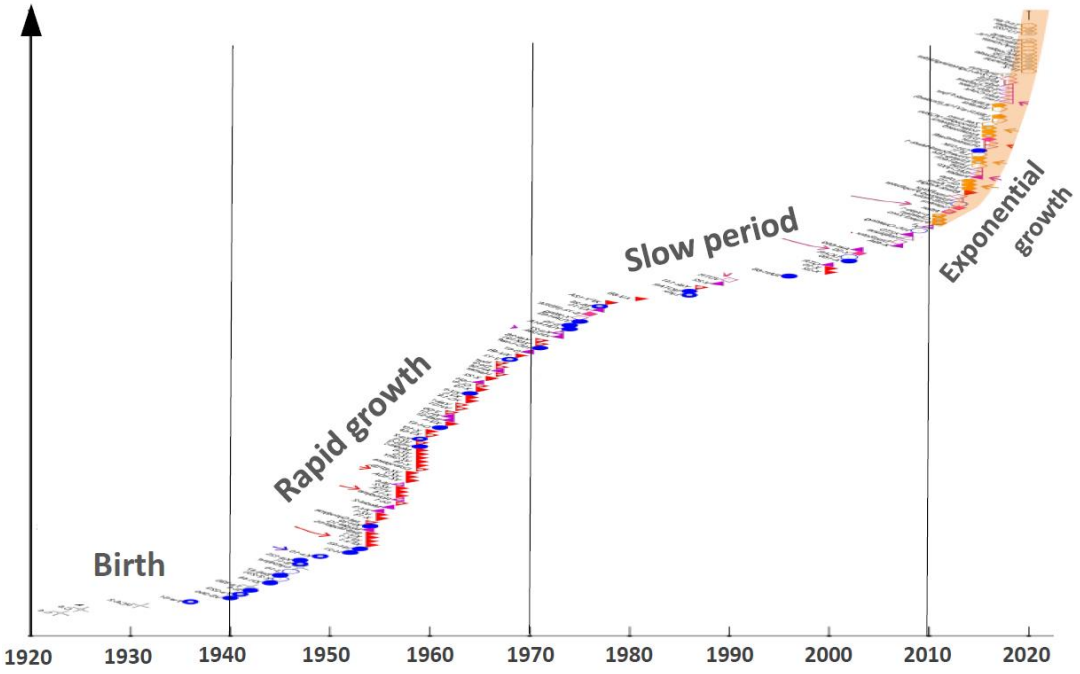

Figure 1.1. The historical trend in VTOL development [5]

Distributed electric propulsion systems freeing the aircraft from mechanical drive systems have made creative designs and shrinking size, weight, and cost possible, facilitating commercial aviation development [6, 7]. When compared to mechanical drive systems, a direct electric drive has benefits like

- working with more than 92% continuous efficiency,
- providing 30% overpower for a few minutes,
- needing no gearbox,
- easily varying rotor rpm,
- having fewer moving parts,
- generating lower noise,
- having no polluting exhaust,
- having a low thermal signature, and
- being altitude independent because of having no oxygen combustion. [5]

In addition to DEP, technological advancements such as

- powerful electric motors,
- silicone carbide inverters,

- better rechargeable batteries,
- lower-cost sensors,
- autonomous flight control,
- lightweight composite structures,
- low-cost manufacturing, and
- better modeling and simulation tools

realize electric VTOL with unconventional concepts [5, 8, 9, 10]. Electric propulsion brings in low-cost fly-by-wire and power-by-wire configurations that could never have been possible with mechanical drive systems and human flight controls. DEP and autonomous flight control are the primary enablers of eVTOL aircraft [8].

Figure 1.2 shows improvement in the specific power of different propulsion systems. While the specific power of turbo-shaft engines slightly increases, the specific power of electric motors reaches turbo-shaft engines' in about 40 years. Therefore, with this progress rate, how electric motors can dominate the propulsion systems of the aircraft industry can be predicted for the future.

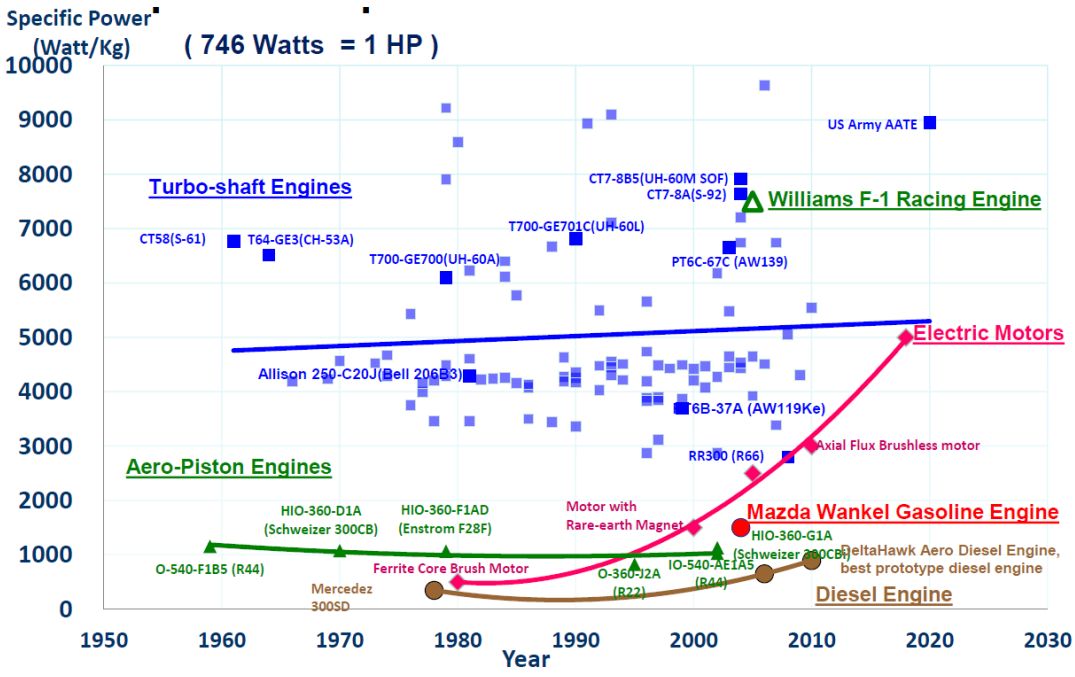

Figure 1.2. Specific power trends of different propulsion systems in years [5]

Besides the technological enhancements, the fact that "green" air transportation is presumed to solve global environmental, economic, and cultural issues because of traffic jams in metropolitans increases the hype about eVTOLs. According to data from the 2016 US Census Bureau, the American Community Survey, and Maryland's State Highway Administration, Americans spend an average of 276 hours commuting to and from work – 26% of them trapped over two hours a day in traffic during their commute. The economic cost is billions of dollars annually through lost productivity, which increases when it is scaled up to the whole world's traffic. As climate change rises as a global issue, concerns about the millions of gallons of gasoline wasted and air pollution caused by carbon emissions, and the noise created by traffic are also increasing. Therefore, eVTOLs are a promising solution to economic, environmental, and cultural issues due to loaded traffic in densely populated cities [11]. In addition, when autonomous flight control technology in eVTOLs and rules and regulations for operations of eVTOLs is considered, the widespread use of eVTOLs is regarded as a possible way to reach zero fatalities in traffic, as the most significant amount of all traffic accidents are caused by human error [12]. Finally, since eVTOL aircraft are predicted to be safer, quieter, cleaner, and cheaper than today's fossil-fuel-burning aircraft, which are expensive to buy, operate, and maintain [7, 10], they are interpreted as a potential replacement for conventional VTOL aircraft for the future [13].

With these justifications for the need for the eVTOL industry, the financial lift started by Uber Elevate is to be bringing about the eVTOL revolution. Uber Technologies, the cell phone app rent-a-ride provider, published a 97 pages white paper titled "Uber Elevate: Fast-Forwarding to a Future of On-Demand Urban Air Transportation" on October 27, 2016. Uber's vision — shared by a growing number of aviation experts, designers, real estate developers, civic leaders, community partners, and many other stakeholders — is to use eVTOL as "air taxis" to revolutionize transport in and around metropolitan centers. Uber Elevate raised public awareness and helped to initiate an ecosystem needed to realize the eVTOL revolution and fill the gaps by focusing on the connection between vehicle requirements, product design, market

opportunities, and operating economics. Using the urban demand data that Uber has accumulated since 2009, a business model for "air taxis" to shift the ground commuters to the sky became possible. Uber's ability to access and analyze this reliable data source having price and time sensitivity created an opportunity for transition to Advanced Air Mobility (AAM). The AAM movement was accelerated by supporting research efforts, creating a requirement list, offering feasibility from infrastructure to public acceptance, and giving an available customer to the eVTOL industry [14, 15, 16, 17].

Uber Elevate partners, major aerospace companies (OEMs), and investors outside the aerospace industry provided funding for eVTOL companies. Between 2011 and 2020, approximately $5B had been invested, and in 2021, it almost doubled. In addition, airlines and other operators have ordered more than 2000 eVTOL aircraft from American and European eVTOL developers [7, 18, 19, 20].

Rising investments in the Advanced Air Mobility industry accelerated the research and developments to overcome the challenges of integrating eVTOLs in public. Consequently, since 2010, when the first electric tiltrotor aircraft design, AgustaWestland Project Zero, was introduced, more than 700 eVTOL concepts with tilt-propeller, multi-propeller, ducted-fan, etc., have already been announced to date. It is growing at a pace of 100 concepts per year, i.e., about two new eVTOL concepts each week. In Figure 1.3, exponential growth in the number of OEMs and startup companies working on eVTOL since 2015 can be seen. By April 2021, more than two dozen companies have flown their prototype eVTOL aircraft: Joby Aviation, Kitty Hawk (Heaviside), Lilium, Volocopter, EHang, LIFT Aircraft, Hoversurf, Kitty Hawk (Flyer), Opener BlackFly, and the Boeing Cargo Air Vehicle, etc., as shown in Table 1.1. As seen in Figure 1.4, according to the VFS World eVTOL Aircraft Directory database, by September 2020, 129 out of 300 companies were actively developing their eVTOL aircraft, and 43 were at the large-scale demonstrator phase. Of these, three aircraft had gone into batch or series production – namely, the EHang 216, the Kitty Hawk Flyer (since discontinued), and the Opener BlackFly – each with around 100 units [1, 21, 19, 22, 20].

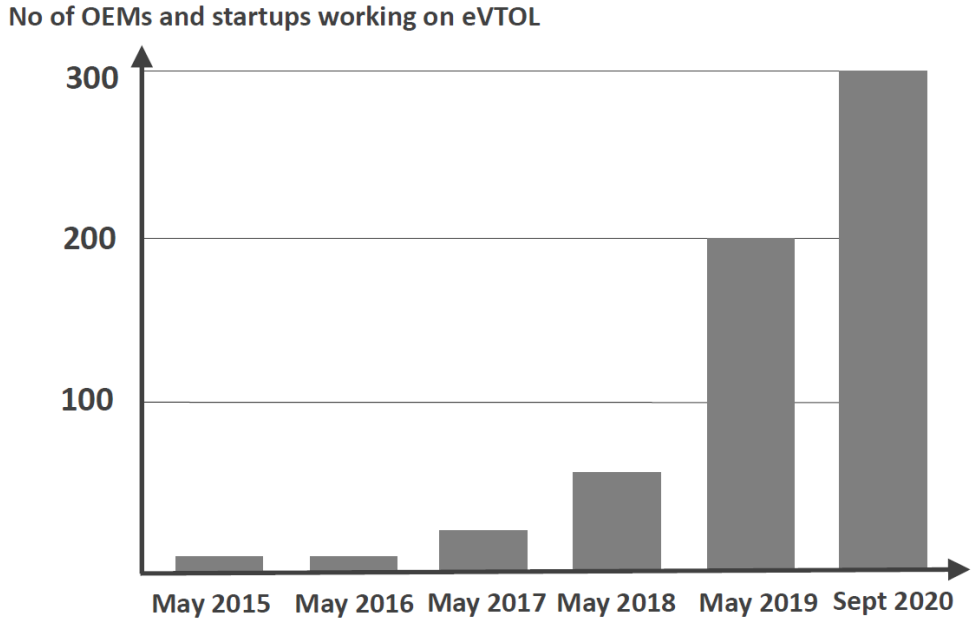

Figure 1.3. Exponential growth in eVTOL companies [5]

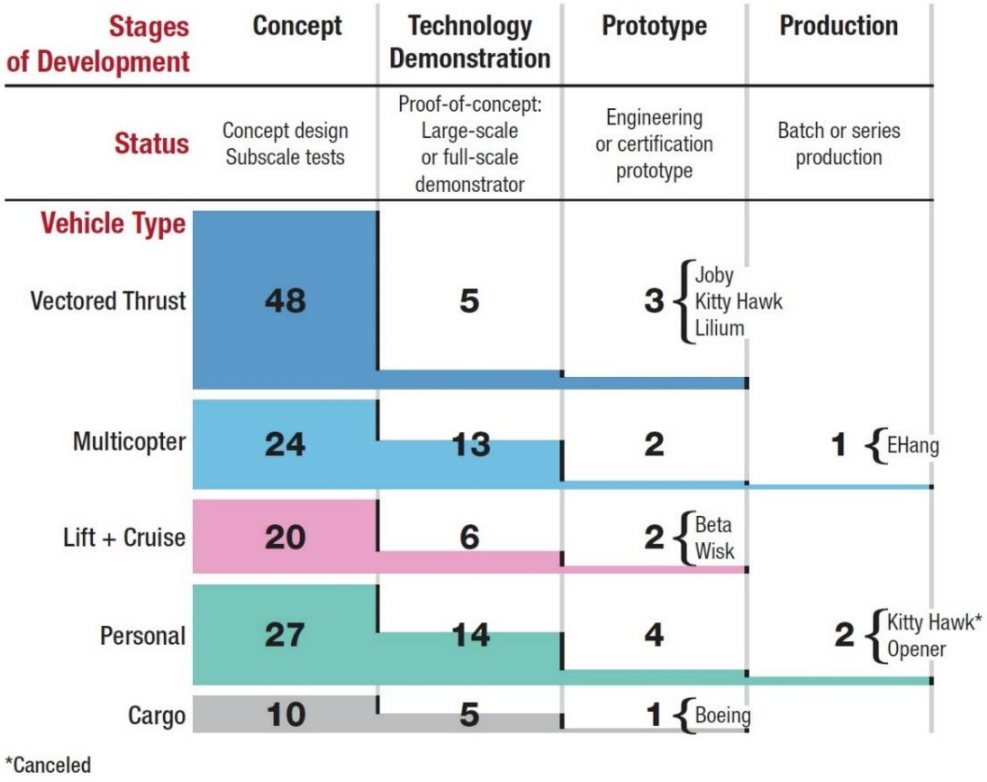

Figure 1.4. Progress of the 129 eVTOL aircraft in the phase of active development (Graphic is produced by Aviation Week) [20]

In Figure 1.4 and Figure 1.5, existing eVTOL concepts are given. So far, they are grouped into four categories. They can be listed from the highest availability to the lowest as multi-rotor, vectored thrust, lift and cruise, and electric helicopters and gyrocopters [5].

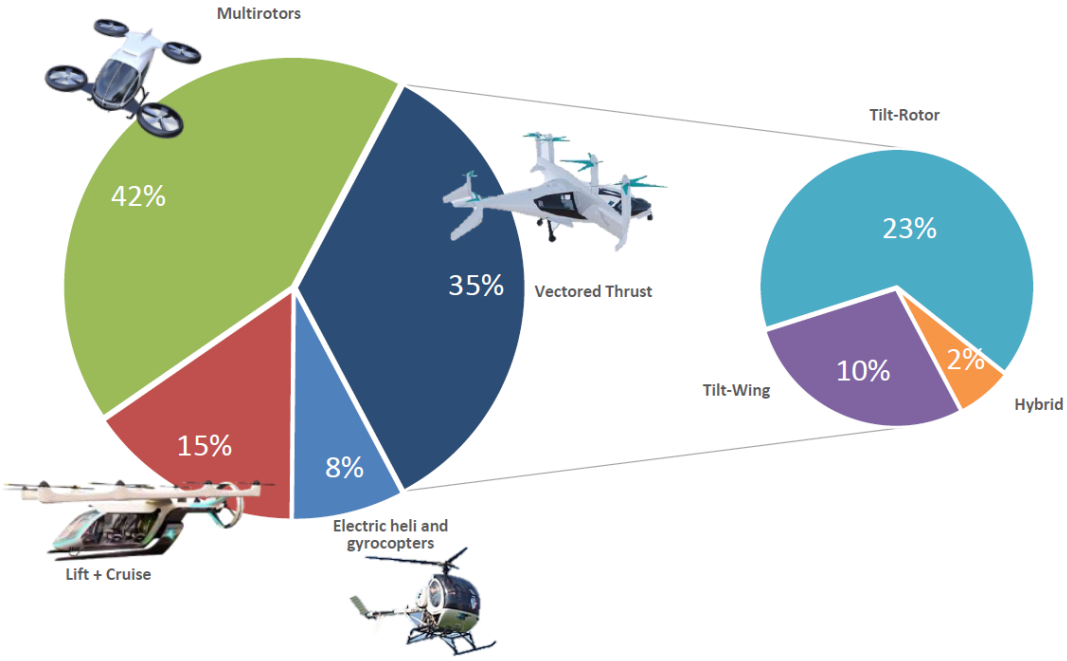

Figure 1.5. Existing electric VTOL concepts [5]

According to NASA, Advanced Air Mobility is an air transportation system moving people and cargo to local, regional, intraregional, and urban places using eVTOLs [3]. Although it seems that the design purpose of eVTOLs is mainly concentrated on AAM, they are also designed to serve in other mission profiles such as medical, military, surveillance, tourism, disaster relief, etc. [23, 24, 5, 25].

Operating cost is one of the factors considered in which concept is more suitable for the mission. Today, the company Blade charges $14 per passenger mile for helicopter operations [5]. According to Uber cost models, helicopters today cost about $9 per passenger mile in air taxi service. An eVTOL priced around $2.5M per vehicle could be $6 per passenger mile at startup. A mature service with 75% load factors and around 2000 hours per year could push the number down to just $2 per passenger mile [26], as shown in Figure 1.6.

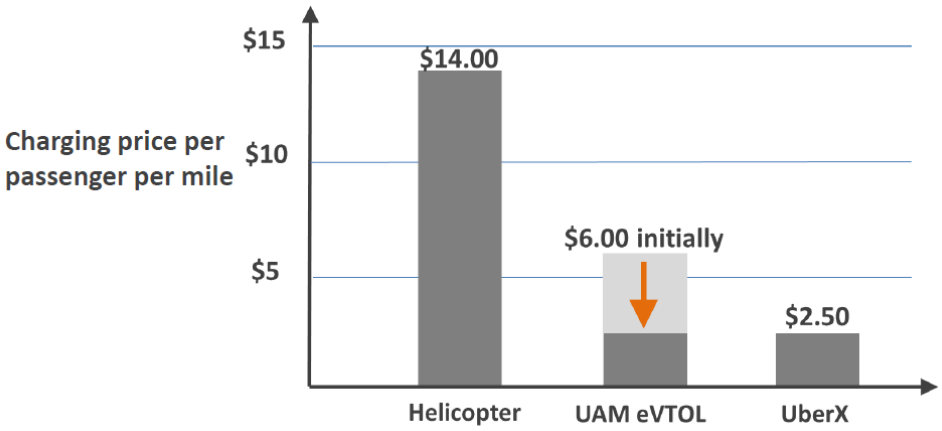

Figure 1.6. Charging price per passenger per mile for different VTOL concepts [5]

1.2 Rotor and Propeller Modeling in Literature

There are many eVTOL studies in the literature, and they are getting more sophisticated as time goes by. However, the rotor and propeller models used so far are mostly simplified models for a specific purpose. Therefore, a generic, versatile, high-fidelity dynamic rotor and propeller model was missing, which is applicable for all simulation applications for every eVTOL concept.

Rotor and propeller models used in eVTOL applications in the literature can be grouped into four. Table 1.2 summarizes rotor and propeller modeling methods in the literature.

Table 1.2. Rotor and propeller modeling methods

Rotor & Propeller Modeling Methods
$\text{Thrust} = \kappa \times \Omega^2$
Basic Empirical Equations Basic Thrust & Power Estimations
Blade Element Momentum Theory
Commercial or Open Source Dynamic Modeling or Performance Calculation and Pre-sizing Tools

In control applications like [27], the thruster is modeled with the simplest expression, calculating the thrust using $\text{Thrust} = \kappa \times \Omega^2$. In conceptual design applications like [28, 29], or control applications like [30], basic empirical equations and basic thrust and power estimations are used to model the effect of the thruster. Blade element momentum theory is utilized in handling quality assessment applications like [31]. In more advanced studies, like a concept design study [32], quasi-static dynamic rotor modeling is used.

In addition, commercial or open source dynamic modeling or performance calculation and pre-sizing tools are used in many studies. A blade element momentum theory solver CHARM is used in a concept design study [33], NDARC and CAMRAD II are used in [34], and NDARC and SUAVE are used in [35]. For a dynamic stability analysis study [36], FLIGHTLAB is used. For a handling quality assessment under turbulence study [37], or a control application [38], RMAC is used. NDARC is used in a handling quality assessment application [39]. For a concept design study [40], HYDRA is used. Many more tools are available for eVTOL simulation applications, and their number is increasing as the eVTOL industry grows.

1.3 Objective of the Thesis

This thesis presents an in-house versatile, dynamic rotor and propeller model for electric VTOL modeling and simulation applications. Modeling and simulation provide a basis for the life-cycle of an air vehicle from development to operation. High fidelity dynamic models are needed for applications such as isolated rotor simulations, flight dynamics simulations, performance calculations, stability analyses, sensitivity analyses, optimization, and trade studies in the conceptual and preliminary design phases, autopilot developments, handling-quality assessments, hardware in the loop tests, software in the loop tests, engineering simulators and pilot-training simulators, etc. Especially, parametric, generic, and physics-based models give the freedom of applicability to every field of research. The rotor and

propeller model presented in this thesis promises a wide range of usage areas for eVTOL simulation applications since it is a user-friendly, all-parametric, and computationally robust tool. This thesis aims to reflect the transformative potential of eVTOL to carry different types of thrust sources using one generic mathematical model having a versatile use involving dynamic models of varying rotor and propeller types.

1.4 Organization of the Thesis

This thesis is comprised of six chapters.

Chapter 1 is an introductory chapter presenting the motivation and objective behind this dissertation. General knowledge about electric VTOL aircraft and their enablers and progress in the considerably young electric VTOL industry are presented. Rotorcraft dynamic modeling and dynamic rotor models and their fidelity in recent eVTOL studies and commercial and open source tools used in eVTOL development are discussed.

Chapter 2 describes the methods used for aerodynamic and dynamic rotor and propeller modeling.

Chapter 3 explains the details of implementing the rotor and propeller model in the MATLAB Simulink environment.

Chapter 4 shows the model validation by comparing model outputs and wind tunnel test data of the isolated rotor of the S-76 helicopter in hover and forward fight.

Chapter 5 demonstrates various steady state and transient simulations of different eVTOL configurations using the dynamic rotor and propeller model. The purpose of this chapter is to show the applicability and versatility of this model.

Chapter 6 is the conclusion chapter summarizing the previous chapters and discussing the outcomes of this thesis. The limitation of this study and future work to improve it are presented in this chapter.

CHAPTER 2

AERODYNAMIC AND DYNAMIC MODELING METHODOLOGIES

The purpose of all thrusters (rotor, propeller, and fan) is to convert the rotational energy to a momentum change as thrust or vice versa (windmill, gyrocopter, or helicopter in autorotation) using rotating blades generating pressure change across their disk area. However, they are differentiated according to their capability of off-axis control, usage for edgewise flight, and solidity. Therefore, the thrusters used for edgewise flight and can generate axial and non-axial forces and moments using cyclic blade pitch inputs are called rotors. Thrusters used for the axial flight using only the axial control through variable blade pitch or rpm with a solidity less than 0.5 are called propellers. Like propellers, the thrusters used for the axial flight using only the axial control through variable blade pitch or rpm but with a solidity of more than 0.5 are called fans [41].

In the scope of this thesis, articulated rotor, propeller, ducted rotor or propeller, and coaxial rotor or propeller are modeled as they are the most encountered thruster configurations for eVTOL aircraft.

Rotor models are classified according to the attachments of blades to the mast as teetering, articulated, and hingeless (or bearingless) rotors, as presented in Figure 2.1. They are similar in flapping amplitude and response to disturbances and cyclic blade pitch inputs [42]. In this model, an articulated rotor with a flapping hinge is modeled; however, the flap dynamics of a hingeless rotor can also be reflected in the model with an effective hinge offset greater than the geometric equivalent of the articulated rotor (e') or additional approximate spring force (K_β) [43, 42, 44]. In Figure 2.2, hingeless rotor modeling is illustrated; the first rotor in the schematic can be modeled as either the second or the third rotor.

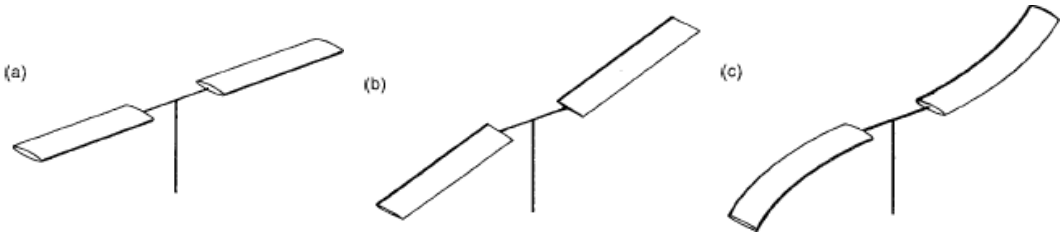

Figure 2.1. Rotor model classifications: (a) teetering; (b) articulated; (c) hingeless or bearingless [42]

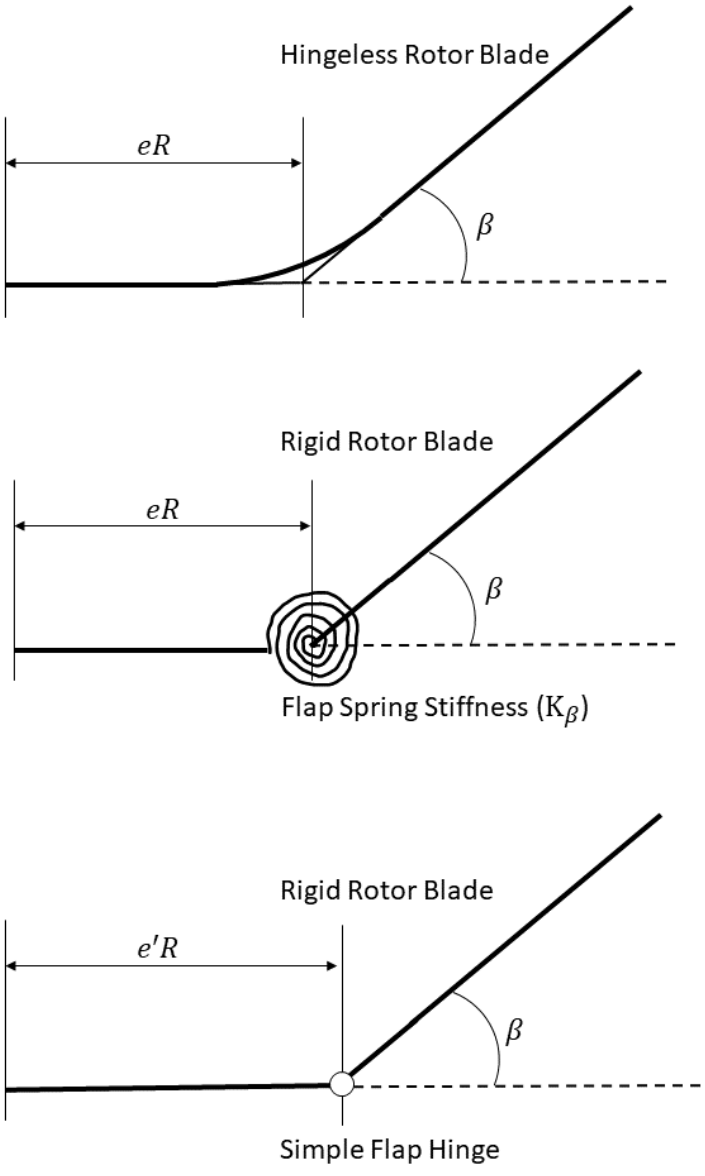

Figure 2.2. Hingeless rotor modeling [44]

2.1 Blade Element Theory

The rotor and propeller model presented in this thesis is based on blade element theory. The blade element theory (BET) estimates the radial and azimuthal aerodynamic loading distribution. It is a rotor design tool as it considers the spanwise change in the rotor blade geometric properties like twist, chord, taper, sweep, and airfoil shape [45, 46, 47]. The BET applies the lifting-line theory [43] to a rotating blade. The main assumption is that the blade section behaves like a quasi-two-dimensional airfoil. Therefore, the BET predicts better for rotors with a high aspect ratio, i.e., low disk loading. Introducing the tip-loss effect to the model increases the model's fidelity for rotors with both low and high disk loading. Since the aerodynamic forces and moments generated by the airfoil are calculated with the local velocities according to that section's induced angle of attack, the BET solution requires a rotor wake estimate [45, 46, 47]. Integration of the air loads over the rotor disk gives the total aerodynamic forces and moments on the rotor hub. The trapezoidal rule is used for integration over the blade. Then, each blade's aerodynamic forces and moments found using BET are added together in the hub-fixed frame to find the total aerodynamic hub forces and moments.

Figure 2.3 shows a blade element isolated from the blade, the local velocities that the blade element encountered, U_T, U_P, and U_R, pitch angle, inflow angle, and angle of attack of the blade element, and the aerodynamic forces, lift and drag, and pitch moment generated on that blade section for any flight condition.

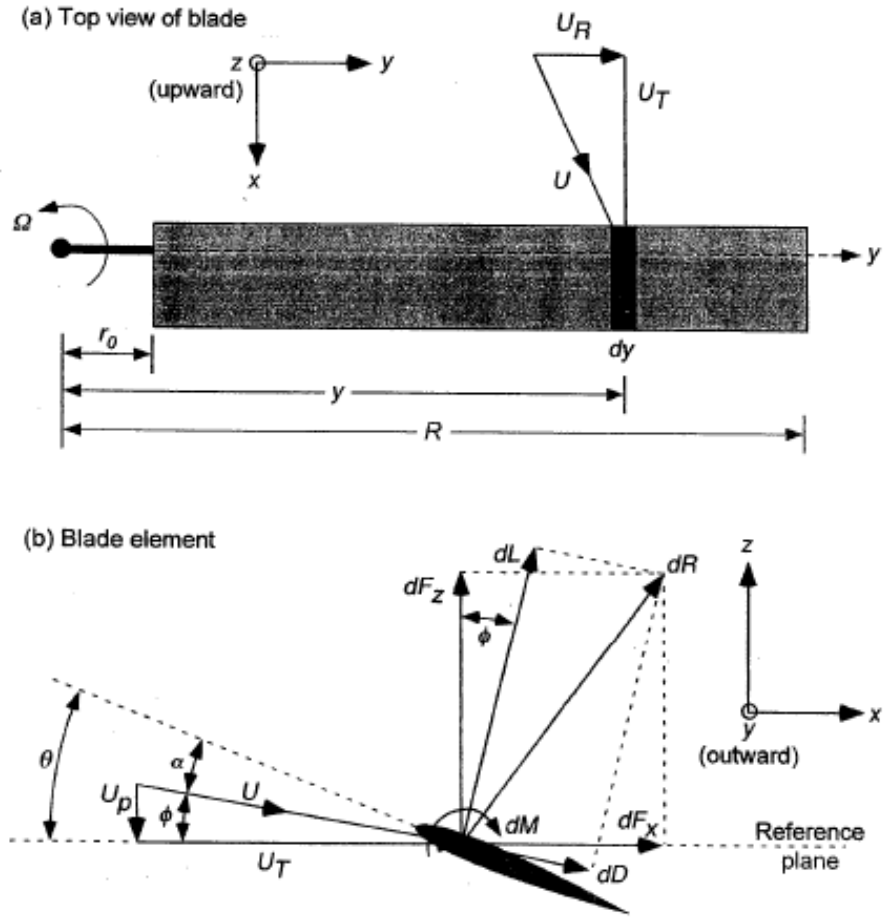

Figure 2.3. Blade element representation on a counterclockwise rotating rotor: (a) Radial position of the blade element; (b) Local air velocities and angles on the blade element and the aerodynamic forces and moments produced by the blade element [47]

2.2 Aerodynamic Root Cutout and Tip Loss Effects

The aerodynamic root cutout is the radial position where the lifting portion of the blade starts. The rotor's root cutout area has a high drag coefficient due to the mechanical parts. Therefore, its effect is higher on profile power compared to induced power [45].

Due to the discrete vortices shed by the finite number of blades, the rotor wake is constrained to a smaller area than the nominal wake boundary. Outboard this area, the lifting capability of the rotor is lost, which is called the tip loss effect [45].

Figure 2.4 shows the actual lift distribution over the blade and the blade element theory solution.

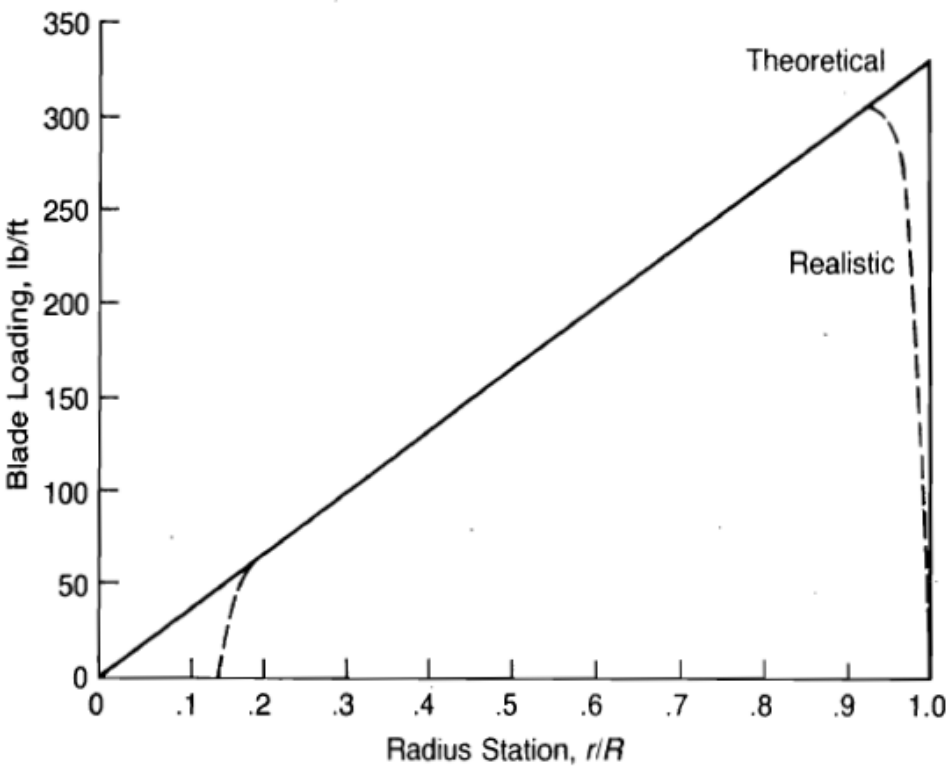

Figure 2.4. Illustration of aerodynamic root cutout and tip loss effect on blade loading [48]

The tip loss effect is included in the empirical equation for the tip loss factor first derived for hover by Prandtl. It correlates with the Goldstein-Lock calculations for lightly loaded rotors [43, 47, 49, 46, 45, 48]. It no longer applies in forward flight; however, since there is no exact theory for tip loss, it can be used approximately [49].

$$B = 1 - \frac{\sqrt{2C_T}}{b} \qquad 2.1$$

The tip loss factor, B, decreases with decreasing number of blades because of the blade-to-blade interference. Also, it reduces with the increasing thrust because of the spacing of the vortex sheets below the rotor (helical pitch of the wake) [47].

Since blade element theory cannot cover the tip loss effect, a correction is required. By defining an effective radius, the loss of lift capacity of the rotor at the blade tips is implemented in the blade element model [45, 49].

$$R_e = BR \tag{2.2}$$

The lift integration should be between the root cutout to the effective radius. However, the drag integration should be done from the root cutout to the tip [48].

A smaller effective area due to tip loss and root cutout effect means higher disk loading, which implies higher induced power [45]. Therefore, an induced power parameter is introduced for inflow correction [45].

$$\kappa = \frac{1}{\sqrt{B^2 - \left(\frac{r_R}{R}\right)^2}} \tag{2.3}$$

For non-uniform inflow correction, κ, is changing to Equation 2.4 [45]:

$$\kappa = \frac{4\sqrt{2}}{5\sqrt{B^2 - \left(\frac{r_R}{R}\right)^2}} \tag{2.4}$$

2.3 Generating Aerodynamic Coefficients of Airfoils

An airfoil is a two-dimensional geometry composed of thickness distribution, camber line, and chord line. It generates lift, drag, and a pitch moment. Since the BET requires the aerodynamic characteristics of the airfoil of the blade element, those forces and that moment are needed to be estimated. Empirical methods like wind tunnel tests, Computational Fluid Dynamics (CFD) analysis, and tabulated or presented data in the literature [50, 51] can be used for this purpose [43].

The aerodynamic coefficients are the functions of the angle of attack, Mach number, Reynolds number, roughness effect, and some aerodynamic devices like flaps, slats, spoilers, etc. Assuming that since the search of interest area is beyond the laminar to turbulent boundary layer transition point for the rotating blades, the Reynolds number parameter is neglected. There is no aerodynamic device on the rotating blade airfoil, so they are neglected too. Also, the roughness effect can be ignored for simulation purposes. Therefore, aerodynamic coefficients depend on the angle of attack and the Mach number parameters [43].

$$C_l = C_l(\alpha, M) \quad 2.5$$

$$C_d = C_d(\alpha, M) \quad 2.6$$

$$C_m = C_m(\alpha, M) \quad 2.7$$

Figure 2.5 and Figure 2.6 show the change in lift and drag coefficients with angle of attack and Mach number. As can be seen in Figure 2.5 and Figure 2.6, increasing the Mach number increases the lift-curve slope and drag coefficient of the airfoil. In addition, with the increasing Mach number, the center of pressure moves aft, increasing the airfoil's nose-down moment. Therefore, the Mach number effect in the airfoil moment needs to be reflected in the quasi-static model in the case of the absence of a $C_m$table.

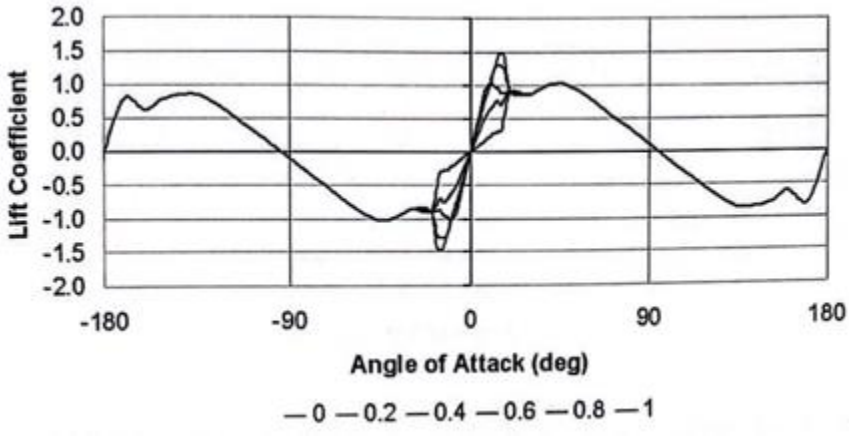

Figure 2.5. Lift coefficient table of NACA0015 [43]

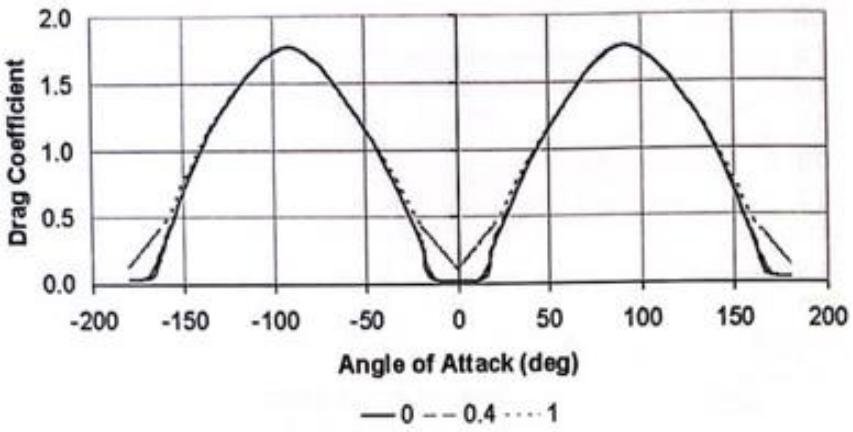

Figure 2.6. Drag coefficient table of NACA0015 [43]

After the airfoil stalled, the Mach number effect is also ignored since the data-gathering process is only rigorous for $M = 0$.

$\alpha = [-15^o, 15^o]$ range is called the linear range for every airfoil. Assuming that the airfoils operate in the linear range, the most thorough analyses are required in this interval. In the absence of aerodynamic coefficient data below considerations can be used in the linear range for simulation purposes [43].

- The lift curve slope is nearly 5.73 or 2π as in thin airfoil theory.
- Drag is constant and $C_{d_0} \sim 0.01 - 0.015$.
- The moment coefficient is zero.

2.4 Rotor and Propeller Models

In the scope of this thesis, partially articulated rotor, propeller, ducted rotor or propeller, and coaxial rotor or propeller models are implemented. Having different pros and cons, they are selected according to the mission and design purpose of the eVTOL in various configurations.

2.4.1 Articulated Rotor Model

When the articulated rotor model is activated, blades gain a degree of freedom in the out-of-plane direction. A flap hinge is added to the model so the blades can flap up or down freely. Second-order flapping dynamics are computed using Euler numeric time-domain integration method twice on the flapping acceleration found by Euler's equations at the flap hinge.

- For maneuvering flight simulation, second-order flapping dynamics give a better response than quasi-static solutions because the quasi-static solution assumes that the flapping motion has high enough damping with high enough frequency that all transients die out rapidly.
- In addition, it presumes harmonic motion in which the periodic terms do not affect the stability of the whole system. Therefore, the quasi-static solution is not conclusive about the rotor stability.
- Also, the quasi-static solution is mostly limited to first harmonics since adding higher harmonics is cumbersome. Hence, making an aeroelastic analysis due to the higher harmonic forcing functions with a quasi-static solution is difficult. However, the aeroelastic analysis is easier with a time-domain integration flapping solution.

The effect of higher harmonic forcing functions in this model is not very much perceived. A rigid blade assumption is made for all the rotor and propeller models, and higher harmonics in the inflow model are not calculated. Even if there was forcing at higher harmonics, they decrease rapidly, and the action is directed towards rigid body motion due to the rigid blade assumption. However, in aeroelastic analysis, it can be noticed that higher harmonics can force an elastic mode that is not damped. Therefore, the elastic model and the Peters-He inflow model with higher states should be implemented for rotor stability analysis [43].

In Figure 2.7, the blade shape of the Lynx helicopter rotor at the advancing and retreating side at 150 knots flight is given as an example of an elastic blade. The flapping of a rigid blade versus an elastic blade can be observed in this figure.

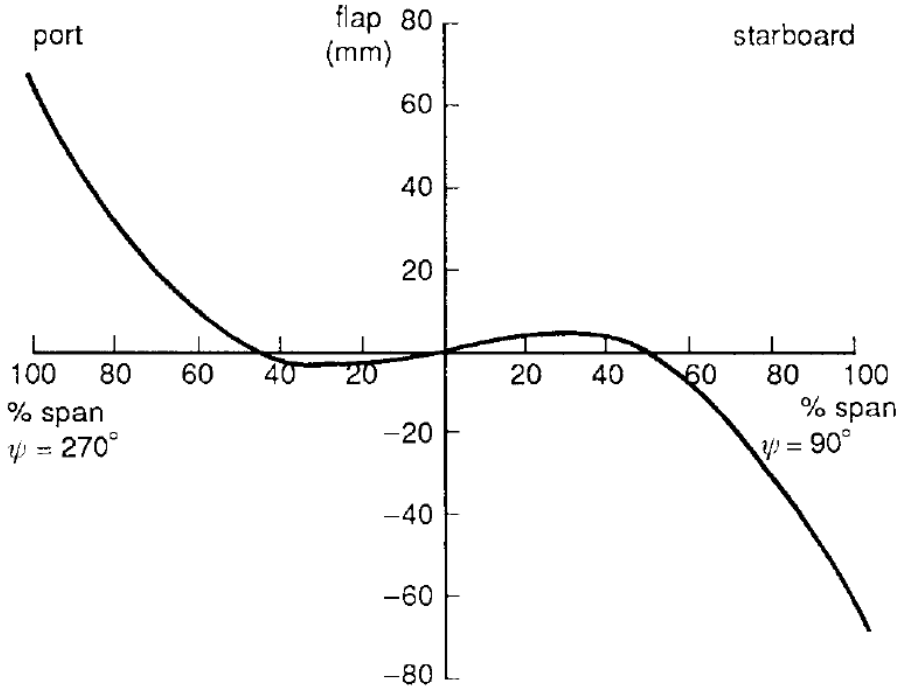

Figure 2.7. An example blade shape at the advancing and retreating side of a rotor [42]

2.4.1.1 Flap Dynamics

Euler's equations about the flap hinge location govern the motion of the rigid blade in the out-of-plane direction. Equation 2.8 shows Euler's equation about the hinge point of a blade:

$$\check{J}_{Blade} \cdot \vec{\alpha}_{Blade} + \vec{\omega}_{Blade} \times \check{J}_{Blade} \cdot \vec{\omega}_{Blade} + m\vec{r}_{BldCG2Hng} \times \vec{a}_{Hinge} = \sum \vec{M}_{Aero} \quad 2.8$$

where,

- $-\vec{\omega}_{Blade} \times \check{J}_{Blade} \cdot \vec{\omega}_{Blade}$ is gyroscopic moment.

Linear acceleration of the flap hinge is given in Equation 2.9:

$$\vec{a}_{Hinge} = \vec{a}^{Hub}_{Hinge2Hub} + 2\vec{\omega}_{Hub} \times \vec{V}^{Hub}_{Hinge2Hub} + \vec{\alpha}_{Hub} \times \vec{r}_{Hinge2Hub} + \vec{\omega}_{Hub} \times \left(\vec{\omega}_{Hub} \times \vec{r}_{Hinge2Hub}\right) + \vec{a}_{Hub} \quad (2.9)$$

where,

- $-2\vec{\omega}_{Hub} \times \vec{V}^{Hub}_{Hinge2Hub}$ is Coriolis acceleration and
- $-\vec{\omega}_{Hub} \times \left(\vec{\omega}_{Hub} \times \vec{r}_{Hinge2Hub}\right)$ is centrifugal acceleration.

Since the hinge is attached to the hub, it does not have linear acceleration and velocity relative to the hub-fixed frame originating at the hub:

$$\vec{a}^{Hub}_{Hinge2Hub} = \vec{0} \quad (2.10)$$

$$\vec{V}^{Hub}_{Hinge2Hub} = \vec{0} \quad (2.11)$$

Inertia matrix, angular acceleration vector of the blade, and angular velocity vector of the blade in Equation 2.8 are as Equation 2.12, Equation 2.13, and Equation 2.14:

$$\check{J}_{Blade} = I_B \vec{u}_2^{Blade} \vec{u}_2^{Blade} + I_B \vec{u}_3^{Blade} \vec{u}_3^{Blade} \quad (2.12)$$

$$\vec{\alpha}_{Blade} = \ddot{\beta}\vec{u}_2^{Blade} + \ddot{\Omega}\vec{u}_3^{Hub} + \vec{\alpha}_{Hub} \quad (2.13)$$

$$\vec{\omega}_{Blade} = \dot{\beta}\vec{u}_2^{Blade} + \dot{\Omega}\vec{u}_3^{Hub} + \vec{\omega}_{Hub} \quad (2.14)$$

Equation 2.12, Equation 2.13, and Equation 2.14 are substituted in Equation 2.8:

$$\begin{aligned}(I_B \vec{u}_2^{Blade} \vec{u}_2^{Blade} + I_B \vec{u}_3^{Blade} \vec{u}_3^{Blade}) \cdot (\ddot{\beta}\vec{u}_2^{Blade} + \ddot{\Omega}\vec{u}_3^{Hub} + \vec{\alpha}_{Hub}) \\ + (\dot{\beta}\vec{u}_2^{Blade} + \dot{\Omega}\vec{u}_3^{Hub} + \vec{\omega}_{Hub}) \times (I_B \vec{u}_2^{Blade} \vec{u}_2^{Blade} \\ + I_B \vec{u}_3^{Blade} \vec{u}_3^{Blade}) \cdot (\dot{\beta}\vec{u}_2^{Blade} + \dot{\Omega}\vec{u}_3^{Hub} + \vec{\omega}_{Hub}) \\ + m\vec{r}_{BldCG2Hng} \times (\vec{\alpha}_{Hub} \times \vec{r}_{Hinge2Hub} \\ + \vec{\omega}_{Hub} \times \left(\vec{\omega}_{Hub} \times \vec{r}_{Hinge2Hub}\right) + \vec{a}_{Hub}) = \sum \vec{M}_{Aero}\end{aligned} \quad (2.15)$$

If there is a spring in the system, a spring term is added to the right-hand side of Equation 2.15:

$$\begin{aligned}(I_B\vec{u}_2^{Blade}\vec{u}_2^{Blade} + I_B\vec{u}_3^{Blade}\vec{u}_3^{Blade}) \cdot (\ddot{\beta}\vec{u}_2^{Blade} + \ddot{\Omega}\vec{u}_3^{Hub} + \vec{\alpha}_{Hub}) \\ + (\dot{\beta}\vec{u}_2^{Blade} + \dot{\Omega}\vec{u}_3^{Hub} + \vec{\omega}_{Hub}) \times (I_B\vec{u}_2^{Blade}\vec{u}_2^{Blade} \\ + I_B\vec{u}_3^{Blade}\vec{u}_3^{Blade}) \cdot (\dot{\beta}\vec{u}_2^{Blade} + \dot{\Omega}\vec{u}_3^{Hub} + \vec{\omega}_{Hub}) \\ + m\vec{r}_{BldCG2Hng} \times (\vec{\alpha}_{Hub} \times \vec{r}_{Hinge2Hub} \\ + \vec{\omega}_{Hub} \times \left(\vec{\omega}_{Hub} \times \vec{r}_{Hinge2Hub}\right) + \vec{a}_{Hub}) \\ = \sum \vec{M}_{Aero} - K_\beta\beta\vec{u}_2^{Blade}\end{aligned} \quad 2.16$$

This equation is the final system of equations for the blade motion, and the second equation of the system, Equation 2.16, corresponds to the flapping motion.

2.4.2 Propeller Model

The propeller model has only one degree of freedom around the axis of rotation. In case other models are not used, the propeller model is activated as the default model. This default model is based on BET and the available dynamic inflow models. The stall delay correction is not used but can be implemented for the higher-fidelity propeller model.

2.4.3 Ducted Rotor and Propeller Model

The ducted (shrouded) rotors/propellers/fans are frequently used in the eVTOL designs because of their advantages relative to a conventional rotor of the same size, safety, improved performance in hover, and less noise generation due to the masking effect of the duct. The typical rotor employed in the ducted rotor is small, stiff, and high-solidity, providing the loading capacity for agile maneuvers when they are evaluated from a handling-quality perspective. In addition, they have a considerably larger collective range than an unducted rotor or propeller, assisting achieve the desired maximum thrust. They are less prone to vortex ring state due to much higher

induced velocities and the duct itself preventing the establishment of airflow recirculation. In contrast, the added weight of the duct and the supporting structure, extra drag on the duct in forward flight, and extra complexity and the cost they bring are the side effects of ducted rotors or propellers [47, 52, 45, 53, 54, 55].

The ducted fan model requires two additional implementations on the model.

Unsteady momentum theory, based on the conservation of momentum, is used to calculate the inflow through the rotor. The difference between the dynamic uniform inflow explained in 2.5.1, and the unsteady momentum theory is that the uniform dynamic inflow theory states that the air mass with a spherical volume, not cylindrical, is accelerated through the rotor disk by the rotor/propeller/fan thrust.

The duct thrust is the function of the rotor/propeller/fan thrust and the inflow solution. It is found by taking the difference between total thrust and rotor/propeller/fan thrust. Rotor/propeller/fan thrust is calculated using the model's existing blade element theory implementation. The highest contribution of the duct is seen around the hover condition at high collective angles [52].

The model implies that in hover, half of the thrust is generated by the rotor/propeller/fan, and half of the thrust is created by the duct when there is no wake contraction. Although the rotor/propeller/fan thrust is halved, the power required becomes only $\frac{1}{\sqrt{2}}$ times less since the inflow of a ducted rotor/propeller/fan is $\sqrt{2}$ times larger than an open rotor/propeller/fan with the same disk area. In other words, the thrust and the power of a ducted rotor/propeller/fan with a half disk area of an open rotor/propeller/fan are the same with an open rotor/propeller/fan [52, 47, 45].

Figure 2.7 shows a sketch of a ducted rotor/propeller/fan connected to the body, producing thrust in the z-body fixed frame direction. In the figure, the ducted rotor performs an axial flight with w velocity.

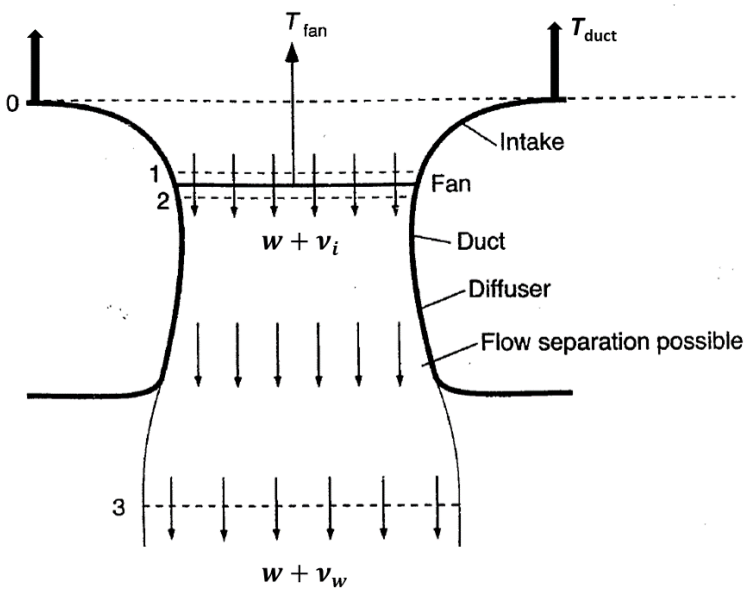

Figure 2.8. Illustration of ducted rotor/propeller/fan in an arbitrary flight condition [47]

It is assumed that for ducted rotors/propellers/fans, the slipstream is attached to the walls inside the duct. Furthermore, experiments have proven no wake contraction after the duct exit [55].

In the steady momentum analysis, mass conservation gives the relation between inflow at the rotor disk, v_i, and the far wake, v_w. Bernouilli's equation upstream and downstream of the duct gives the rotor/propeller/fan thrust, T_{fan}. Finally, the momentum theory gives the total thrust of the ducted rotor/propeller/fan, T_{total}.

Mass conservation yields the relation in Equation 2.18. In Equation 2.18, the tip gap between the blade tip and the duct wall is neglected.

$$\rho A_1(w + v_i) = \rho A_3(w + v_w) \tag{2.17}$$

$$v_w = \frac{w + v_i}{A_3/A_1} - w \tag{2.18}$$

The ratio of duct exit area to rotor disk area is defined as the diffuser expansion ratio, σ_d. When $\sigma_d = 1$, the duct is ideal where $v_i = v_w$. For an open rotor/propeller/fan $2v_i = v_w$.

$$\sigma_d = \frac{A_3}{A_1} \tag{2.19}$$

where $A_1 = A_2 = \pi R^2$.

Momentum theory yields Equation 2.20:

$$T_{total} = \rho A_1 \sqrt{u^2 + v^2 + (w + v_i)^2} \left(\frac{w + v_i}{\sigma_d} - w \right) \tag{2.20}$$

Applying Bernouilli's equation yields the pressure difference across the rotor disk, or T_{fan}/A_1:

$$p_0 + \frac{1}{2}\rho(u^2 + v^2 + w^2) = p_1 + \frac{1}{2}\rho(w + v_i)^2 \tag{2.21}$$

$$p_3 + \frac{1}{2}\rho\left(u^2 + v^2 + \left(\frac{w + v_i}{\sigma_d}\right)^2\right) = p_2 + \frac{1}{2}\rho(w + v_i)^2 \tag{2.22}$$

where $p_0 = p_3$.

$$T_{fan} = (p_2 - p_1)A_1 \tag{2.23}$$

Using Equation 2.21 and Equation 2.22, rotor/propeller/fan thrust, T_{fan}, is found as Equation 2.24:

$$T_{fan} = \rho A_1 \left| w + \frac{1}{2} v_w \right| v_w \tag{2.24}$$

It should be noted that forward speed does not appear in the T_{fan} expression, as the rotor/propeller/fan operates under only the local flow conditions. Absolute value is to manage the case of reverse flow through the duct [52]. For example, when the diffuser expansion ratio is less than 1, the induced velocity is throttled through the upstream [55].

Unsteady momentum theory introduces the integral of the time rate of change of momentum inside the control volume to the momentum conservation equation. Total thrust is the sum of the momentum fluxes and the term $\rho A_1 H_M \dot{v}$. H_M is the effective height of the air cylinder accelerated by the total thrust.

$$T_{total} = \rho A_1 H_M \dot{v}_i + \rho A_1 \sqrt{u^2 + v^2 + (w + v_i)^2} \left(\frac{w + v_i}{\sigma_d} - w \right) \qquad 2.25$$

Unsteady inflow effects likewise appear in Bernouilli's equation; therefore, rotor/propeller/fan thrust expression has the additional term $\rho A_1 H_F \dot{v}$. H_F is the effective height of the air cylinder accelerated by the rotor/propeller/fan thrust. It can be calculated from actuator disk theory [45] ($H_F = \frac{8R}{3\pi}$ for open rotors) or found empirically [52].

$$T_{fan} = \rho A_1 H_F \dot{v}_i + \rho A_1 \left| w + \frac{1}{2} v_w \right| v_w \qquad 2.26$$

H_M and H_F decide the dynamic response of the ducted rotor/propeller/fan to input, like collective. $H_M = H_F$ results in pure lag in response and $H_M < H_F$ results in reversal of the sign of response at high frequency [52].

T_{fan} can also be calculated using the blade element theory. Rotor/propeller/fan thrust found from BET and Bernouilli's equation have to be the same. Therefore, air velocity induced by the rotor/propeller/fan can be found by equating them.

$$\dot{v}_i = \frac{T_{fan} - \rho A_1 \left| w + \frac{1}{2} v_w \right| v_w}{\rho A_1 H_F} \qquad 2.27$$

This model is suitable for real-time simulations since the dynamic system is always stable [52].

The duct thrust contribution is found by subtracting the rotor/propeller/fan thrust from the total thrust calculation.

$$T_{duct} = T_{total} - T_{fan} \qquad 2.28$$

The Goodman's tip correction covers the declining effect of tip vortices due to duct. As the gap between the duct wall and the blade tip decreases, Goodman's tip loss factor approaches 1, and as the gap distance goes to infinity, it approaches Prandtl's tip loss factor, which is explained in 2.2.

Additional enhancements to the ducted fan model can be made by introducing duct-fan interference correction and adding the effect of the duct on the edgewise velocity, including swirl losses which are higher at higher rotational speeds, and the effect of stator blades on the inflow swirl conditions, including the aerodynamic forces of the stator blades, and adding a correction for high solidity.

2.4.4 Coaxial Rotor and Propeller Model

Considering the need for smaller footprints, reducing the net size of the rotors for the same weight, and not requiring any anti-torque generating component are the two main advantages that make coaxial rotor designs favorable, especially for eVTOLs. One drawback is that the aerodynamic efficiency of the rotor system becomes less due to the interaction between rotor wakes. Another is the swirl losses in the downstream wake in thrust generation, which gains importance, especially for the high disk loading propellers.

Assuming that the rotors are sufficiently close to each other, the interference-induced power factor, κ_{int}, is found as in Equation 2.29 from momentum theory.

$$\kappa_{int} = \frac{(P_i)_{CoaxialRotor}}{2(P_i)_{IsolatedRotor}} = \sqrt{2} \qquad 2.29$$

However, this is an overestimation compared to experiments.

Usually, the lower rotor is placed in the vena contracta of the upper rotor. By utilizing the momentum theory and the application of the interference-induced power factor, κ_{int}, is calculated with the assumption that the upper rotor's wake affects the inner half of the area of the lower rotor. The lower rotor is in the fully developed slipstream of the upper rotor. The upper rotor is not disturbed by the lower rotor's wake. In Figure 2.9, the wake of the coaxial rotor is illustrated.

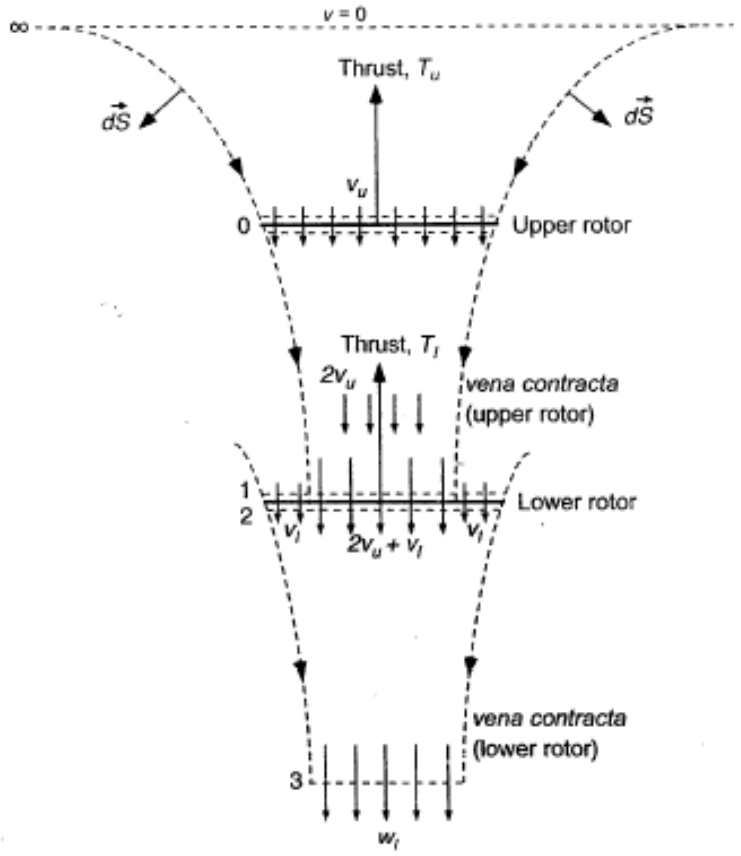

Figure 2.9. Coaxial rotor wake analysis [47]

If the lower rotors generate the same thrust, the interference-induced power factor is as in Equation 2.30:

$$\kappa_{int} = \frac{(P_i)_{CoaxialRotor}}{2(P_i)_{IsolatedRotor}} = \frac{1+\sqrt{17}}{4} = 1.281 \qquad 2.30$$

However, the empirical value for the interference-induced power factor is found as [47]:

$$\kappa_{int} \sim 1.16 \qquad 2.31$$

This empirical value is used to calculate the relation between the inflow of upper and lower rotors:

$$v_l \sim 0.32 v_u \qquad 2.32$$

This inflow relation is used for the coaxial rotor model.

2.5 Inflow Model

The fidelity of the rotor model can be increased by using a more established inflow model. As the complexity increases in the inflow model, the fidelity increases. However, it brings a higher computational load [56]. Therefore, the appropriate selection is needed according to the scope of the application.

In this rotor model, two different dynamic inflow theories are employed since, in real-time simulations, dynamic inflow models are commonly used. The uniform dynamic inflow model is sufficient for hover and axial flight simulations. For edgewise flight simulations, longitudinal inflow variation is necessary to correct the longitudinal aerodynamic force and moment distribution affecting the lateral moment imbalance of the articulated rotor. Pitt-Peters dynamic inflow model can be used for this purpose [56]. For higher levels of fidelity, Peters-He generalized dynamic wake theory with higher states should be implemented in the model.

2.5.1 Uniform Dynamic Inflow Model

Dynamic uniform inflow calculates the velocity of the air mass passing through the rotor disk using the thrust extracted from the application of the blade element theory. The theory states that the thrust is equal to momentum flux through the rotor disk and the total air mass accelerated by the thrust. The air mass that is accelerated by the rotor has a spherical volume centered on the rotor hub [43, 56].

$$\dot{v} = \frac{T - 2\rho\pi R^2 \sqrt{u^{TPP^2} + v^{TPP^2} + (v + w^{TPP})^2} v}{\frac{4}{3}\pi(kR)^3\rho} \tag{2.33}$$

In Equation 2.33, k is the effective radius gain.

$$0.76 \leq k \leq 0.84 \tag{2.34}$$

2.5.2 Pitt-Peters Dynamic Inflow Model

The Pitt-Peters inflow model is based on the actuator disk theory. It estimates the wake of the rotor in the radial direction at all azimuth locations [57, 58, 59, 60, 56, 45]. It contains both quasi-steady and unsteady parts. The quasi-steady part gives the inflow solution on the rotor disk:

$$\lambda(r,\psi) = \lambda_0 + \lambda_{1s}\left(\frac{r}{R}\right)\sin(\psi) + \lambda_{1c}\left(\frac{r}{R}\right)\cos(\psi) \qquad 2.35$$

where r is the radial location and ψ is the azimuthal location.

According to the Pitt-Peters inflow model, the air is accelerated by the hub's aerodynamic thrust, aerodynamic roll moment, and aerodynamic pitch moment. The directions of the forcing terms are defined in 3.1.1.1. They are a function of sectional blade lift, Equation 2.36, Equation 2.37, and Equation 2.38:

$$C_T = \frac{1}{\rho(\pi R^2)(\Omega R)^2}\int_0^{2\pi}\int_0^R L dr d\psi \qquad 2.36$$

$$C_L = \frac{1}{\rho(\pi R^2)(\Omega R)^2 R}\int_0^{2\pi}\int_0^R L r sin(\psi) dr d\psi \qquad 2.37$$

$$C_M = -\frac{1}{\rho(\pi R^2)(\Omega R)^2 R}\int_0^{2\pi}\int_0^R L r cos(\psi) dr d\psi \qquad 2.38$$

The unsteady part is apparent in the time lag term of the dynamic linear system, Equation 2.39:

$$\frac{1}{\Omega}\widehat{M}\begin{bmatrix}\dot{\lambda}_0\\ \dot{\lambda}_{1s}\\ \dot{\lambda}_{1c}\end{bmatrix} + \widehat{V}\widehat{L}^{-1}\begin{bmatrix}\lambda_0\\ \lambda_{1s}\\ \lambda_{1c}\end{bmatrix} = \begin{bmatrix}C_T\\ C_L\\ -C_M\end{bmatrix} \qquad 2.39$$

where $\widehat{M}$, $\widehat{V}$, and $\widehat{L}$ are mass, flow parameter, and influence coefficient matrices, respectively. They are obtained from Equation 2.40, Equation 2.41, and Equation 2.45:

$$\widehat{M} = \frac{1}{\pi}\begin{bmatrix} \frac{128}{75} & 0 & 0 \\ 0 & \frac{16}{45} & 0 \\ 0 & 0 & \frac{16}{45} \end{bmatrix} \quad 2.40$$

$$\widehat{V} = \begin{bmatrix} V_T & 0 & 0 \\ 0 & \frac{\mu_r^2 + (\lambda_r + \lambda_0)\lambda_r}{V_T} & 0 \\ 0 & 0 & \frac{\mu_r^2 + (\lambda_r + \lambda_0)\lambda_r}{V_T} \end{bmatrix} \quad 2.41$$

The inflow and advance ratio of the TPP are given in Equation 2.42 and Equation 2.43. Non-dimensional total velocity is calculated in Equation 2.44:

$$\lambda_r = \lambda_0 + \frac{|\bar{V}_{Hub}^{TPP}| \sin(\alpha_{TPP})}{\Omega R} \quad 2.42$$

$$\mu_r = \frac{|\bar{V}_{Hub}^{TPP}| \cos(\alpha_{TPP})}{\Omega R} \quad 2.43$$

$$V_T = \sqrt{\lambda_r^2 + \mu_r^2} \quad 2.44$$

$$\hat{L} = \begin{bmatrix} 0.5 & 0 & -\frac{15}{64}\pi\sqrt{\frac{1-\sin(\alpha_{TPP})}{1+\sin(\alpha_{TPP})}} \\ 0 & \frac{4}{1+\sin(\alpha_{TPP})} & 0 \\ \frac{15}{64}\pi\sqrt{\frac{1-\sin(\alpha_{TPP})}{1+\sin(\alpha_{TPP})}} & 0 & \frac{4\sin(\alpha_{TPP})}{1+\sin(\alpha_{TPP})} \end{bmatrix} \quad 2.45$$

The angle of attack TPP is expressed as in Equation 2.46:

$$\alpha_{TPP} = \tan^{-1}\frac{|\lambda_r|}{\mu_r} \quad 2.46$$

The effect of the sideslip must be covered, and the wake distortion model must be added to correct the inflow estimations.

2.6 Numerical Solution

Fixed step, Euler integration is used to solve the dynamic systems [43]. For a state x:

$$x^{t+1} = x^t + \dot{x}^t dt \qquad 2.47$$

where dt is the time step.

Euler integration is selected because it is the simplest among the other numerical methods, and the model is evaluated once per time step. The one drawback is that it causes excessive error building up. A smaller step size could minimize the error; however, since a smaller step size also increases the computational load, it makes it harder to reach real-time simulation. Therefore, step size selection needs to be done carefully.

2.7 Trim Algorithm

This thesis uses controllers to obtain trim conditions in the model applications as the trim algorithm.

2.7.1 Isolated Rotor

For isolated rotor comparisons in Chapter 4, Model Validation, integral controllers are used to bring the rotor model to the state where it generates the reference thrust and reference moments in collective, roll, and pitch channels. Collective and cyclic inputs are produced from the controllers' output and fed back to the rotor model. The errors between the reference values and the outputs of the rotor model are minimized until the desired cost function is reached. Reference thrust, reference roll moment, and reference pitch moment are attained from the wind tunnel test data to compare the test data and the model outputs. Figure 2.10 shows the block diagram of isolated rotor trim algorithm.

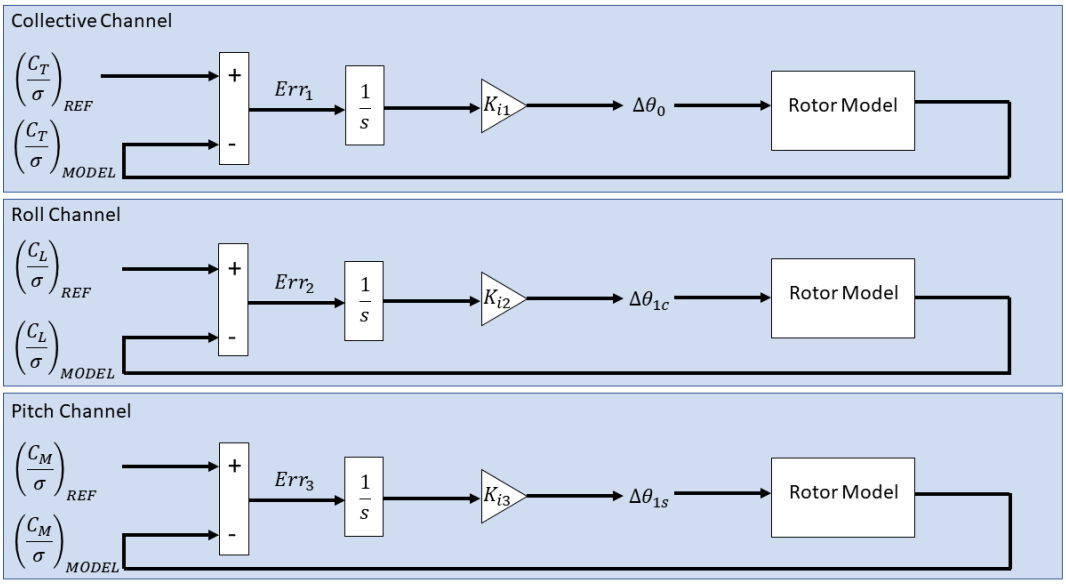

Figure 2.10. Block diagram of isolated rotor trim algorithm

$$Cost = Err_1^2 + Err_2^2 + Err_3^2 \qquad 2.48$$

When the cost function $Cost \leq 10^{-15}$ is obtained, the trim is accomplished.

Integral gains are not scheduled with forward speed in the model validation application. Therefore, as the airspeed gets higher, reaching the desired trim condition becomes more difficult. For better performance, gains are needed to be tuned at each forward speed. For this application, gains are selected as $K_{i1} = K_{i2} = K_{i3} = 1$.

2.7.2 eVTOL Application

In the eVTOL application, Chapter 5, there are eight rotors on the top and two propellers at the back of the eVTOL configurations. The PI controllers trim the eVTOL to hover condition and then accelerate to 20 knots forward flight. Each rotor and propeller is driven with a separate electric motor. The identification number of motors and rotors and propellers that are driven by those motors are identical. The motors are grouped to control the eVTOL in five channels. The delta voltage outputs

are fed to the motors in $(+)\ \Delta Thrust$ column with the same delta voltage, and to the motors in $(-)\ \Delta Thrust$ column with delta voltage multiplied by -1. In Table 2.1, the groups are given. Each motor might get delta voltage input from several control channels. For example, for an eVTOL in forward flight pitch-up maneuver, motor #1 might get input from the heave channel to maintain the thrust, from the pitch channel to generate pitch moment, and from the roll and yaw channel to stabilize the air vehicle. Positive delta voltage input increases the rotational speed of the rotor or propeller; consequently, the thrust gets higher. Negative delta voltage input decreases the rotational speed of the rotor or propeller; consequently, the thrust gets lower. By manipulating the thrust values of each rotor and propeller, a control moment is generated due to the force imbalance in the desired channel.

Table 2.1. Control channels

	Motor ID Numbers	
Control Channels	$(+)$ $\boldsymbol{\Delta Thrust}$	$(-)$ $\boldsymbol{\Delta Thrust}$
Heave	1,2,3,4,5,6,7,8	-
Pitch	1,2,5,6	3,4,7,8
Roll	5,6,7,8	1,2,3,4
Yaw	1,2,7,8	3,4,5,6
Forward Speed	9,10	-

Figure 2.11 shows the block diagram of the five channels' eVTOL flight dynamics model trim algorithm.

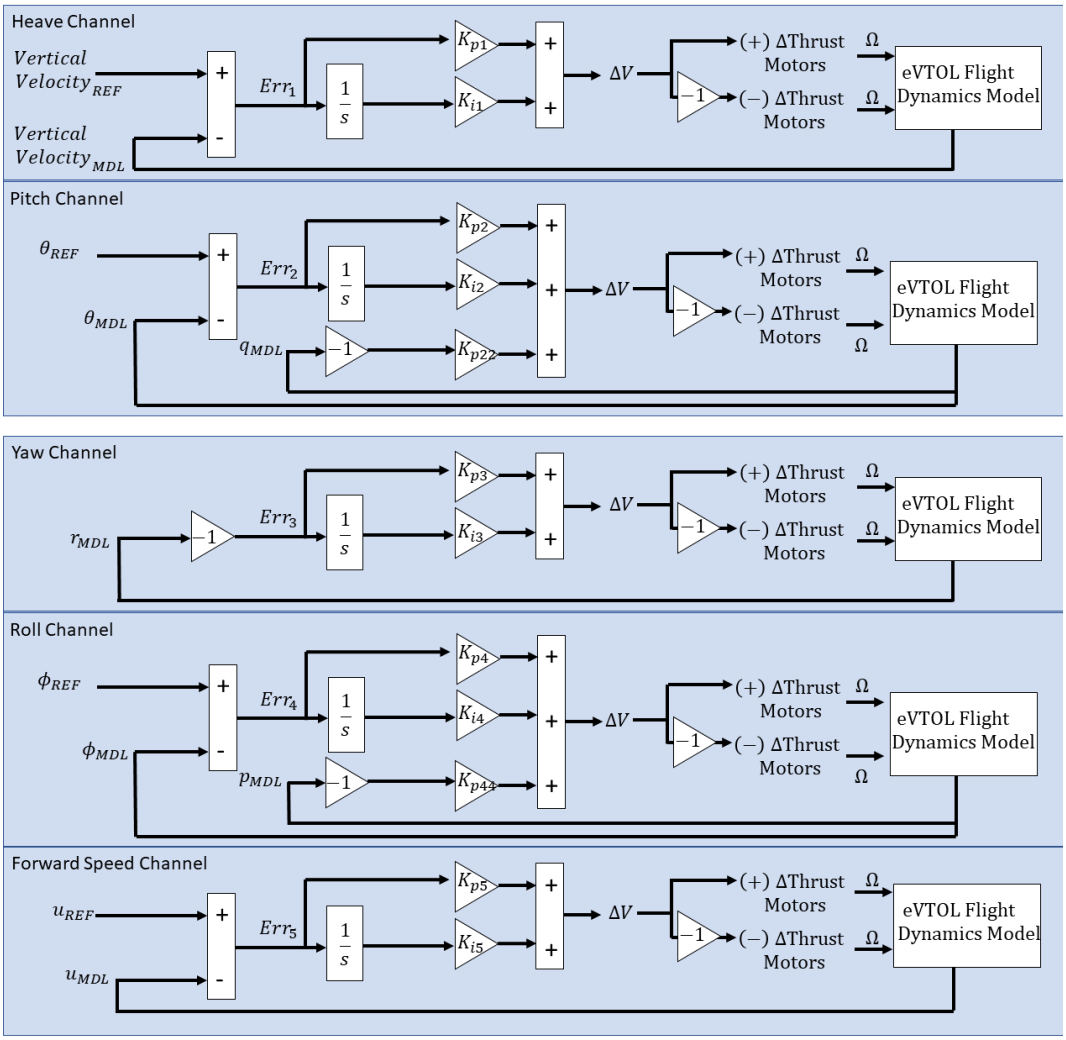

Figure 2.11. Block diagram of eVTOL flight dynamics model trim algorithm

$$Cost = Err_1^2 + Err_2^2 + Err_3^2 + Err_4^2 + Err_5^2 + p^2 + q^2 \qquad 2.49$$

When the cost function $Cost \leq 10^{-5}$ is obtained, the trim is accomplished. For better performance, gains are needed to be tuned at each forward speed.

As a fourth configuration, the propellers at the back are modeled as constant rpm, variable pitch propellers. The rotational speeds of the propellers are held at 2000 rpm, and delta collective pitch angle is used to provide forward speed control. In that case, the forward speed channel changes to Figure 2.12.

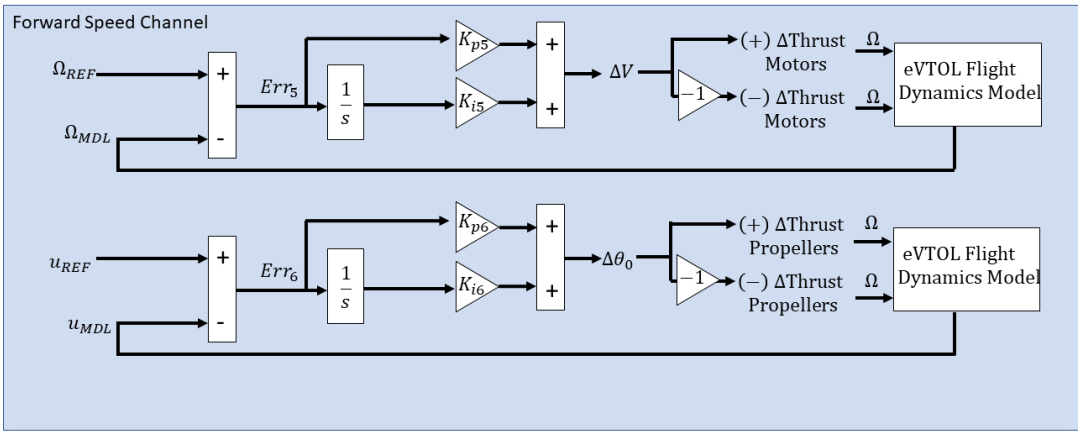

Figure 2.12. Block diagram forward speed control channel for constant rpm, variable pitch control propellers

CHAPTER 3

IMPLEMENTATION OF DYNAMIC ROTOR AND PROPELLER MODEL

The rotor and propeller model is developed in a MATLAB-Simulink environment using a MATLAB Function block. MATLAB Function block is used to generate a MATLAB function code in Simulink. It is applicable for embeddable C/C++ code generation. Since it is cheap in terms of build and simulation time, it becomes preferable as the model promises to make any number of rotor or propeller simulations possible. The subsystem is treated as an atomic unit to enable code generation. The sample time is set to 0.0025 seconds. Fixed-step, Euler solver is used.

The model's structure consists of various functions and an input set that rules them. Each function is a mathematical model of a different part, bringing additional functionality to the model. The ones to be used are selected through the flags in the input set. Functions are finding forces created by a blade element, total forces and moments on a blade, total forces and moments on the hub, flapping dynamics, duct thrust, rotor inflow, and coaxial rotor inflow, and total forces and moments of the coaxial rotor. By just modifying the inputs to the model, every design choice can be reflected in the model. Multiple rotor configurations can be positioned and oriented in the model according to the selected eVTOL design for the analysis. In Table 3.1, inputs to the model are listed.

Table 3.1. Input set to the rotor and propeller model

Rotor Configuration	Propeller	
	Articulated rotor	
	Ducted fan	
	Coaxial rotor	
Rotor	Rotor identification number	
	Number of blades	
	Direction of rotation	
	Hub location w.r.t. c.g.	Fuselage station
		Buttline
		Waterline
	Shaft tilt	Lateral
		Longitudinal
	Radius	
	Root cutout	
	Swashplate Phase Angle	
Blade	Linear twist	Linear twist angle per radial location
	Nonlinear twist	Twist distribution over the radius
	Linear chord	Root chord length
		Taper ratio
	Nonlinear chord	Chord length distribution over the radius
Flapping	Blade mass	
	First mass moment	
	Flapping inertia	
	Hinge offset	
	Hub spring stiffness	
	Precone angle	
	Pitch-Flap coupling (Delta-3 angle)	
Aerodynamic	Airfoil variation over the radius	
	Aerodynamic data of each airfoil	C_l(AoA,Mach)
		C_d(AoA,Mach)
Inflow Selection	Pitt-Peters 3 states dynamic inflow model	
	Uniform dynamic inflow model	
Simulation Conditions	Body translational and rotational velocities	
	Body translational and rotational accelerations	
	Rotational speed and acceleration	
	Blade pitch inputs	θ_0
		θ_{1s}
		θ_{1c}
	Delta shaft tilt	Lateral
		Longitudinal
	Pitt-Peters inflow coefficients of upper rotor/propeller	
	Uniform inflow velocity of upper rotor/propeller	
	Uniform inflow acceleration of upper rotor/propeller	
	Air density	
	Speed of sound	
	C.g. position of the eVTOL	

Inputs, given through the input ports in the left-hand side MATLAB Function block, also listed in the "Simulation Conditions" part of Table 3.1, are updated every sample time. The rest of the inputs are set at the beginning and fixed throughout the simulation.

Inputs having constraints like flags or saturated inputs are given through the subsystem's mask. In Figure 3.1, mask parameters of subsystem "Rotor" are presented.

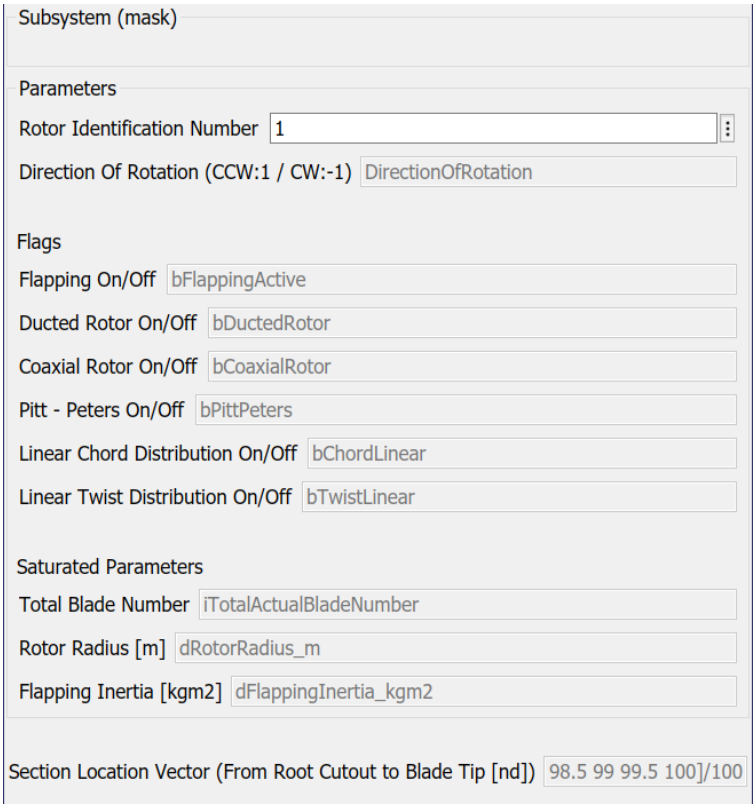

Figure 3.1. Mask parameters of subsystem "Rotor."

Six flags are in the input set to operate the functions and parameters, which are boolean-type inputs. Three of them are to designate the rotor configuration between propeller, articulated, ducted rotor, and coaxial rotor choices, and one of them is to select the dynamic inflow solution. One of them is to decide whether the chord length is linearly distributed according to the taper ratio or not. Lastly, one is to determine twist distribution type, linear or non-linear, along the span.

The input summary table for type, unit, constraint, etc., is in Appendix A. The rotor and propeller model is summarized in the flow chart presented in Figure 3.2. In this model, all inputs are in SI Units, and all calculations are done in SI Units.

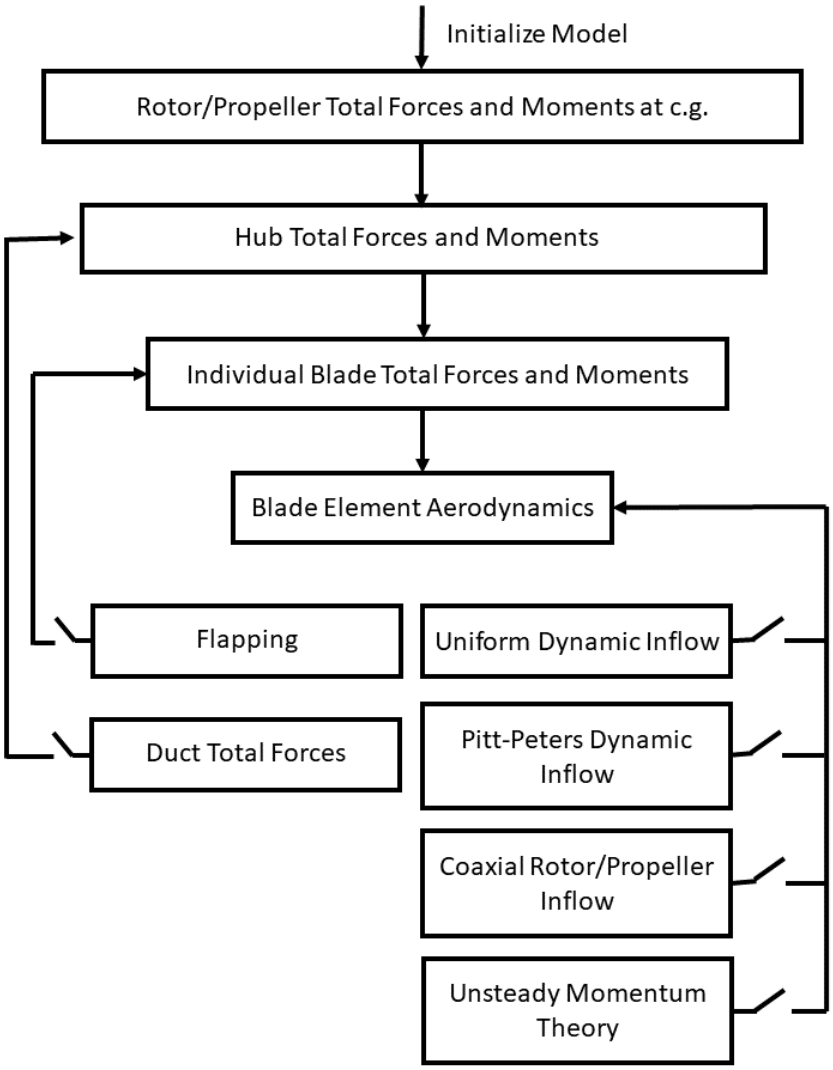

Figure 3.2. Rotor and propeller model flow chart

3.1 Tools

There are four functions independent from the structure of the model used as tools that bring capabilities that MATLAB does not offer in its libraries. These functions are repetitively used in the model, facilitating the implementation.

3.1.1 Transformation Matrix

The Transformation Matrix function navigates between different coordinate systems to make calculations in space. The transformation matrix defined for this tool is based on Rotated Frame, 321(Yaw-Pitch-Roll) sequence.

$$T(\phi,\theta,\psi) = \hat{C}^{(a,b)} = \begin{bmatrix} c\psi c\theta & c\psi s\theta s\phi - s\psi c\phi & c\psi s\theta c\phi + s\psi s\phi \\ s\psi c\theta & s\psi s\theta s\phi + c\psi c\phi & s\psi s\theta c\phi - c\psi s\phi \\ -s\theta & c\theta s\phi & c\theta c\phi \end{bmatrix} \quad 3.1$$

The transformation matrix from a-Frame to b-Frame ($\hat{C}^{(a,b)}$) is given in Equation 3.1, where ϕ is roll angle, θ is pitch angle, and ψ is yaw angle. In the implementation descriptions, the transformation matrix is used with $T(\phi,\theta,\psi)$ expression. If the transpose of the transformation matrix is employed, the "T" superscript is used.

3.1.1.1 Coordinate Systems

Several coordinate systems are utilized to describe the dynamics and kinematics of the eVTOL, its rotors and propellers, and their components in space. In Figure 3.3 and Figure 3.4, representations of these coordinate systems and their relative positions are presented.

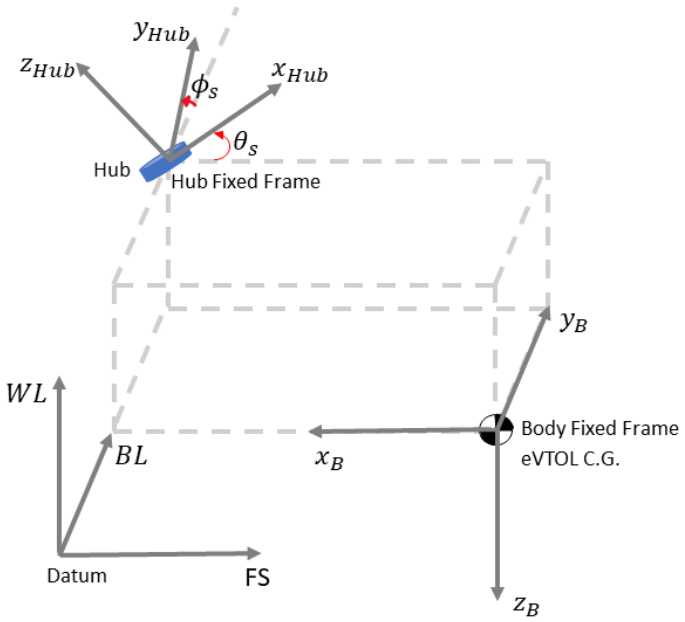

Figure 3.3. Body Fixed Frame and Hub Fixed Frame relative representations

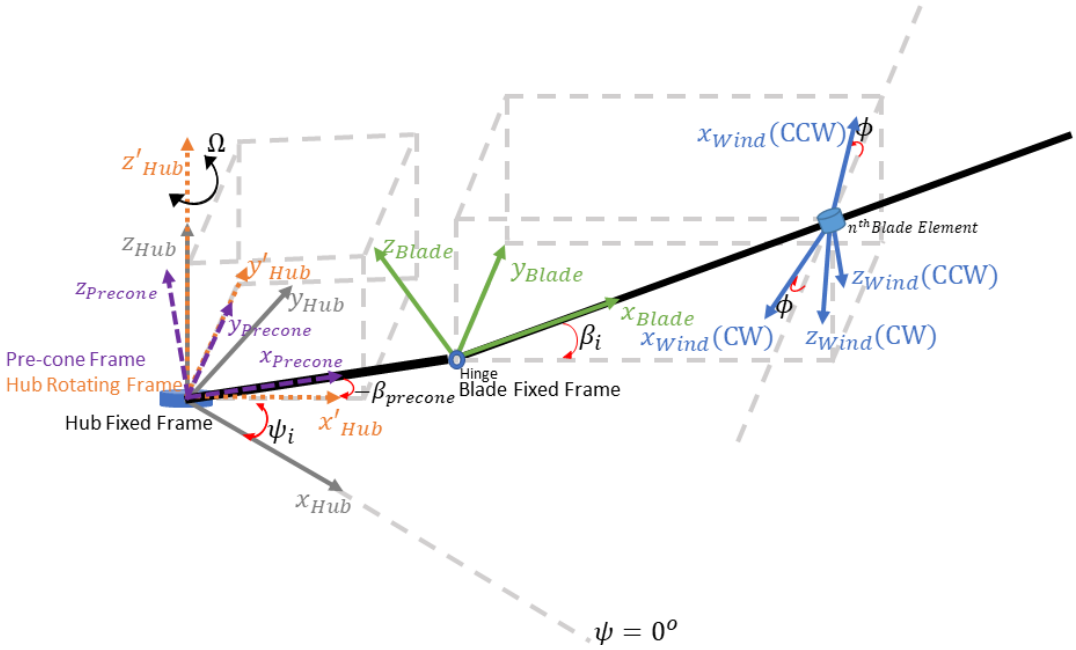

Figure 3.4. Hub Fixed Frame, Hub Rotating Frame, Pre-cone Frame, Blade Fixed Frame, and Wind Frame relative representations

The eVTOL's center of gravity and hub positions are defined in Aircraft Station Coordinate System, fixed to a datum point selected arbitrarily. In common practices, the datum point is at the nose or ahead of the nose of the aircraft, on the plane of

symmetry, and either at the ground or nose tip or somewhere between them. The x-axis, Fuselage Station (FS), points aft. The y-axis, Butt (Buttock) Line (BL), points to the starboard. The z-axis, Water Line (WL), indicates upward. They are mutually orthogonal [43].

Body Fixed Frame defines the 6-DOF motion of the aircraft. It is fixed to the aircraft's center of gravity and translates and rotates with the aircraft. The x-axis of it points to the nose. The z-axis indicates downwards and is orthogonal to the x-axis. The right-hand rule indicates the y-axis, pointing to the starboard.

Five more frames are specified on the rotor to describe rotor dynamics.

Hub Fixed Frame is used as a bridge between the aircraft and the rotor or propeller. It defines the rotor or propeller's total forces and moments. The kinematics of the aircraft is transferred to the rotor or the propeller through Hub Fixed Frame. It is a fixed frame. The origin is on the hub. The x-axis points to the $\psi = 0$ location on the hub plane. The z-axis is pointing upwards and orthogonal to the x-axis. The right-hand rule indicates the y-axis, pointing to the starboard. Hub Rotating Frame rotates around the z-axis with rotational speed Ω. The z-axis of the Hub Fixed Frame and Hub Rotating Frame coincide. The x-axis of it points to the blade tip with $\beta_{precone} = 0$ and $\beta_i = 0$. The right-hand rule indicates the y-axis.

There is an intermediate frame fixed to the hub, Precone Frame. It rotates with the blade. The x-axis of it points to the blade tip with $\beta_i = 0$. The z-axis indicates upwards and is orthogonal to the x-axis. The right-hand rule indicates the y-axis.

Equations of motion of the blade are defined on the Blade Fixed Frame. It is fixed to the flap hinge and rotates with the blade. The x-axis of it points to the blade tip. The z-axis indicates upwards and is orthogonal to the x-axis. The right-hand rule indicates the y-axis. The origin coincides with the hub when there is no hinge or hinge offset.

The Wind Frame is defined for aerodynamic calculations on the blade element. The x-axis is aligned with the local free stream velocity on the blade element. The positive direction is decided by the direction where the airfoil's leading edge faces. Therefore, it varies with the direction of the rotation. The z-axis is pointing downwards. It is orthogonal to the x-axis.

In addition, for inflow estimations, Tip Path Plane Frame is used. The z-axis points upwards in the direction of the thrust of the rotor or propeller. The TPP Frame can be seen in Figure 3.5.

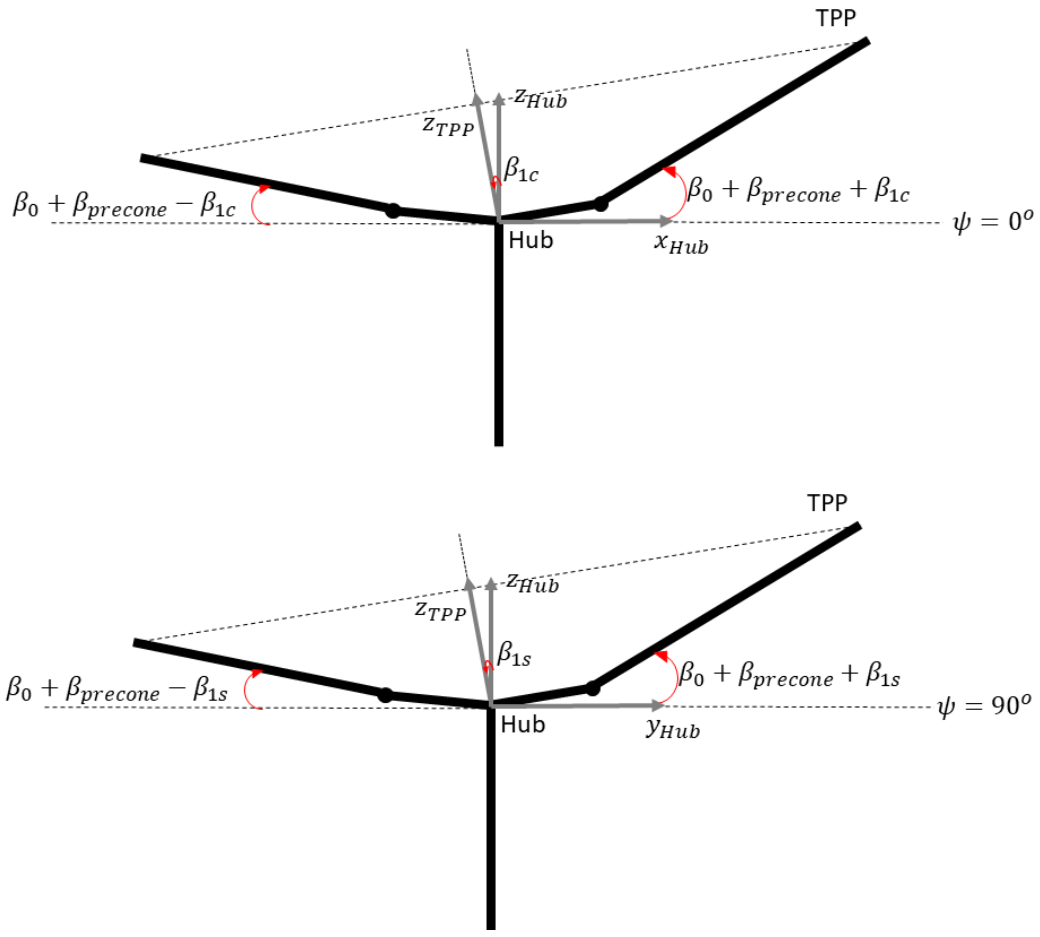

Figure 3.5. Tip Path Plane Frame

In Table 3.2, Euler angles of the RFB-321 sequence are given. The transformation between frames is done using these Euler angles.

Table 3.2. Euler angles between reference frames

Frame Transformation	*Euler Angles*		
$F_{(Datum)}^{AircraftStation} \rightarrow F_{(C.G.)}^{Body}$	$\phi = 0$	$\theta = \pi$	$\psi = 0$
$F_{(C.G.)}^{Body} \rightarrow F_{(Hub)}^{Hub}$	$\phi = \phi_s$	$\theta = -\theta_s - \pi$	$\psi = 0$
$F_{(Hub)}^{Hub} \rightarrow F_{(Hub)}^{Precone}$	$\phi = 0$	$\theta = -\beta_{precone}$	$\psi = DoR \cdot \psi_i$
$F_{(Hub)}^{Hub} \rightarrow F_{(Hinge)}^{Blade}$	$\phi = 0$	$\theta = \beta_i - \beta_{precone}$	$\psi = DoR \cdot \psi_i$
$F_{(Hinge)}^{Blade} \rightarrow F_{(BladeElement)}^{Wind}$	$\phi = \pi$	$\theta = -\phi$	$\psi = DoR \cdot \frac{\pi}{2}$
$F_{(Hub)}^{Hub} \rightarrow F_{(Hub)}^{TPP}$	$\phi = \beta_{1s}$	$\theta = -\beta_{1c}$	$\psi = 0$

3.1.2 Linear Interpolation

This tool is used for linear interpolation when necessary. It is a curve fitting method to create new data points between two existing points. It does not extrapolate beyond the interval of the existing points. It saturates the data to prevent overestimations. The implementation is given in Figure 3.6 and Equation 3.2.

$$y_0 = y_1 + (x_0 - x_1)\frac{y_2 - y_1}{x_2 - x_1} \tag{3.2}$$

$$y_0 = \max_{y_0 \leq y_2} y_0 \tag{3.3}$$

$$y_0 = \min_{y_0 \geq y_1} y_0 \tag{3.4}$$

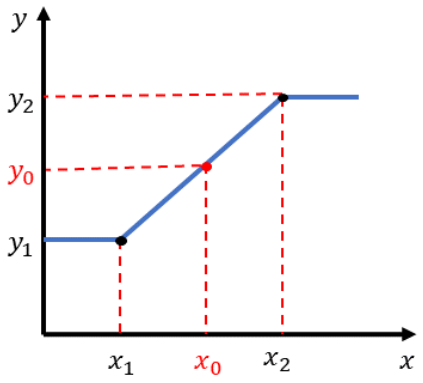

Figure 3.6. Linear interpolation tool representation

3.1.3 1D Lookup Table

This tool replicates a Simulink function, "1-D Lookup Table." It uses the Linear Interpolation tool between multiple breakpoints. Figure 3.8 shows the "1-D Lookup Table" image and block parameters in Simulink.

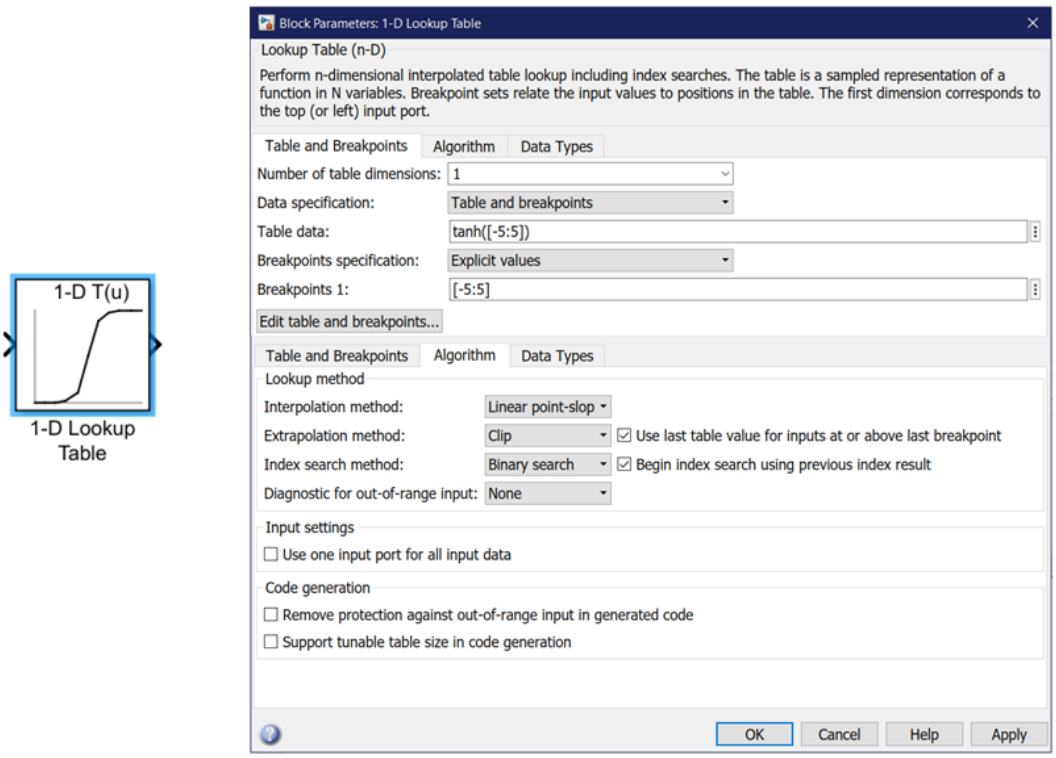

Figure 3.7. 1-D Lookup Table in Simulink

3.1.4 2D Look-up Table

This tool replicates a Simulink function, "2-D Lookup Table." It uses the Linear Interpolation tool between multiple breakpoints in two dimensions. Figure 3.8 shows Simulink's "2-D Lookup Table" image and block parameters.

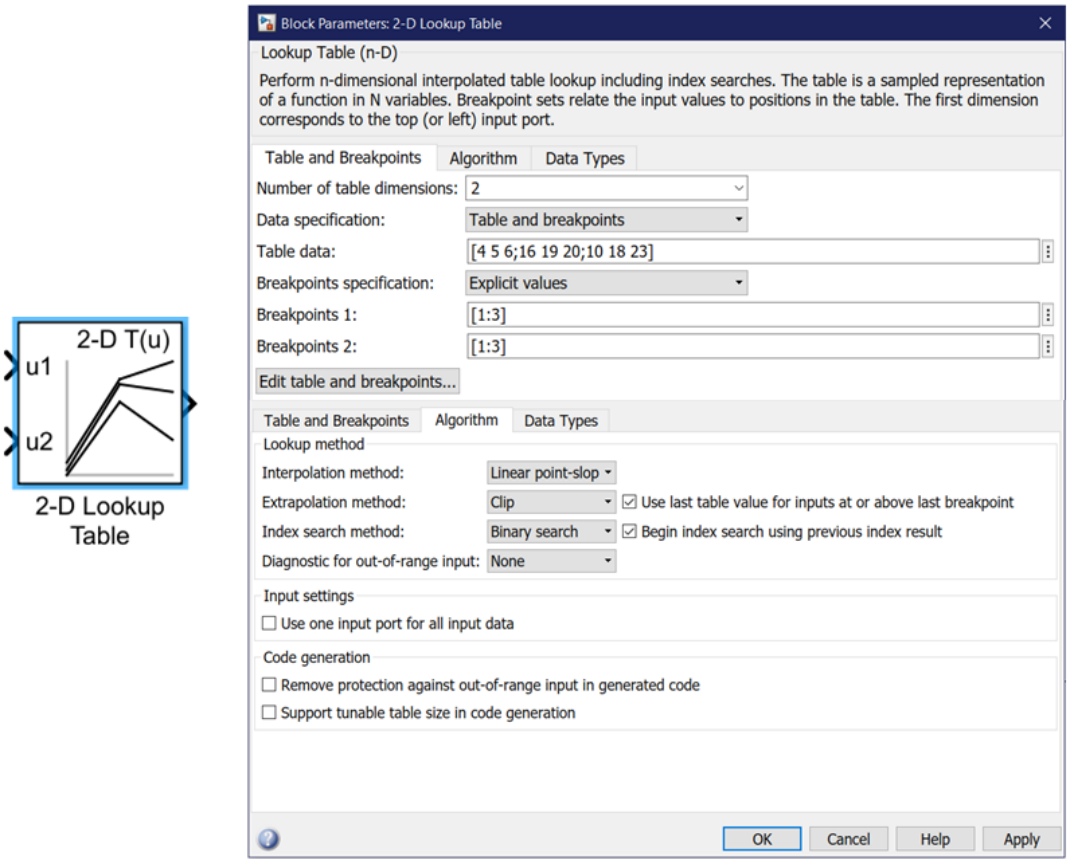

Figure 3.8. 2-D Lookup Table in Simulink

3.2 Rotor and Propeller Aerodynamics, Dynamics, and Kinematics

The main structure of the model consists of several MATLAB functions calculating the aerodynamics, dynamics, and kinematics of the rotor and the propeller. They all have an interconnection between them. Outputs of one function are inputs to the other function. As the MATLAB name indicates, the program is optimized for matrix operations. Therefore, all calculations are done using matrices in space. The rotor and propeller MATLAB Model's structure is presented in Figure 3.10, Figure 3.11, and Figure 3.12. Block diagrams show the input and output relation between each function.

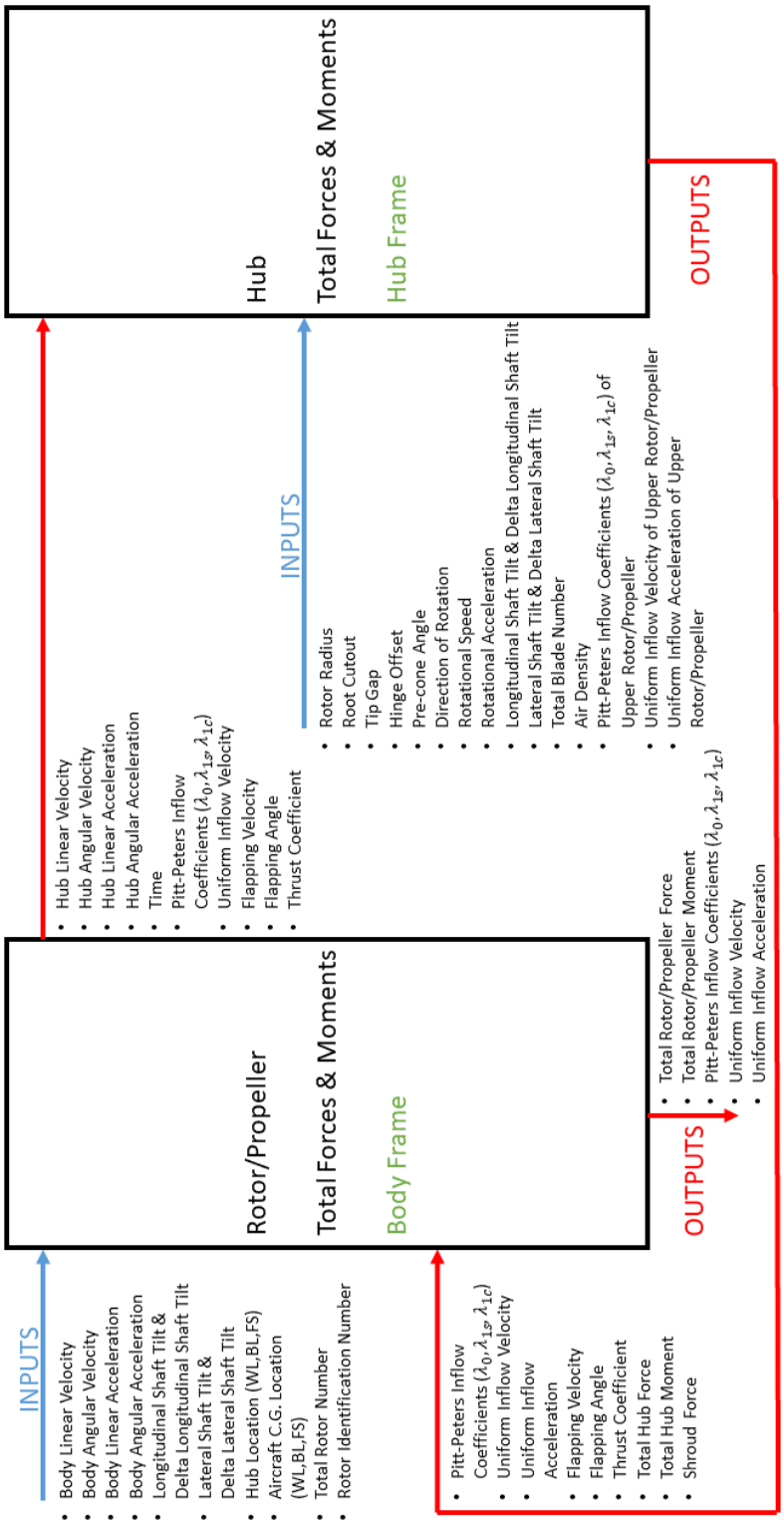

Figure 3.9. Block diagram of the Input/Output relation between Rotor/Propeller Total Forces and Moments Function and its subfunction Hub Total Forces and Moments Function

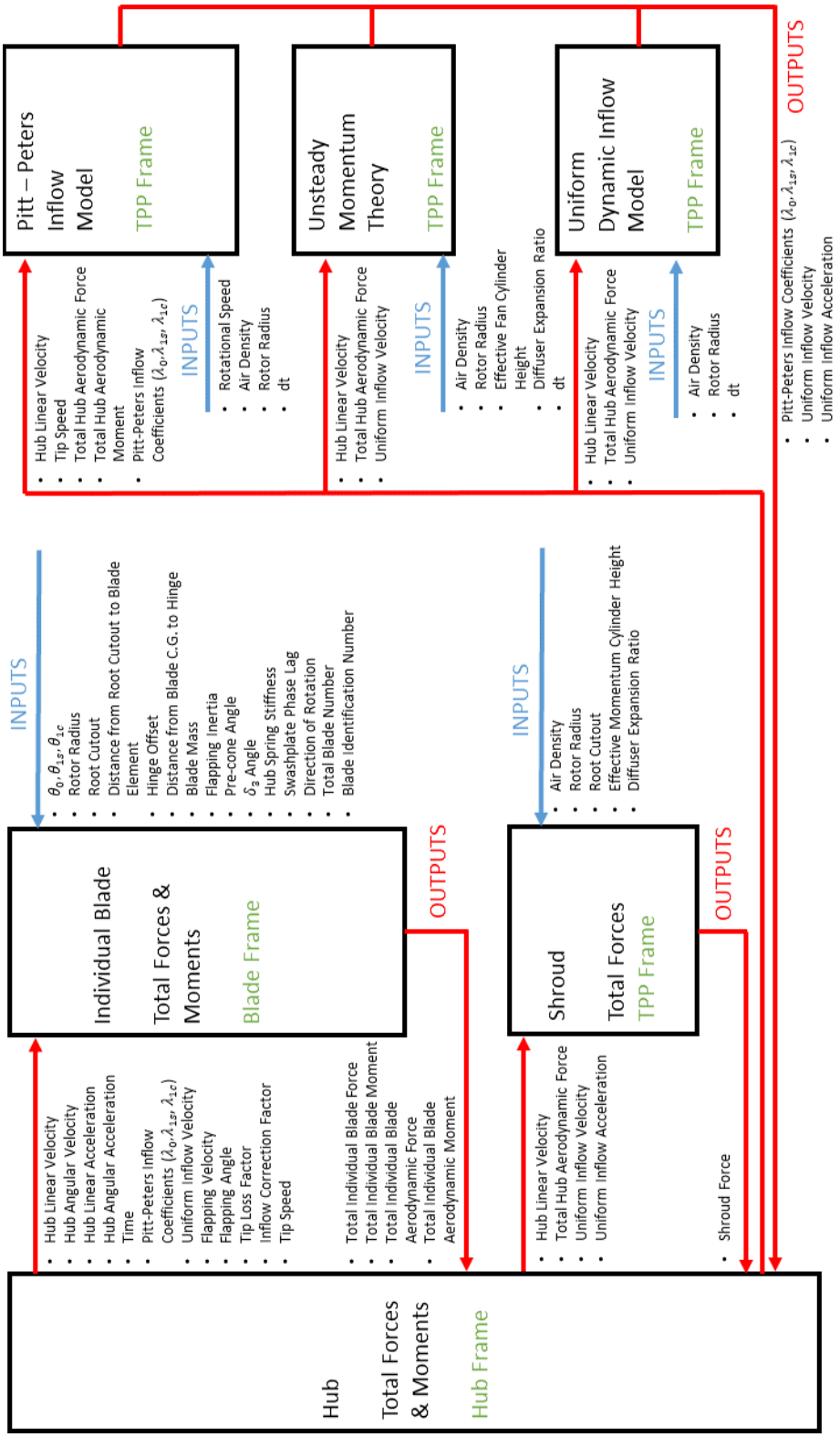

Figure 3.10. Block diagram of the Input/Output relation between Hub Total Forces and Moments Function and its subfunctions

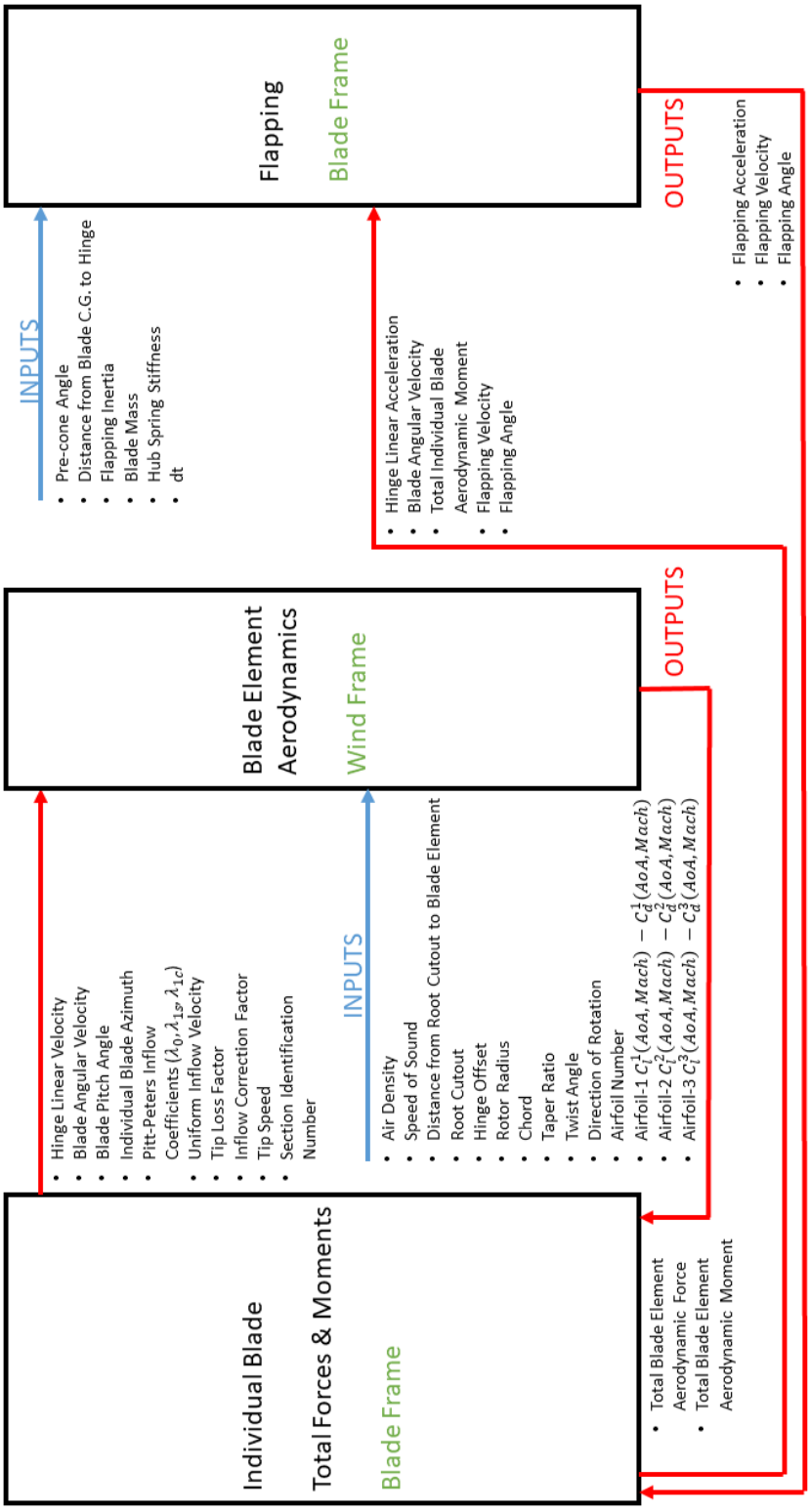

Figure 3.11. Block diagram of the Input/Output relation between Individual Blade Total Forces and Moments Function and its subfunctions

This model structure performs the base calculations in the Blade Element Aerodynamics function. Every other function is either an outer layer to this function or an auxiliary function computing necessary components like inflow. In a sample time, calculations start from the outer coat, then move to the core function layer by layer, and finally go from the inner layer to the outer and output the hub forces and moments for 6-DOF calculations of the aircraft.

Firstly, the aerodynamic forces generated are found using the wake estimation and the local velocities on the blade section. Later, they are integrated from the root cutout to the effective radius to find the total aerodynamic forces produced by the blade. Total forces and moments generated at the hub by each individual blade are found separately, transferring blade aerodynamic, inertial, centrifugal, Coriolis forces and moments, and gyroscopic moments to the hub.

After one iteration is finished, the blades are rotated by $\Omega \cdot dt$ at the next sample time, and new forces and moments are found at the new azimuth location using the new local velocities. The same procedure is applied when calculating the forces and moments generated by the blades.

3.2.1.1 Rotor/Propeller Total Forces and Moments

This function is the main function that every subfunction of the rotor and propeller model belongs to it. All inputs are fed in this function and desired outputs of this model are designated here. Inputs are defined in three ways, the input set from the workspace of MATLAB, the mask of the subsystem, and real-time simulation outputs. Outputs, in this case, are the total forces and moments of the rotor and propeller model in the Body Fixed Frame.

Persistent parameters are used as a "Memory Block" in Simulink; they save the final values of these parameters until the next function call. They are local to the function in which they are declared.

Six persistent parameters are initialized in this function: time, Pitt-Peters inflow parameters, uniform inflow velocity, flapping velocity in Blade Frame, flapping angle, and thrust coefficient. They can be seen in Table 3.3. Those parameters are used before being calculated. Therefore, they need to be initialized.

Table 3.3. Persistent parameters

Persistent Parameter	*Initial Value*
time	0
$\begin{bmatrix}\lambda_0\\ \lambda_{1s}\\ \lambda_{1c}\end{bmatrix}$	$\begin{bmatrix}0.01\\ 0\\ 0\end{bmatrix}$
ν	0
β	$[0 \quad 0 \quad ... \quad 0]$
$\dot{\bar{\beta}}^{Blade}$	$\begin{bmatrix}0 & 0 & ... & 0\\ 0 & 0 & ... & 0\\ 0 & 0 & ... & 0\end{bmatrix}$
C_T	0

The flapping angle and flapping velocity are initialized for every individual blade. A total b number of induvial blades exist on the rotor or propeller hub.

Hub velocities and accelerations are computed in this function as inputs to the Hub Total Forces and Moments Function.

$$\bar{r}_{Hub2CG}^{Body} = \begin{bmatrix}FS_{Hub}\\ BL_{Hub}\\ WL_{Hub}\end{bmatrix}^{Body} - \begin{bmatrix}FS_{CG}\\ BL_{CG}\\ WL_{CG}\end{bmatrix}^{Body} \tag{3.5}$$

$$\bar{V}_{Hub}^{Body} = \begin{bmatrix}u\\ v\\ w\end{bmatrix} + \begin{bmatrix}p\\ q\\ r\end{bmatrix} \times \bar{r}_{Hub2CG}^{Body} \tag{3.6}$$

$$\bar{V}_{Hub}^{Hub} = T^T(\phi_s + \Delta\phi_s, -(\theta_s + \Delta\theta_s) - \pi, 0)\, \bar{V}_{Hub}^{Body} \tag{3.7}$$

$$\bar{a}_{Hub}^{Body} = \begin{bmatrix}\dot{u}\\ \dot{v}\\ \dot{w}\end{bmatrix} + \begin{bmatrix}\dot{p}\\ \dot{q}\\ \dot{r}\end{bmatrix} \times \bar{r}_{Hub2CG}^{Body} \tag{3.8}$$

$$\bar{a}_{Hub}^{Hub} = T^T(\phi_s + \Delta\phi_s, -(\theta_s + \Delta\theta_s) - \pi, 0)\, \bar{a}_{Hub}^{Body} \tag{3.9}$$

$$\bar{\omega}_{Body}^{Body} = \begin{bmatrix} p \\ q \\ r \end{bmatrix} \quad 3.10$$

$$\bar{\omega}_{Body}^{Hub} = T^T(\phi_s + \Delta\phi_s, -(\theta_s + \Delta\theta_s) - \pi, 0)\ \bar{\omega}_{Body}^{Body} \quad 3.11$$

$$\bar{\alpha}_{Body}^{Body} = \begin{bmatrix} \dot{p} \\ \dot{q} \\ \dot{r} \end{bmatrix} \quad 3.12$$

$$\bar{\alpha}_{Body}^{Hub} = T^T(\phi_s + \Delta\phi_s, -(\theta_s + \Delta\theta_s) - \pi, 0)\ \bar{\alpha}_{Body}^{Body} \quad 3.13$$

Time is integrated at the end of this function with Euler integration before the next sample time iteration.

$$time^{t+1} = time^t + dt \quad 3.14$$

3.2.1.2 Hub Total Forces and Moments

Isolated rotor and propeller model calculations are done in this function.

Rotational velocity and acceleration:

The direction of rotation parameter used in the model is $DoR = -1$ if the rotation is clockwise and $DoR = +1$ if the rotation is counterclockwise.

$$\bar{\Omega}_{Hub}^{Hub} = \begin{bmatrix} 0 \\ 0 \\ DoR \cdot \Omega \end{bmatrix}^{Hub} \quad 3.15$$

$$\bar{\dot{\Omega}}_{Hub}^{Hub} = \begin{bmatrix} 0 \\ 0 \\ DoR \cdot \dot{\Omega} \end{bmatrix}^{Hub} \quad 3.16$$

Tip loss and inflow correction factors are calculated to reflect the pressure loss at the blade tip. They are input to the Individual Blade Total Forces and Moments and Blade Element Aerodynamics Functions.

$$B = 1 - \frac{\sqrt{2|C_T^t|}}{b} \quad 3.17$$

Inflow correction factor calculation varies with the inflow theory utilized. If the Pitt-Peters inflow model is activated, the inflow correction factor is computed as in Equation 3.18 due to losses caused by non-uniform inflow; otherwise, Equation 3.19 is used.

$$\kappa = \frac{4\sqrt{2}}{5 \max\limits_{\kappa' \geq 0.01} \kappa'} \tag{3.18}$$

$$\kappa = \frac{1}{\max\limits_{\kappa' \geq 0.01} \kappa'} \tag{3.19}$$

where κ' is given in Equation 3.20, which is saturated to prevent the model's diverging to infinity or computing NaN.

$$\kappa' = \sqrt{\left| B^2 - \left(\frac{r_R}{R}\right)^2 \right|} \tag{3.20}$$

For ducted rotors and propellers, the effect of these factors is linearly decayed with the tip gap between the duct and the blade tip. Theoretically, they converge to 1 asymptotically as the tip gap becomes 0; however, the Linear Interpolation tool is used to model this effect. Figure 3.3 shows changes in tip loss and inflow correction factors for ducted rotors and propellers.

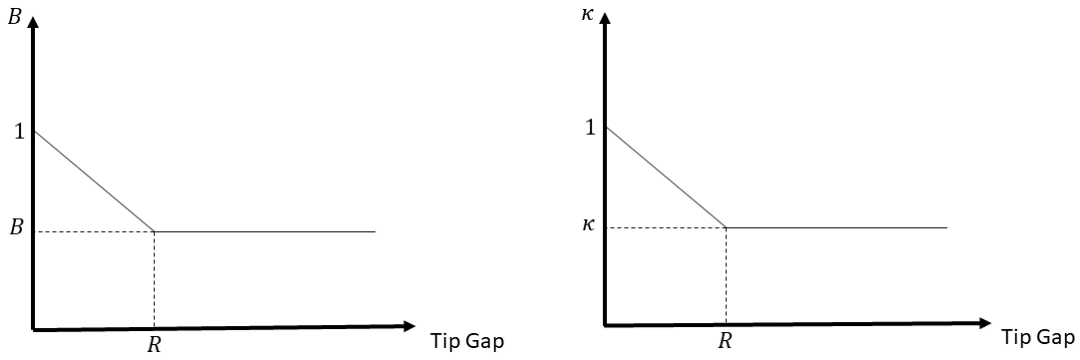

Figure 3.12. Tip loss and inflow correction factors for ducted rotors and propellers

Total forces and moments generated by the blades are found in this function. Total aerodynamic forces and moments on the rotor hub are used in the inflow estimations.

$$\bar{F}_{Hub}^{Hub} = \sum_{i=1}^{b} \bar{F}_{i}^{Hub} \quad 3.21$$

$$\bar{M}_{Hub}^{Hub} = \sum_{i=1}^{b} \bar{M}_{i}^{Hub} \quad 3.22$$

$$\overline{F_{Aero}}_{Hub}^{Hub} = \sum_{i=1}^{b} \overline{F_{Aero}}_{i}^{Hub} \quad 3.23$$

$$\overline{M_{Aero}}_{Hub}^{Hub} = \sum_{i=1}^{b} \overline{M_{Aero}}_{i}^{Hub} \quad 3.24$$

When the rotor blades are free to flap, blade attitudes are converted from Individual Blade Coordinates (IBC) to Multi-blade Coordinates (MBC) [42]. Since there are just cyclic inputs and the maximum 3-states inflow model is used, only the first harmonics of the flapping are excited. Therefore, the first harmonics of the flapping and the steady term are calculated at every sample time.

$$\beta_i^t = \beta_0 + \beta_{1s} sin(\psi_i) + \beta_{1c} \cos(\psi_i) \quad 3.25$$

$$\beta_0 = \frac{1}{b} \sum_{i=1}^{b} -\beta_i^t \quad 3.26$$

$$\beta_{1s} = \frac{2}{b} \sum_{i=1}^{b} -\beta_i^t \sin(\psi_i) \quad 3.27$$

$$\beta_{1c} = \frac{2}{b} \sum_{i=1}^{b} -\beta_i^t \cos(\psi_i) \quad 3.28$$

Coning angle is the angle between the hub plane and the line from the hub to the blade tip. The representation of coning angle is shown in Figure 3.13.

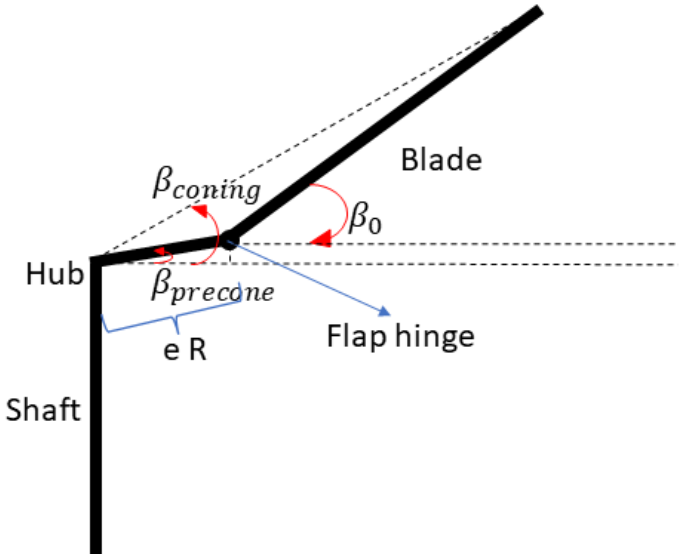

Figure 3.13. Coning angle representation

$$\beta_{coning} = \tan^{-1}\frac{eR\sin(\beta_{precone}) + (R - eR)\sin(\beta_0)}{eR\cos(\beta_{precone}) + (R - eR)\cos(\beta_0)} \quad 3.29$$

Inflow and thrust coefficient calculations are done in Tip Path Plane (TPP) Frame.

$$\bar{V}_{Hub}^{TPP} = T^T(\beta_{1s}, -\beta_{1c}, 0)\,\bar{V}_{Hub}^{Hub} \quad 3.30$$

$$\overline{F_{Aero}}_{Hub}^{TPP} = T^T(\beta_{1s}, -\beta_{1c}, 0)\,\overline{F_{Aero}}_{Hub}^{Hub} \quad 3.31$$

$$\overline{M_{Aero}}_{Hub}^{TPP} = T^T(\beta_{1s}, -\beta_{1c}, 0)\,\overline{M_{Aero}}_{Hub}^{Hub} \quad 3.32$$

Thrust is defined as the force generated by the rotor in the direction perpendicular to the TPP. Therefore, the third component of aerodynamic forces resolved in the TPP Frame gave the rotor thrust. By non-dimensionalizing it, the thrust coefficient is attained.

$$C_T^{t+1} = \frac{\overline{F_{Aero}}_{Hub}^{TPP}(3)}{\rho(\pi R^2)(\Omega R)^2} \quad 3.33$$

The rotor or propeller's total forces and moments are obtained at the end of this function.

$$\bar{F}_{Hub}^{Body} = T(\phi_s + \Delta\phi_s, -(\theta_s + \Delta\theta_s) - \pi, 0)\left(\bar{F}_{Hub}^{Hub} + \bar{F}_{Shroud}^{Hub}\right) \quad 3.34$$

$$\bar{M}_{Hub}^{Body} = \bar{r}_{Hub2CG}^{Body} \times \bar{F}_{Hub}^{Body} + T(\phi_s + \Delta\phi_s, -(\theta_s + \Delta\theta_s) - \pi, 0)\bar{M}_{Hub}^{Hub} \quad 3.35$$

3.2.1.3 Individual Blade Total Forces and Moments

This function is called for each blade consecutively in a "for" loop within a sample time. It involves rotor dynamics calculations due to external aerodynamic forces and moments and inertial forces and moments due to accelerations.

In this rotor and propeller model, blades are rotated around the z_{Hub}-axis with Ω. They are placed on the rotor disk plane with equal azimuth intervals. The first blade is positioned at the $\psi = 0^o$. Azimuth locations on the rotor disk plane are given in Figure 3.14.

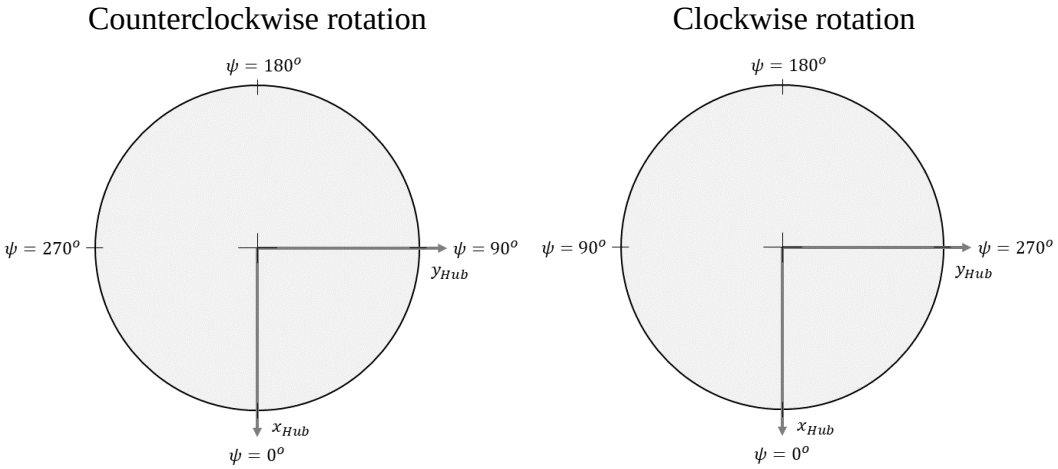

Figure 3.14. Azimuth locations on the rotor disk plane

$$\psi_i = mod\left(DoR \cdot \overline{\Omega}_{Hub}^{Hub}(3) \cdot time^t + \frac{2\pi(i-1)}{b}, 2\pi\right) \qquad 3.36$$

For a four-bladed rotor $(b = 4)$ with $\Omega = 30$ rad/s rotational speed in the counterclockwise direction, the blades' initial positions and positions at the following sample time $(dt = 0.0025)$ are shown in Figure 3.15.

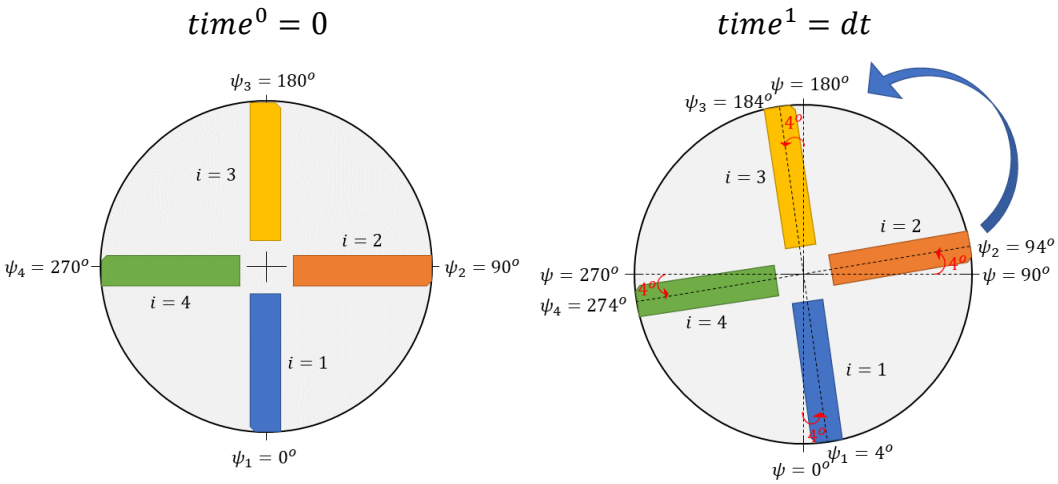

Figure 3.15. Representation of counterclockwise rotation

Similarly, the same rotor with clockwise rotation is like in Figure 3.16.

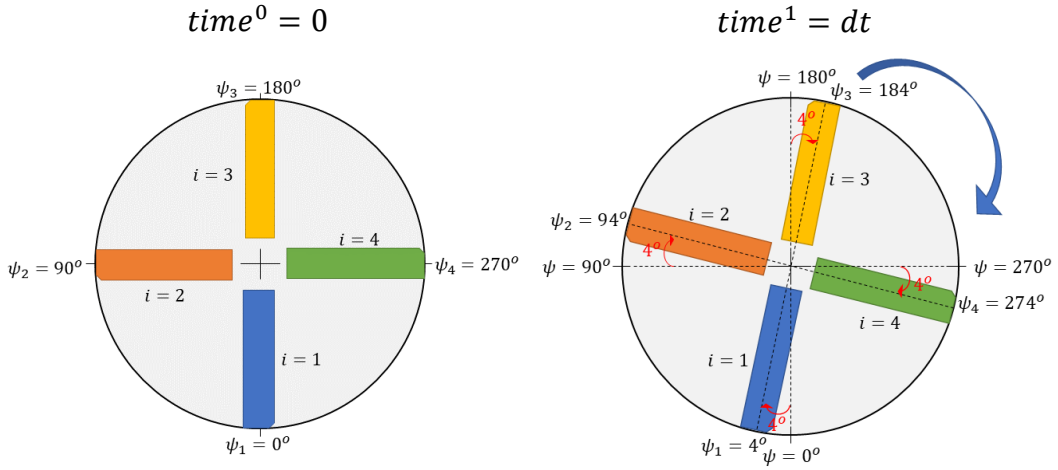

Figure 3.16. Representation of clockwise rotation

Velocity calculation at flap hinge location:

$$\bar{r}^{Hub}_{Hinge2Hub} = T\left(0, -\beta_{precone}, DoR \cdot \psi_i\right) \begin{bmatrix} eR \\ 0 \\ 0 \end{bmatrix}^{Precone} \quad 3.37$$

$$\bar{V}^{Hub}_{Hinge} = \bar{V}^{Hub}_{Hub} + \left(\bar{\omega}^{Hub}_{Body} + \bar{\Omega}^{Hub}_{Hub}\right) \times \bar{r}^{Hub}_{Hinge2Hub} \quad 3.38$$

$$\bar{V}^{Blade}_{Hinge} = T^T\left(0, \beta^t_i - \beta_{precone}, DoR \cdot \psi_i\right) \bar{V}^{Hub}_{Hinge} \quad 3.39$$

Blade angular velocity:

$$\bar{\omega}_i^{Hub} = \bar{\omega}_{Body}^{Hub} + \bar{\Omega}_{Hub}^{Hub} + T\left(0, \beta_i^t - \beta_{precone}, DoR \cdot \psi_i\right) \begin{bmatrix} 0 \\ \dot{\beta}_i^t \\ 0 \end{bmatrix}^{Blade} \quad 3.40$$

$$\bar{\omega}_i^{Blade} = T^T\left(0, \beta_i^t - \beta_{precone}, DoR \cdot \psi_i\right) \bar{\omega}_i^{Hub} \quad 3.41$$

Linear acceleration at flap hinge location:

$$\overline{a_{centripetal}}_{Hinge}^{Hub} = \left(\bar{\omega}_{Body}^{Hub} + \bar{\Omega}_{Hub}^{Hub}\right) \times \left(\bar{\omega}_{Body}^{Hub} + \bar{\Omega}_{Hub}^{Hub}\right) \times \bar{r}_{Hinge2Hub}^{Hub} \quad 3.42$$

$$\bar{a}_{Hinge}^{Hub} = \bar{a}_{Hub}^{Hub} + \left(\bar{\alpha}_{Body}^{Hub} + \dot{\bar{\Omega}}_{Hub}^{Hub}\right) \times \bar{r}_{Hinge2Hub}^{Hub} + \overline{a_{centripetal}}_{Hinge}^{Hub} \quad 3.43$$

$$\bar{a}_{Hinge}^{Blade} = T^T\left(0, \beta_i^t - \beta_{precone}, DoR \cdot \psi_i\right) \bar{a}_{Hinge}^{Hub} \quad 3.44$$

Blade pitch angle:

$$\theta_i = \theta_0 + \theta_{1s} \sin(\psi_i + \Delta\psi) + \theta_{1c} \cos(\psi_i + \Delta\psi) - \tan(\delta_3) \tan(-\beta_i^t) \quad 3.45$$

δ_3 angle causes the blade pitch angle to be smaller with a flap-up motion. The implementation of pitch-flap coupling is taken from [49]. It should be noted that there are possible combinations of rotor Lock number and δ_3 angle causing a divergent solution [43].

Total aerodynamic forces and moments acting on each blade are calculated using blade element theory. Aerodynamic forces generated on blade elements are computed through Blade Element Aerodynamics Function using the linear velocities at flap hinge location, angular velocities of the blade, and the blade pitch angle found in this function. The total aerodynamic forces and moments are found by integrating the lift and drag forces from the second blade section from the blade root cutout to the last blade section at the blade tip.

Blade elements are getting smaller as getting to the blade tip increases the accuracy in aerodynamic calculations since the blade tip is under more complex aerodynamic effects and sees more velocity. The number of blade elements can be selected according to the number of structural nodes on the blade and the number of dynamic inflow model states. As this model uses a rigid blade assumption with a low state inflow model, the blade element number is the model developers' choice.

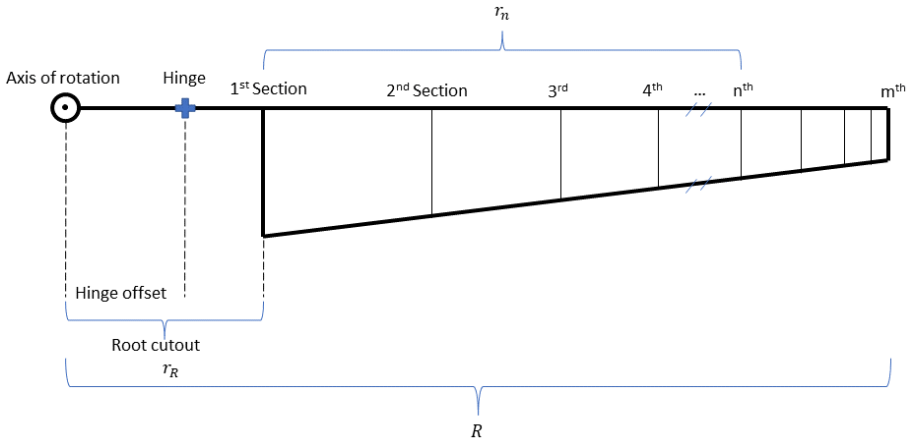

Figure 3.17. Representation of the blade elements

The trapezoidal rule is used for integration.

$$\overline{F_{Aero}}_1^{Blade} = 0 \tag{3.46}$$

$$\overline{M_{Aero}}_1^{Blade} = 0 \tag{3.47}$$

$$r_1 = 0 \tag{3.48}$$

$$\overline{F_{Aero}}_i^{Blade} = \frac{1}{2}\sum_{n=2}^{m}(\overline{F_{Aero}}_n^{Blade} + \overline{F_{Aero}}_{n-1}^{Blade})(r_n - r_{n-1}) \tag{3.49}$$

$$\overline{M_{Aero}}_i^{Blade} = \frac{1}{2}\sum_{n=2}^{m}(\overline{M_{Aero}}_n^{Blade} + \overline{M_{Aero}}_{n-1}^{Blade})(r_n - r_{n-1}) \tag{3.50}$$

$$\overline{F_{Aero}}_i^{Hub} = T\left(0, \beta_i^t - \beta_{precone}, DoR \cdot \psi_i\right)\overline{F_{Aero}}_i^{Blade} \tag{3.51}$$

$$\overline{M_{Aero}}_i^{Hub} = T\left(0, \beta_i^t - \beta_{precone}, DoR \cdot \psi_i\right)\overline{M_{Aero}}_i^{Blade} \tag{3.52}$$

If flapping is active, the blade is allowed to flap. Flapping dynamics are computed utilizing the Flapping Function. The flapping acceleration of the blade is used to calculate the total angular acceleration of the blade and, consequently, the inertial acceleration contribution to the total blade forces and moments.

$$\bar{\alpha}_i^{Hub} = \bar{\alpha}_{Body}^{Hub} + \bar{\dot{\Omega}}_{Hub}^{Hub} + T\left(0, \beta_i^t - \beta_{precone}, DoR \cdot \psi_i\right)\begin{bmatrix} 0 \\ \ddot{\beta}_i^t \\ 0 \end{bmatrix}^{Blade} \tag{3.53}$$

$$\bar{\alpha}_i^{Blade} = T^T\left(0, \beta_i^t - \beta_{precone}, DoR \cdot \psi_i\right)\bar{\alpha}_i^{Hub} \tag{3.54}$$

Total interaction forces and moments at flap hinge location are calculated using Newton-Euler equations for rigid bodies.

If flapping inertia is missing in the input set, it can be predicted with Equation 3.55.

$$I_B = \frac{1}{3}(mR^2) \tag{3.55}$$

$$\hat{J}_i^{Blade} = \begin{bmatrix} 0 & 0 & 0 \\ 0 & I_B & 0 \\ 0 & 0 & I_B \end{bmatrix} \tag{3.56}$$

$$\begin{aligned} \bar{F}_i^{Blade} = {} & \overline{F_{Aero}}_i^{Blade} \\ & - m_b \left(\bar{a}_{Hinge}^{Blade} + \bar{\alpha}_i^{Blade} \times \begin{bmatrix} d_{BldCG2Hng} \\ 0 \\ 0 \end{bmatrix}^{Blade} \right. \\ & \left. + \bar{\omega}_i^{Blade} \times \bar{\omega}_i^{Blade} \times \begin{bmatrix} d_{BldCG2Hng} \\ 0 \\ 0 \end{bmatrix}^{Blade} \right) \end{aligned} \tag{3.57}$$

$$\begin{aligned} \bar{M}_i^{Blade} = {} & \overline{M_{Aero}}_i^{Blade} - \hat{J}_i^{Blade} \bar{\alpha}_i^{Blade} - \bar{\omega}_i^{Blade} \times \hat{J}_i^{Blade} \bar{\omega}_i^{Blade} \\ & - m_b \left(\begin{bmatrix} d_{BldCG2Hng} \\ 0 \\ 0 \end{bmatrix}^{Blade} \times \bar{a}_{Hinge}^{Blade} \right) \\ & + \begin{bmatrix} -d_{BldCG2Hng} \\ 0 \\ 0 \end{bmatrix}^{Blade} \\ & \times m_b \left(\bar{a}_{Hinge}^{Blade} + \bar{\alpha}_i^{Blade} \times \begin{bmatrix} d_{BldCG2Hng} \\ 0 \\ 0 \end{bmatrix}^{Blade} \right. \\ & \left. + \bar{\omega}_i^{Blade} \times \bar{\omega}_i^{Blade} \times \begin{bmatrix} d_{BldCG2Hng} \\ 0 \\ 0 \end{bmatrix}^{Blade} \right) \end{aligned} \tag{3.58}$$

If flapping is active, the moment in the flap direction cancels out due to the flap hinge.

$$\bar{M}_i^{Blade}(2) = 0 \tag{3.59}$$

Total individual blade forces and moments transferred to the hub are the output of this function.

$$\bar{F}_i^{Hub} = T\left(0, \beta_i^t - \beta_{precone}, DoR \cdot \psi_i\right)\bar{F}_i^{Blade} \tag{3.60}$$

$$\bar{M}_i^{Hub} = \bar{r}_{Hinge2Hub}^{Hub} \times \bar{F}_i^{Hub} + T\left(0, \beta_i^t - \beta_{precone}, DoR \cdot \psi_i\right)\left(\bar{M}_i^{Blade} + K_\beta \begin{bmatrix} 0 \\ \beta_i^t \\ 0 \end{bmatrix}^{Blade}\right) \tag{3.61}$$

3.2.1.4 Blade Element Aerodynamics

Aerodynamic forces generated by the blade section are calculated using the local air velocities and the rotor wake estimation.

Root cutout is saturated to prevent the model's diverging to infinity or computing NaN.

$$r_R = \min_{r_R \le R - 0.001}(r_R) \tag{3.62}$$

Effective radius:

$$R_e = BR \tag{3.63}$$

Chord calculation:

If the linear chord selection is activated, the chord of the blade element is calculated using the root chord, taper ratio, and distance from root cutout.

$$c_t = c_r \lambda \tag{3.64}$$

$$c_n = \frac{c_r(\mathrm{R} - \mathrm{r_R} - r_n) + c_t r_n}{R - r_R} \tag{3.65}$$

If the chord is not linearly distributed, a chord distribution table along the radius from the axis of rotation needs to be defined. The chord length is attained from the table according to the blade element's radial position using the 1D Lookup Table tool.

If uniform dynamic inflow or unsteady momentum theory is used to estimate the inflow of the rotor or propeller, the inflow on the blade element is defined as in Equation 3.66.

$$\bar{v}_{i,n}^{Blade} = \begin{bmatrix} 0 \\ 0 \\ \kappa v \end{bmatrix} \tag{3.66}$$

If the Pitt-Peters inflow model is activated instead of uniform inflow calculations, the inflow on the blade element is defined as in Equation 3.67.

$$\bar{v}_{i,n}^{Blade} = \begin{bmatrix} 0 \\ 0 \\ \left(\kappa\lambda_0 + \lambda_{1s}\left(\frac{r_n + r_R}{R}\right)\sin(\psi_i) + \lambda_{1c}\left(\frac{r_n + r_R}{R}\right)\cos(\psi_i)\right)\Omega R \end{bmatrix} \tag{3.67}$$

The inflow estimation is zeroed if the blade element is located behind the aerodynamic root cutout or beyond the effective radius. Effective radius reflects the radial location where the pressure loss occurs.

$$if\ r_n \leq 0\ \&\ (r_n + r_R) \geq R_e \rightarrow\ \bar{v}_{i,n}^{Blade} = \begin{bmatrix} 0 \\ 0 \\ 0 \end{bmatrix} \tag{3.68}$$

If the coaxial rotor/propeller model is activated, an empirical inflow correction to the upper rotor's inflow is applied to find the lower rotor's inflow. It is assumed that the upper rotor is not affected by the lower rotor. The upper rotor's inflow is an input to the lower rotor. If the blade element is located within a $R/\sqrt{2}$ radius from the axis of rotation, the lower rotor's inflow is the inflow of the upper rotor at its vena contracta ($2\bar{v}_{i,n,u}^{Blade}$) and the lower rotor's inflow ($\bar{v}_{i,n,l}^{Blade}$) combined. If the blade element is beyond the $R/\sqrt{2}$ radius location, then it only encounters the lower rotor's inflow.

$$\bar{v}_{i,n,u}^{Blade} = \bar{v}_{i,n,k}^{Blade} \tag{3.69}$$

$$\bar{v}_{i,n,l}^{Blade} = 0.32\bar{v}_{i,n,k}^{Blade} \tag{3.70}$$

$$if\ r_n \leq \frac{R}{\sqrt{2}} \rightarrow\ \bar{v}_{i,n}^{Blade} = 2\bar{v}_{i,n,u}^{Blade} + \bar{v}_{i,n,l}^{Blade} \tag{3.71}$$

$$if\ r_n > \frac{R}{\sqrt{2}} \rightarrow\ \bar{v}_{i,n}^{Blade} = \bar{v}_{i,n,l}^{Blade} \tag{3.72}$$

If the ducted rotor/propeller model is activated together with the coaxial rotor/propeller model, the lower rotor's inflow is the inflow of the upper rotor at its vena contracta ($2\bar{v}_{i,n,u}^{Blade}$) and the lower rotor's inflow ($\bar{v}_{i,n,l}^{Blade}$) combined passing through the whole disk. The same empirical correction is used to find the inflow of the lower rotor since there is no test data for ducted coaxial rotor/propeller inflow. 0.32 correction factor might be higher than the actual for ducted coaxial rotors/propellers.

$$\bar{v}_{i,n,u}^{Blade} = \bar{v}_{i,n,k}^{Blade} \tag{3.73}$$

$$\bar{v}_{i,n,l}^{Blade} = 0.32\bar{v}_{i,n,k}^{Blade} \tag{3.74}$$

$$\bar{v}_{i,n}^{Blade} = 2\bar{v}_{i,n,u}^{Blade} + \bar{v}_{i,n,l}^{Blade} \tag{3.75}$$

Tangential and perpendicular velocity components that the blade element encounters are calculated using the local velocities on the blade element in Blade Frame.

$$\bar{V}_{i,n}^{Blade} = \bar{V}_{Hinge}^{Blade} + \bar{\omega}_{i}^{Blade} \times \begin{bmatrix} r_n + r_R - eR \\ 0 \\ 0 \end{bmatrix}^{Blade} + \bar{v}_{i,n}^{Blade} \tag{3.76}$$

Figure 3.18 and Figure 3.19 show the relationship between the positive direction of tangential velocity and the y_{Blade}-axis for counterclockwise rotor and clockwise rotor. The positive direction of the tangential velocity is determined according to the angle of attack interval defined in aerodynamic coefficient tables. To have the angle of attack between $[-pi, pi]$, the positive direction of tangential velocity should face the leading edge of the airfoil. Therefore, for a counterclockwise rotor, the positive tangential velocity of the blade is in the same direction as the positive y_{Blade}-axis. For a clockwise rotating rotor, the positive tangential velocity of the blade is in the same direction as the negative y-Blade axis. In Equation 3.77, tangential velocity calculation can be seen.

The positive perpendicular velocity of the blade element is in the same direction as the positive z_{Blade}-axis. In Equation 3.78, perpendicular velocity calculation can be seen.

The inflow angle is defined as Equation 3.80.

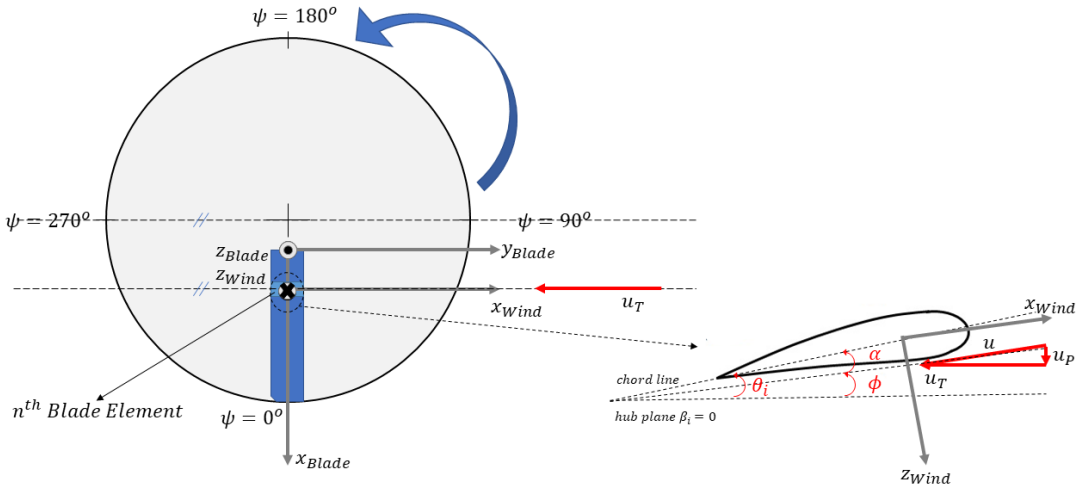

Figure 3.18. Wind Frame representation on the n[th] blade element of the i[th] blade for a counterclockwise rotating rotor with zero flapping assumption

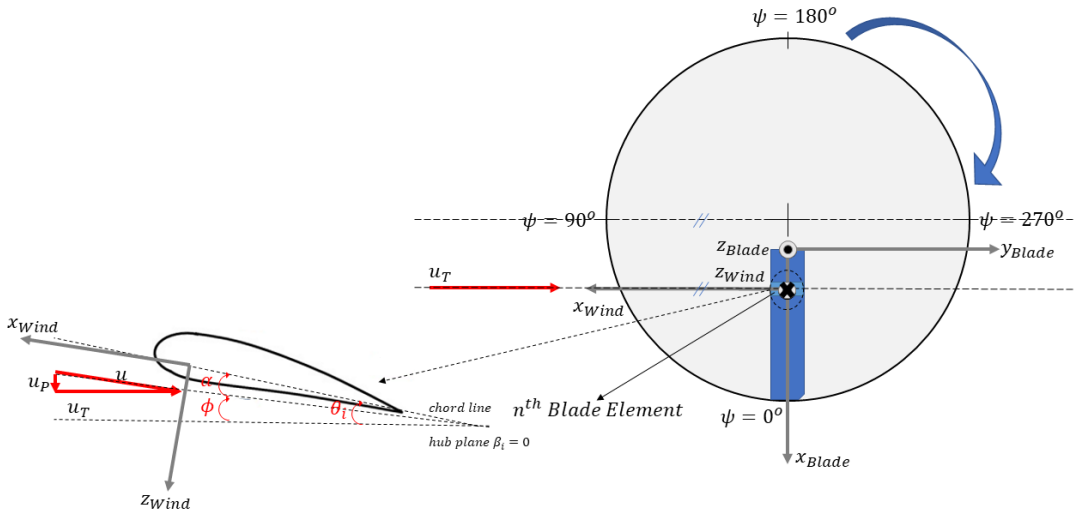

Figure 3.19. Wind Frame representation on the n[th] blade element of the i[th] blade for a clockwise rotating rotor with zero flapping assumption

The local air velocities:

$$U_T = DoR \cdot \bar{V}_{i,n}^{Blade}(2) \quad 3.77$$

$$U_P = \bar{V}_{i,n}^{Blade}(3) \quad 3.78$$

$$U = \sqrt{U_T^2 + U_P^2} \quad 3.79$$

The inflow angle:

$$\phi = \tan^{-1}\left(\frac{U_P}{U_T}\right) \tag{3.80}$$

If the blade twist is not linear along the blade, the twist is determined from the blade twist table according to the blade element's radial position using the 1D Lookup Table tool. Equation 3.65 is used to find the blade twist on the blade element if the blade twist is linearly distributed.

$$\theta_t = d\theta_t \frac{r_n}{R - r_R} \tag{3.81}$$

The angle of attack of the blade element:

$$\alpha = \theta_i - \phi + \theta_t \tag{3.82}$$

Mach number that the blade element sees:

$$M = \frac{U}{c} \tag{3.83}$$

According to the angle of attack and the Mach number that the airfoil encounters, the aerodynamic coefficients are taken from $C_l(\alpha, M)$ and $C_d(\alpha, M)$ 2D tables using the 2D Lookup Table tool. As it is shown in Figure 3.20, up to three different blade sections can be implemented to the model along the radius.

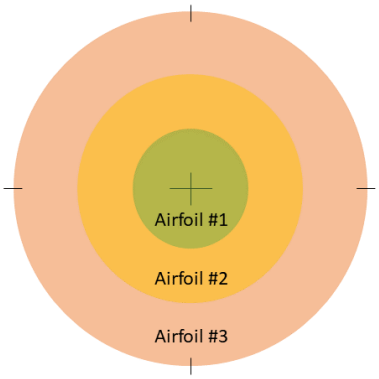

Figure 3.20. Airfoil numbering on the rotor disk

The airfoil of the blade element is decided according to the blade element's distance from the axis of rotation. If the blade element stands between two different airfoils, its aerodynamic coefficients are found by interpolating the coefficients of those two airfoils.

Aerodynamic force calculations:

$$L = \frac{1}{2}\rho U^2 c_n C_l \tag{3.84}$$

The lift is zeroed if the blade element is located behind the aerodynamic root cutout or beyond the effective radius.

$$if\ r_n \leq 0\ \&\ (r_n + r_R) \geq R_e \rightarrow\ L = 0 \tag{3.85}$$

$$D = \frac{1}{2}\rho U^2 c_n C_d \tag{3.86}$$

A delta parasite drag coefficient as a flat plate drag area is added to reflect the miscellaneous drag due to the mechanics behind the aerodynamic root cutout. Delta C_{d_0} can be tuned.

$$if\ r_n \leq 0\ \rightarrow\ D = \frac{1}{2}\rho U^2 c_n (C_d + \Delta C_{d_0}) \tag{3.87}$$

Blade element total aerodynamic forces and moments:

$$\overline{F_{Aero}}_{i,n}^{Wind} = \begin{bmatrix} -D \\ 0 \\ -L \end{bmatrix} \tag{3.88}$$

$$\overline{F_{Aero}}_{i,n}^{Blade} = T\left(\pi, -\phi, DoR \cdot \frac{\pi}{2}\right) \overline{F_{Aero}}_{i,n}^{Wind} \tag{3.89}$$

$$\overline{M_{Aero}}_{i,n}^{Blade} = \begin{bmatrix} r_n + r_R - eR \\ 0 \\ 0 \end{bmatrix}^{Blade} \overline{F_{Aero}}_{i,n}^{Blade} \tag{3.90}$$

3.2.1.5 Flapping

In this function, the flapping dynamics of the rotor due to the aerodynamic forces are computed as explained in 2.4.1.1. Adding a flap hinge to the blade enables the flapping degree of freedom: $\ddot{\beta} \neq 0$.

Using Euler equations, the second-order flapping dynamics are calculated. This form of calculation required double integration; therefore, two parameters need to be initialized: flap angle and flapping velocity. As the rotor model is based on a rotating frame, at each sample time, the blades are moved $\Omega \cdot dt$ along with their kinematics.

Time integration indicates that the blades will have the states determined by the integration results after a certain time.

$$\begin{aligned}\overline{\overline{M_{Inertial_i}}}^{Blade} = {} & \overline{\overline{M_{Aero_i}}}^{Blade} - K_\beta \begin{bmatrix} 0 \\ \beta_i^t \\ 0 \end{bmatrix} \\ & - \hat{J}_i^{Blade} T\left(0, \beta_i^t - \beta_{precone}, DoR \cdot \psi_i\right)\left(\bar{\alpha}_{Body}^{Hub} + \bar{\Omega}_{Hub}^{Hub}\right) \\ & - \bar{\omega}_i^{Blade} \times \hat{J}_i^{Blade} \bar{\omega}_i^{Blade} \\ & - m_b \left(\begin{bmatrix} d_{BldCG2Hng} \\ 0 \\ 0 \end{bmatrix}^{Blade} \times \bar{a}_{Hinge}^{Blade} \right)\end{aligned} \tag{3.91}$$

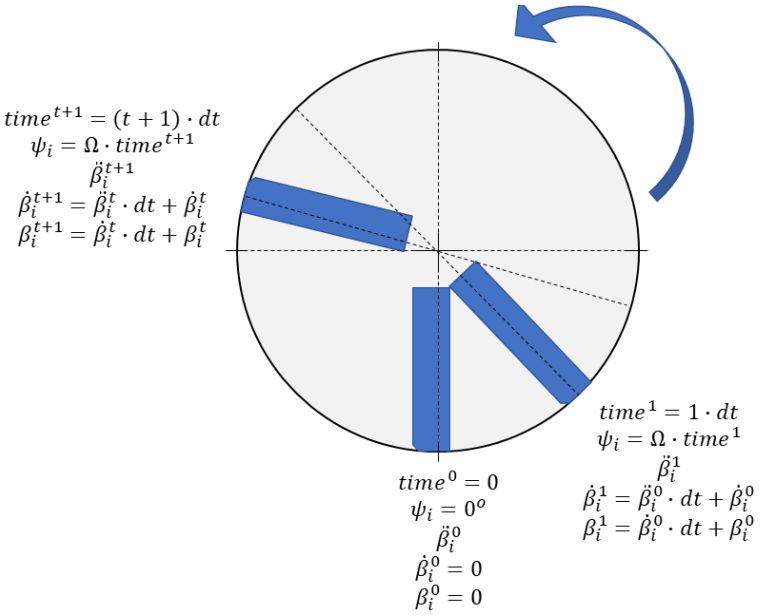

Figure 3.21. Flapping dynamics for a counterclockwise rotor

$$\ddot{\beta}_i^t = \frac{\overline{M_{Inertial_i}}^{Blade}(2)}{I_B} \tag{3.92}$$

$$\overline{\ddot{\beta}_i^t}^{Blade} = \begin{bmatrix} 0 \\ \ddot{\beta}_i^t \\ 0 \end{bmatrix} \tag{3.93}$$

$$\dot{\beta}_i^{t+1} = \ddot{\beta}_i^t dt + \dot{\beta}_i^t \tag{3.94}$$

$$\overline{\dot{\beta}_i^{t+1}}^{Blade} = \begin{bmatrix} 0 \\ \dot{\beta}_i^{t+1} \\ 0 \end{bmatrix} \tag{3.95}$$

$$\beta_i^{t+1} = \dot{\beta}_i^t dt + \beta_i^t \tag{3.96}$$

3.2.1.6 Inflow Models

Three different inflow models are implemented. They can be selected according to the desired level of fidelity.

3.2.1.6.1 Pitt-Peters Dynamic Inflow Model

In this function, the Pitt-Peters inflow model is implemented in the rotor and propeller model, which is explained in 2.5.2.

All calculations are done in the TPP Frame.

TPP angle of attack is initialized at the beginning of the function. TPP angle of attack is a persistent parameter.

$$\alpha_{TPP}^{t} = 0 \tag{3.97}$$

λ_0 is saturated to prevent the model's diverging to infinity or computing NaN.

$$\lambda_0^t = \max_{\lambda_0 \geq 10^{-5}} (\lambda_0^t) \tag{3.98}$$

The inflow ratio and the advance ratio of the TPP:

$$\lambda_r = \lambda_0^t + \frac{\sqrt{\bar{V}_{Hub}^{TPP}(1)^2 + \bar{V}_{Hub}^{TPP}(2)^2 + \bar{V}_{Hub}^{TPP}(3)^2}\sin(\alpha_{TPP}^t)}{\Omega R} \tag{3.99}$$

$$\mu_r = \frac{\sqrt{\bar{V}_{Hub}^{TPP}(1)^2 + \bar{V}_{Hub}^{TPP}(2)^2 + \bar{V}_{Hub}^{TPP}(3)^2}\cos(\alpha_{TPP}^t)}{\Omega R} \tag{3.100}$$

The angle of attack and sideslip of TPP:

$$\alpha_{TPP}^{t+1} = \tan^{-1}\frac{|\lambda_r|}{\mu_r} \tag{3.101}$$

$$\beta_{TPP} = \tan^{-1}\frac{-\bar{V}_{Hub}^{TPP}(2)}{-\bar{V}_{Hub}^{TPP}(1)} \tag{3.102}$$

Non-dimensional total velocity is calculated in Equation 3.103.

$$V_T = \sqrt{\lambda_r^2 + \mu_r^2} \tag{3.103}$$

Mass, flow parameter, and influence coefficient matrices:

$$\widehat{M} = \frac{1}{\pi}\begin{bmatrix} \frac{128}{75} & 0 & 0 \\ 0 & \frac{16}{45} & 0 \\ 0 & 0 & \frac{16}{45} \end{bmatrix} \tag{3.104}$$

$$\hat{V} = \begin{bmatrix} V_T & 0 & 0 \\ 0 & \frac{\mu_r^2 + (\lambda_r + \lambda_0^t)\lambda_r}{V_T} & 0 \\ 0 & 0 & \frac{\mu_r^2 + (\lambda_r + \lambda_0^t)\lambda_r}{V_T} \end{bmatrix} \tag{3.105}$$

$$\hat{L} = \begin{bmatrix} 0.5 & 0 & -\frac{15}{64}\pi\sqrt{\frac{1-\sin(\alpha_{TPP}^t)}{1+\sin(\alpha_{TPP}^t)}} \\ 0 & \frac{4}{1+\sin(\alpha_{TPP}^t)} & 0 \\ \frac{15}{64}\pi\sqrt{\frac{1-\sin(\alpha_{TPP}^t)}{1+\sin(\alpha_{TPP}^t)}} & 0 & \frac{4\sin(\alpha_{TPP}^t)}{1+\sin(\alpha_{TPP}^t)} \end{bmatrix} \tag{3.106}$$

Aerodynamic forcing terms [45]:

$$\bar{\tau} = \begin{bmatrix} C_T \\ C_L \\ -C_M \end{bmatrix} = \begin{bmatrix} \frac{\overline{F_{Aero}}_{Hub}^{TPP}(3)}{\rho(\pi R^2)(\Omega R)^2} \\ \frac{\overline{M_{Aero}}_{Hub}^{TPP}(1)}{\rho(\pi R^2)(\Omega R)^2 R} \\ \frac{-\overline{M_{Aero}}_{Hub}^{TPP}(2)}{\rho(\pi R^2)(\Omega R)^2 R} \end{bmatrix} \tag{3.107}$$

$$\begin{bmatrix} \dot{\lambda}_0 \\ \dot{\lambda}_{1s} \\ \dot{\lambda}_{1c} \end{bmatrix}^t = \left(\widehat{M}^{-1} \left(\bar{\tau} - \hat{V}(\hat{L} + \Delta\hat{L})^{-1} \begin{bmatrix} \lambda_0 \\ \lambda_{1s} \\ \lambda_{1c} \end{bmatrix}^t \right) \right) \Omega \quad 3.108$$

$$\begin{bmatrix} \lambda_0 \\ \lambda_{1s} \\ \lambda_{1c} \end{bmatrix}^{t+1} = \begin{bmatrix} \dot{\lambda}_0 \\ \dot{\lambda}_{1s} \\ \dot{\lambda}_{1c} \end{bmatrix}^t dt + \begin{bmatrix} \lambda_0 \\ \lambda_{1s} \\ \lambda_{1c} \end{bmatrix}^t \quad 3.109$$

3.2.1.6.2 Uniform Dynamic Inflow Model

In this function uniform, dynamic inflow model by Dreier is implemented [43], which is explained in 2.5.1.

$$\dot{\nu}^t = \frac{\overline{F_{Aero}}_{Hub}^{TPP}(3) - \rho(\pi R^2)\sqrt{\bar{V}_{Hub}^{TPP}(1)^2 + \bar{V}_{Hub}^{TPP}(2)^2 + \left(\nu^t + \bar{V}_{Hub}^{TPP}(3)\right)^2}\,\nu^t}{\frac{4}{3}\rho\pi(0.8R)^3} \quad 3.110$$

$$\nu^{t+1} = \dot{\nu}^t dt + \nu^t \quad 3.111$$

3.2.1.6.3 Unsteady Momentum Theory

This inflow model is activated when the ducted rotor or propeller model is used. The model is explained in 2.4.3.

$$\dot{\nu}^t = \frac{\overline{F_{Aero}}_{Hub}^{TPP}(3)}{\rho(\pi R^2)H_F} - \frac{\rho(\pi R^2)\left|\bar{V}_{Hub}^{TPP}(3) + 0.5\left(\frac{\bar{V}_{Hub}^{TPP}(3) + \nu^t}{\sigma_d} - \bar{V}_{Hub}^{TPP}(3)\right)\right|\left(\frac{\bar{V}_{Hub}^{TPP}(3) + \nu^t}{\sigma_d} - \bar{V}_{Hub}^{TPP}(3)\right)}{\rho(\pi R^2)H_F} \quad 3.112$$

$$\nu^{t+1} = \dot{\nu}^t dt + \nu^t \quad 3.113$$

Where $H_F = 2.5R$ is selected since it is inferred in [52] that it fits the best to the wind tunnel test data.

3.2.1.7 Shroud Total Forces

Shroud force is calculated as explained in 2.4.3.

$$
\begin{aligned}
&F_{Shroud} \\
&= \rho(\pi R^2) H_M \dot{v}^t \\
&+ \rho(\pi R^2) \sqrt{\bar{V}_{Hub}^{TPP}(1)^2 + \bar{V}_{Hub}^{TPP}(2)^2 + \left(v^t + \bar{V}_{Hub}^{TPP}(3)\right)^2} \left(\frac{\bar{V}_{Hub}^{TPP}(3) + v^t}{\sigma_d} - \bar{V}_{Hub}^{TPP}(3) \right) \\
&- \overline{F_{Aero}}_{Hub}^{TPP}(3)
\end{aligned}
\tag{3.114}
$$

When the coaxial rotor/propeller model is activated, the inflow acceleration and the inflow of the upper rotor are corrected by a correction factor while calculating the shroud force of the lower rotor.

$$
\begin{aligned}
&F_{Shroud} \\
&= \rho(\pi R^2) H_M 0.32 \dot{v}_k^t \\
&+ \rho(\pi R^2) \sqrt{\bar{V}_{Hub}^{TPP}(1)^2 + \bar{V}_{Hub}^{TPP}(2)^2 + \left(0.32 v_k^t + \bar{V}_{Hub}^{TPP}(3)\right)^2} \left(\frac{\bar{V}_{Hub}^{TPP}(3) + 0.32 v_k^t}{\sigma_d} \right. \\
&\left. - \bar{V}_{Hub}^{TPP}(3) \right) - \overline{F_{Aero}}_{Hub}^{TPP}(3)
\end{aligned}
\tag{3.115}
$$

$$
\bar{F}_{Shroud}^{Hub} = \begin{bmatrix} 0 \\ 0 \\ F_{Shroud} \end{bmatrix} \tag{3.116}
$$

Where $H_M = H_F$.

CHAPTER 4

MODEL VALIDATION

In this chapter, comparisons between the test data of the full-scale isolated rotor of the S-76 helicopter, performed at the NASA Ames 80- by-120-foot wind tunnel, and the trim results of the rotor model with the same rotor parameters are given. The wind tunnel test data are obtained from the document [61], and the rotor parameters belonging to the S-76 helicopter are found in the documents [61, 62, 63, 56]. Some of those parameters are given in Table 4.1. Blade chord and twist radial distributions are shown in Appendix B. Airfoils' 2D aerodynamic lift, and drag coefficient tables are provided in Appendix C. As the S-76 main rotor blade has two different airfoil profiles, the aerodynamic coefficients are found in the transition region by making linear interpolation between these airfoils' data. From aerodynamic root cutout to 80% inboard of the radial location, SC1095-R8 airfoil is used, and from 84% outboard of the radial location to the blade tip, SC1095 airfoil is used.

Table 4.1. S-76 main rotor properties (SI Units)

Parameter	*Value*
Radius [m]	6.71
Number of Blades	4
Solidity	0.0748
Hinge Offset	0.037R
Blade Mass [kg]	44.37
Flapping Inertia [kg-m^2]	554.08
First Mass Moment [kg-m]	129.35
Hub Spring [N-m/rad]	1616
Pitch-Flap Coupling [°]	16.96
Nominal RPM	293

The wind tunnel measurements of the S-76 main rotor are gathered under steady-state conditions. In wind tunnel tests, the isolated rotor is trimmed to the designated thrust at a selected shaft angle and a wind tunnel speed from 0 to 100 knots with lateral & longitudinal flapping angles held at ± 0.2 degrees.

The presented data were corrected for aerodynamic tares accounting for the aerodynamic forces on the rotor hub, shaft, and mechanical parts. However, corrections for the tunnel wall effects were not applied to the data. Therefore, this error should not be forgotten in the discussion part of the comparison figures. The error caused by the wall effects can be summarized such that the isolated rotor thrust and power measurements in the wind tunnel tests are higher than they should be when the thrust and torque generated by the rotor on the whirl tower are compared, as theory and experiments indicate [64]. The wall effects are observed mainly at very low wind tunnel velocities [65]. Therefore, the wall effects are investigated with hover tests by performing the same hover tests a different shaft angles and by rotating the heading of the rotor test setup by $\psi = 90°$ to the east wall.

Figure 4.1 shows the schematic of the wind tunnel, and Figure 4.2 illustrates the rotation of the rotor heading from the tunnel inlet to the east wall. Figure 4.3 shows the test setup. Figure 4.4 presents the shaft tilt notation to the forward and aft.

In the measurements, the rotor's thrust is collected perpendicular to the TPP of the rotor, and the torque is measured from the shaft of the rotor. As seen in Figure 4.3 and Figure 4.4, the free stream velocity V^{∞} is parallel to the tunnel floor.

In this thesis, the model is validated under steady-state conditions assuming that the model is also valid under quasi-steady conditions. Model trim is accomplished using the integral controllers driving the rotor model to the desired thrust and pitch and roll moments in an acceptable tolerance. The articulated rotor configuration with Pitt-Peters dynamic inflow is simulated for the comparisons.

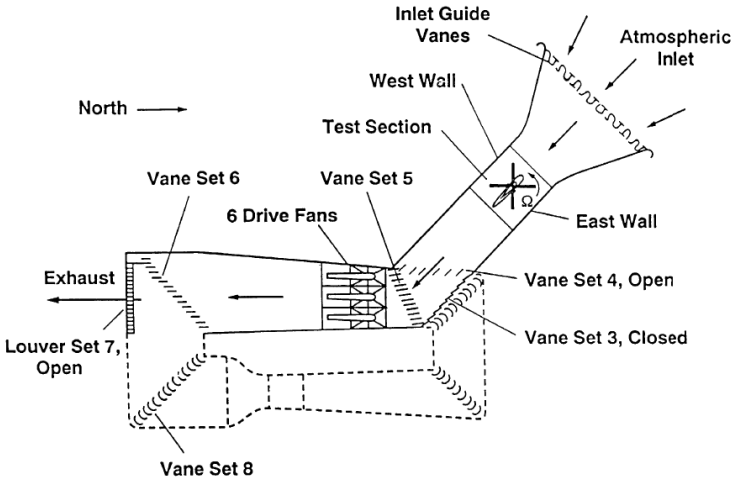

Figure 4.1. Schematic of 80-by-120 foot wind tunnel circuit [61]

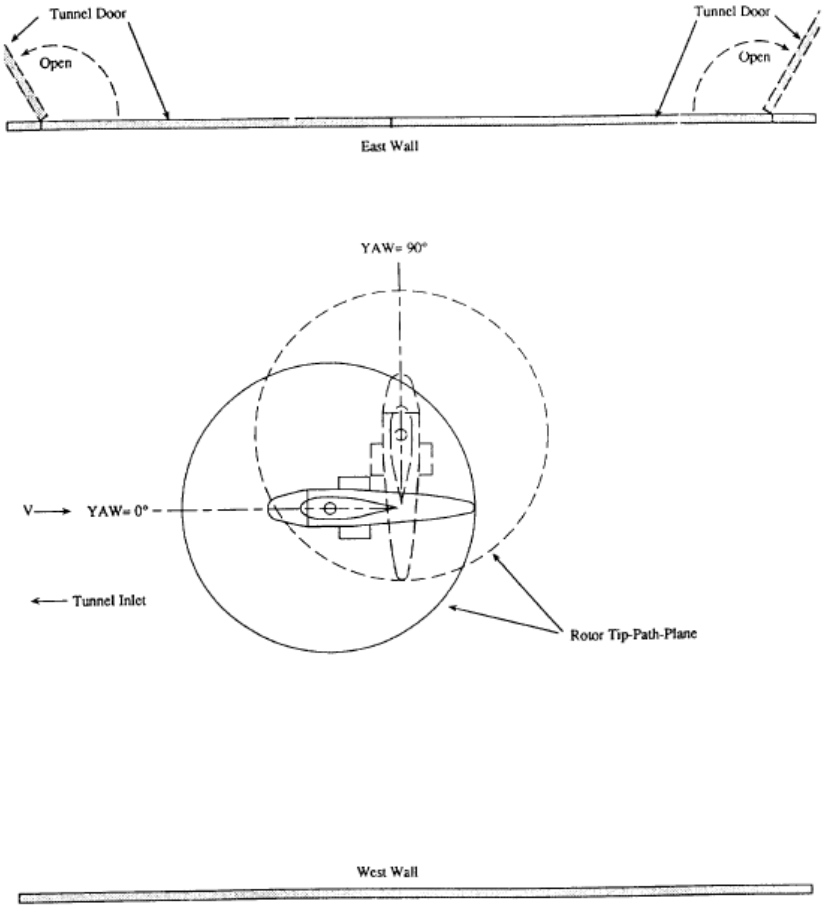

Figure 4.2. Illustration of the rotation of the rotor heading from the tunnel inlet to the east wall [61]

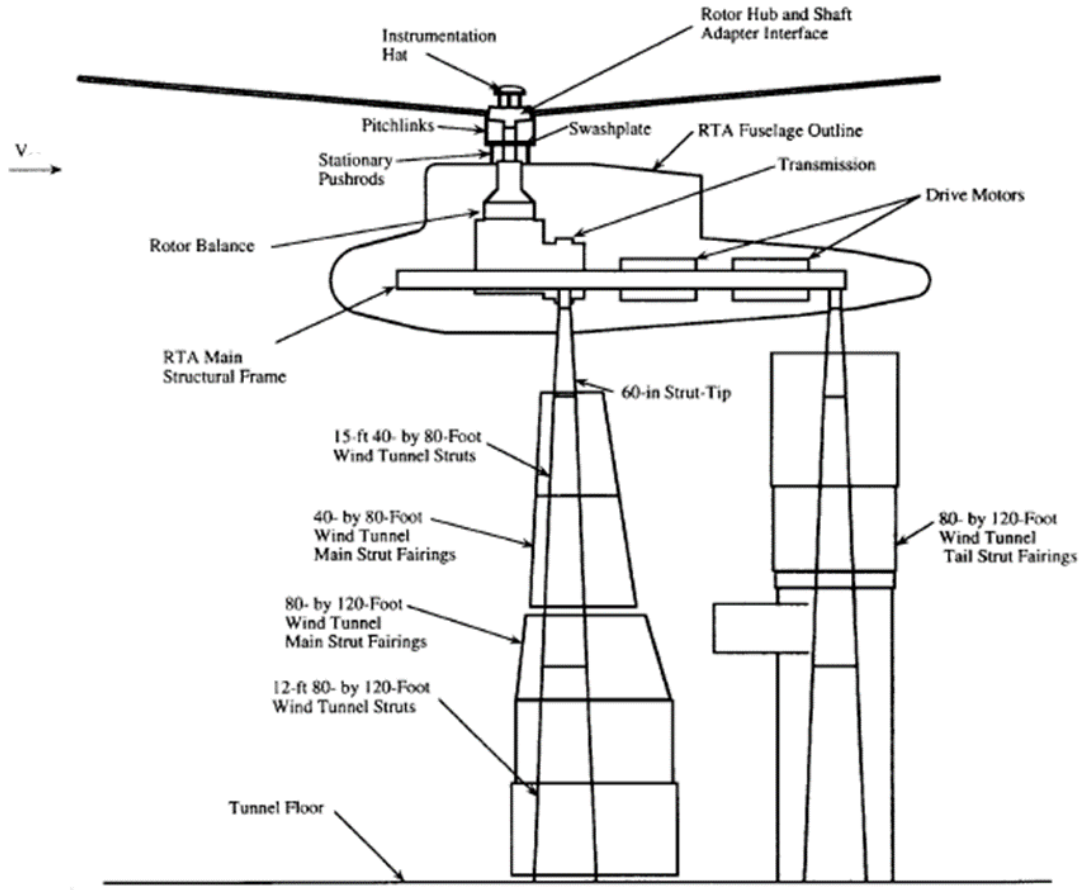

Figure 4.3. Schematic of S-76 rotor test setup in the 80-by-120 foot wind tunnel [61]

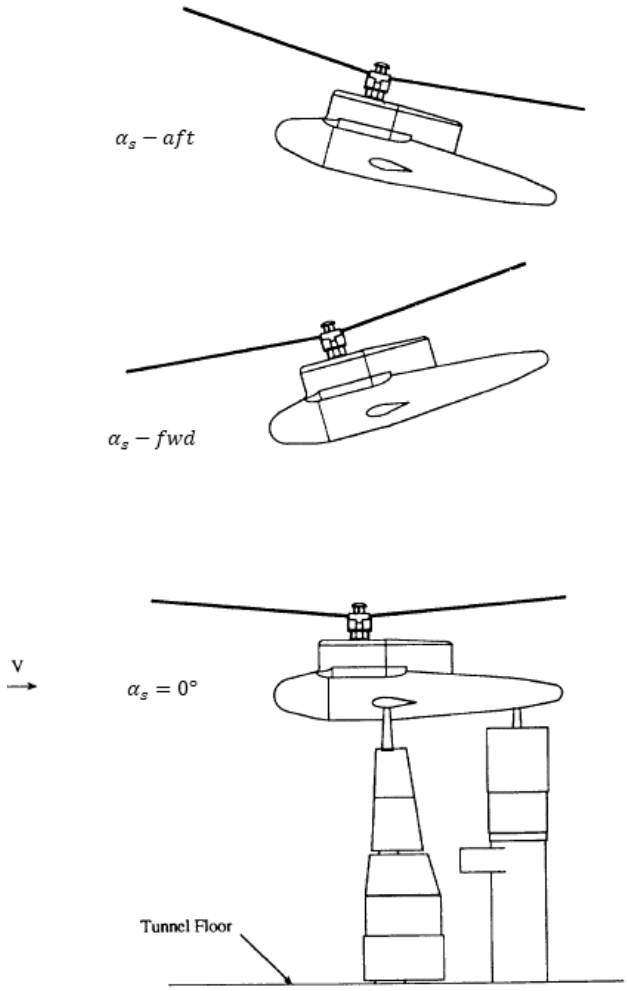

Figure 4.4. Illustration of the shaft tilt [61]

4.1 Hover

From Figure 4.5 to Figure 4.11, the model is compared with the wind tunnel test data at hover conditions. Test cases are almost at the same air densities. All available test data at different shaft angles (θ_s) and at different headings (ψ) are shown in the figures. Since the wind tunnel wall effects are present in the test data, comparing the mean of all the available test data is assumed to be eliminated those effects. As the shaft angle does not change the outputs of the rotor model in hover, an arbitrary shaft angle ($\theta_s = 0°$) is selected in the simulations. Wind tunnel performance data for hover tests are given in Appendix D.

In Figure 4.5, the rotor power coefficient as a function of the rotor thrust coefficient in hover is given. Figure 4.6 compares the model results with the wind tunnel test results for the relation between the collective angle and the normalized rotor thrust coefficient in hover. Similarly, in Figure 4.7, a comparison is made between the model results and the wind tunnel test data regarding the coning angle and the rotor thrust coefficient to see whether the relation between aerodynamic and centrifugal loads is modeled correctly [48]. The on-axis response of the rotor is compared in Figure 4.8, Figure 4.9, Figure 4.10, and Figure 4.11.

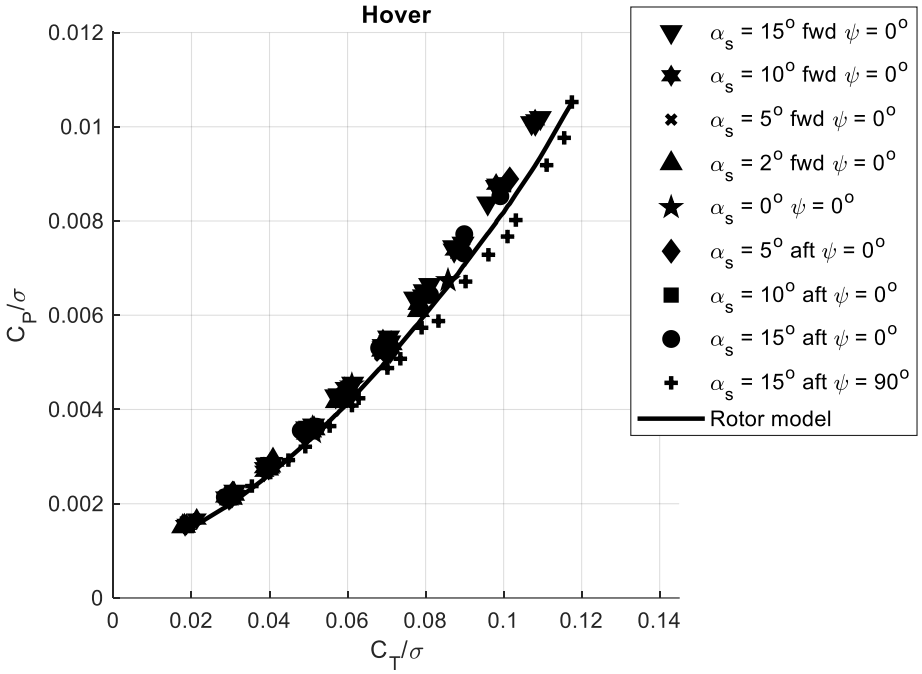

Figure 4.5. Rotor power coefficient as a function of rotor thrust coefficient, hover

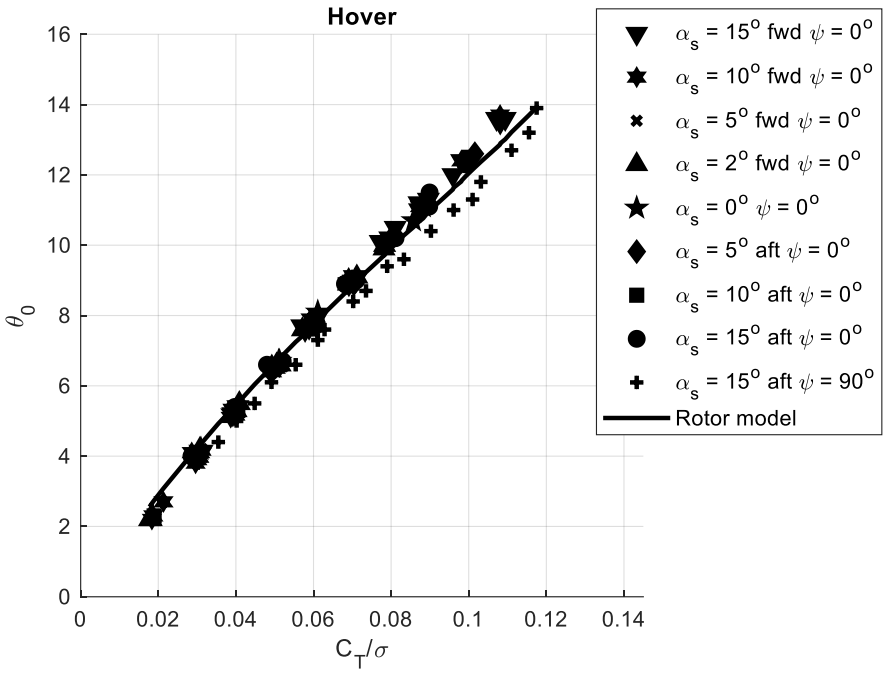

Figure 4.6. Relation between the collective angle and the rotor thrust coefficient, hover

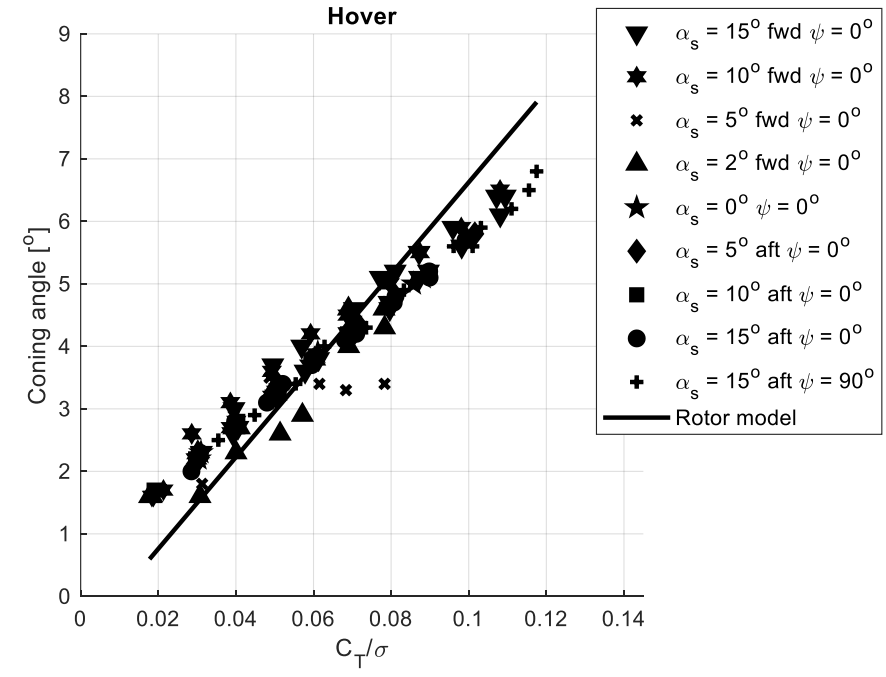

Figure 4.7. Relation between the coning angle and the rotor thrust coefficient, hover

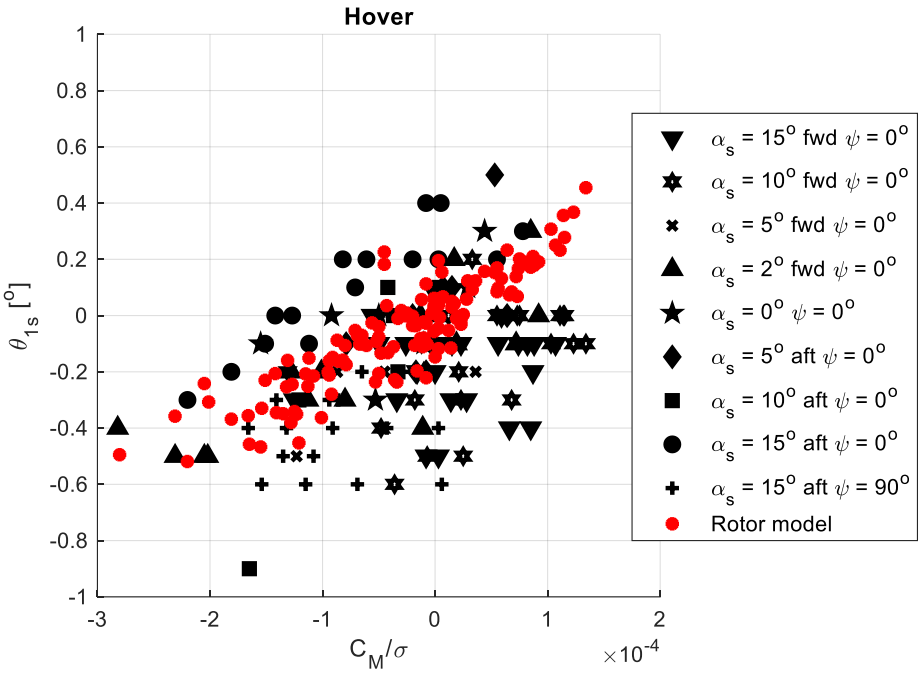

Figure 4.8. Pitch control vs. Pitch moment, hover

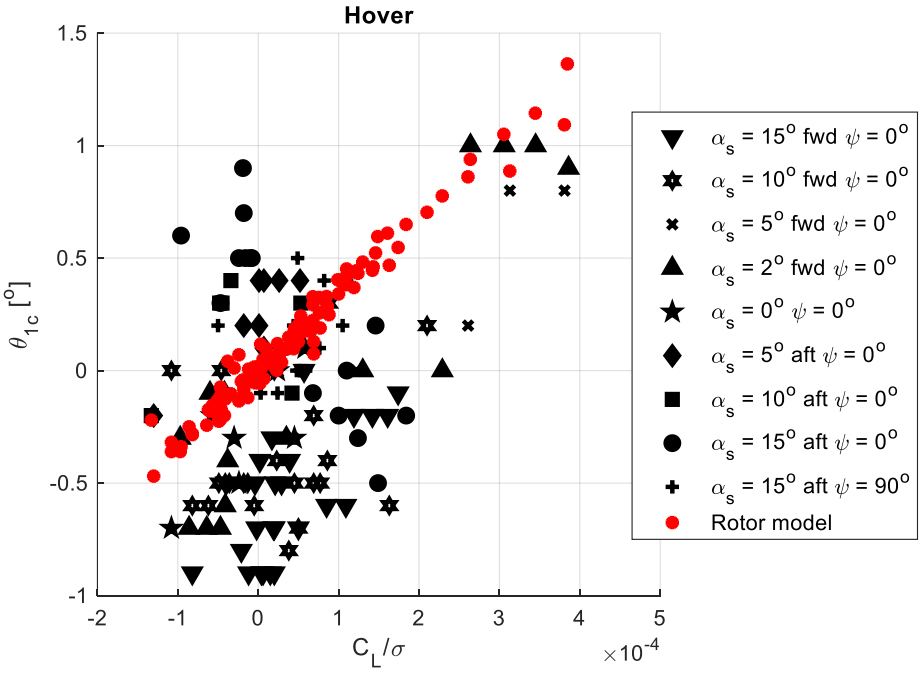

Figure 4.9. Roll control vs. Roll moment, hover

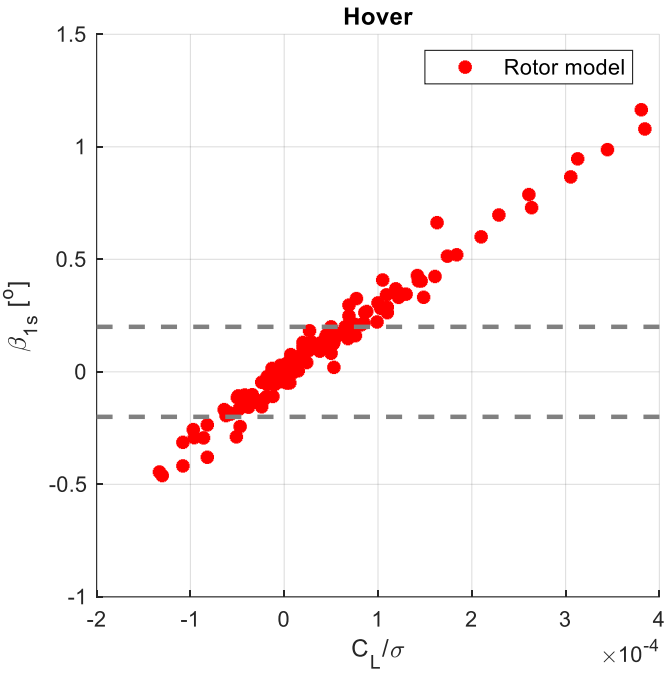

Figure 4.10. Lateral blade flapping, hover

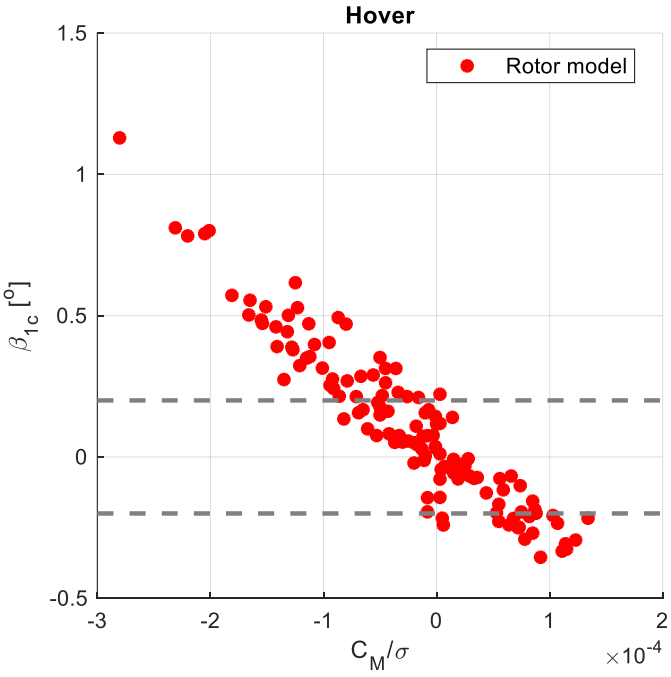

Figure 4.11. Longitudinal blade flapping, hover

4.1.1 Observations

In the power coefficient versus normalized thrust coefficient plot, the normalized rotor power coefficient represents the rotor disk's mean profile drag and induced drag coefficients. Similarly, the normalized rotor thrust coefficient gives the mean lift coefficient over the rotor disk. Therefore, these plots are lift-over drag plots of the whole rotor affected by solidity, the number of blades, tip Mach number, and blade profile [48]. Assuming that the model uses all the geometric properties of the S-76 main rotor correctly, these plots verify the aerodynamic characteristic of the blade profile, inflow estimation, and 3D aerodynamic effects besides the whole mathematical model. Since the model agrees with the test data, it is concluded that the model indicates the lift-drag ratio with good compatibility. The inflow estimation of the model reflects the reality in hover. 3D aerodynamic effects that are modeled are sufficient for steady-state simulations at this level of fidelity.

In addition to what normalized power coefficient versus normalized thrust coefficient plots validate, the normalized rotor thrust coefficient versus the collective angle plots validate the blades' twist distribution and torsional elasticity. Since blades are modeled rigid, the 3D aerodynamic effects and inflow estimations cover the torsional bending, assuming that the twist distribution is modeled correctly. It is seen that the model results in the same thrust value at the corresponding collective pitch angle with the actual rotor according to the wind tunnel test data.

Figure 4.7 shows that the model agrees with the rotor according to the test data, with approximately one degree of error at maximum. Harmonic balancing results in β_0 in hover as expressed in Equation 4.1 retrieved from [44]. According to this relation, the error is caused by the error in the geometric parameters like spring constant, the blade's center of gravity, blade mass, or hinge offset, or by the slight difference in θ_0 at maximum and minimum thrust values which can be seen in Figure 4.6.

$$\beta_0 = \frac{\gamma(1-e)^2\left(1+\frac{2}{3}e+\frac{1}{3}e^2\right)}{8\left(1+\varepsilon+\frac{K_\beta}{I_B\Omega^2}\right)}\theta_0 \quad 4.1$$

where, γ is the Lock's number,

$$\gamma = \frac{\rho a c R^4}{I_B} \quad 4.2$$

$$\varepsilon = \frac{m_b d_{BldCG2Hng} e R^2}{I_B} \quad 4.3$$

In the on-axis response figures, pitch-up and roll-left moments are positive according to the Hub Fixed Frame. ± 0.2 degrees limits are shown with gray dashed lines in the flapping figures.

It is concluded that the cyclic inputs show the same trend as the test data, cyclic input directions are correct, and cyclic input amounts are compatible. However, it is seen that the model's corresponding longitudinal and lateral flappings are not within the limits of the wind tunnel tests, which is explained by the theory [44] in Equation 4.4 and Equation 4.5. The magnitude of the first harmonics of the flapping should be close to the cyclic blade feathering angles magnitudes in hover. Therefore, the blade pitch angle figures indicate that the flapping angles have not been held within limits strictly in the wind tunnel tests.

$$\beta_{1s} = \frac{\gamma(1-e)^2\left(1+\frac{2}{3}e+\frac{1}{3}e^2\right)}{8\left(\left(\varepsilon+\frac{K_\beta}{I_B\Omega^2}\right)^2+n^2\right)}\left(n\theta_{1c}+\left(\varepsilon+\frac{K_\beta}{I_B\Omega^2}\right)\theta_{1s}\right) \quad 4.4$$

$$\beta_{1c} = \frac{\gamma(1-e)^2\left(1+\frac{2}{3}e+\frac{1}{3}e^2\right)}{8\left(\left(\varepsilon+\frac{K_\beta}{I_B\Omega^2}\right)^2+n^2\right)}\left(\left(\varepsilon+\frac{K_\beta}{I_B\Omega^2}\right)\theta_{1c}-n\theta_{1s}\right) \quad 4.5$$

where,

$$n = \frac{\gamma}{8}(1-e)^3\left(1+\frac{1}{3}e\right) \quad 4.6$$

4.2 Forward Flight

This section presents forward flight test comparisons between the wind tunnel test data and the model for thrust sweep conditions at constant wind speeds with varying shaft angles. Steady-state simulations are done under the same conditions. Wind tunnel performance data for forward flight thrust sweep tests are given in Appendix D.

4.2.1 Forward Flight - 20 Knot

From Figure 4.12 to Figure 4.18, the model is compared with the wind tunnel test data at 20 knots forward flight conditions with shaft 2° forward shaft angle. Figure 4.12 shows the rotor power coefficient as a function of the thrust coefficient. Figure 4.13 compares the model results with the wind tunnel test results for the relation between the collective angle and the normalized rotor thrust coefficient. Similarly, in Figure 4.14, a comparison is made between the model results and the wind tunnel test data regarding the coning angle and the rotor thrust coefficient. The on-axis response of the rotor is compared in Figure 4.15, Figure 4.16, Figure 4.17, and Figure 4.18. In the figures, pitch-up and roll-left moments are positive according to the Hub Fixed Frame. ± 0.2 degrees limits are shown with gray dashed lines in the flapping figures. Since there are no TPP angle measurements in the test data, the blade flappings need not be demonstrated further. Also, Figure 4.15 and Figure 4.16 show an inflow model comparison for 20 knots airspeed.

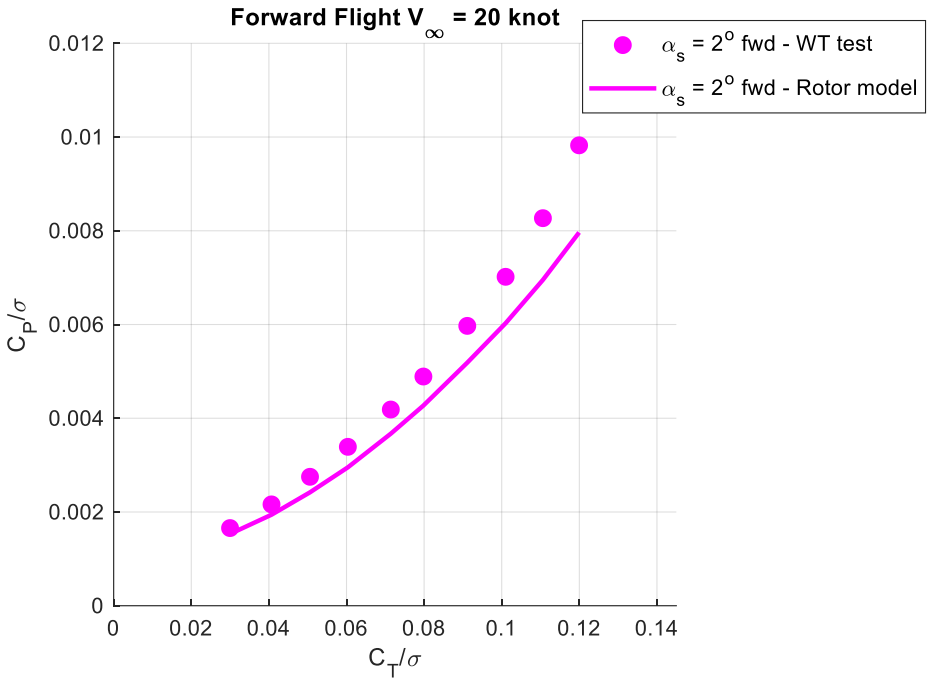

Figure 4.12. Rotor power coefficient as a function of rotor thrust coefficient, 20 knots forward flight

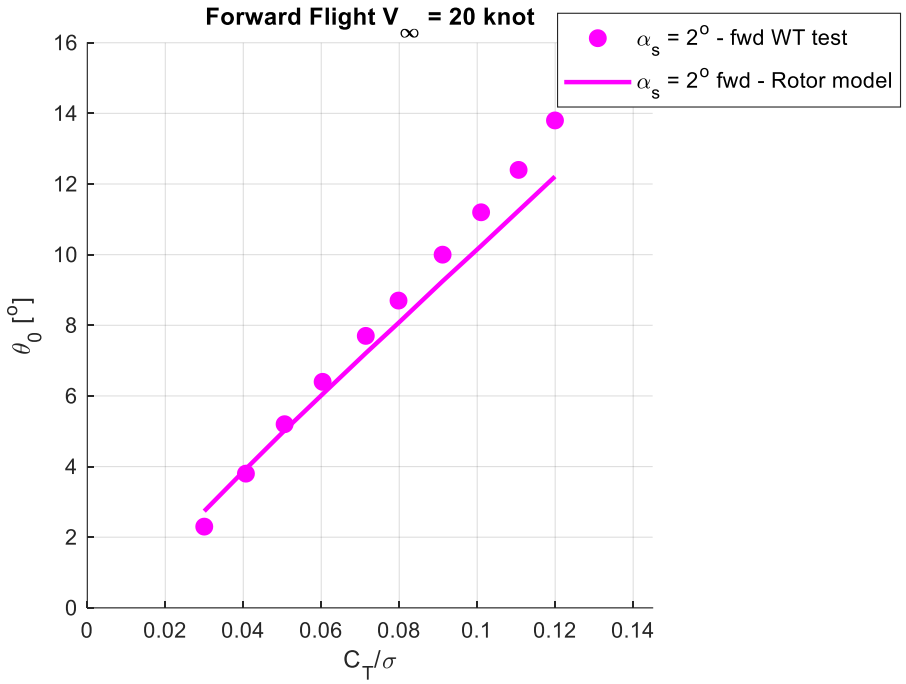

Figure 4.13. Relation between the collective angle and the rotor thrust coefficient, 20 knots forward flight

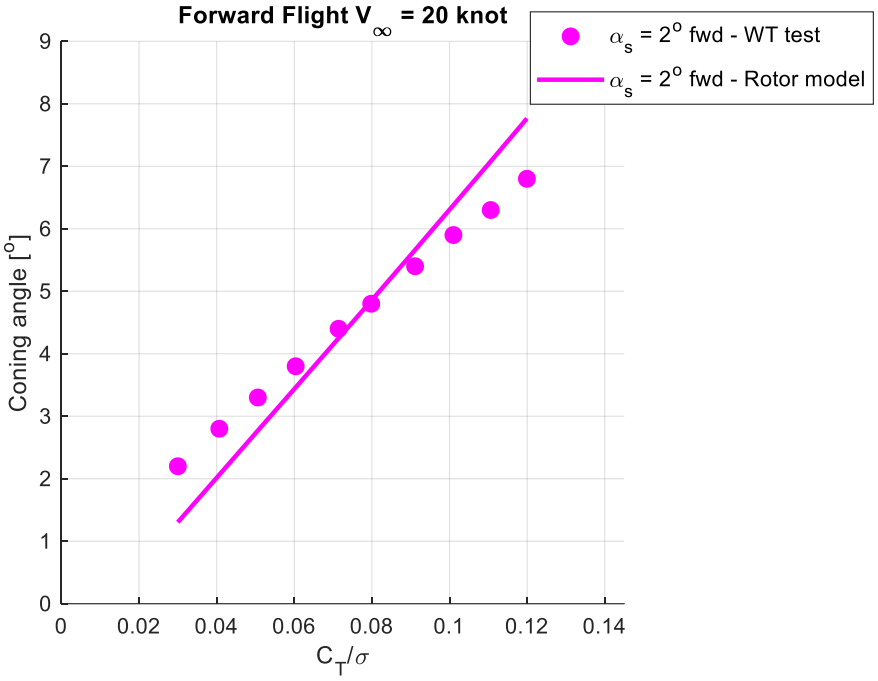

Figure 4.14. Relation between the coning angle and the rotor thrust coefficient, 20 knots forward flight

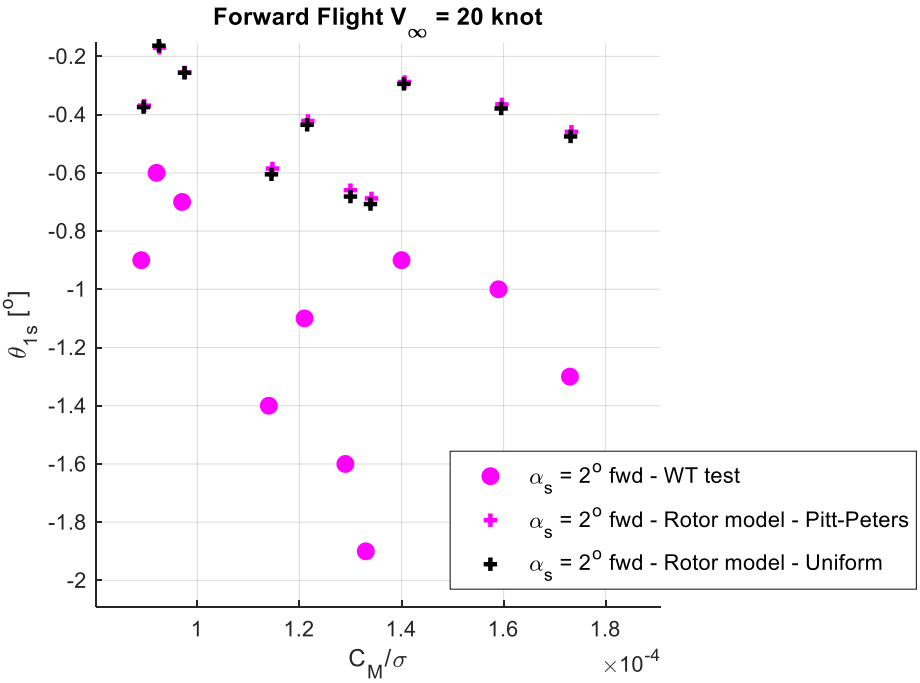

Figure 4.15. Pitch control vs. Pitch moment, 20 knots forward flight, 2° forward shaft angle

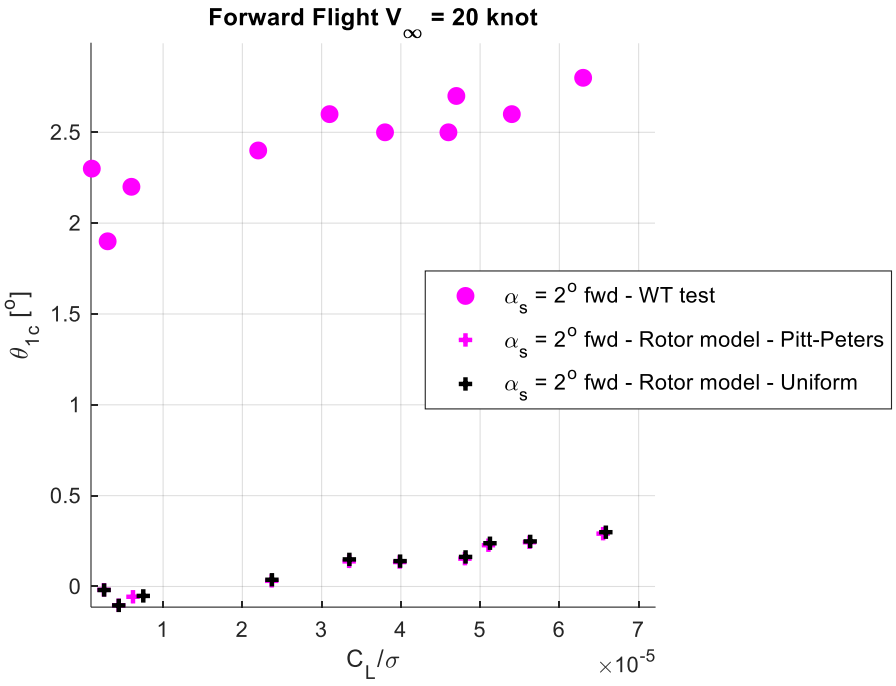

Figure 4.16. Roll control vs. Roll moment, 20 knots forward flight, 2° forward shaft angle

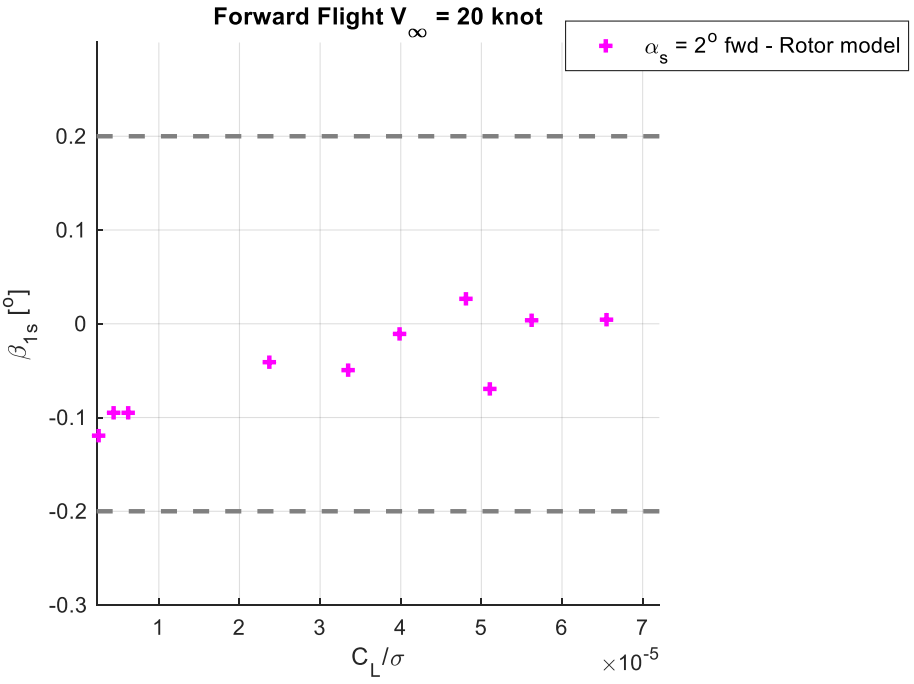

Figure 4.17. Lateral blade flapping, 20 knots forward flight, 2° forward shaft angle

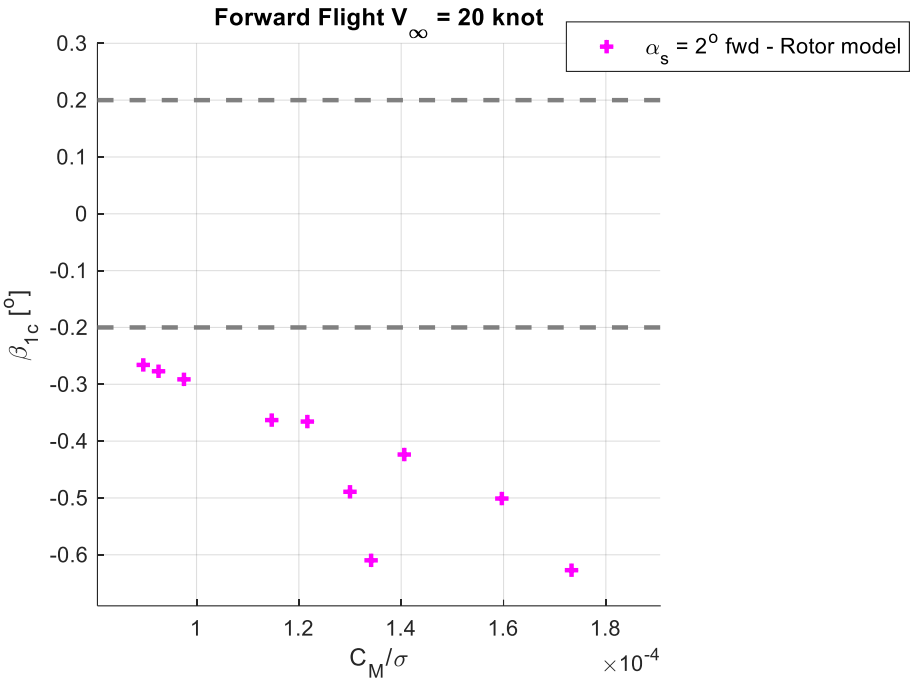

Figure 4.18. Longitudinal blade flapping, 20 knots forward flight, 2° forward shaft angle

4.2.2 Forward Flight - 30 Knot

From Figure 4.19 to Figure 4.23, the model is compared with the wind tunnel test data at 30 knots forward flight conditions with a 0° forward shaft angle. Figure 4.19 shows the rotor power coefficient as a function of the thrust coefficient. Figure 4.20 compares the model results with the wind tunnel test results for the relation between the collective angle and the normalized rotor thrust coefficient. Similarly, in Figure 4.21, a comparison is made between the model results and the wind tunnel test data regarding the coning angle and the rotor thrust coefficient. The on-axis response of the rotor is compared in Figure 4.22 and Figure 4.23.

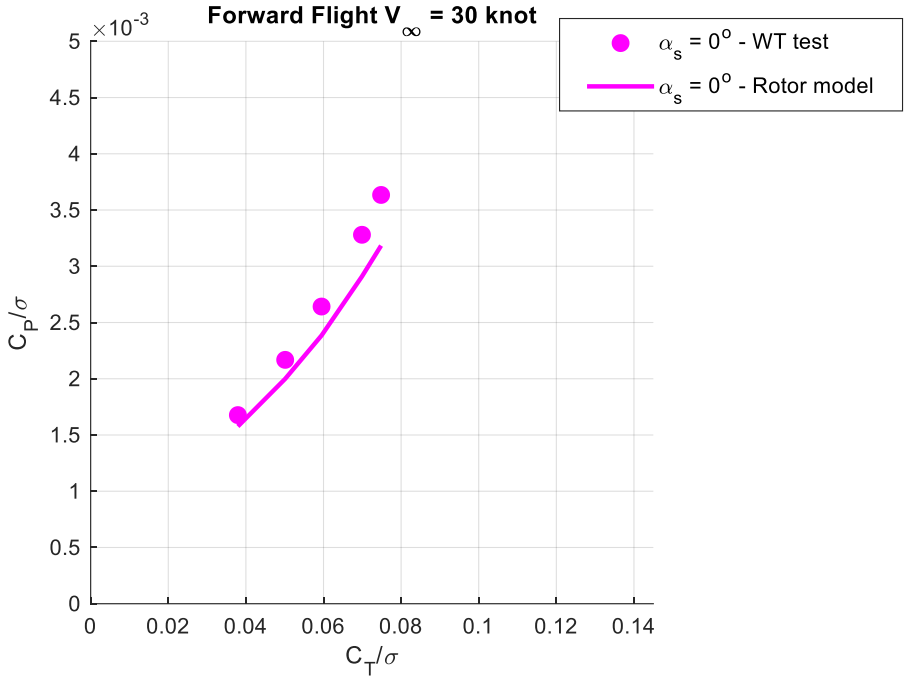

Figure 4.19. Rotor power coefficient as a function of rotor thrust coefficient, 30 knots forward flight

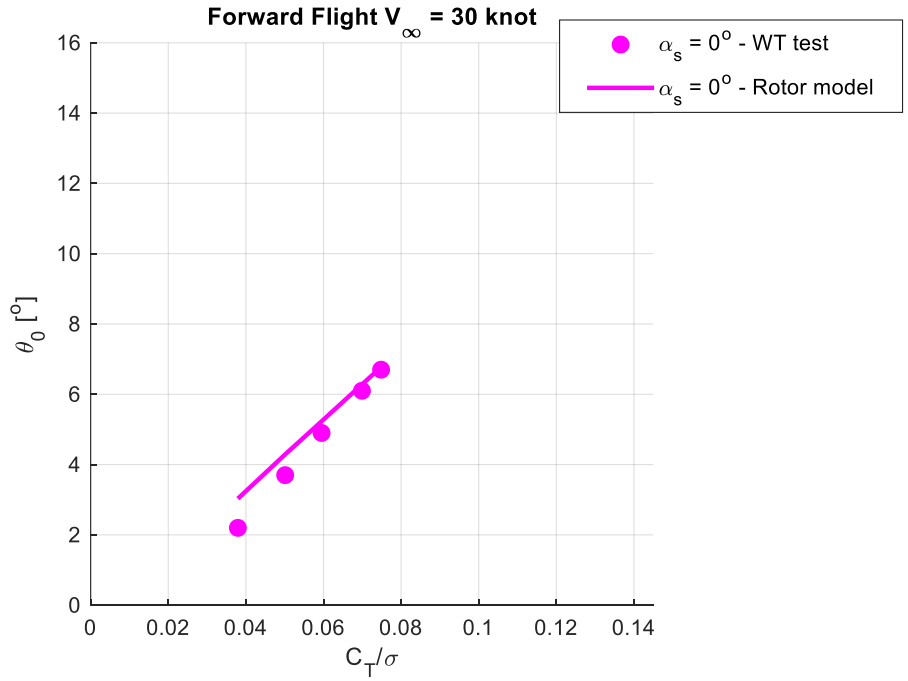

Figure 4.20. Relation between the collective angle and the rotor thrust coefficient, 30 knots forward flight

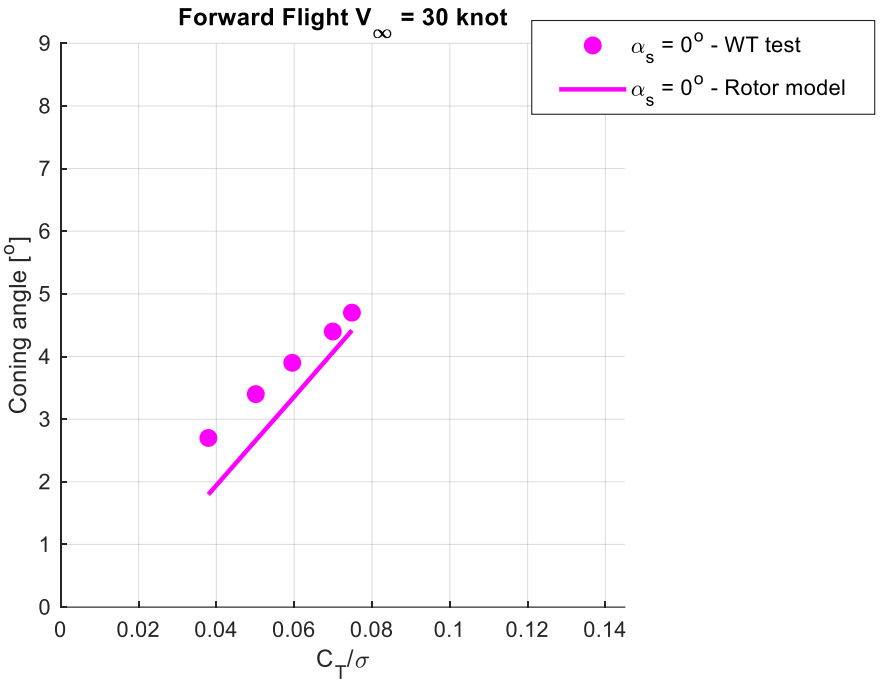

Figure 4.21. Relation between the coning angle and the rotor thrust coefficient, 30 knots forward flight

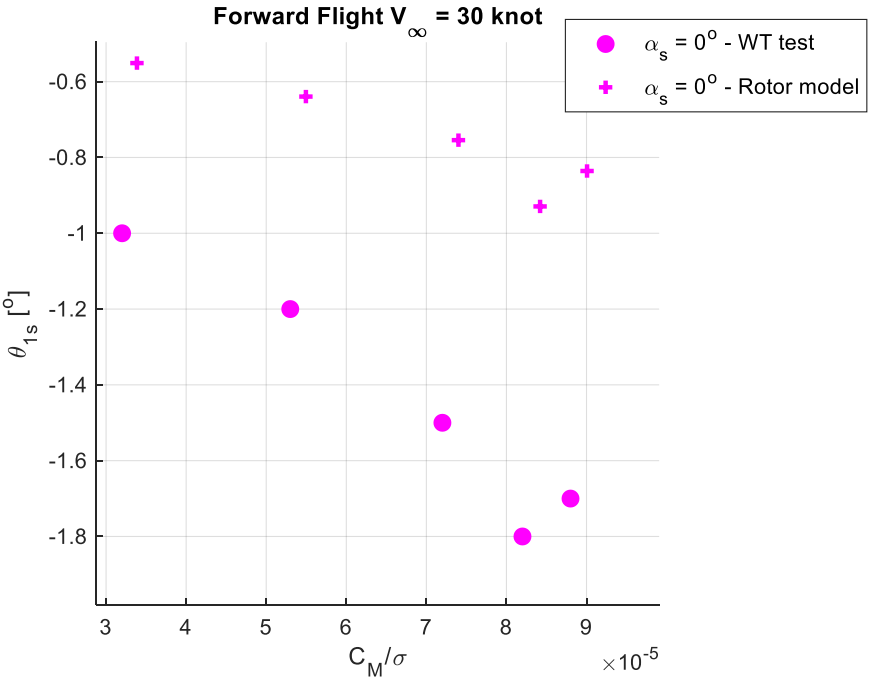

Figure 4.22. Pitch control vs. Pitch moment, 30 knots forward flight, 0° shaft angle

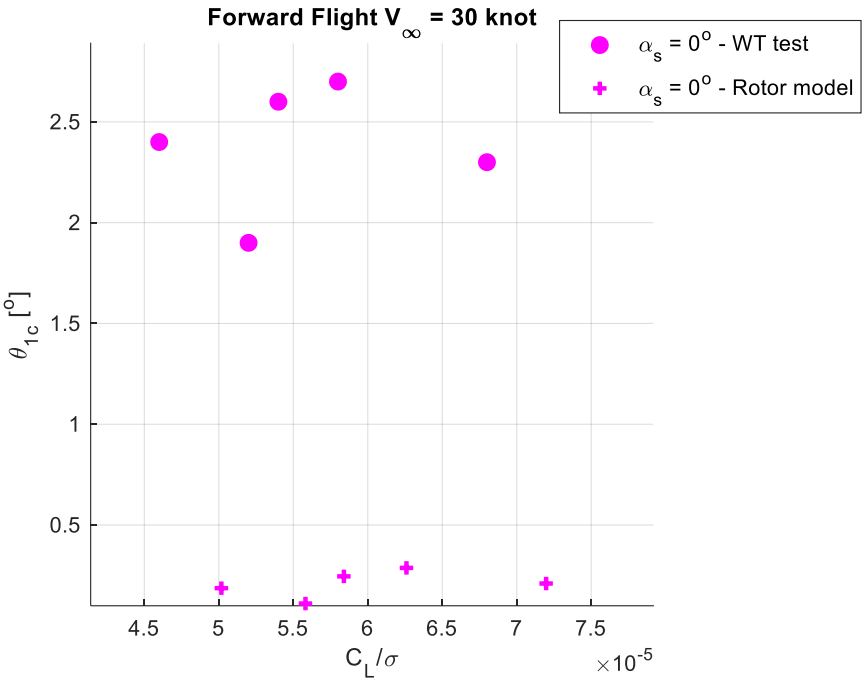

Figure 4.23. Roll control vs. Roll moment, 30 knots forward flight, 0° shaft angle

4.2.3 Forward Flight - 40 Knot

From Figure 4.24 to Figure 4.34, the model is compared with the wind tunnel test data at 40 knots forward flight conditions with 10° forward, 2° forward, 5° aft, and 10° aft shaft angles. Figure 4.24 shows the rotor power coefficient as a function of the thrust coefficient. Figure 4.25 compares the model results with the wind tunnel test results for the relation between the collective angle and the normalized rotor thrust coefficient. Similarly, in Figure 4.26, a comparison is made between the model results and the wind tunnel test data regarding the coning angle and the rotor thrust coefficient. In Figure 4.27, Figure 4.28, Figure 4.29, and Figure 4.30, the pitch axis response and in Figure 4.31, Figure 4.32, Figure 4.33, and Figure 4.34, the roll axis response are compared for different shaft angles.

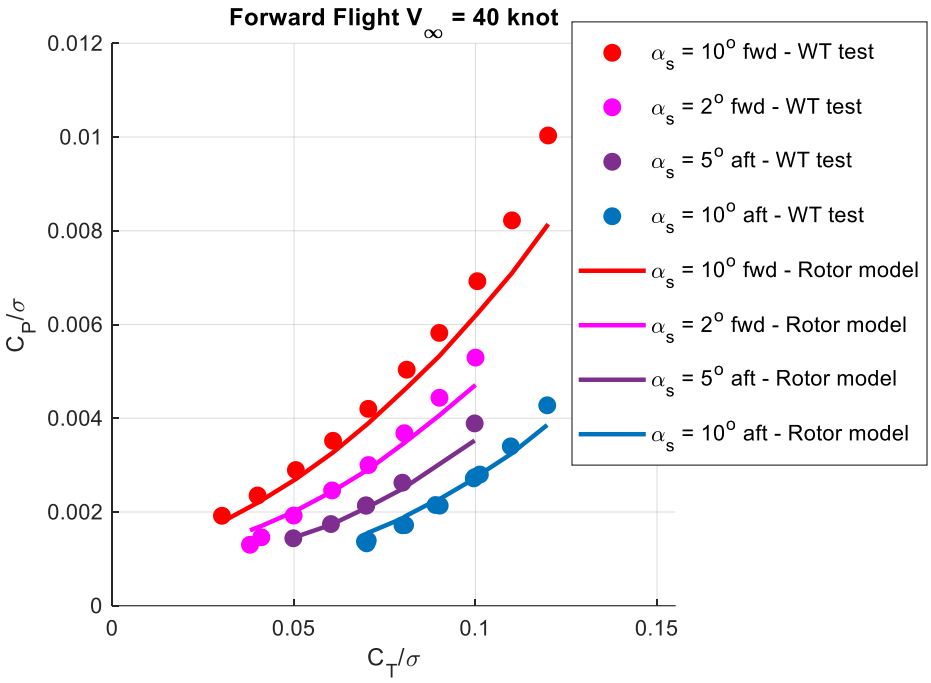

Figure 4.24. Rotor power coefficient as a function of rotor thrust coefficient, 40 knots forward flight

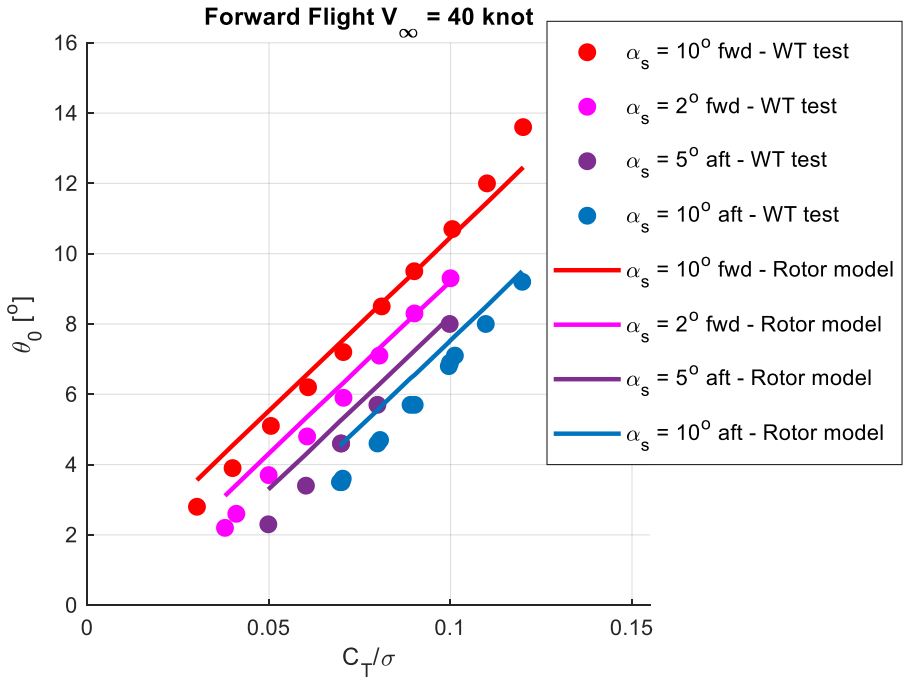

Figure 4.25. Relation between the collective angle and the rotor thrust coefficient, 40 knots forward flight

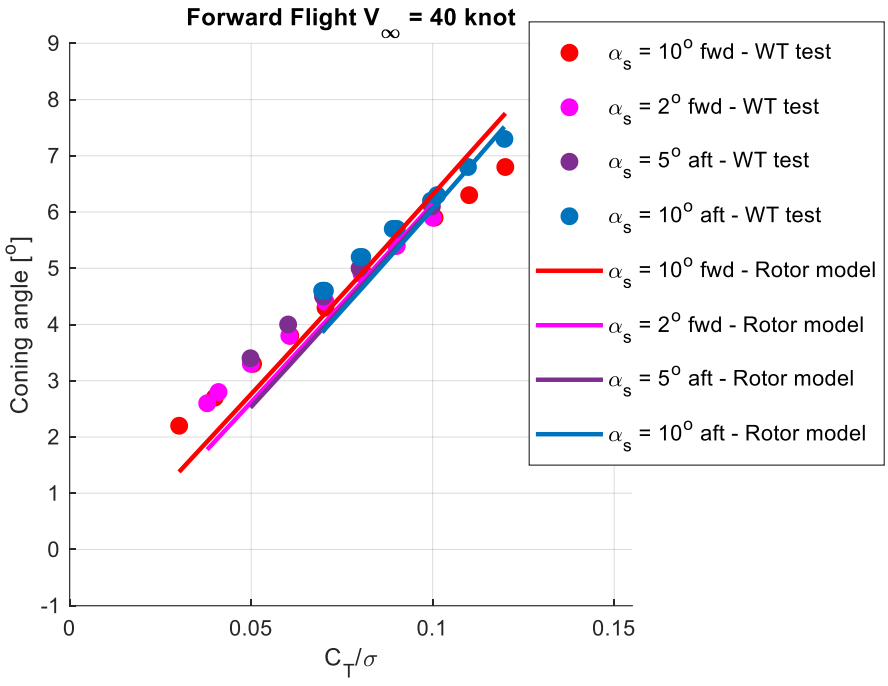

Figure 4.26. Relation between the coning angle and the rotor thrust coefficient, 40 knots forward flight

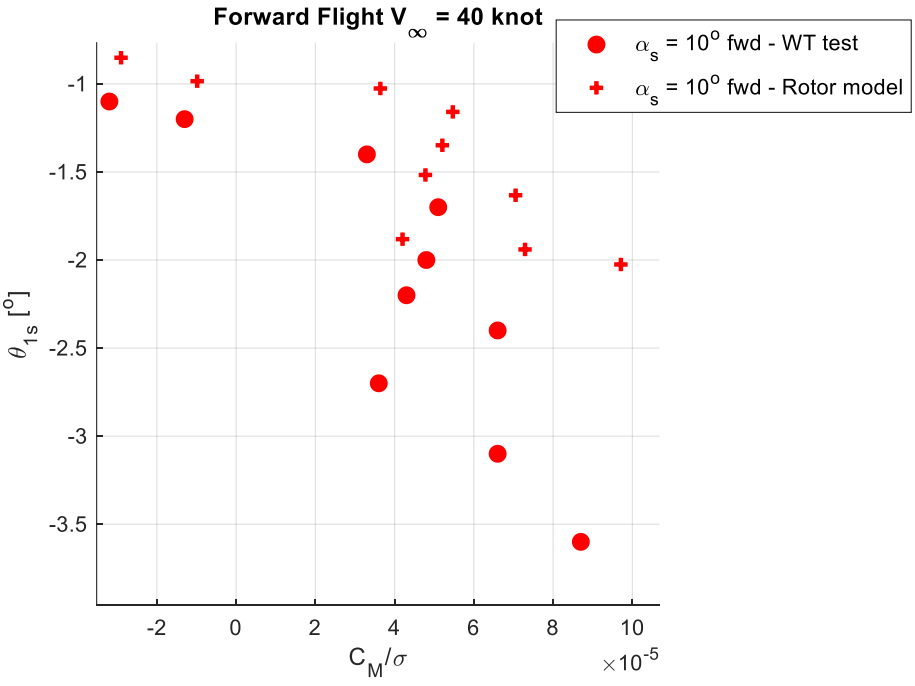

Figure 4.27. Pitch control vs. Pitch moment, 40 knots forward flight, 10° forward shaft angle

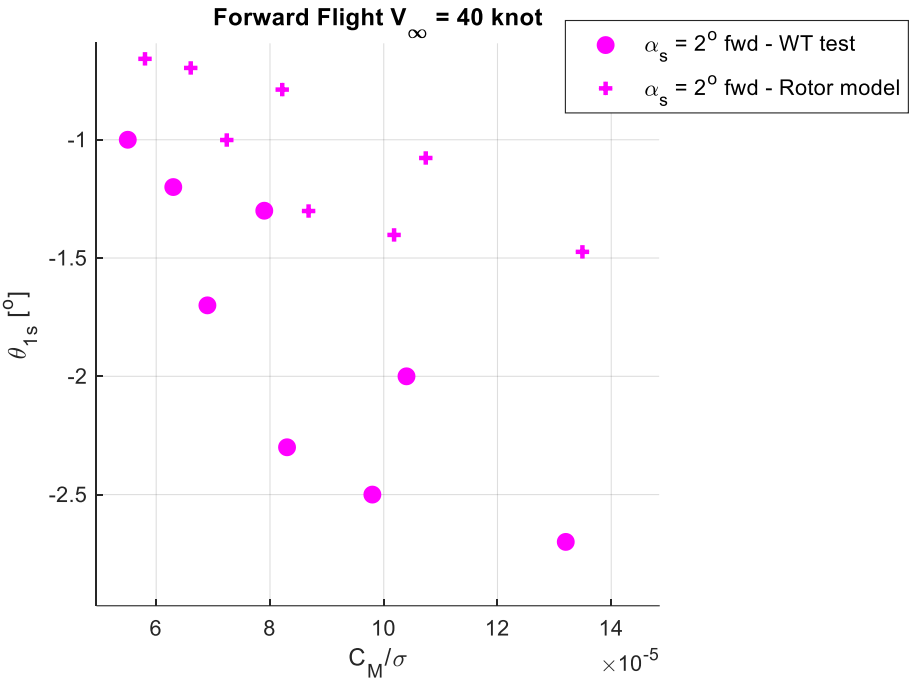

Figure 4.28. Pitch control vs. Pitch moment, 40 knots forward flight, 2° forward shaft angle

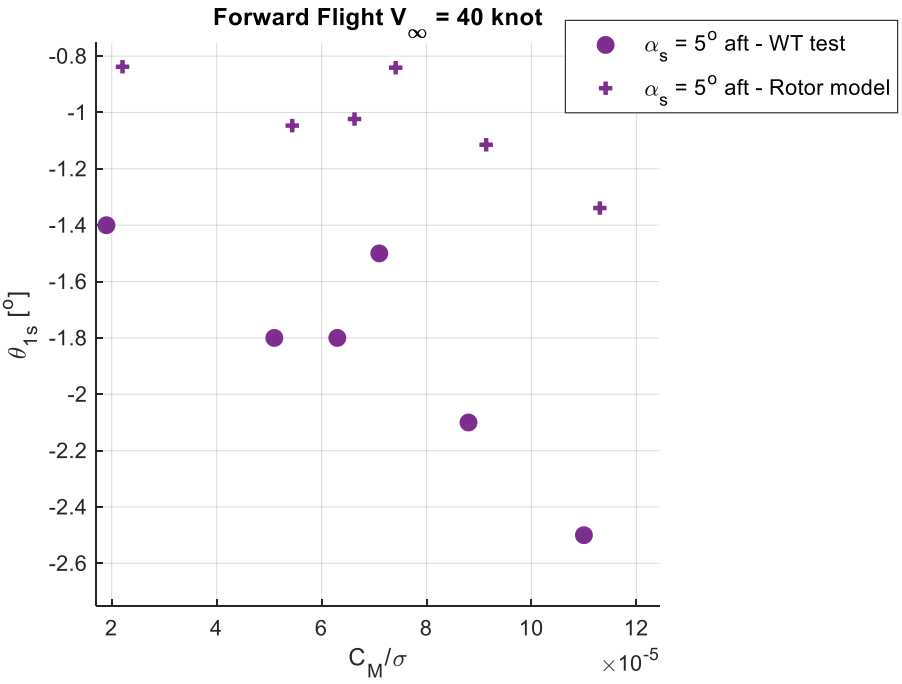

Figure 4.29. Pitch control vs. Pitch moment, 40 knots forward flight, 5° aft shaft angle

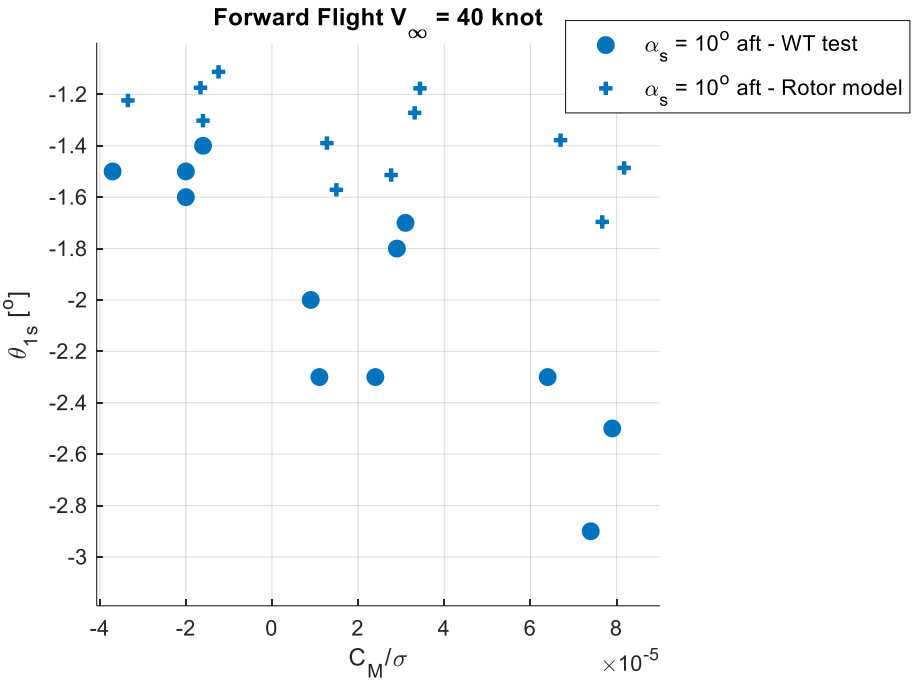

Figure 4.30. Pitch control vs. Pitch moment, 40 knots forward flight, 10° aft shaft angle

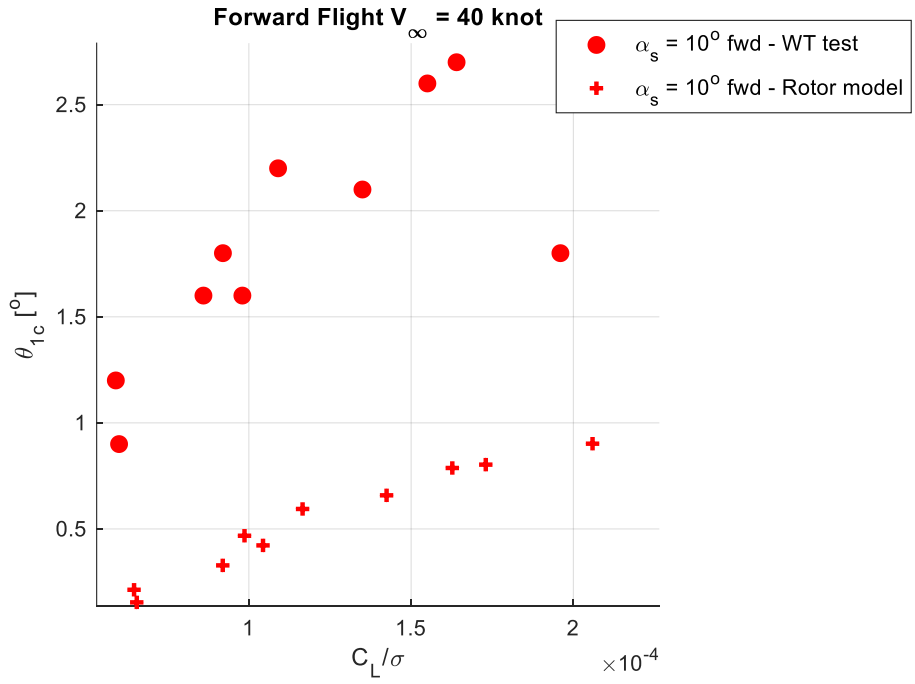

Figure 4.31. Roll control vs. Roll moment, 40 knots forward flight, 10° forward shaft angle

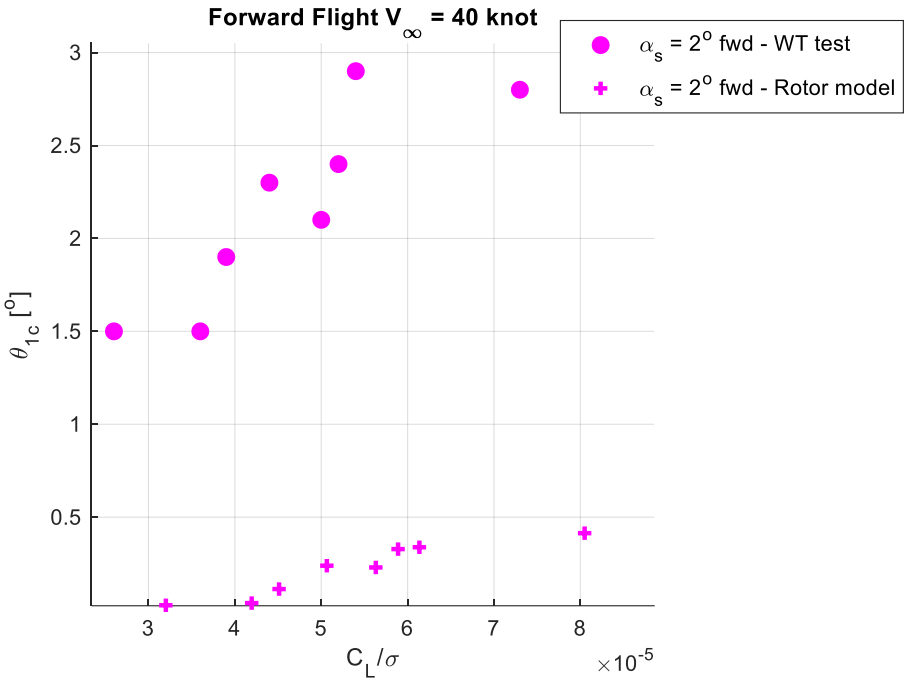

Figure 4.32. Roll control vs. Roll moment, 40 knots forward flight, 2° forward shaft angle

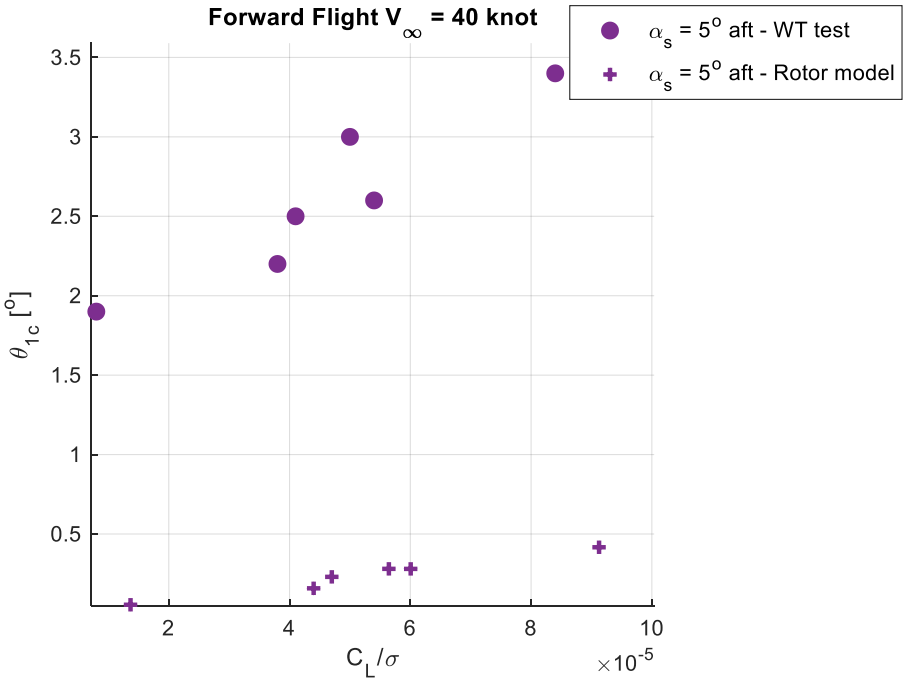

Figure 4.33. Roll control vs. Roll moment, 40 knots forward flight, 5° aft shaft angle

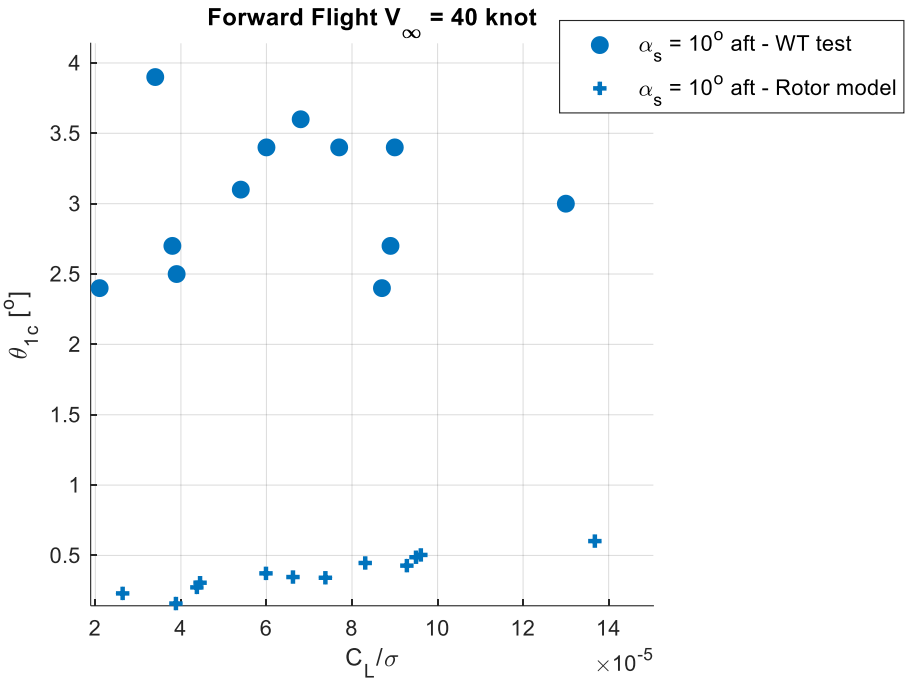

Figure 4.34. Roll control vs. Roll moment, 40 knots forward flight, 10° forward shaft angle

4.2.4 Forward Flight - 50 Knot

From Figure 4.35 to Figure 4.41, the model is compared with the wind tunnel test data at 50 knots forward flight conditions with 5° aft and 10° aft shaft angles. Figure 4.35 shows the rotor power coefficient as a function of the thrust coefficient. Figure 4.36 compares the model results with the wind tunnel test results for the relation between the collective angle and the normalized rotor thrust coefficient. In Figure 4.37, a comparison is made between the model results and the wind tunnel test data regarding the coning angle and the rotor thrust coefficient. In Figure 4.38 and Figure 4.39, the pitch axis response and in Figure 4.40 and Figure 4.41, the roll axis response are compared for different shaft angles.

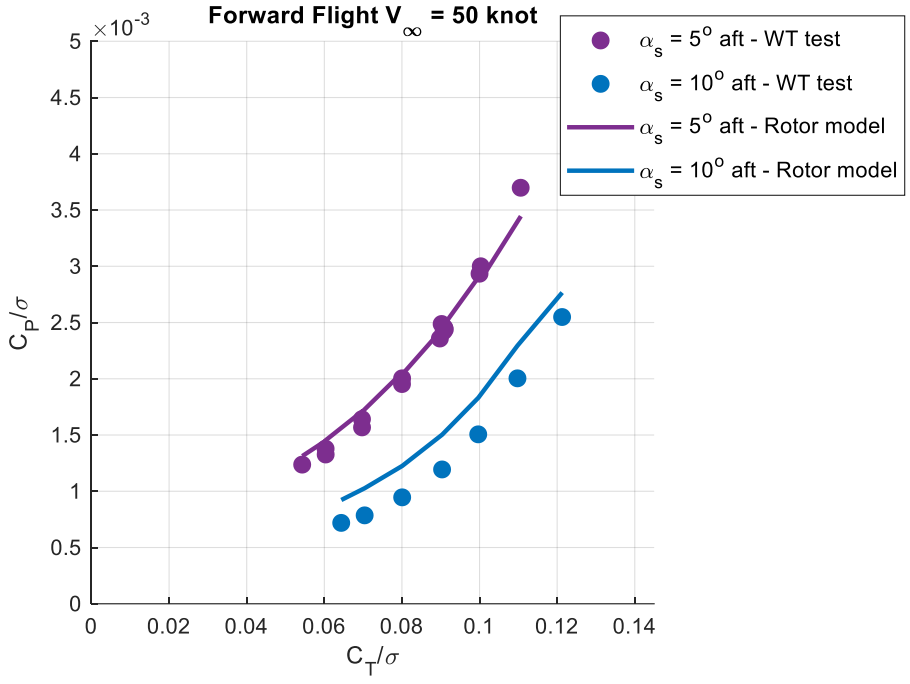

Figure 4.35. Rotor power coefficient as a function of rotor thrust coefficient, 50 knots forward flight

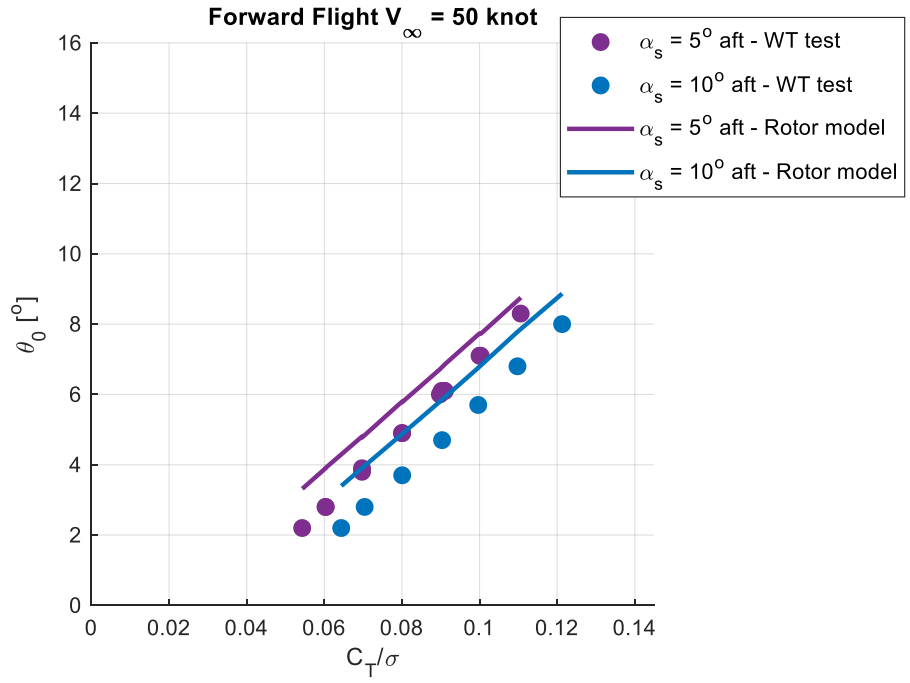

Figure 4.36. Relation between the collective angle and the rotor thrust coefficient, 50 knots forward flight

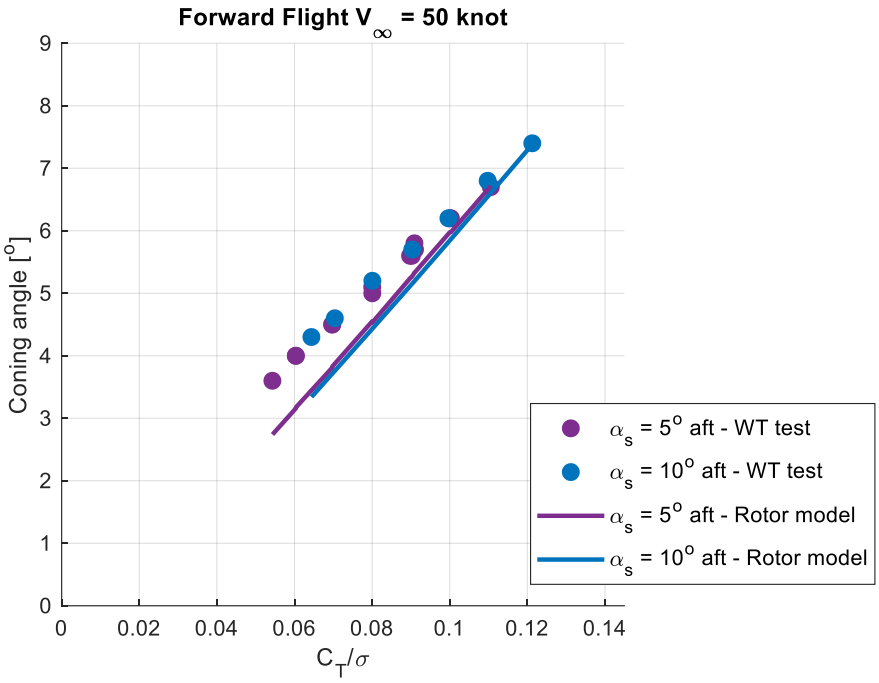

Figure 4.37. Relation between the coning angle and the rotor thrust coefficient, 50 knots forward flight

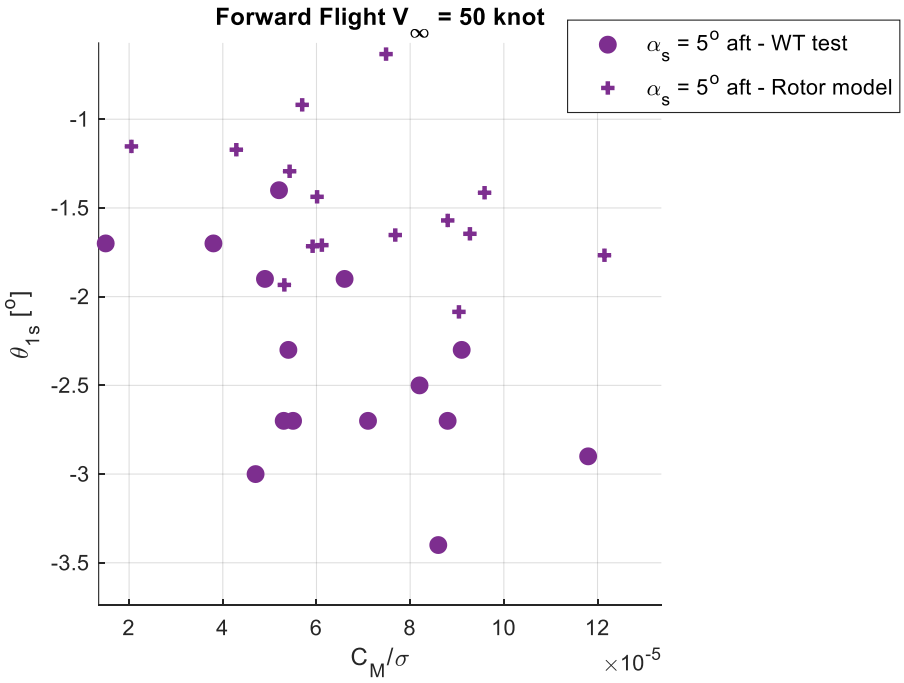

Figure 4.38. Pitch control vs. Pitch moment, 50 knots forward flight, 5° aft shaft angle

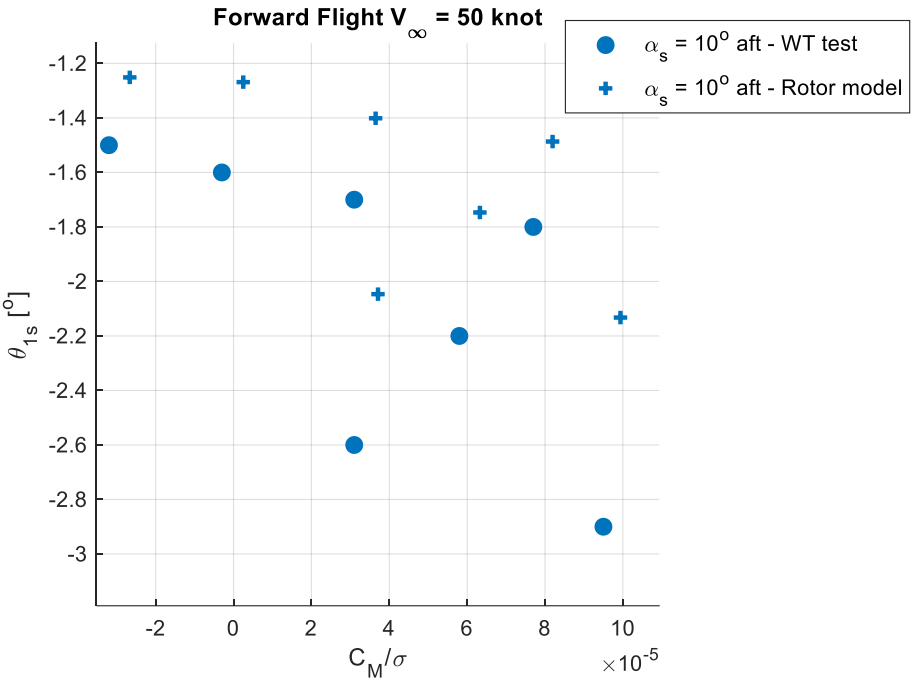

Figure 4.39. Pitch control vs. Pitch moment, 50 knots forward flight, 10° aft shaft angle

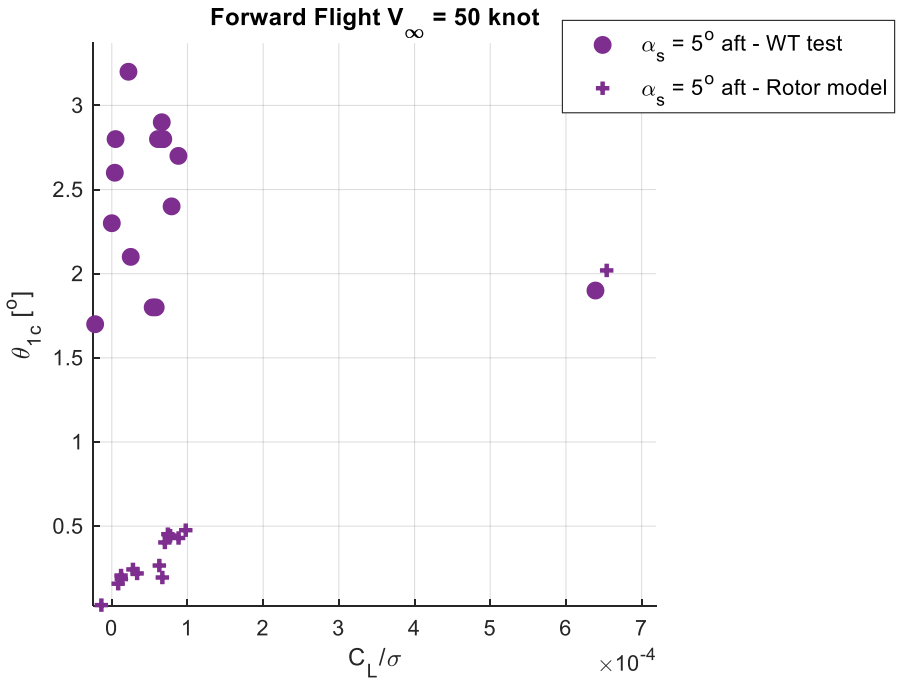

Figure 4.40. Roll control vs. Roll moment, 50 knots forward flight, 5° aft shaft angle

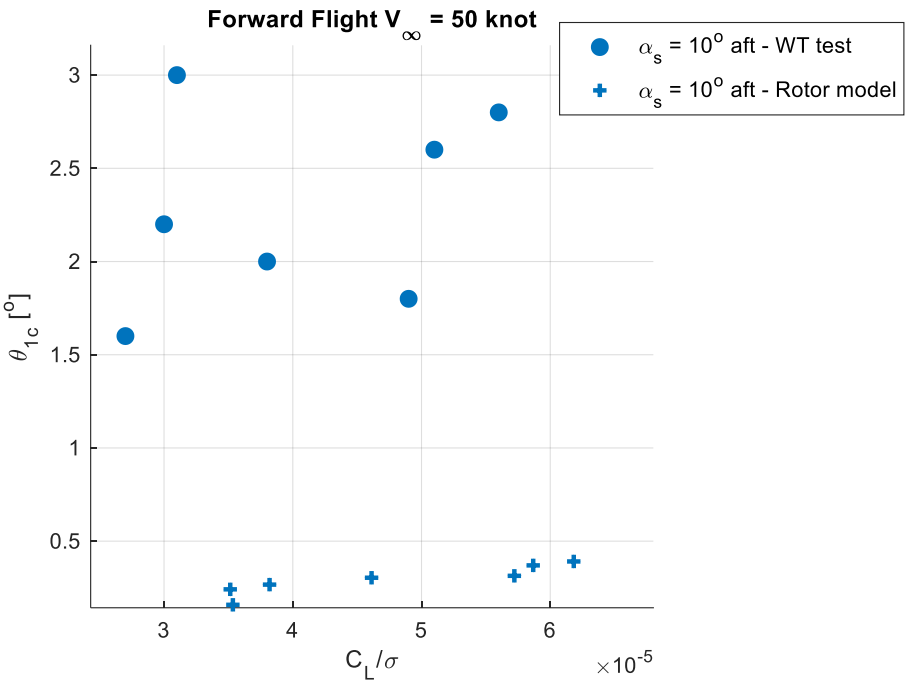

Figure 4.41. Roll control vs. Roll moment, 50 knots forward flight, 10° aft shaft angle

4.2.5 Forward Flight - 60 Knot

From Figure 4.42 to Figure 4.52, the model is compared with the wind tunnel test data at 60 knots forward flight conditions with 10° forward, 2° forward, 5° aft, and 10° aft shaft angles. Figure 4.42 shows the rotor power coefficient as a function of the thrust coefficient. Figure 4.43 compares the model results with the wind tunnel test results for the relation between the collective angle and the normalized rotor thrust coefficient. In Figure 4.44, a comparison is made between the model results and the wind tunnel test data regarding the coning angle and the rotor thrust coefficient. In Figure 4.45, Figure 4.46, Figure 4.47, and Figure 4.48, the pitch axis response and in Figure 4.49, Figure 4.50, Figure 4.51, and Figure 4.52, the roll axis response are compared for different shaft angles.

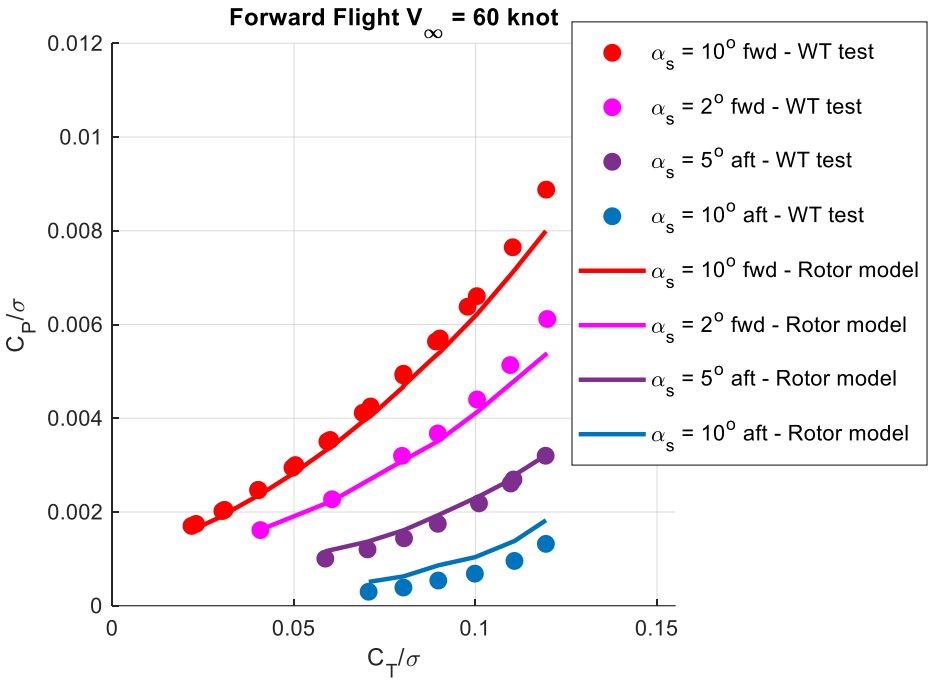

Figure 4.42. Rotor power coefficient as a function of rotor thrust coefficient, 60 knots forward flight

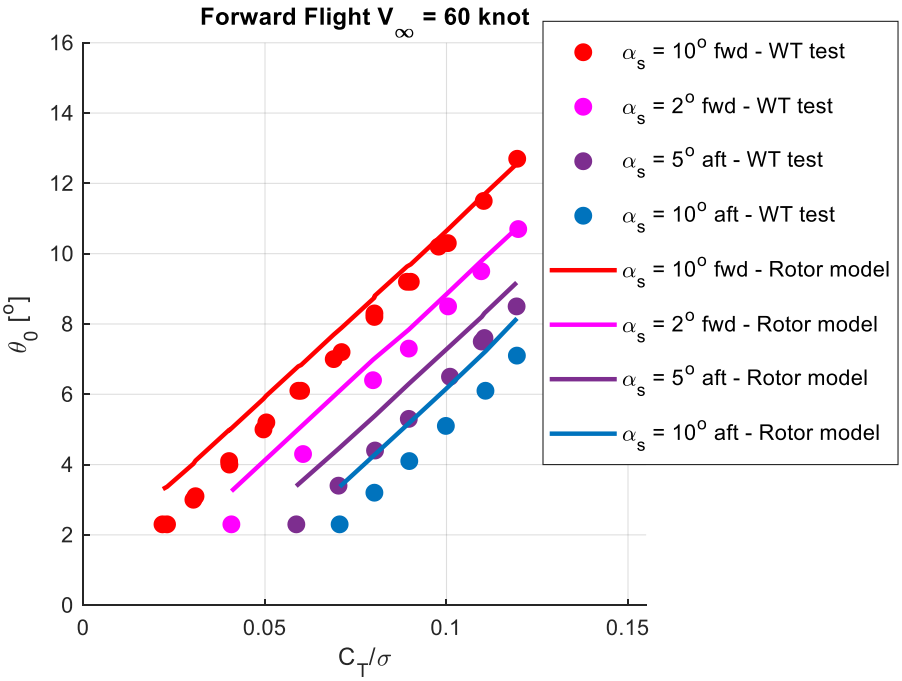

Figure 4.43. Relation between the collective angle and the rotor thrust coefficient, 60 knots forward flight

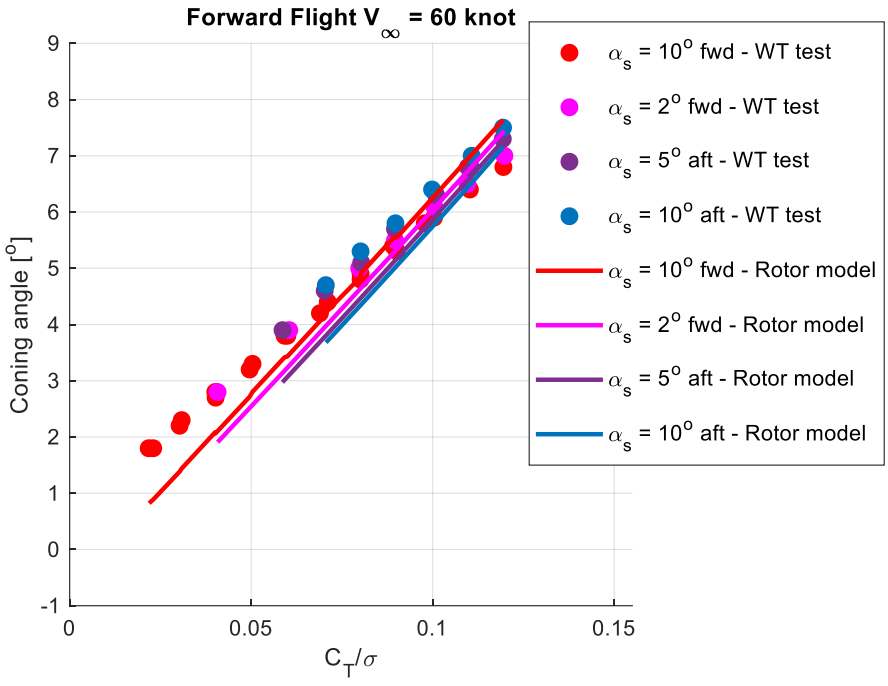

Figure 4.44. Relation between the coning angle and the rotor thrust coefficient, 60 knots forward flight

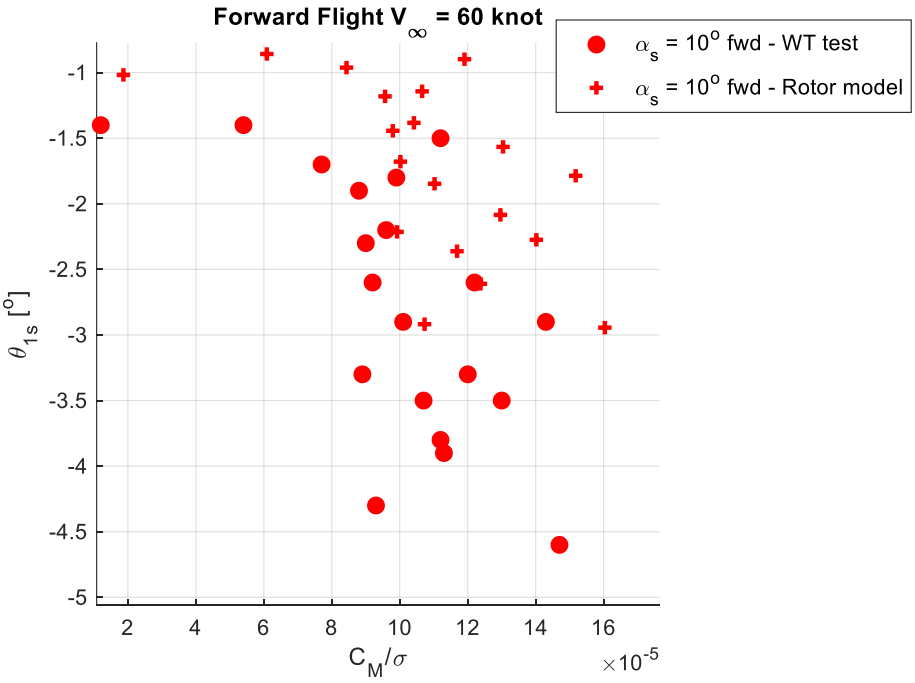

Figure 4.45. Pitch control vs. Pitch moment, 60 knots forward flight, 10° forward shaft angle

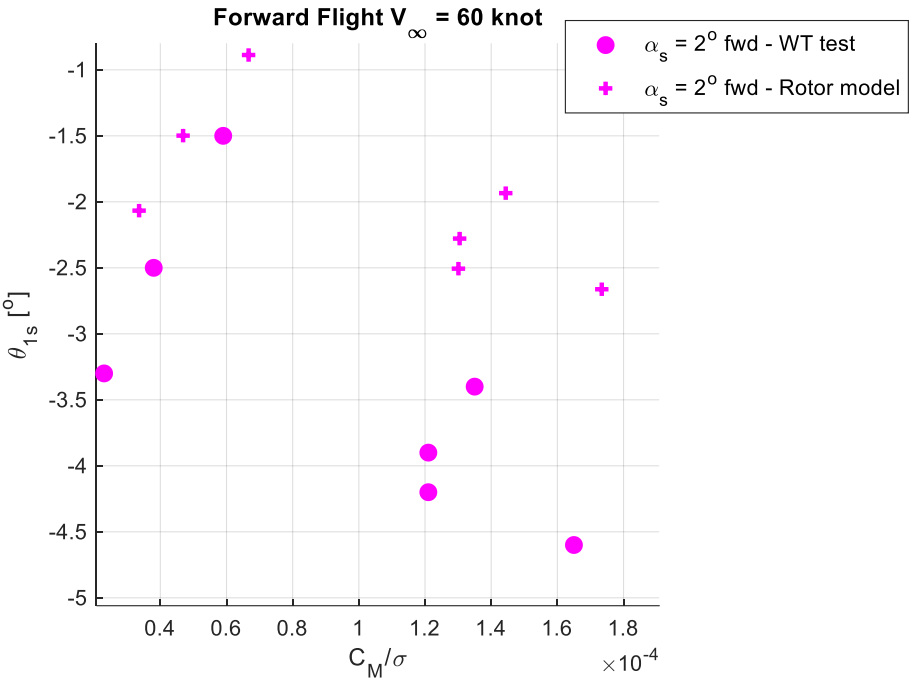

Figure 4.46. Pitch control vs. Pitch moment, 60 knots forward flight, 2° forward shaft angle

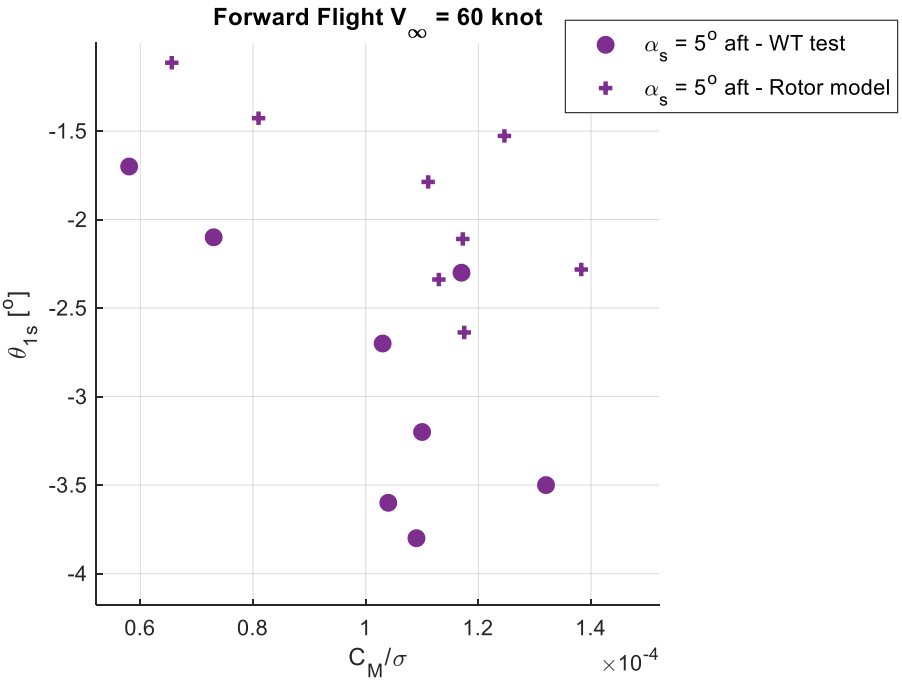

Figure 4.47. Pitch control vs. Pitch moment, 60 knots forward flight, 5° aft shaft angle

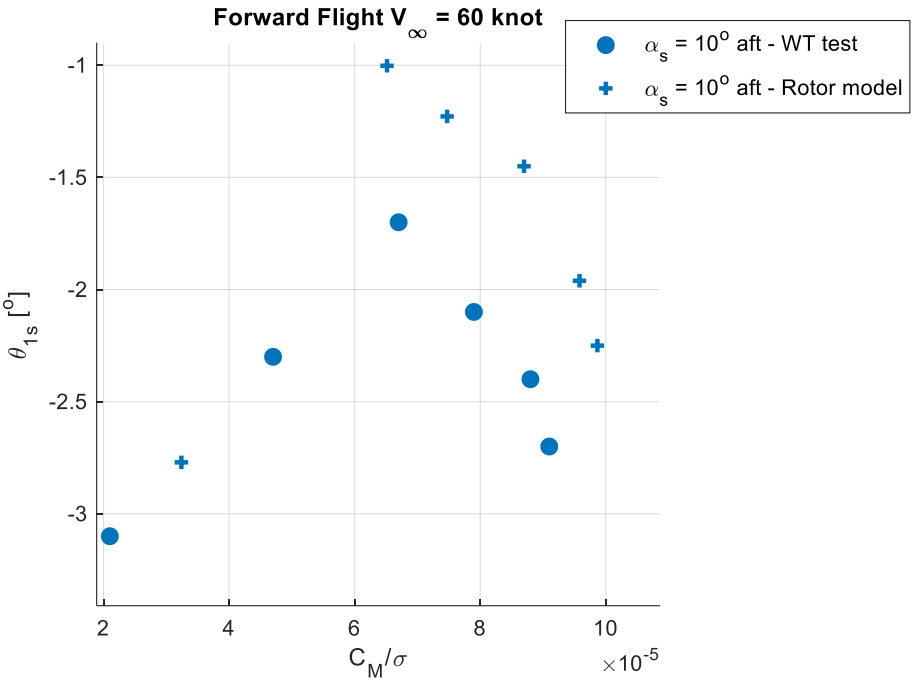

Figure 4.48. Pitch control vs. Pitch moment, 60 knots forward flight, 10° aft shaft angle

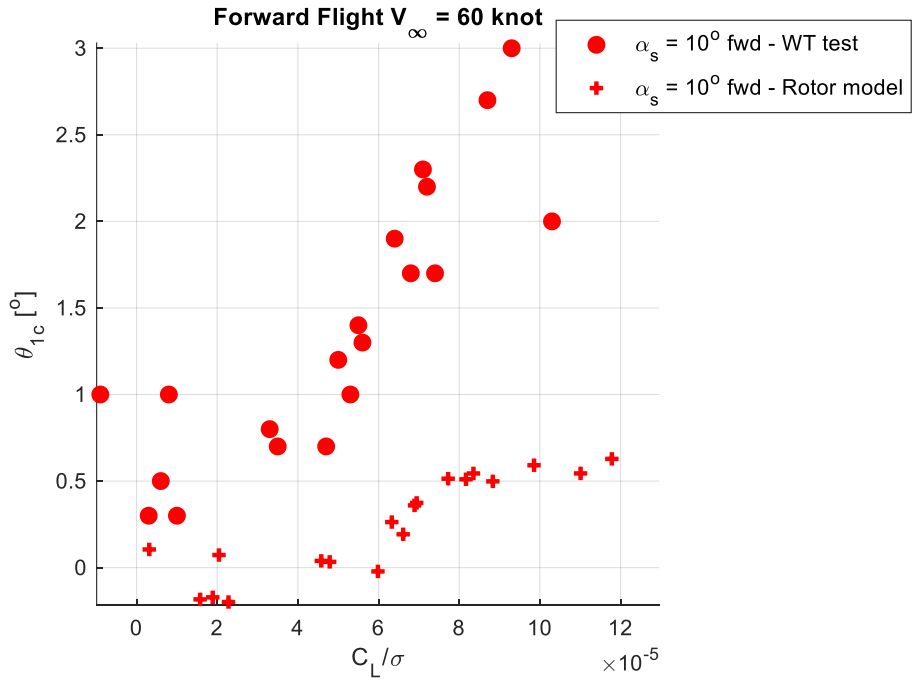

Figure 4.49. Roll control vs. Roll moment, 60 knots forward flight, 10° forward shaft angle

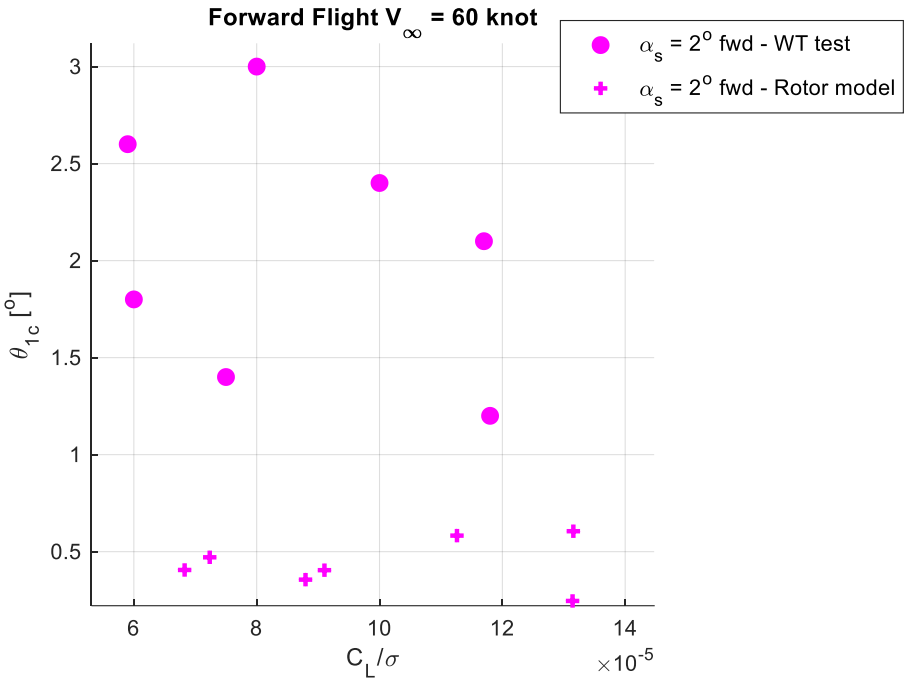

Figure 4.50. Roll control vs. Roll moment, 60 knots forward flight, 2° forward shaft angle

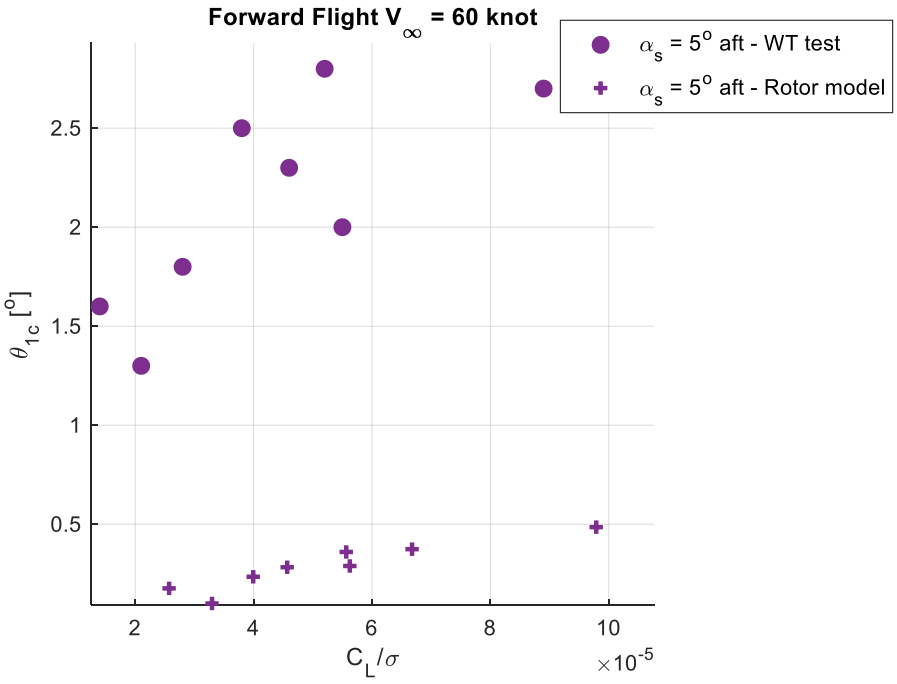

Figure 4.51. Roll control vs. Roll moment, 60 knots forward flight, 5° aft shaft angle

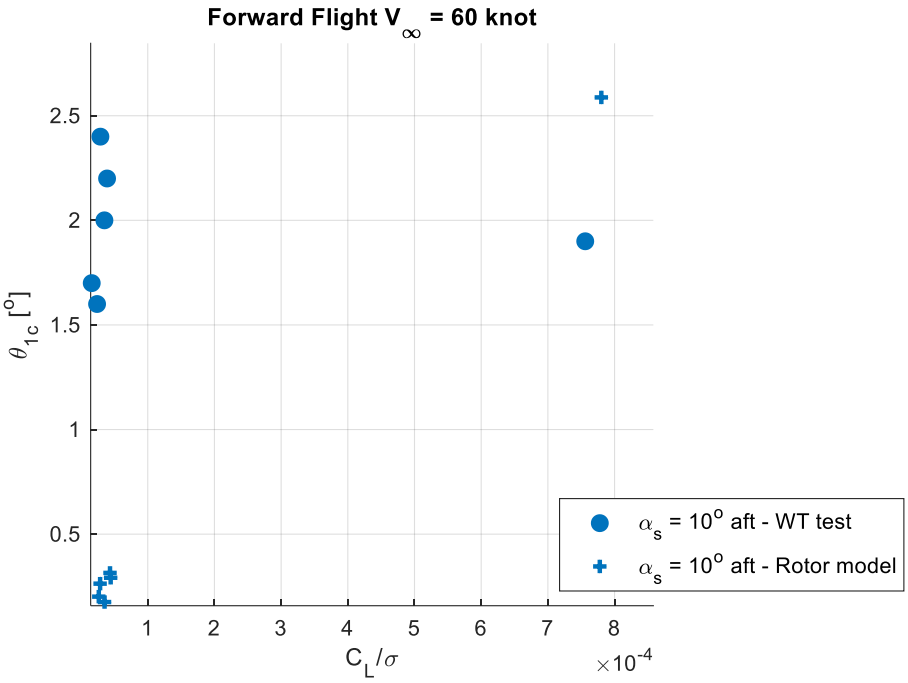

Figure 4.52. Roll control vs. Roll moment, 60 knots forward flight, 10° aft shaft angle

4.2.6 Forward Flight - 80 Knot

From Figure 4.53 to Figure 4.61, the model is compared with the wind tunnel test data at 80 knots forward flight conditions with 10° forward, 2° forward, and 5° aft shaft angles. Figure 4.53 shows the rotor power coefficient as a function of the thrust coefficient. Figure 4.54 compares the model results with the wind tunnel test results for the relation between the collective angle and the normalized rotor thrust coefficient. In Figure 4.55, a comparison is made between the model results and the wind tunnel test data regarding the coning angle and the rotor thrust coefficient. In Figure 4.56, Figure 4.57, and Figure 4.58, the pitch axis response and in Figure 4.59, Figure 4.60, and Figure 4.61, the roll axis response are compared for different shaft angles.

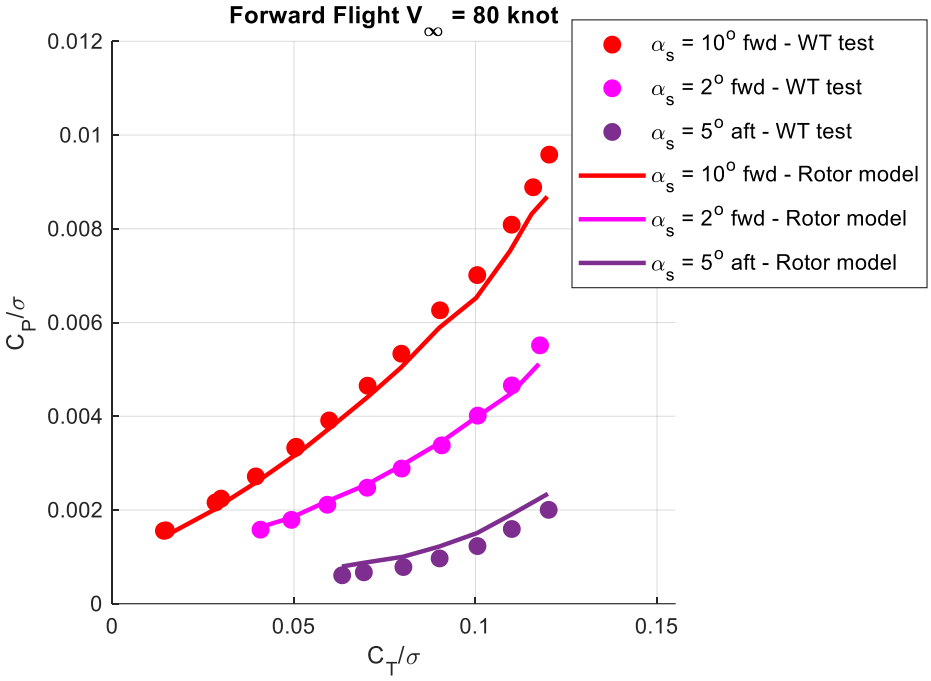

Figure 4.53. Rotor power coefficient as a function of rotor thrust coefficient, 80 knots forward flight

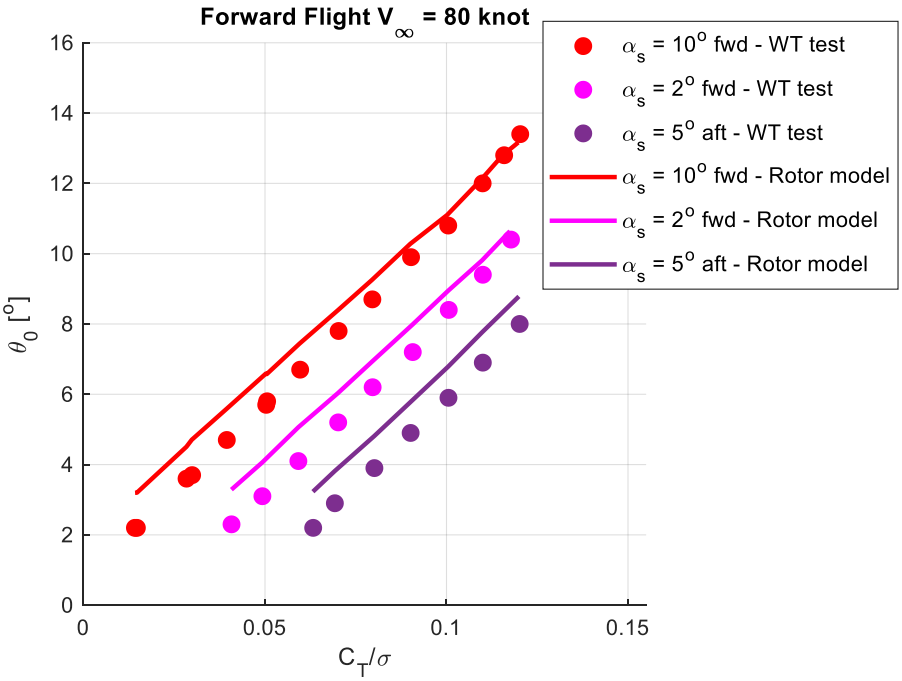

Figure 4.54. Relation between the collective angle and the rotor thrust coefficient, 80 knots forward flight

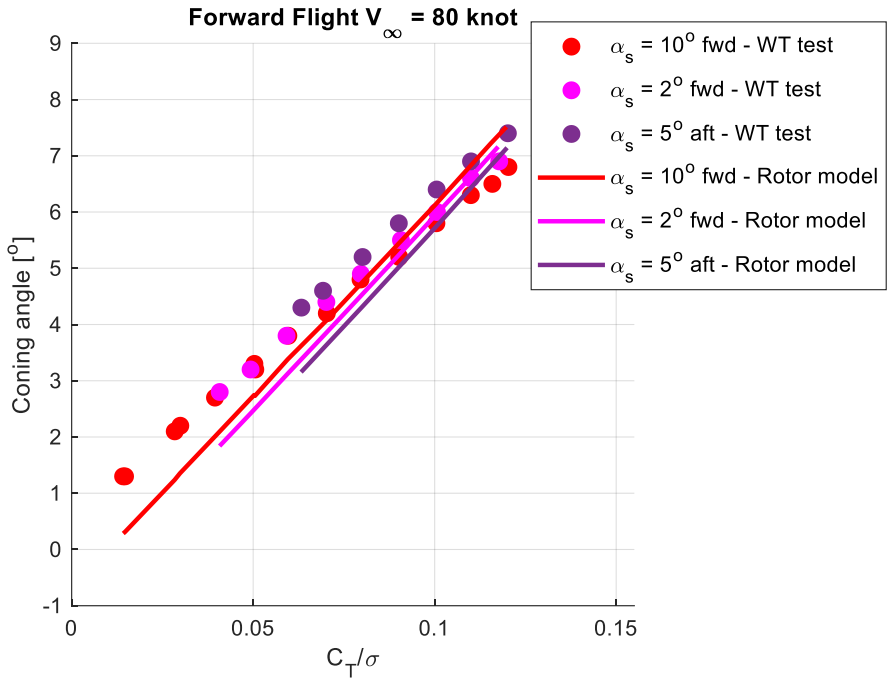

Figure 4.55. Relation between the coning angle and the rotor thrust coefficient, 80 knots forward flight

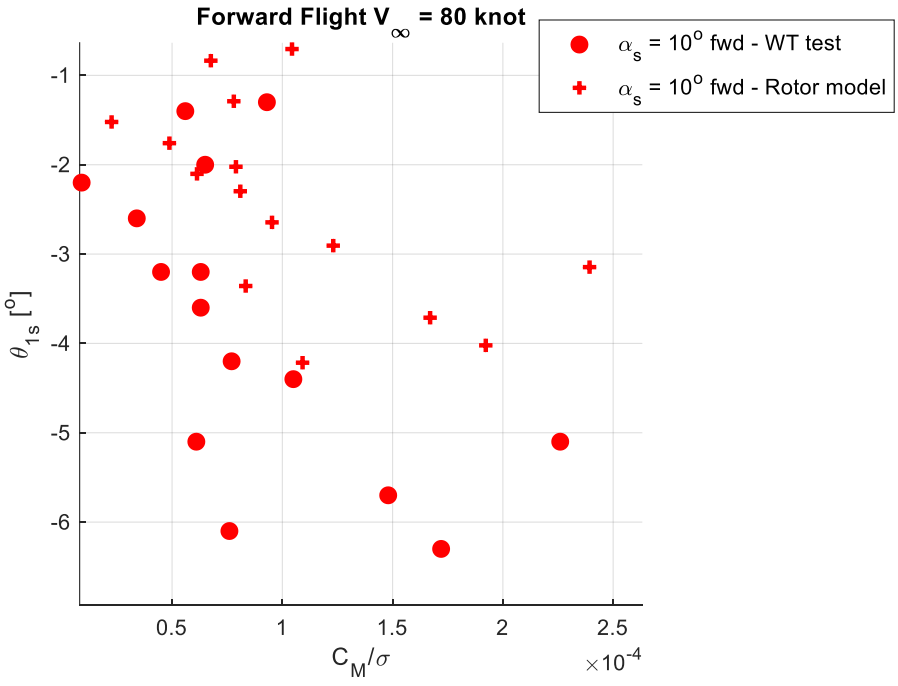

Figure 4.56. Pitch control vs. Pitch moment, 80 knots forward flight, 10° forward shaft angle

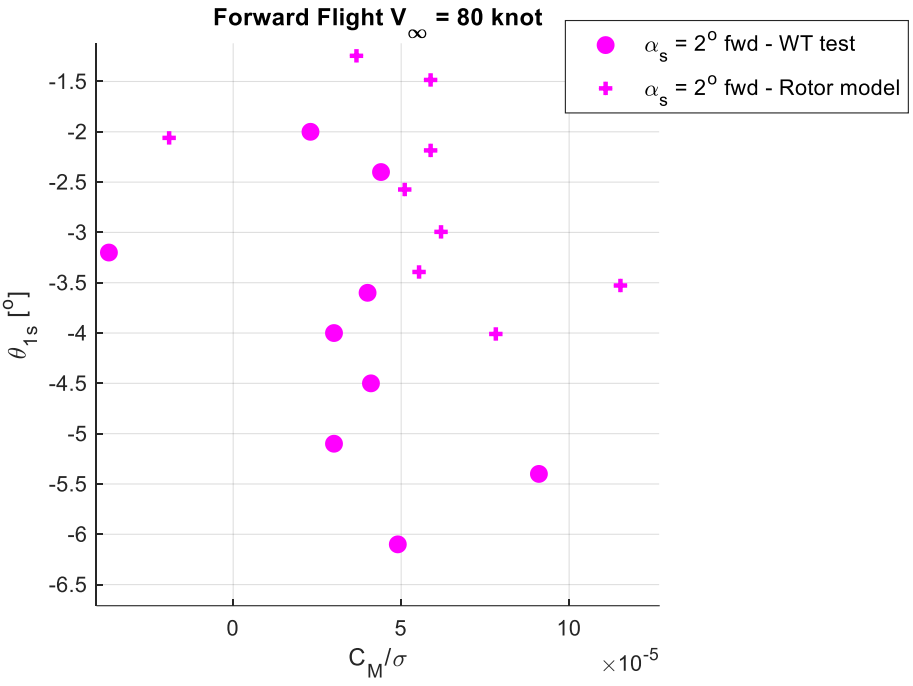

Figure 4.57. Pitch control vs. Pitch moment, 80 knots forward flight, 2° forward shaft angle

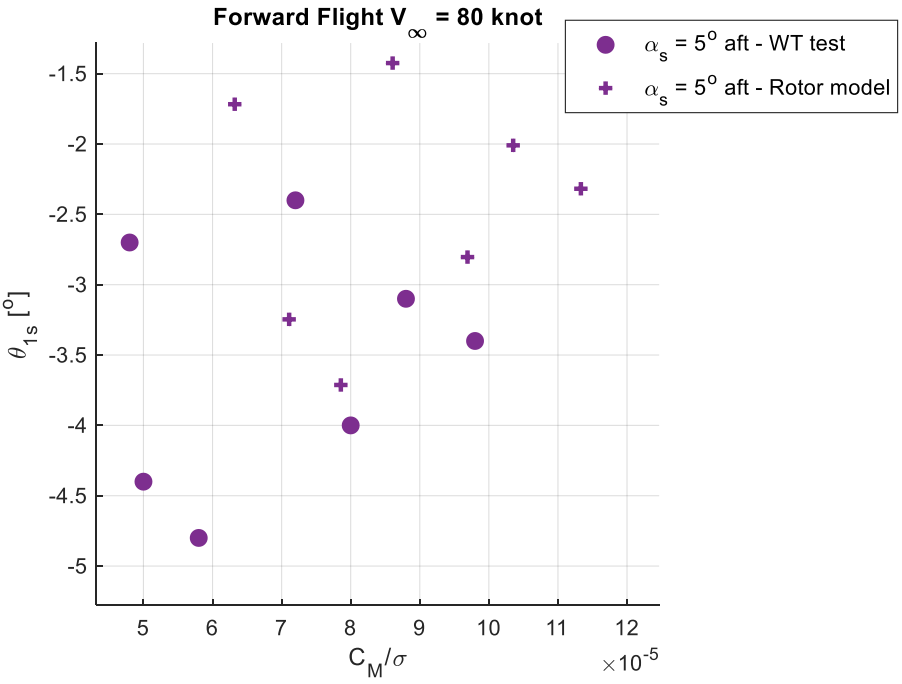

Figure 4.58. Pitch control vs. Pitch moment, 80 knots forward flight, 5° aft shaft angle

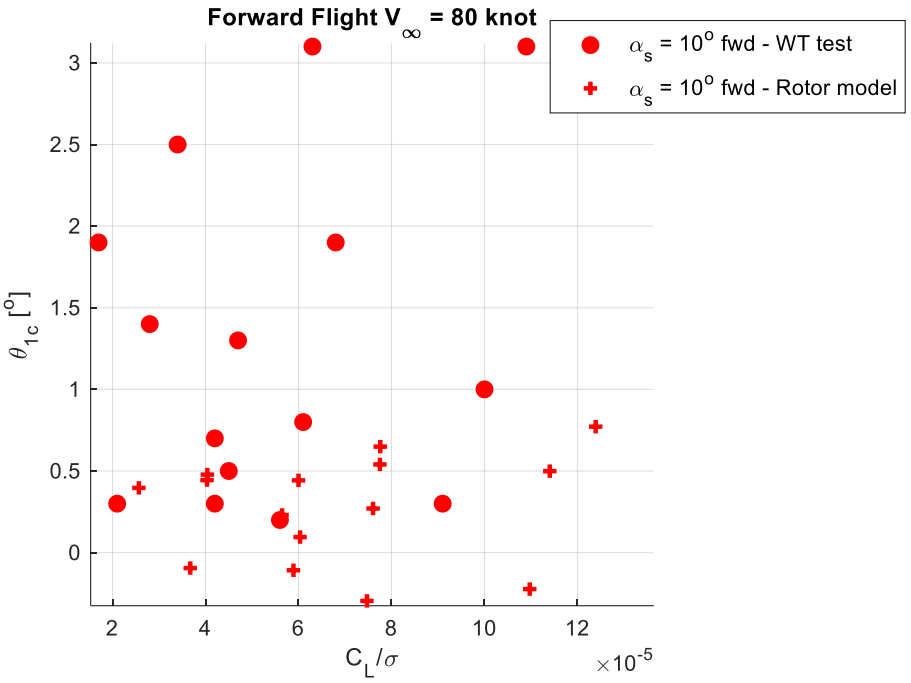

Figure 4.59. Roll control vs. Roll moment, 80 knots forward flight, 10° forward shaft angle

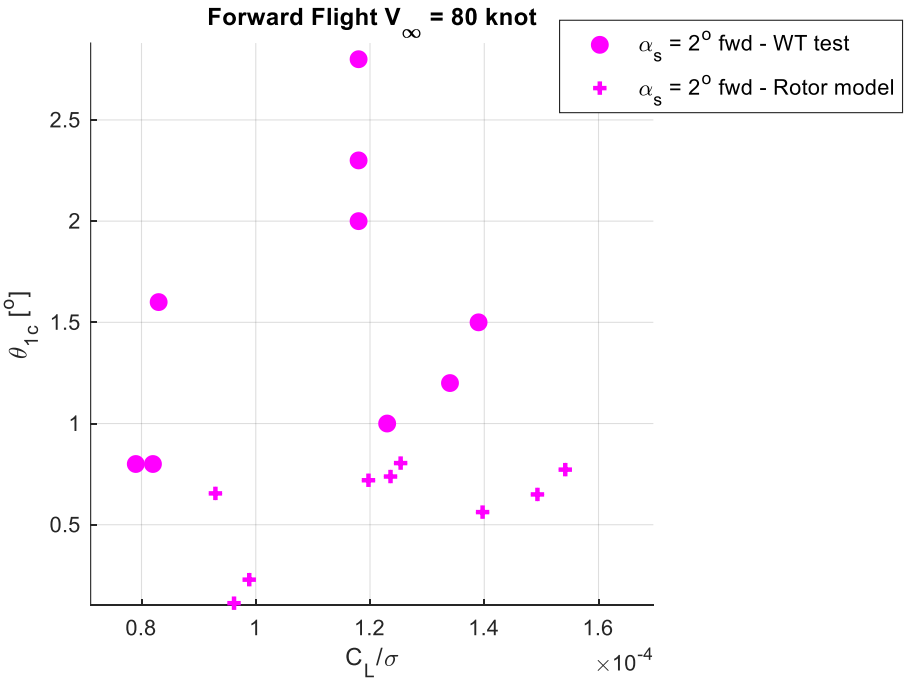

Figure 4.60. Roll control vs. Roll moment, 80 knots forward flight, 2° forward shaft angle

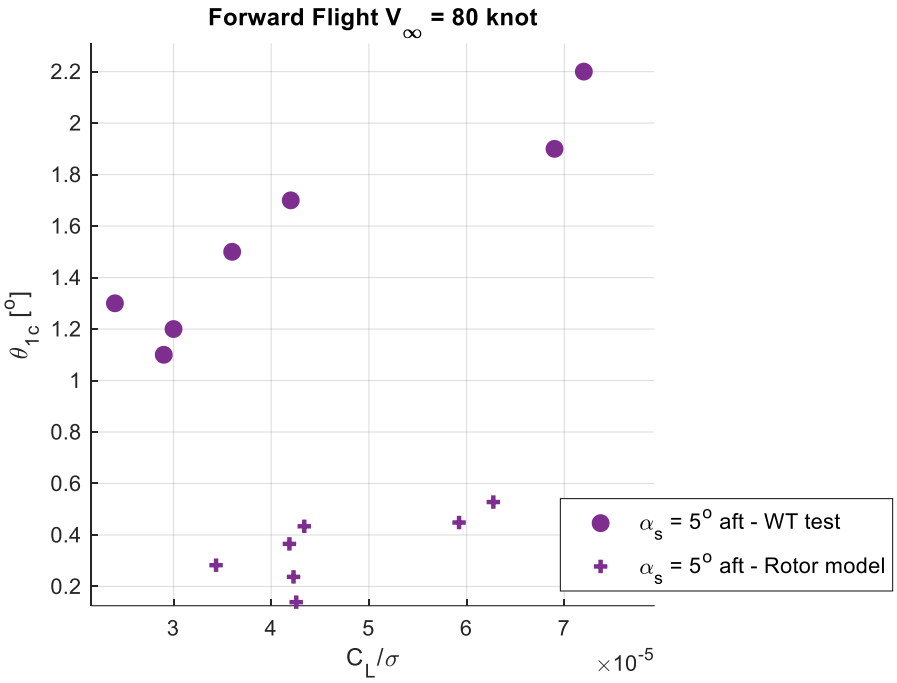

Figure 4.61. Roll control vs. Roll moment, 80 knots forward flight, 5° aft shaft angle

4.2.7 Forward Flight - 100 Knot

From Figure 4.62 to Figure 4.70, the model is compared with the wind tunnel test data at 100 knots forward flight conditions with 10° forward, 2° forward, and 5° aft shaft angles. Figure 4.62 shows the rotor power coefficient as a function of the thrust coefficient. Figure 4.63 compares the model results with the wind tunnel test results for the relation between the collective angle and the normalized rotor thrust coefficient. In Figure 4.64, a comparison is made between the model results and the wind tunnel test data regarding the coning angle and the rotor thrust coefficient. In Figure 4.65, Figure 4.66, and Figure 4.67, the pitch axis response and in Figure 4.68, Figure 4.69, and Figure 4.70, the roll axis response are compared for different shaft angles.

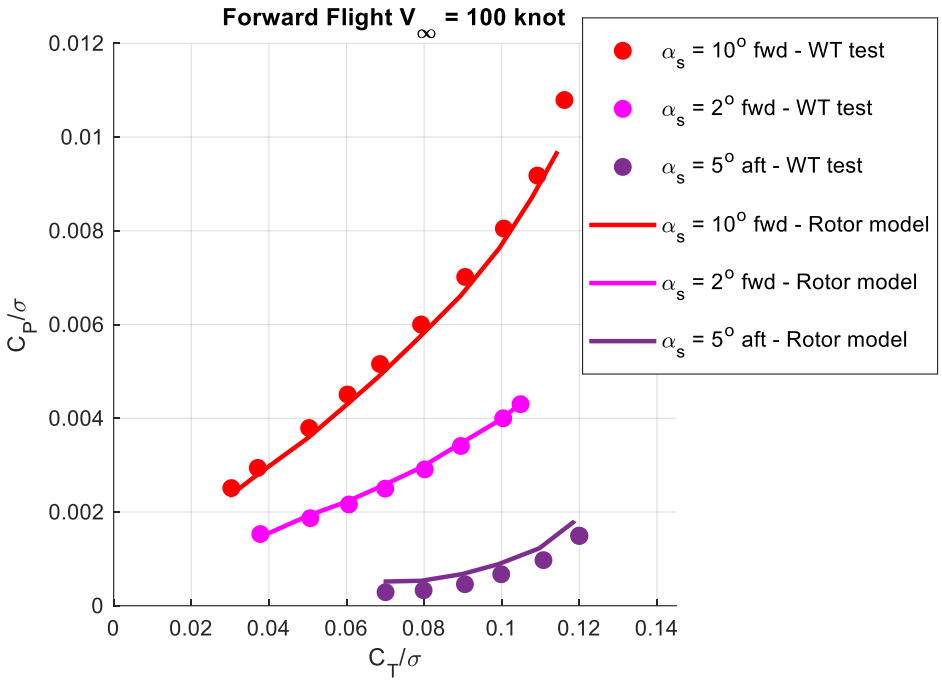

Figure 4.62. Rotor power coefficient as a function of rotor thrust coefficient, 100 knots forward flight

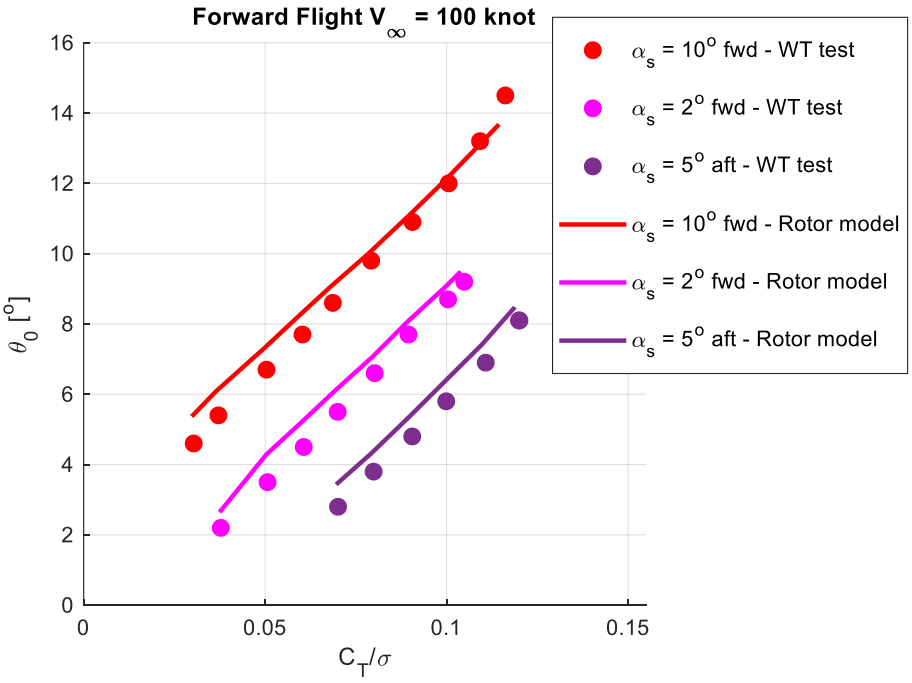

Figure 4.63. Relation between the collective angle and the rotor thrust coefficient, 100 knots forward flight

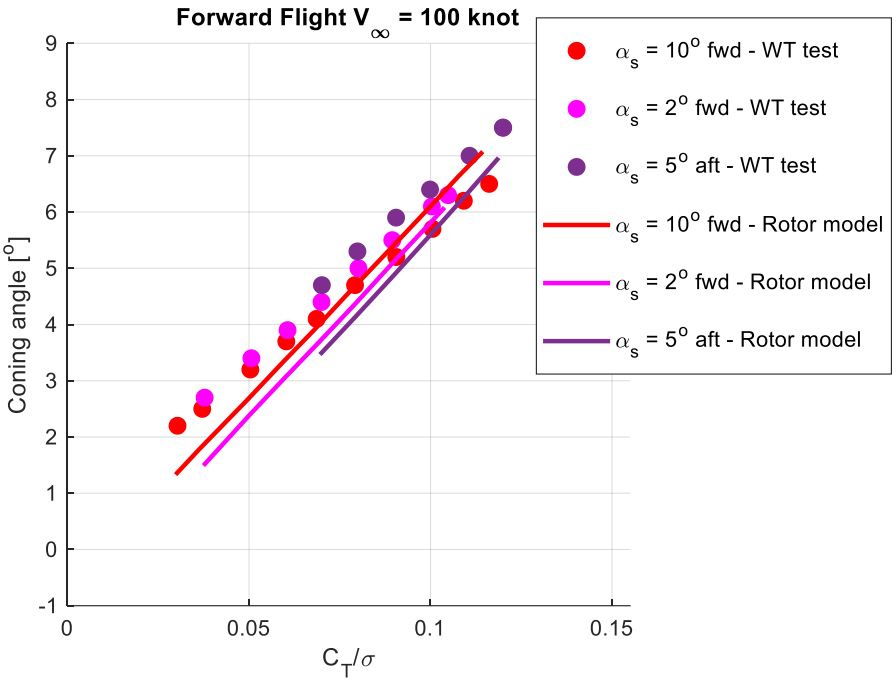

Figure 4.64. Relation between the coning angle and the rotor thrust coefficient, 100 knots forward flight

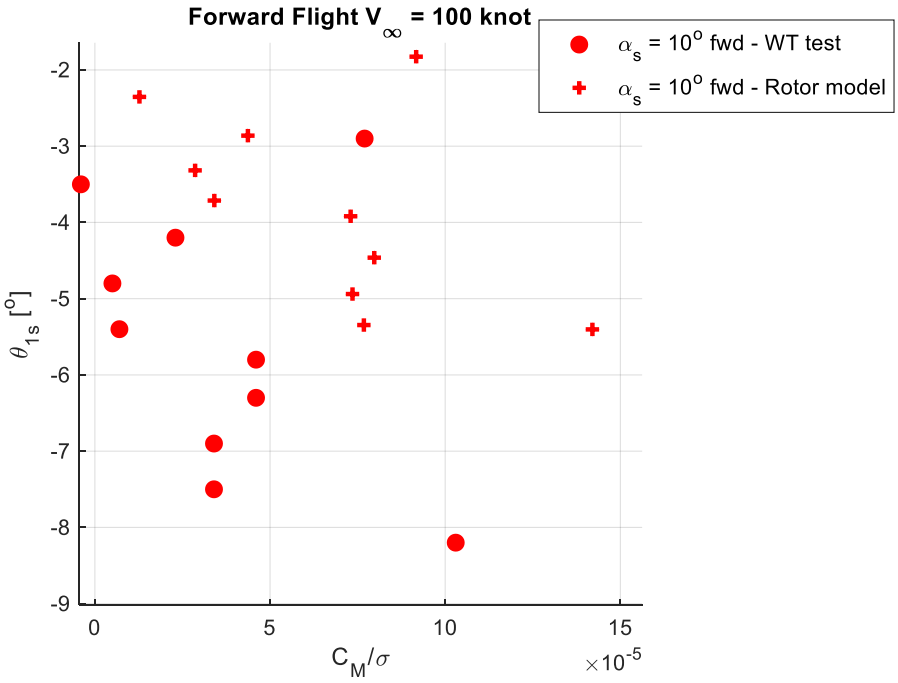

Figure 4.65. Pitch control vs. Pitch moment, 100 knots forward flight, 10° forward shaft angle

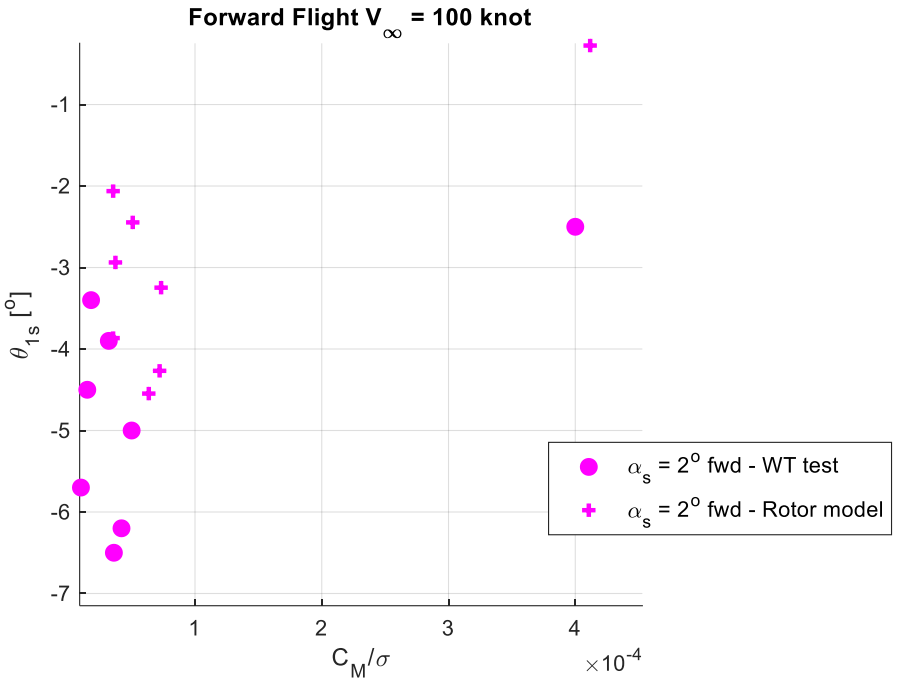

Figure 4.66. Pitch control vs. Pitch moment, 100 knots forward flight, 2° forward shaft angle

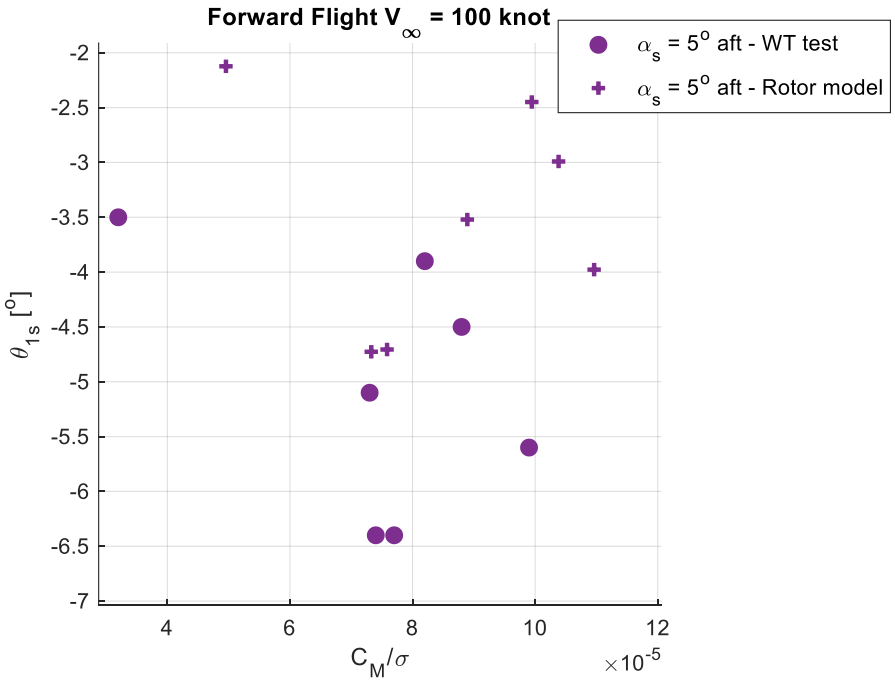

Figure 4.67. Pitch control vs. Pitch moment, 100 knots forward flight, 5° aft shaft angle

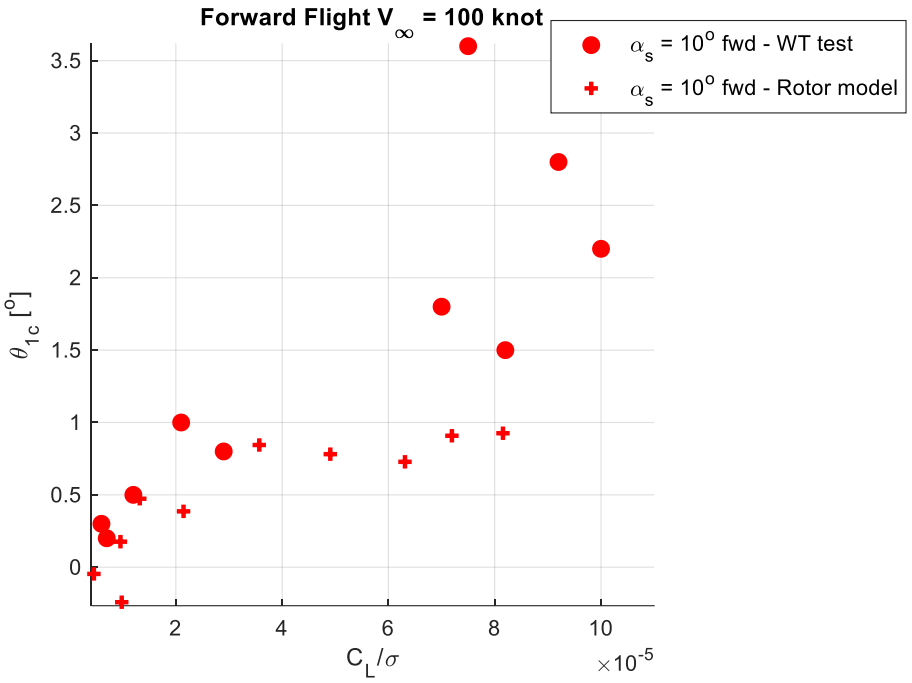

Figure 4.68. Roll control vs. Roll moment, 100 knots forward flight, 10° forward shaft angle

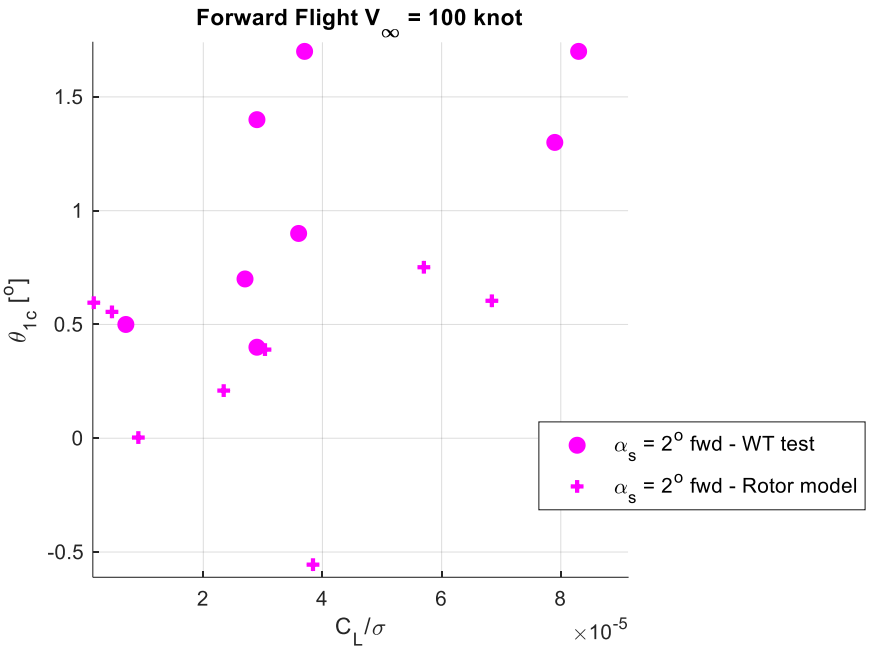

Figure 4.69. Roll control vs. Roll moment, 100 knots forward flight, 2° forward shaft angle

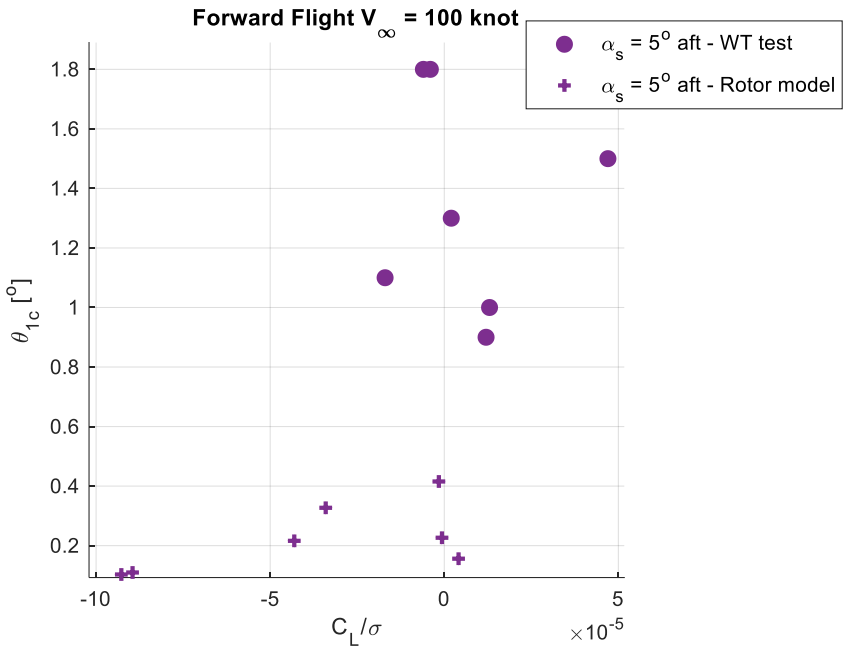

Figure 4.70. Roll control vs. Roll moment, 100 knots forward flight, 5° aft shaft angle

4.2.8 Observations

The power and collective angle figures are investigated for all forward speeds and shaft angles. Observations are listed below:

1. As the flow coming below the rotor increases through the increase in speed and the increase in aft shaft tilt, the model requires more power than the actual rotor.
2. As the flow coming above the rotor increases through the increase in speed and forward tilt, the model requires less power than the actual rotor and becomes more efficient.
3. As the thrust gets higher, the delta power requirement of the model is less than the actual rotor.
4. At low thrust values, the model's collective angle is higher than the actual rotor's. As the thrust increases, the collective angle of the model becomes less compared to the collective angle of the actual rotor.

These facts indicate five possible causes:

1. The aerodynamic data of the blade's profile is wrong.
2. Inflow estimation is more than the actual inflow generated by the rotor.
3. The 3D aerodynamic effects modeled (Tip Loss Effect) do not reflect the losses they caused in reality.
4. The collective need is not captured at higher loads without the torsional elasticity model.
5. Pitch-Flap coupling is wrong.

Model corrections can be done by either changing the aerodynamic data of the blade's airfoils at the corresponding angle of attack and Mach number, by making an inflow correction, modeling additional 3D aerodynamic effects like yawed flow, modeling the torsional elasticity, or correcting the mechanical parameters. Since the model shows a correct trend with the test data, the current model is sufficient for steady-state simulations at this level of fidelity.

When the coning angle figures are investigated, it is presumed that the model agrees with the rotor according to the test data, with approximately one degree of error at maximum. As in hover, the error might be caused by the error in the geometric parameters like spring constant, the blade's center of gravity, blade mass, or hinge offset, or by the slight difference in θ_0 at maximum and minimum thrust values.

Finally, the on-axis response figures show that the cyclic inputs show the same trend as the test data, and cyclic input directions are correct. For all the speed and shaft angle variations, it is seen that there are approximately constant cyclic angle differences for the given pitch and roll moments. As the pitch-up moment increases the θ_{1s} difference gets bigger, up to 3 degrees, and As the roll-left moment increases the θ_{1c} difference gets bigger, up to -3 degrees. Dynamic wake distortion modeling can solve this deficiency in the model. Also, it is seen in Figure 4.15 and Figure 4.16 that the inflow model variation between the uniform dynamic model and Pitt-Peters dynamic model is not effective at 20 knots airspeed.

4.2.8.1 Forward Flight – Power Performance

Figure 6.1 shows the power curve of the main rotor of the S-76 helicopter obtained by the rotor model with 2 degrees of shaft angle at $C_T/\sigma = 0.06$. Minimum power is required at 80 knots.

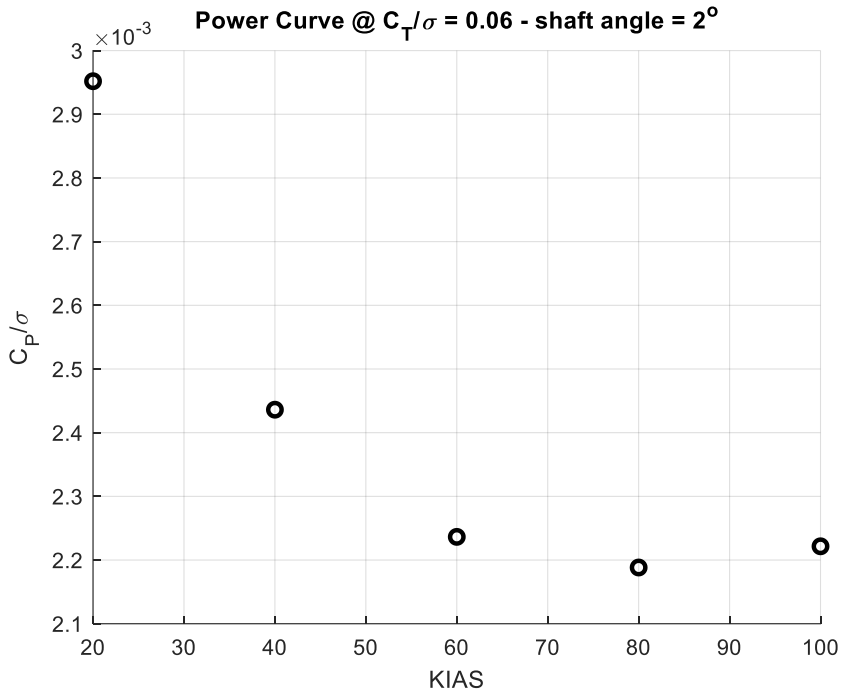

Figure 4.71. The power curve of the main rotor of S-76 obtained by the rotor model

CHAPTER 5

ELECTRIC VTOL SIMULATION APPLICATION

This chapter presents example applications of the rotor/propeller model described in this thesis for four different eVTOL configurations. Figure 5.1 shows a block diagram of a generic flight dynamics model of an example eVTOL concept with n number of rotors/propellers. In addition to the rotor/propeller model, several other components composing the air vehicle are modeled. Some utilities, like the wind/gust model, are brought into this flight dynamics model. The block diagram shows that the powerplant is powered by the battery, which rotates the rotors/propellers. The torque output of the rotors/propellers is fed back to the powerplant. Rotors/propellers can be controlled by either variable rpm, the powerplant's output, or the variable blade pitch, which is the output of the flight controls model. There might be additional airframe components like a wing and a body on the eVTOL. The control of eVTOL can also be provided by the aerodynamic surfaces on them. The deflections of those are the output of the flight controls model. The motor power can be controlled by generating the pulse-width modulation (PWM) signal input to the motor's electronic speed controller (ESC), which manipulates the battery's voltage output. The PWM signal is also an output of the flight controls model. With many possible control channels, the flight controls are a control allocation problem for an eVTOL. If all the controls mentioned are used, the system becomes over-actuated. There might also be a ground reactions model if take-off and landing are to be simulated. Mass, CG, and inertia information of the eVTOL is obtained from the weight and balance model. Air density, pressure altitude, air temperature, etc., and wind information comes from the atmosphere and wind model. Total forces and moments generated by the rotor/propellers and the airframe and weight are used in the 6-DOF rigid body motion model—components of eVTOL use the resultant rigid body states.

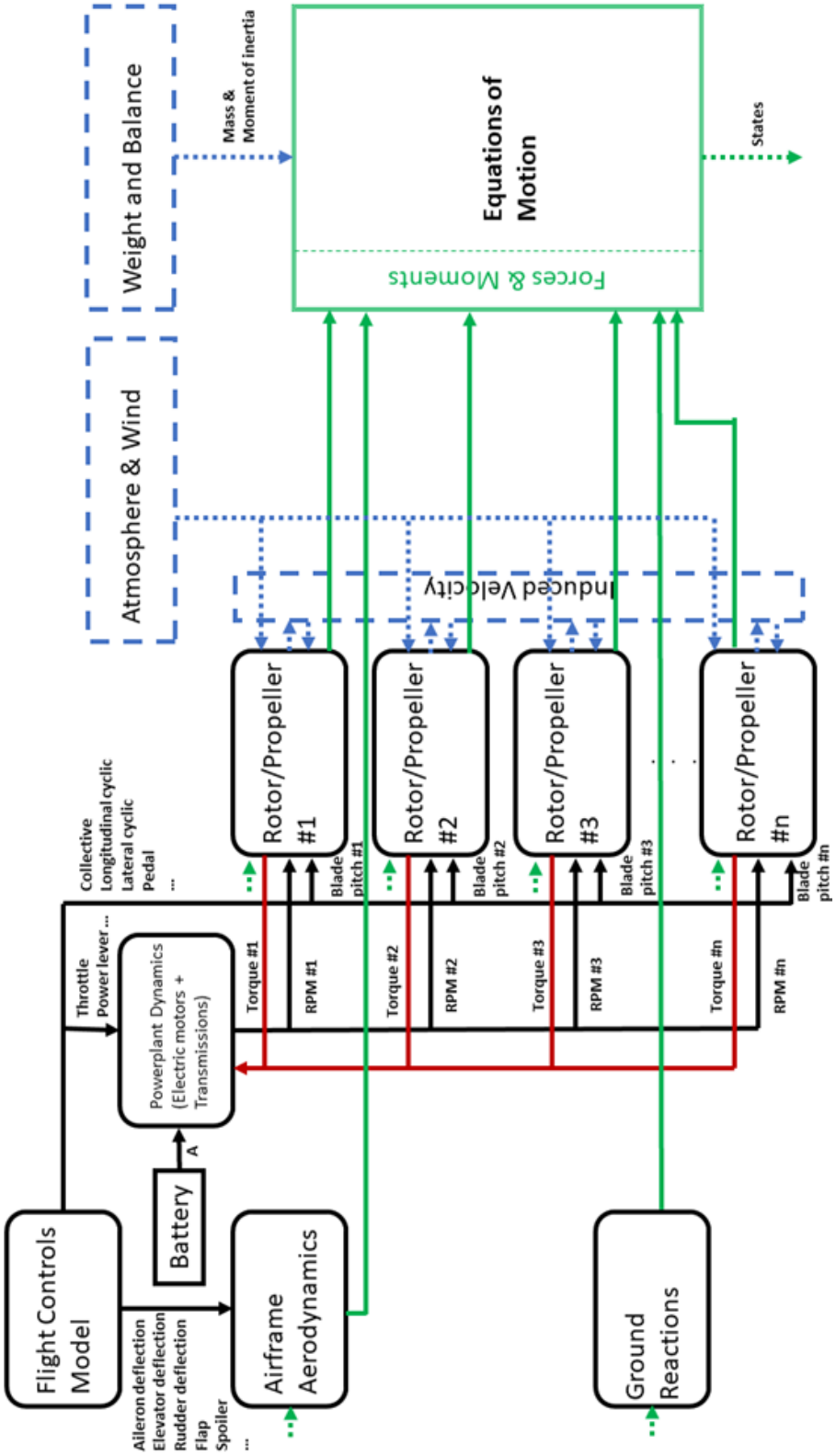

Figure 5.1. Flight dynamics model flow chart of a generic eVTOL concept

Different concepts can be tried and compared easily by making quick changes in rotor/propeller size, location, etc., in this simple eVTOL flight dynamics representation.

5.1 Model Definitions

Four different eVTOL concepts are investigated using this flight dynamics model. The models used are described in this section.

5.1.1 Battery

In these applications, the battery is used as an infinite energy source. It provides the required voltage to the system.

5.1.2 Electric Motor

A brushless direct current electric motor (BLDC) model is implemented [30, 66, 67]. They are preferred in eVTOL concepts because of their rapid speed response and disturbance rejection abilities. Figure 5.2 presents a schematic of the BLDC motor model with BLDC dynamics and an ESC.

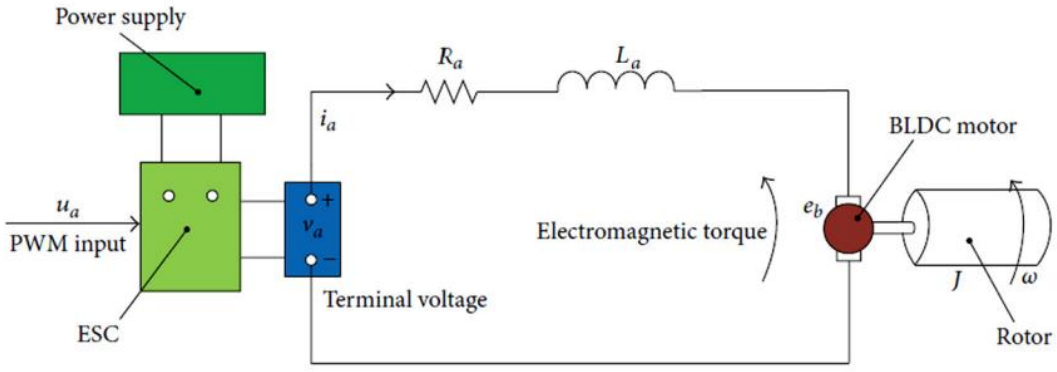

Figure 5.2. BLDC motor system [68]

The electrical dynamics of a BLDC motor are given in Equation 5.1. The current of the BLDC motor system and electromagnetic torque are found using the electrical dynamics.

$$L_a \dot{i_a} = -R_a i_a - e_b + V_a \quad 5.1$$

where i_a is the armature current, L_a is the equivalent circuit armature inductance, R_a is the equivalent resistance, and V_a is the voltage applied at the armature.

e_b is the motor-back electromotive force (back-EMF), and it is calculated as Equation 5.2.

$$e_b = K_e \Omega_m \quad 5.2$$

where K_e is the back-EMF constant and Ω_m is the rotational speed of the motor.

Since the inductance on the current BLDC motors has extremely low values, on the order of a few micro Henry, for the direct drive response, the inductance contribution to the tension of the circuit is neglected. Therefore, the electrical dynamics can be assumed instantaneous.

The armature current is calculated as Equation 5.3.

$$L_a \approx 0\ [mH] \rightarrow R_a i_a = -K_e \Omega_m + V_a \quad 5.3$$

The coupled motor-rotor/propeller mechanical equation of motion is given in Equation 5.4.

$$\left(I_r + J_m \left(\frac{\Omega_m}{\Omega} \right)^2 \right) \dot{\Omega} = K_m \frac{\Omega_m}{\Omega} i_a + Q - B_{loss} \left(\frac{\Omega_m}{\Omega} \right)^2 \Omega \quad 5.4$$

where Ω is the rotor/propeller rpm, I_r is the rotor/propeller rotational moment of inertia, J_m is the inertia of the high-speed drive components (motor and coupled transmission components), $\frac{\Omega_\mathrm{m}}{\Omega}$ drive system gear ratio, K_m is the motor torque constant, Q is the rotor/propeller torque with the drive system, and B_{loss} is the linear representation of mechanical friction or viscous loss in the drive system.

Since it is assumed that no electromagnetic loss occurs, mechanical power generated and dissipated electrical power are equal. Therefore, $K_m = K_e$.

Table 5.1 shows BLDC electric motor parameters used in the simulation application.

Table 5.1. BLDC electric motor parameters

Parameters	*Values*
Gear ratio, $\frac{\Omega_m}{\Omega}$	16
Armature resistance [Ohms]	0.5
Back-EMF constant [V/(rad/s)]/ Torque constant [N/A]	1.2
Linear friction and viscous loss constant	0.15
Rotor/propeller rotational inertia [kg-m^2]	70
Motor and transmission inertia [kg-m^2]	20

5.1.3 Wing

In the application, lift and cruise type eVTOLs are simulated. Therefore, two horizontal Wings and one vertical wing are attached to the body to be used in the cruise. One horizontal wing is positioned to align the aerodynamic center with the center of gravity. The other horizontal wing is at the back, top of the rotors and propellers. The vertical wing is positioned at the back of eVTOL. The wing configuration is the same for all the eVTOLs.

The forces and moments over a finite wing are only calculated in the linear region before the stall. Therefore, it should be noted that in real-time simulation, this discontinuity would result in jumps. Since this is just an analysis simulation, a continuous model is not needed to make the model simplified. All aerodynamic forces are calculated in the wind frame.

5.1.3.1 Horizontal Wing

Forces and moments of the wing are generated on the aerodynamic center. The position of the wing aerodynamic center with respect to the center of gravity of the body is calculated to carry the forces and moments to the center of gravity of the eVTOL.

$$\bar{r}^{Body}_{WingAC2CG} = \begin{bmatrix} FS_{WingAC} \\ BL_{WingAC} \\ WL_{WingAC} \end{bmatrix}^{Body} - \begin{bmatrix} FS_{CG} \\ BL_{CG} \\ WL_{CG} \end{bmatrix}^{Body} \quad 5.5$$

The airspeed that the wing encounters:

$$\bar{V}^{Body}_{Wing} = \begin{bmatrix} u \\ v \\ w \end{bmatrix} + \begin{bmatrix} p \\ q \\ r \end{bmatrix} \times \bar{r}^{Body}_{WingAC2CG} \quad 5.6$$

The angle of attack of the wing:

$$\alpha_{Wing} = i_{Wing} + \tan^{-1} \frac{\bar{V}^{Body}_{Wing}(3)}{\bar{V}^{Body}_{Wing}(1)} \quad 5.7$$

Aerodynamic forces are calculated as below.

Lift:

$$C_L = C_{L_\alpha} \alpha_{Wing} + C_{L_0} \quad 5.8$$

$$C_L \leq C_{L_{MAX}} \,\&\, C_L \geq C_{L_{MIN}} \rightarrow$$
$$L_{Wing} = \frac{1}{2} \rho \left(\bar{V}^{Body}_{Wing}(1)^2 + \bar{V}^{Body}_{Wing}(3)^2 \right) A_{ref} C_L \quad 5.9$$

$$C_L > C_{L_{MAX}} \,\&\, C_L < C_{L_{MIN}} \rightarrow$$
$$L_{Wing} = 0 \quad 5.10$$

Drag:

$$C_L \leq C_{L_{MAX}} \,\&\, C_L \geq C_{L_{MIN}} \rightarrow$$
$$C_D = C_{D_0} + \frac{C_L^2}{\pi e AR} \tag{5.11}$$

where e is Oswald efficiency factor.

$$C_L > C_{L_{MAX}} \,\&\, C_L < C_{L_{MIN}} \rightarrow$$
$$C_D = 1 \tag{5.12}$$

$$D_{Wing} = \frac{1}{2}\rho\left(\bar{V}_{Wing}^{Body}(1)^2 + \bar{V}_{Wing}^{Body}(3)^2\right)A_{ref}C_D \tag{5.13}$$

The pitch moment is neglected, $C_M = 0$.

$$\overline{F_{Aero}}_{Wing}^{Wind} = \begin{bmatrix} -D \\ 0 \\ -L \end{bmatrix} \tag{5.14}$$

$$\overline{F_{Aero}}_{Wing}^{Body} = T\left(0, i_{Wing} - \alpha_{Wing}, 0\right)\overline{F_{Aero}}_{Wing}^{Wind} \tag{5.15}$$

$$\overline{M_{Aero}}_{Wing}^{Body} = \bar{r}_{WingAC2CG}^{Body} \times \overline{F_{Aero}}_{Wing}^{Body} \tag{5.16}$$

Table 5.2 shows horizontal wing parameters used in the simulation application.

Table 5.2. Horizontal wing parameters

	Horizontal Wing 1	*Horizontal Wing 2*
AC position [m], Body-fixed frame	$\begin{bmatrix} 0 \\ 0 \\ -1 \end{bmatrix}$	$\begin{bmatrix} -3 \\ 0 \\ -1.5 \end{bmatrix}$
Reference Area [m^2]	10	5
Slope of C_L vs. α curve	5.73	-5.73
Maximum C_L	2	2
Minimum C_L	-2	-2
C_L at $\alpha = 0$	0.5	0
C_{D_0}	0.01	0.01
Oswald efficiency factor	0.9	0.9
Aspect ratio	10	5
Incidence angle [^{o}]	2	0

5.1.3.2 Vertical Wing

The vertical wing is the same as 90 degrees rotated horizontal wing.

The sideslip of the wing:

$$\alpha_{Wing} = i_{Wing} + \tan^{-1} \frac{\bar{V}_{Wing}^{Body}(2)}{\bar{V}_{Wing}^{Body}(1)} \qquad 5.17$$

Aerodynamic forces are calculated on the following page.

Lift:

$$C_L = C_{L_\alpha}\alpha_{Wing} + C_{L_0} \tag{5.18}$$

$$C_L \leq C_{L_{MAX}} \,\&\, C_L \geq C_{L_{MIN}} \rightarrow$$
$$L_{Wing} = \frac{1}{2}\rho\left(\bar{V}_{Wing}^{Body}(1)^2 + \bar{V}_{Wing}^{Body}(2)^2\right)A_{ref}C_L \tag{5.19}$$

$$C_L > C_{L_{MAX}} \,\&\, C_L < C_{L_{MIN}} \rightarrow$$
$$L_{Wing} = 0 \tag{5.20}$$

Drag:

$$C_L \leq C_{L_{MAX}} \,\&\, C_L \geq C_{L_{MIN}} \rightarrow$$
$$C_D = C_{D_0} + \frac{C_L^2}{\pi e AR} \tag{5.21}$$

where e is Oswald efficiency factor.

$$C_L > C_{L_{MAX}} \,\&\, C_L < C_{L_{MIN}} \rightarrow$$
$$C_D = 1 \tag{5.22}$$

$$D_{Wing} = \frac{1}{2}\rho\left(\bar{V}_{Wing}^{Body}(1)^2 + \bar{V}_{Wing}^{Body}(2)^2\right)A_{ref}C_D \tag{5.23}$$

The pitch moment is neglected, $C_M = 0$.

$$\overline{F_{Aero}}_{Wing}^{Wind} = \begin{bmatrix} -D \\ -L \\ 0 \end{bmatrix} \tag{5.24}$$

$$\overline{F_{Aero}}_{Wing}^{Body} = T\left(0,0,i_{Wing} - \alpha_{Wing}\right)\overline{F_{Aero}}_{Wing}^{Wind} \tag{5.25}$$

$$\overline{M_{Aero}}_{Wing}^{Body} = \bar{r}_{WingAC2CG}^{Body} \times \overline{F_{Aero}}_{Wing}^{Body} \tag{5.26}$$

Table 5.3 shows vertical wing parameters used in the simulation application.

Table 5.3. Vertical wing parameters

	Vertical Wing
AC position [m], Body-fixed frame	$\begin{bmatrix} -3 \\ 0 \\ -0.5 \end{bmatrix}$
Reference Area [m^2]	5
Slope of C_L vs. α curve	5.73
Maximum C_L	2
Minimum C_L	-2
C_L at $\alpha = 0$	0
C_{D_0}	0.01
Oswald efficiency factor	0.9
Aspect ratio	5
Incidence angle [^{o}]	0

5.1.4 Body

The body generates drag forces on the three-axis. The drag forces are applied from the center of gravity; no moment is generated due to the body. Flat-plate model is used to compute the forces. All aerodynamic forces are calculated in the body-fixed frame.

$$\overline{F_{Aero}}_{Body}^{Body}(1) = -\frac{1}{2}\rho u|u|C_{D_X} \quad 5.27$$

$$\overline{F_{Aero}}_{Body}^{Body}(2) = -\frac{1}{2}\rho v|v|C_{D_Y} \quad 5.28$$

$$\overline{F_{Aero}}_{Body}^{Body}(3) = -\frac{1}{2}\rho w|w|C_{D_Z} \quad 5.29$$

Table 5.4 shows body drag force coefficients used in the simulation application.

Table 5.4. Flat-plate drag area of the body

C_{D_X} [m^2]	1
C_{D_Y} [m^2]	1
C_{D_Z} [m^2]	1

5.1.5 Weight and Balance

Mass, the center of gravity, and the moment of inertia of eVTOL do not change in flight. Therefore, they are just initialized at the beginning and then kept fixed. Weight is defined in the body-fixed frame using the Euler angles.

$$\bar{W}_{Body}^{Body} = T^T(\phi, \theta, \psi) MTOW\, \bar{g} \tag{5.30}$$

Mass and moment of inertia values of the blades of rotors and propellers are extracted from the whole air vehicle in 6-DOF equations if the equations of motion of blades are calculated separately.

Table 5.5 shows the mass, CG, and inertia values used in the simulation application.

Table 5.5. CG, mass, inertia

CG position [m], Body-fixed frame	$\begin{bmatrix} 0 \\ 0 \\ 0 \end{bmatrix}$
Mass [kg]	2200
Moment of Inertia [kg-m^2]	$\begin{bmatrix} 18252.9 & 0 & 0 \\ 0 & 12168.6 & 0 \\ 0 & 0 & 4056.2 \end{bmatrix}$

5.1.6 Atmosphere

The standard atmosphere model is used at sea level, with zero delta ISA conditions. Air density is 1.225 kg/m^{3,} and the speed of sound is 340.294 m/s.

5.1.7 Inflow

The dynamic uniform inflow model is used in the simulations, which causes a deficiency in the aerodynamic pitch moment of the eight rotors at the top in forward flight. However, the simulations are done at 20 knots, and at 20 knots, the wake skew angle becomes only about 30 degrees [44]. Also, since there is no interaction model available, the inflow solver will not affect other components' forces and moments; it just affects the rotor itself, which is small enough. Therefore, Pitt-Peters inflow model selection will not make much difference in the results of this simulation application, and the dynamic uniform inflow model is sufficient in the scope of this application.

5.1.8 Equations of Motion

Newton-Euler equations at the center of gravity of eVTOL and rotational kinematics are solved. Total forces and moments generated by all the components and weight are input to the 6-DOF rigid body motion.

$$MTOW\vec{a}_{CG} = \sum \vec{F}_{Total} \tag{5.31}$$

$$\check{J}_{CG} \cdot \vec{\alpha}_{CG} + \vec{\omega}_{CG} \times \check{J}_{CG} \cdot \vec{\omega}_{CG} = \sum \vec{M}_{Total} \tag{5.32}$$

Euler angles are defined as in Equation 5.33.

$$\begin{bmatrix} p \\ q \\ r \end{bmatrix} = \begin{bmatrix} 1 & 0 & -s\theta \\ 0 & c\phi & s\phi c\theta \\ 0 & -s\phi & c\phi c\theta \end{bmatrix} \begin{bmatrix} \dot{\phi} \\ \dot{\theta} \\ \dot{\psi} \end{bmatrix} \tag{5.33}$$

5.2 Model Application

In the model application, lift and cruise type four eVTOL configurations, trimmed to hovering flight, then using pilot models, the eVTOLs are accelerated to 20 knots forward flight. The control method is described in 2.7.2.

5.2.1 Configuration 1

In configuration #1, there are eight fixed-pitch rotors at the top of the eVTOL and two fixed-pitch propellers at the back. Rotor and propeller properties of configuration #1 are presented in Table 5.6. Figure 5.3 shows the aft view and top view of configuration #1. The NACA0012 airfoil data is obtained using JavaFoil, an airfoil analysis program. Airfoil data is given in Appendix

Table 5.6. Rotor and propeller properties of configuration #1

	#1	**#2**	**#3**	**#4**	**#5**	**#6**	**#7**	**#8**	**#9**	**#10**
Direction of Rotation	CCW	CCW	CW	CW	CW	CW	CCW	CCW	CCW	CW
Blade number	5	5	5	5	5	5	5	5	5	5
Hub position [m], Body-fixed frame	$\begin{bmatrix} 2 \\ 1 \\ -1 \end{bmatrix}$	$\begin{bmatrix} 1 \\ 1 \\ -1 \end{bmatrix}$	$\begin{bmatrix} -1 \\ 1 \\ -1 \end{bmatrix}$	$\begin{bmatrix} -2 \\ 1 \\ -1 \end{bmatrix}$	$\begin{bmatrix} 2 \\ -1 \\ -1 \end{bmatrix}$	$\begin{bmatrix} 1 \\ -1 \\ -1 \end{bmatrix}$	$\begin{bmatrix} -1 \\ -1 \\ -1 \end{bmatrix}$	$\begin{bmatrix} -2 \\ -1 \\ -1 \end{bmatrix}$	$\begin{bmatrix} -3 \\ -1.5 \\ 0 \end{bmatrix}$	$\begin{bmatrix} -3 \\ 1.5 \\ 0 \end{bmatrix}$
θ_s [º]	0	0	0	0	0	0	0	0	90	90
Radius [m]	0.5	0.5	0.5	0.5	0.5	0.5	0.5	0.5	1	1
r_R [m]	0.1	0.1	0.1	0.1	0.1	0.1	0.1	0.1	0.2	0.2
Chord [m]	0.2	0.2	0.2	0.2	0.2	0.2	0.2	0.2	0.3	0.3
Taper	1	1	1	1	1	1	1	1	1	1
θ_t [º], linear	-8	-8	-8	-8	-8	-8	-8	-8	-8	-8
Airfoil, NACA	0012	0012	0012	0012	0012	0012	0012	0012	0012	0012

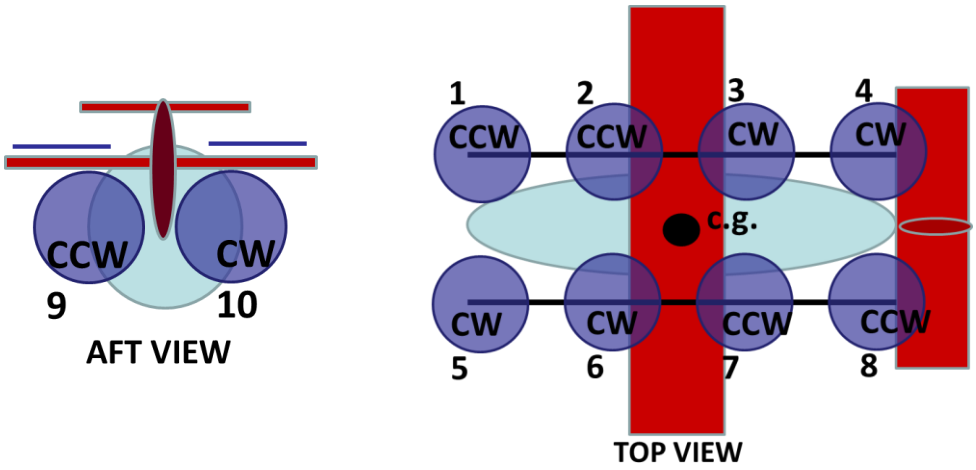

Figure 5.3. Aft view and top view of configuration #1

5.2.2 Configuration 2

In configuration #2, four corotating coaxial, fixed-pitch rotors are at the top of the eVTOL, and two fixed-pitch propellers are at the back. Rotor and propeller properties of configuration #2 are presented in Table 5.7. Figure 5.4 shows the aft view and top view of configuration #2.

Table 5.7. Rotor and propeller properties of configuration #2

	#1	**#2**	**#3**	**#4**	**#5**	**#6**	**#7**	**#8**	**#9**	**#10**
Direction of Rotation	CCW	CCW	CW	CW	CW	CW	CCW	CCW	CCW	CW
Blade number	5	5	5	5	5	5	5	5	5	5
Hub position [m], Body-fixed frame	$\begin{bmatrix} 2 \\ 1 \\ -1 \end{bmatrix}$	$\begin{bmatrix} 2 \\ 1 \\ -1 \end{bmatrix}$	$\begin{bmatrix} -2 \\ 1 \\ -1 \end{bmatrix}$	$\begin{bmatrix} -2 \\ 1 \\ -1 \end{bmatrix}$	$\begin{bmatrix} 2 \\ -1 \\ -1 \end{bmatrix}$	$\begin{bmatrix} 2 \\ -1 \\ -1 \end{bmatrix}$	$\begin{bmatrix} -2 \\ -1 \\ -1 \end{bmatrix}$	$\begin{bmatrix} -2 \\ -1 \\ -1 \end{bmatrix}$	$\begin{bmatrix} -3 \\ -1.5 \\ 0 \end{bmatrix}$	$\begin{bmatrix} -3 \\ 1.5 \\ 0 \end{bmatrix}$
θ_s [º]	0	0	0	0	0	0	0	0	90	90
Radius [m]	0.5	0.5	0.5	0.5	0.5	0.5	0.5	0.5	1	1
r_R [m]	0.1	0.1	0.1	0.1	0.1	0.1	0.1	0.1	0.2	0.2
Chord [m]	0.2	0.2	0.2	0.2	0.2	0.2	0.2	0.2	0.3	0.3
Taper	1	1	1	1	1	1	1	1	1	1
θ_t [º], linear	-8	-8	-8	-8	-8	-8	-8	-8	-8	-8
Airfoil, NACA	0012	0012	0012	0012	0012	0012	0012	0012	0012	0012

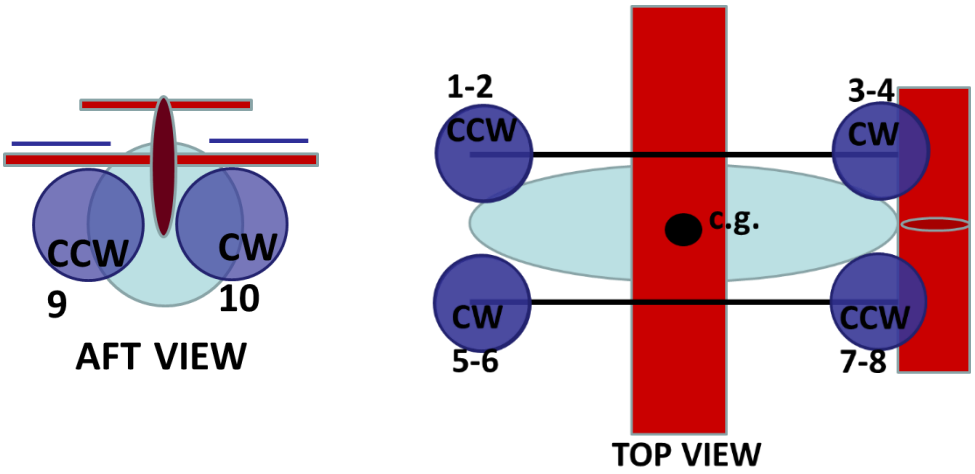

Figure 5.4. Aft view and top view of configuration #2

5.2.3 Configuration 3

In configuration #3, four ducted corotating coaxial, fixed-pitch rotors are at the top of the eVTOL, and two fixed-pitch propellers are at the back. The rotor and propeller properties of configuration #2 are the same as in Table 5.7. Additionally, there are parameters defined for the duct shown in Table 5.8. Figure 5.5 shows the aft view and top view of configuration #3.

Table 5.8. Duct properties of configuration #3

	#1	**#2**	**#3**	**#4**	**#5**	**#6**	**#7**	**#8**	**#9**	**#10**
Diffuser expansion ratio	1	1	1	1	1	1	1	1	1	1
Tip gap [m]	0.01	0.01	0.01	0.01	0.01	0.01	0.01	0.01	0.01	0.01

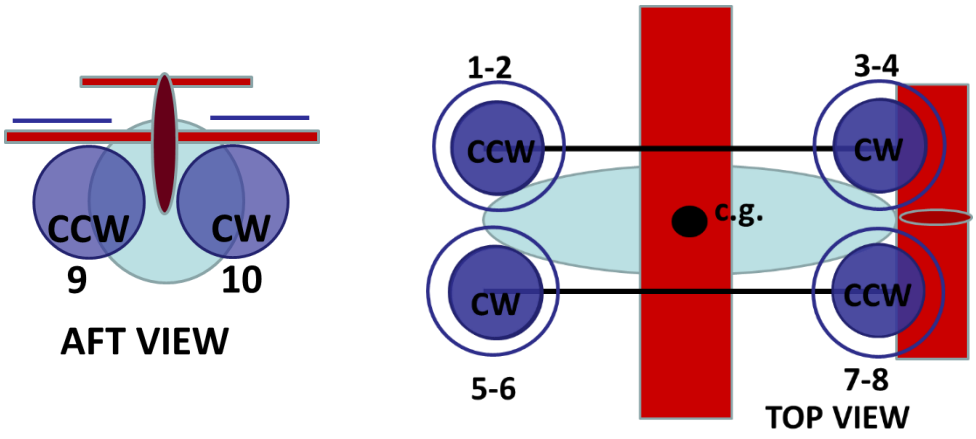

Figure 5.5. Aft view and top view of configuration #3

5.2.4 Configuration 4

Configuration #4 is the same as configuration #3, except the propellers of configuration #4 are fixed-rpm, variable pitch propellers.

5.3 Simulation Results

Simulation results are presented in this section. In the figures, configurations are color coded. Blue is designated for the first configuration, red is designated for the second configuration, magenta is the third, and brown is the fourth. In the simulation, the first 100 seconds are reserved for hover trimming. For 50 seconds afterward, the eVTOL is held in hover using the same controllers. Then in 150. second, the air vehicle started to accelerate to 20 knots. Forward speed controllers are given a 20-knot reference speed at that moment. Then they try to accelerate forward using the controllers as a pilot model. After 30 seconds, the simulation stops. In Figure 5.6, the velocities, in Figure 5.7, the attitudes, and in Figure 5.8, the rotational speeds of four different configurations are presented. The collective input of configuration #4 is shown in Figure 5.9.

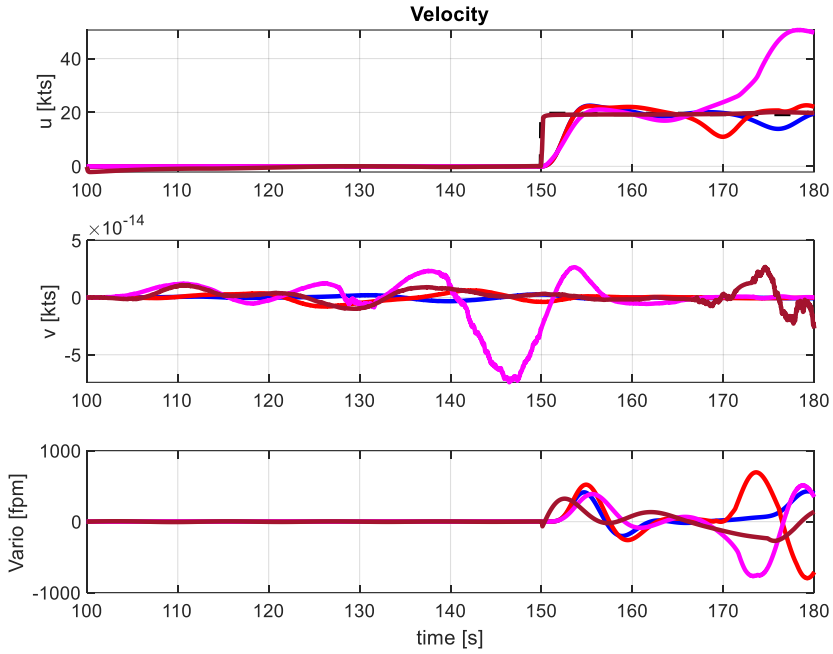

Figure 5.6. Velocities of eVTOLs with four different configurations

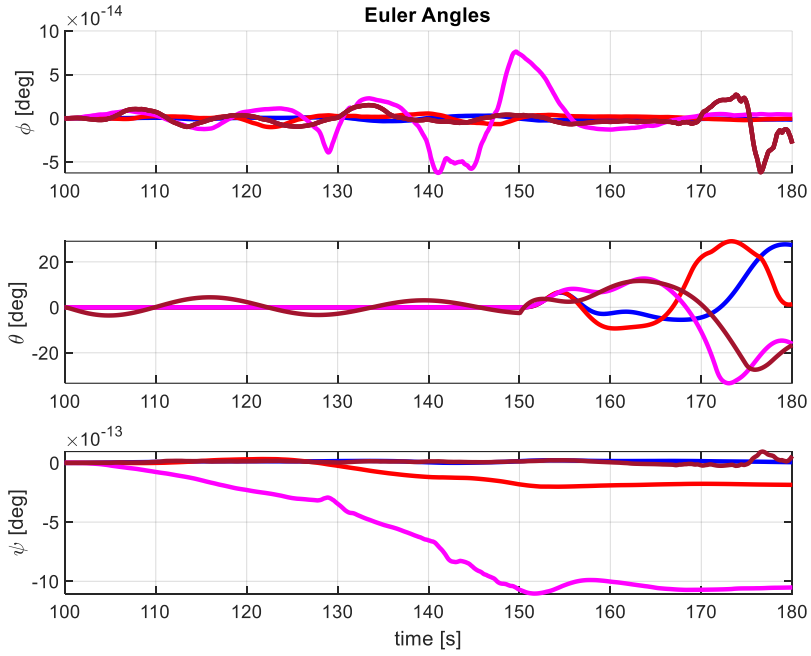

Figure 5.7. Attitudes of eVTOLs with four different configurations

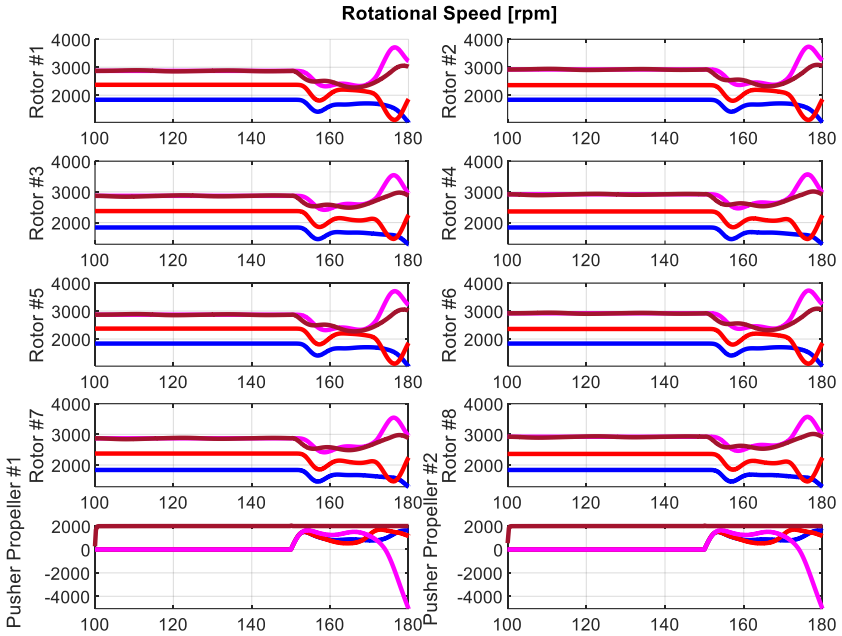

Figure 5.8. Rotational speeds of rotors and propellers of eVTOLs with four different configurations

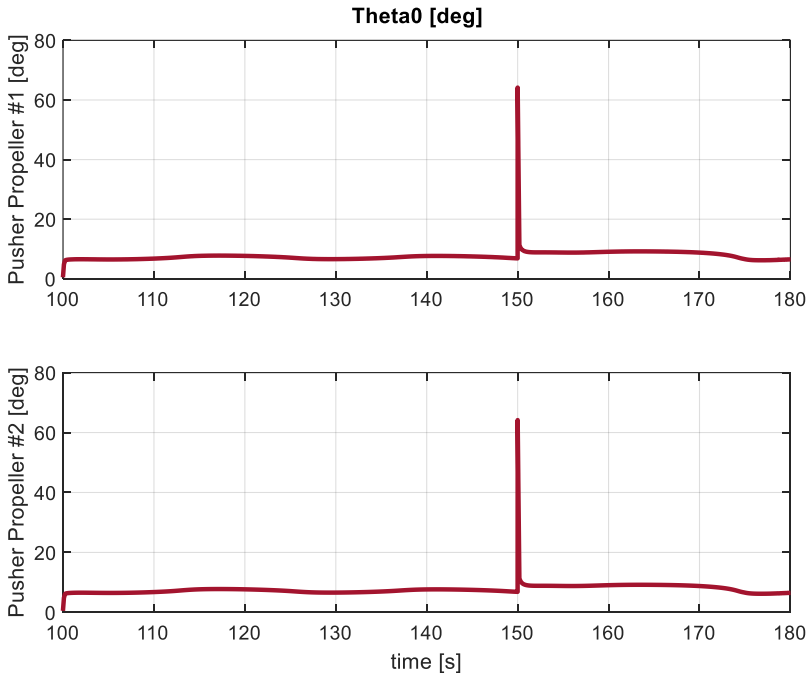

Figure 5.9. Collective input of configuration #4

All the configurations are in hover trim for the first 50 seconds. The propellers are held still in hover trim. In hover, configurations have zero degrees of attitude. Then the pilot model follows a 20-knot forward speed reference while trying to preserve other states and keep the system stable. Due to the inertia of the propellers and the driving system of the first three configurations, the propellers do not reach the rotational speed generating the thrust that pushes the eVTOL to 20 knots within the first five seconds. After 5 seconds of the reference input, the air vehicle reaches the desired speed. However, due to the airspeed, the wings generate lift force, which can be seen in the rise in vertical speed in 5 seconds after reference input, leading the rotors to slow down. Since the dynamics of the rotors and the driving systems are slow, controllers in the heave channel hardly maintain the zero vertical speed. Also, because of the moments generated by the wings, the pitch attitude deviates from zero with increasing speed. The pitch controllers are loose that they hardly follow the zero pitch angle. The variations in pitch angle are between -20 to 20 degrees. The other attitudes are successfully held at zero degrees throughout the simulation. After 20 seconds of the reference input, the system starts to diverge, which can be seen in the third configuration the most. Therefore, after 30 seconds, the simulation stops.

The responses of the first three configurations are very similar, while the fourth one is significantly different. Since the fourth configuration is accelerated with the collective control on the propellers at the back, the fourth configuration reaches 20 knots immediately after the 20-knot velocity reference is attained. The dynamics between the collective input and the thrust generation are so fast that the forward speed control is fast enough to overcome the other disturbances. However, as in the other three configurations, the pitch moment formation is hardly overcome by the controllers in the pitch channel.

An important outcome of these applications is to see the versatility of the rotor and propeller model presented in this thesis. Four different configurations are simulated and compared using this model. The effect of different rotor configurations can be seen in the trim rotational speeds of rotors in hover conditions. For the first configuration, the trim rotational speed is about 2000 rpm. When the eight rotors are

modified into coaxial rotors in the second configuration, the increase in the inflow of the lower rotors leads to a decrease in thrust. Therefore, since the required thrust is the same, the trim rotational speeds of the rotors rise to 2500 rpm in hover. When a duct is added to the coaxial rotors in the third and fourth configuration, the inflow is increased, this time for the upper and lower rotor together, and the thrust decreases consequently. Therefore, the trim rotational speeds of the rotors rise to 3000 rpm in hover to have the same thrust.

CHAPTER 6

CONCLUSION

In this thesis, propeller, articulated rotor, ducted rotor/propeller, coaxial rotor/propeller, and corresponding aerodynamic models are implemented in a dynamic rotor model in an in-house code written in MATLAB to reduce the rotor modeling workload for various eVTOL applications. A dynamic rotor/propeller model is used to represent all rotors and propellers of the configuration, which allows the designer to quickly simulate and try different eVTOL configurations for various eVTOL simulation applications like performance calculations, stability analyses, sensitivity analyses, optimization, and trade studies.

The model is compared with isolated rotor wind tunnel tests for the S-76 rotor model in hover and forward flight conditions. The results show good agreement. However, adding a dynamic wake distortion model, modeling additional 3D aerodynamic effects like yawed flow, and modeling the torsional elasticity can further increase the model's fidelity.

Example applications are performed to demonstrate the versatility of the dynamic rotor/propeller model for modeling four different multi-rotor eVTOL configurations. Rotor, coaxial rotor, and ducted rotor models are compared, and the inflow effect on them is observed. It is seen that since the inflow increases, the angle of attack decreases, and the thrust decreases from rotor to coaxial rotor, from coaxial rotor to ducted coaxial rotor. Propellers modeled in the application are controlled in two ways: rpm control and collective control. The difference between each control is investigated. It is seen that the slow dynamics in the rpm control make it harder to control than the collective control.

Other capabilities, such as another degree of freedom in the lead-lag direction, can be implemented for the fully-articulated rotor model to improve the mathematical model. Blade sweep can be modeled to reflect the aerodynamic benefits of the blade tip designs. Teetering rotor model can be implemented for modeling small-sized eVTOLs. A torsional elasticity model can be added, which is especially important in the high torque region. Aerodynamic models such as dynamic stall, reversed flow effect, stall delay, swirl effect, ground effect, and vortex ring state can be implemented for higher fidelity. Modeling of interference of the rotors to each other, which is also important for high-fidelity eVTOL simulations, can be implemented. Peters-He generalized dynamic wake theory with higher states and elastic model can be implemented to see the effect of higher harmonic forcing functions. The stall delay correction can be implemented for the propeller model. For a ducted rotor, additional enhancements can be made by introducing duct-fan interference correction and adding the effect of the duct on the edgewise velocity, including swirl losses which are higher at higher rotational speeds, and the effect of stator blades on the inflow swirl conditions, including the aerodynamic forces of the stator blades, and adding a correction for high solidity.

REFERENCES

[1] The Vertical Flight Society, 7 July 2022. [Online]. Available: https://evtol.news/.

[2] M. Hirschberg, "Commentary: An Expanded View of Electric Flight," *Vertiflite,* pp. 4-5, May/June 2022.

[3] SMG Consulting, "Advanced Air Mobility Insights," 10 July 2022. [Online]. Available: https://aamrealityindex.com/.

[4] K. I. Swartz, "The eVTOL Industry in Transition," *Vertiflite,* pp. 34-39, March/April 2019.

[5] J. Wang, "Introduction to eVTOL and UAM, 2020 eVTOL Short Course," The Vertical Flight Society, 2020.

[6] N. Zart, "AAM for Business Aviation," *Vertiflite,* p. 62, November/December 2021.

[7] The Vertical Flight Society, "VFS eVTOL Directory Reaches 500 Concepts," *Vertiflite,* p. 38, September/October 2021.

[8] M. Hirschberg, "Commentary: Looking Back: A Vertical Retrospective on Electric VTOL," *Vertiflite,* pp. 6-7, November/December 2020.

[9] F. Colucci, "Virtually Vertical Again," *Vertiflite,* pp. 42-48, July/August 2021.

[10] F. Colucci, "TVF 2022: Vehicles and Volts," *Vertiflite,* pp. 42-49, March/April 2022.

[11] J. M. Doyle, "HopFlyt Hops to the Future," *Vertiflite,* pp. 42-45, January/February 2020.

[12] N. Zart and J. Sherman, "Advanced Air Mobility Makes Waves at CES 2022," *Vertiflite*, pp. 38-40, March/April 2022.

[13] R. Whittle, "The eVTOL View from Europe," *Vertiflite*, pp. 32-34, January/February 2020.

[14] M. Hirschberg, "Commentary: Uber's Legacy: Elevating the Electric VTOL Revolution," *Vertiflite*, pp. 4-5, January/February 2021.

[15] K. I. Swartz, "Joby Transitions," *Vertiflite*, pp. 42-46, January/February 2021.

[16] M. Hirschberg, "Commentary: Looking Back: A Vertical Retrospective on Electric VTOL," *Vertiflite*, pp. 6-7, November/December 2020.

[17] R. Whittle, "The Demand for On-Demand Mobility," *Vertiflite*, pp. 34-38, January/February 2017.

[18] M. Hirschberg, "Turning Point," *Vertiflite*, pp. 66-72, July/August 2021.

[19] M. Hirschberg, "Commentary: Capitalizing on the Miraculous eVTOL Gold Rush," *Vertiflite*, pp. 4-5, March/April 2021.

[20] The Vertical Flight Society, "Supporting the Electric VTOL Revolution," *Vertiflite*, p. 64, September/October 2020.

[21] The Vertical Flight Society, "World eVTOL Aircraft Directory," 7 July 2022. [Online]. Available: https://evtol.news/aircraft.

[22] I. Frain, "Electric Vertical HEMS: A New Era in Air Ambulance?," *Vertiflite*, pp. 44-47, March/April 2021.

[23] M. Hirschberg, "Commentary: VFS Expands Support to eVTOL," *Vertiflite*, pp. 4-5, July/August 2019.

[24] N. Zart, "How Ehang Built an eVTOL for the World," *Vertiflite,* pp. 56-61, July/August 2020.

[25] R. Jaworowski and D. Royce, "The World Rotorcraft Market 2021-2030," *Vertiflite,* pp. 36-43, May/June 2021.

[26] F. Colucci, "Forum 75 - The Revolutions Get Real," *Vertiflite,* pp. 28-36, July/August 2019.

[27] T. Lombaerts, J. Kaneshige, S. Schuet, G. Hardy, B. Aponso and K. Shish, "Nonlinear Dynamic Inversion based Attitude Control for a Hovering Quad Tiltrotor eVTOL Vehicle," in *AIAA Guidance, Navigation and Control Conference*, San Diago, 2019.

[28] P.-M. Basset, B. D. Vu, P. Beaumier, G. Reboul and B. Ortun, "Models and Methods at ONERA for the Presizing of eVTOL Hybrid Aircraft Including Analysis of Failure Scenarios," in *AHS International 74th Annual Forum & Technology Display*, Phoenix, 2018.

[29] G. Palaia, K. Abu Salem, V. Cipolla, V. Binante and D. Zanetti, "A Conceptual Design Methodology for e-VTOL Aircraft for Urban Air Mobility," *Applied Sciences,* 2021.

[30] M. D. Pavel, "Understanding the Control Characteristics of Electric Vertical Take-off and Landing (eVTOL) Aircraft for Urban Air Mobility," *Aerospace Science and Technology*, no. 125, 2021.

[31] K. Atci, M. Jones and T. Jusko, "Assessment of the Handling Qualities of Multirotor Configurations Using Real Time Simulation," in *Deutscher Luft- und Raumfahrtkongress*, 2021.

[32] U. Saetti, J. Enciu and J. F. Horn, "Performance and Design Optimization of the F-Helix eVTOL Concept," in *75th Annual Forum of the Vertical Flight Society*, 2019.

[33] G. Droandi, M. Syal and G. Bower, "Tiltwing Multi-Rotor Aerodynamic Modeling in Hover, Transition and Cruise Flight Conditions," in *AHS International 74th Annual Forum & Technology Display*, Phoenix, 2018.

[34] W. Johnson and C. Silva, "Observations from Exploration of VTOL Urban Air Mobility Designs," in *7th Asian/Australian Rotorcraft Forum*, Jeju Island, 2018.

[35] J. M. Vegh, E. Botero, M. Clark, J. Smart and J. J. Alonso, "Current Capabilities and Challenges of NDARC and SUAVE for eVTOL Aircraft Design and Analysis," in *AIAA Propulsion and Energy Forum*, Indianapolis, 2019.

[36] F. Brenner, L. F. Gomez, J. Goericke and M. Hasbun, "Comprehensive Simulation for eVTOL Aircraft-Diagnosing Coupled AirframePropulsion Dynamic Instabilities," in *Vertical Flight Society's 78th Annual Forum & Technology Display*, Ft. Worth, 2022.

[37] M. Bahr, E. Ferede and F. Gandhi, "Flight Characteristics of AAM/UAM-Scale Quadcopters Under Atmospheric Turbulence," in *Vertical Flight Society's 78th Annual Forum & Technology Display*, Ft. Worth, 2022.

[38] A. Walter, M. McKay, R. Niemiec, F. Gandhi and T. Berger, "Hover Dynamics & Flight Control of a UAM-Scale Quadcopter with Hybrid RPM & Collective Pitch Control," in *Vertical Flight Society's 78th Annual Forum & Technology Display*, Ft. Worth, 2022.

[39] S. Withrow-Maser, J. Aires, A. Ruan, C. Malpica and S. Schuet, "Evaluation of Heave Disturbance Rejection and Control Response Criteria on the

Handling Qualities Evaluation of Urban Air Mobility (UAM) eVTOL Quadrotors Using the Vertical Motion Simulator," in *VFS Aeromechanics for Advanced Vertical Flight Technical Meeting*, San Jose, 2022.

[40] M. Avera, "VTOL Concepts for Unmanned Payload Delivery Applications," in *75th Annual Forum of the Vertical Flight Society*, 2019.

[41] D. I. Newman, "Coming to Terms: Rotor," *Vertiflite*, pp. 12-13, November/December 2021.

[42] G. D. Padfield, Helicopter flight dynamics : the theory and application of flying qualities and simulation modelling, 2nd ed., Blackwell Publishing Ltd., 2007.

[43] M. E. Dreier, Introduction to helicopter and tiltrotor simulation, Reston: American Institute of Aeronautics and Astronautics, Inc., 2007.

[44] A. K. Cooke and E. W. H. Fitzpatrick, Helicopter Test and Evalutation, Ohio: American Institute of Aeronautics and Astronautics, Inc., 2002.

[45] W. Johnson, Rotorcraft Aeromechanics, New York: Cambridge University Press, 2013.

[46] W. Johnson, Helicopter Theory, New York: American Institute of Aeronautics and Astronautics, Inc., 1994.

[47] J. G. Leishman, Principles of Helicopter Aerodynamics, New York: Cambridge University Press, 2006.

[48] R. W. Prouty, Helicopter Performance, Stability, and Control, Malabar, Florida: Krieger Publishing Company, 1989.

[49] A. R. S. Bramwell, Helicopter Dynamics, London: Edward Arnold Ltd., 1976.

[50] I. H. Abbott and A. E. Von Doenhoff, Theory of Wing Sections, Dover, New York, 1959, pp. 449-687.

[51] C. C. Crtizos, H. H. Heyson and B. W. Boswinkle, Aerodynamic Characteristics o NACA 0012 Airfoil Section at Angles of Attack 0 to 180, 1955.

[52] B. D. Kothmann and S. J. Ingle, "RAH-66 Comanche Linear Aeroservoelastic Stability Analysis: Model Improvements and Fight Test Correlation," in *American Helicopter Society 54th Annual Forum*, Washington, DC, 1998.

[53] R. Mouille and F. d'Ambra, "The 'Fenestron' a Shrouded Tail Rotor Concept for Helicopters," in *42nd Annual Forum of the American Helicopter Society*, Washington, 1986.

[54] C. He and H. Xin, "An Unsteady Ducted Fan Model for Rotorcraft Flight Simulators," in *62nd Annual Forum of the American Helicopter Society*, Phoenix, 2006.

[55] C. Stahlhut, "Aerodynamic Performance Modelin of Ducted Fans and Shrouded Propellers for Preliminary Design," in *American Helicopter Society 70th Annual Forum*, Montreal, 2014.

[56] F. Güner, "Comparison of Rotor Inflow Models for Fight Simulation Fidelity," Middle East Technical University, Ankara, 2016.

[57] D. M. Pitt and D. A. Peters, "Rotor Dynamic Inflow Derivatives and Time Constants from Various Inflow Models," in *9th European Rotorcraft Forum*, 1977.

[58] D. M. Pitt, "Rotor Dynamic Inflow Derivatives and Time Constants from Various Inflow Models," Washington University, 1980.

[59] D. M. Pitt and D. A. Peters, "Theoretical Prediction of Dynamic Inflow Derivatives," *Vertica,* vol. 5, no. 1, 1981.

[60] D. A. Peters and N. HaQuang, "Dynamic Inflow for Practical Application," *Journal of American Helicopter Society*, vol. 34, no. 4, 1988.

[61] P. M. Shinoda, "Full-Scale S-76 Rotor Performance and Loads at Low Speeds," NASA TM 110379, 1996.

[62] Q. K. Nguyen, "Dynamic Analysis of Rotor Blade Undergoing Rotor Power," NASA TM 102865, 1990.

[63] D. Jepson, R. Moffitt, K. Hilzinger and J. Bissel, "Analysis and Correlation of Test Data From an Advanced Technology Rotor System," NASA CR 3714, 1983.

[64] V. J. Rossow, "Effect of Ground and/or Ceiling Planes on Thrust of Rotors in Hover," National Aeronautics and Space Administration, Ames Research Center, Moffett Field, California, 1985.

[65] P. M. Shinoda, "Wall Interaction Effects for Full-Scale Helicopter Rotor in the NASA Ames 80- by 120-Foot Wind Tunnel," in *AGARD 73rd Fluid Dynamics Panel Meeting and Symposium on Wall Interference, Support Interference, and Flow Field Measurements*, Brussels, Belgium, 1993.

[66] MathWorks, "DC Motor," [Online]. Available: https://www.mathworks.com/help/sps/ref/dcmotor.html. [Accessed 2022].

[67] B. Hieb, "Creating a High-Fidelity Model of an Electric Motor for Control System Design and Verification," MathWorks, [Online]. Available: https://www.mathworks.com/company/newsletters/articles/creating-a-high-fidelity-model-of-an-electric-motor-for-control-system-design-and-verification.html. [Accessed 2022].

[68] C. Xiang, X. Wang, Y. Ma and B. Xu, "Practical Modeling and Comprehensive System Identification of BLDC Motor," *Math. Probl. Eng.*, 2015.

[69] J. G. Leishman, Principles of helicopter aerodynamics, New York: Cambridge University Press, 2006.

[70] C. He and H. Xin, "An Unsteady Ducted Fan Model for Rotorcraft Flight Simulation," in *American Helicopter Society 62nd Annual Forum*, Phoenix, 2006.

[71] "Vahana Configuration Trade Study - Part I," Airbus, 2021. [Online]. Available: https://acubed.airbus.com/blog/vahana/vahana-configuration-trade-study-part-i/.

[72] "eVTOL Aircraft Directory," Vertical Flight Society, 2021. [Online]. Available: https://evtol.news/aircraft. [Accessed 2021].

[73] "Autonomous & Electric VTOL Meeting Sets New Record," *Vertiflite*, March/April 2021.

[74] "Advanced Air Mobility Reality Index," SGM Consulting, 2021. [Online]. Available: https://aamrealityindex.com/.

[75] F. Colucci, "Forum 76: Survivable, Sustainable, Resilient," *Vertiflite,* pp. 32-35, November/December 2020.

[76] M. Hirschberg, "Commentary: VFS Expands Support the eVTOL," *Vertiflite,* pp. 4-5, July/August 2019.

[77] F. Colucci, "ART:Master Model Makers," *Vertiflite,* pp. 24-26, November/December 2020.

[78] O. C. Carholt, E. Fresk, G. Andrikopoulos and G. Nikolakopoulos, "Design, Modelling and Control of a Single Rotor UAV," in *AIAA*, 2016.

APPENDICES

A. Rotor and Propeller Model Input Parameters Summary

This appendix includes detailed information about the parameters in the input set to the Rotor and Propeller MATLAB Simulink Model mentioned in Chapter 3.

Table A.1. Input parameters summary table

Parameter					
Name	**Type**	**Dimension**	**Unit**	**Min**	**Max**
iTotalRotorNumber	uint8	Scalar		[1]	
iRotorIDNumber	uint8	Scalar		[1]	
bFlappingActive	boolean				
bPittPeters	boolean				
bDuctedRotor	boolean				
bCoaxialRotor	boolean				
iTotalActualBladeNumber	uint8	Scalar		[2]	
DirectionOfRotation	int8	Scalar		[-1]	[1]
dFuselageStationHubWrtDatumBodyFrame_m	double	Scalar	m		
dButtLineHubWrtDatumBodyFrame_m	double	Scalar	m		
dWaterLineHubWrtDatumBodyFrame_m	double	Scalar	m		
dLateralShaftTilt_rad	double	Scalar	rad	[-π]	[π]
dLongitudinalShaftTilt_rad	double	Scalar	rad	[-π/2]	[π/2]
dRotorRadius_m	double	Scalar	m	[0.1]	
dRootCutout_m	double	Scalar	m		
dSwashplatePhaseLag_rad	double	Scalar	rad	[-π]	[π]
dBladeMass_kg	double	Scalar	kg		
dFlappingInertia_kgm2	double	Scalar	kgm^2	[0.000001]	
dBladeCg2HingeRotorFrame_m	double	Scalar	m		
dHingeOffset_nd	double	Scalar		[0]	[1]
dHubSpringStiffness_Nm	double	Scalar	Nm		
dPreconeAngle_rad	double	Scalar	rad	[-π/2]	[π/2]
dDelta3_rad	double	Scalar	rad	[-π/2]	[π/2]
bTwistLinear	boolean				
dTwistAngle_rad	double	Scalar	rad	[-π]	[π]
TwistTable_RadiusVector_m	double	Column vector	m		
TwistTable_TwistAngle_rad	double	Column vector	rad	[-π]	[π]
bChordLinear	boolean				
dRootChord_m	double	Scalar	m		

dTaperRatio_nd	double	Scalar		[0]	[1]
ChordTable_RadiusVector_m	double	Column vector	m		
ChordTable_Chord_m	double	Column vector	m		
BladeAirfoilTable_AirfoilNumber	uint8	Scalar		[1]	[3]
BladeAirfoilTable_RadiusVector_m	double	2D Matrix	m		
AirfoilAerodynamicsTable_Cl	double	2D Matrix			
AirfoilAerodynamicsTable_Cl_AoA_Deg	double	Row vector	deg	[-180]	[180]
AirfoilAerodynamicsTable_Cl_Mach_nd	double	Column vector			
AirfoilAerodynamicsTable_Cd	double	2D Matrix			
AirfoilAerodynamicsTable_Cd_AoA_Deg	double	Row vector	deg	[-180]	[180]
AirfoilAerodynamicsTable_Cd_Mach_nd	double	Column vector			
dEffectiveFanCylinderHeight_m	double	Scalar	m		
dEffectiveMomentumCylinderHeight_m	double	Scalar	m		
dDiffuserExpansionRatio_nd	double	Scalar		[0]	[1]
dTipGap_m	double	Scalar	m		

B. S-76 Main Rotor Blade Geometry

The geometric properties of the main rotor blade of the S-76 helicopter are presented in Figure B.1, Figure B.2, and Figure B.3.

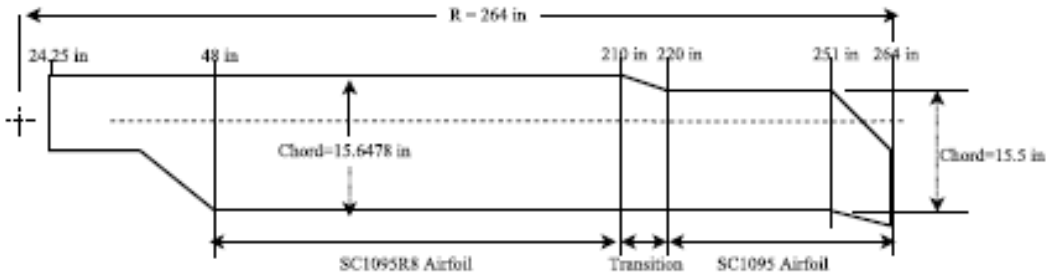

Figure B.1. S-76 main rotor blade planform [63]

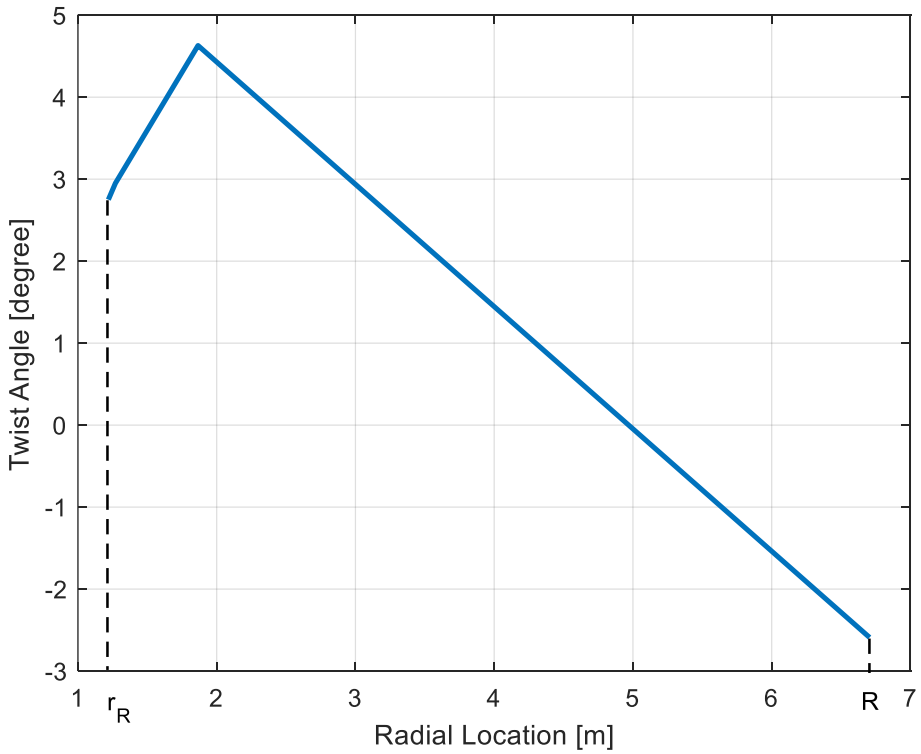

Figure B.2. Twist angle distribution taken from [63]

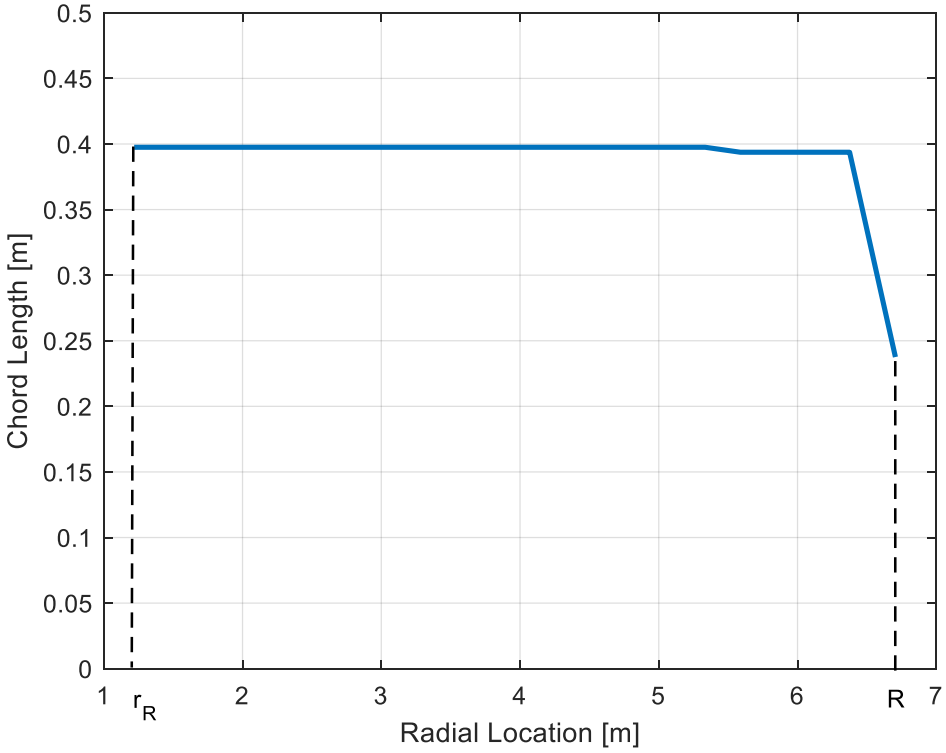

Figure B.3. Chord distribution taken from [63]

C. Aerodynamic Coefficients of the SC1095-R8 and SC1095 Airfoils

The aerodynamic characteristics of the SC1095-R8 and SC1095 airfoils taken from [63] are presented in Table C.1, Table C.2, Table C.3, and Table C.4.

Table C.1. 2D lift coefficient table of the SC1095-R8

Mach / AoA	0	0.3	0.4	0.5	0.6	0.7	0.75	0.8	0.9	1	2
-180	0.000	0.000	0.000	0.000	0.000	0.000	0.000	0.000	0.000	0.000	0.000
-172	0.780	0.780	0.780	0.780	0.780	0.780	0.780	0.780	0.780	0.780	0.780
-160	0.640	0.640	0.640	0.640	0.640	0.640	0.640	0.640	0.640	0.640	0.640
-150	0.556	0.556	0.556	0.556	0.556	0.556	0.556	0.556	0.556	0.556	0.556
-30	-1.000	-1.000	-1.000	-1.000	-1.000	-1.000	-1.000	-0.950	-0.950	-0.950	-0.950
-15	-0.850	-0.850	-0.805	-0.700	-0.700	-0.700	-0.775	-0.809	-0.740	-0.710	-0.710
-10	-0.800	-0.800	-0.740	-0.600	-0.600	-0.600	-0.700	-0.810	-0.670	-0.630	-0.630
-8	-0.744	-0.744	-0.684	-0.656	-0.600	-0.600	-0.700	-0.750	-0.667	-0.623	-0.623
-6	-0.534	-0.534	-0.545	-0.560	-0.580	-0.592	-0.694	-0.690	-0.663	-0.615	-0.615
-5	-0.440	-0.440	-0.450	-0.470	-0.500	-0.550	-0.650	-0.580	-0.575	-0.521	-0.521
-3	-0.204	-0.204	-0.202	-0.215	-0.240	-0.310	-0.380	-0.360	-0.398	-0.334	-0.334
0	0.150	0.150	0.171	0.166	0.140	0.200	0.241	0.070	-0.150	-0.050	-0.050
2	0.386	0.386	0.419	0.421	0.453	0.570	0.630	0.350	0.138	0.200	0.200
4	0.622	0.622	0.668	0.675	0.750	0.810	0.740	0.560	0.390	0.449	0.449
6	0.852	0.852	0.916	0.930	0.900	0.866	0.800	0.705	0.640	0.700	0.700
8	1.076	1.076	1.150	1.040	0.937	0.898	0.845	0.805	0.765	0.806	0.806
9	1.188	1.188	1.220	1.060	0.954	0.914	0.860	0.840	0.788	0.828	0.828
10	1.300	1.300	1.270	1.080	0.971	0.926	0.875	0.842	0.810	0.850	0.850
12	1.440	1.440	1.130	1.110	1.006	0.948	0.905	0.845	0.829	0.865	0.865
15	1.263	1.263	1.125	1.110	1.070	0.980	0.950	0.850	0.858	0.888	0.888
30	1.000	1.000	1.000	1.000	1.000	1.000	1.000	1.000	1.000	1.000	1.000
150	-0.950	-0.950	-0.950	-0.950	-0.950	-0.950	-0.950	-0.950	-0.950	-0.950	-0.950
156	-0.700	-0.700	-0.700	-0.700	-0.700	-0.700	-0.700	-0.700	-0.700	-0.700	-0.700
158	-0.660	-0.660	-0.660	-0.660	-0.660	-0.660	-0.660	-0.660	-0.660	-0.660	-0.660
160	-0.640	-0.640	-0.640	-0.640	-0.640	-0.640	-0.640	-0.640	-0.640	-0.640	-0.640
172	-0.780	-0.780	-0.780	-0.780	-0.780	-0.780	-0.780	-0.780	-0.780	-0.780	-0.780
180	0.000	0.000	0.000	0.000	0.000	0.000	0.000	0.000	0.000	0.000	0.000

Table C.2. 2D drag coefficient table of the SC1095-R8

Mach / AoA	0	0.3	0.4	0.5	0.6	0.7	0.75	0.8	0.9	1	2
-180	0.020	0.020	0.020	0.020	0.020	0.020	0.020	0.020	0.020	0.020	0.020
-179	0.025	0.025	0.025	0.025	0.025	0.025	0.025	0.025	0.025	0.025	0.025
-175	0.065	0.065	0.065	0.065	0.065	0.065	0.065	0.065	0.065	0.065	0.065
-172	0.110	0.110	0.110	0.110	0.110	0.110	0.110	0.110	0.110	0.110	0.110
-150	0.642	0.642	0.642	0.642	0.642	0.642	0.642	0.642	0.642	0.642	0.642
-115	1.880	1.880	1.880	1.880	1.880	1.880	1.880	1.880	1.880	1.880	1.880
-90	1.880	1.880	1.880	1.880	1.880	1.880	1.880	1.880	1.880	1.880	1.880
-65	1.880	1.880	1.880	1.880	1.880	1.880	1.880	1.880	1.880	1.880	1.880
-30	0.630	0.630	0.630	0.630	0.630	0.630	0.630	0.630	0.630	0.630	0.630
-10	0.250	0.250	0.260	0.270	0.288	0.310	0.326	0.225	0.262	0.297	0.297
-9	0.195	0.195	0.207	0.215	0.213	0.258	0.273	0.198	0.236	0.273	0.273
-8	0.141	0.141	0.154	0.161	0.137	0.207	0.221	0.170	0.210	0.248	0.248
-7	0.086	0.086	0.101	0.106	0.109	0.155	0.168	0.146	0.187	0.225	0.225
-6	0.050	0.050	0.062	0.070	0.081	0.094	0.109	0.122	0.163	0.202	0.202
-5	0.031	0.031	0.034	0.038	0.045	0.060	0.085	0.099	0.139	0.177	0.177
-4	0.018	0.018	0.013	0.024	0.025	0.044	0.060	0.075	0.115	0.152	0.152
-3	0.011	0.011	0.010	0.015	0.017	0.027	0.035	0.042	0.091	0.135	0.135
-1	0.010	0.010	0.008	0.009	0.009	0.010	0.012	0.026	0.063	0.109	0.109
0	0.009	0.009	0.008	0.008	0.008	0.010	0.014	0.025	0.060	0.100	0.100
1	0.009	0.009	0.008	0.008	0.008	0.012	0.024	0.042	0.078	0.118	0.118
2	0.010	0.010	0.009	0.008	0.010	0.025	0.048	0.070	0.100	0.136	0.136
3	0.010	0.010	0.009	0.009	0.016	0.048	0.071	0.089	0.119	0.153	0.153
4	0.010	0.010	0.010	0.010	0.025	0.070	0.095	0.108	0.138	0.170	0.170
5	0.011	0.011	0.010	0.011	0.038	0.093	0.115	0.128	0.160	0.193	0.193
6	0.011	0.011	0.011	0.018	0.060	0.115	0.134	0.148	0.182	0.215	0.215
7	0.012	0.012	0.013	0.027	0.086	0.138	0.152	0.167	0.202	0.235	0.235
8	0.012	0.012	0.015	0.044	0.112	0.160	0.173	0.185	0.221	0.255	0.255
9	0.013	0.013	0.018	0.078	0.137	0.183	0.195	0.208	0.242	0.277	0.277
10	0.014	0.014	0.027	0.111	0.163	0.206	0.218	0.230	0.262	0.298	0.298
15	0.114	0.114	0.230	0.280	0.300	0.320	0.330	0.343	0.374	0.408	0.390
30	0.630	0.630	0.630	0.630	0.630	0.630	0.630	0.630	0.630	0.630	0.630
65	1.880	1.880	1.880	1.880	1.880	1.880	1.880	1.880	1.880	1.880	1.880
90	1.516	1.516	1.516	1.516	1.516	1.516	1.516	1.516	1.516	1.516	1.516
150	0.642	0.642	0.642	0.642	0.642	0.642	0.642	0.642	0.642	0.642	0.642
172	0.110	0.110	0.110	0.110	0.110	0.110	0.110	0.110	0.110	0.110	0.110
175	0.065	0.065	0.065	0.065	0.065	0.065	0.065	0.065	0.065	0.065	0.065
179	0.029	0.029	0.029	0.029	0.029	0.029	0.029	0.029	0.029	0.029	0.029
180	0.020	0.020	0.020	0.020	0.020	0.020	0.020	0.020	0.020	0.020	0.020

Table C.3. 2D lift coefficient table of the SC1095

Mach / AoA	0	0.3	0.4	0.5	0.6	0.7	0.75	0.8	0.9	1	2
-180	0.000	0.000	0.000	0.000	0.000	0.000	0.000	0.000	0.000	0.000	0.000
-172	0.780	0.780	0.780	0.780	0.780	0.780	0.780	0.780	0.780	0.780	0.780
-160	0.640	0.640	0.640	0.640	0.640	0.640	0.640	0.640	0.640	0.640	0.640
-150	0.950	0.950	0.950	0.950	0.950	0.950	0.950	0.950	0.950	0.950	0.950
-30	-1.000	-1.000	-1.000	-1.000	-1.000	-1.000	-1.000	-0.950	-0.950	-0.950	-0.950
-15	-0.910	-0.910	-0.685	-0.790	-0.655	-0.745	-0.790	-0.809	-0.740	-0.710	-0.710
-10	-0.880	-0.880	-0.580	-0.720	-0.540	-0.660	-0.720	-0.810	-0.740	-0.630	-0.630
-8	-0.760	-0.760	-0.640	-0.720	-0.590	-0.713	-0.725	-0.750	-0.702	-0.623	-0.623
-6	-0.600	-0.600	-0.580	-0.613	-0.609	-0.740	-0.730	-0.690	-0.663	-0.615	-0.615
-5	-0.500	-0.500	-0.520	-0.520	-0.580	-0.720	-0.720	-0.580	-0.575	-0.521	-0.521
-3	-0.300	-0.300	-0.327	-0.477	-0.354	-0.516	-0.517	-0.360	-0.398	-0.334	-0.334
0	0.041	0.041	0.041	-0.038	0.075	-0.263	0.066	0.070	-0.150	-0.050	-0.050
2	0.269	0.269	0.286	0.255	0.361	-0.094	0.478	0.350	0.133	0.200	0.200
4	0.496	0.496	0.531	0.547	0.647	0.075	0.704	0.560	0.390	0.449	0.449
6	0.723	0.723	0.776	0.840	0.860	0.830	0.745	0.705	0.640	0.700	0.700
8	0.951	0.951	1.021	1.027	0.910	0.870	0.786	0.805	0.765	0.806	0.806
9	1.065	1.065	1.124	1.072	0.930	0.890	0.807	0.840	0.788	0.828	0.828
10	1.157	1.157	1.182	1.078	0.950	0.913	0.827	0.842	0.810	0.850	0.850
12	1.200	1.200	1.138	1.049	1.006	0.960	0.868	0.845	0.829	0.865	0.865
15	1.015	1.015	0.992	0.982	1.090	1.030	0.930	0.850	0.858	0.888	0.888
30	1.000	1.000	1.000	1.000	1.000	1.000	1.000	1.000	1.000	1.000	1.000
150	-0.950	-0.950	-0.950	-0.950	-0.950	-0.950	-0.950	-0.950	-0.950	-0.950	-0.950
156	-0.700	-0.700	-0.700	-0.700	-0.700	-0.700	-0.700	-0.700	-0.700	-0.700	-0.700
158	-0.660	-0.660	-0.660	-0.660	-0.660	-0.660	-0.660	-0.660	-0.660	-0.660	-0.660
160	-0.640	-0.640	-0.640	-0.640	-0.640	-0.640	-0.640	-0.640	-0.640	-0.640	-0.640
172	-0.780	-0.780	-0.780	-0.780	-0.780	-0.780	-0.780	-0.780	-0.780	-0.780	-0.780
180	0.000	0.000	0.000	0.000	0.000	0.000	0.000	0.000	0.000	0.000	0.000

Table C.4. 2D drag coefficient table of the SC1095

Mach / AoA	0	0.3	0.4	0.5	0.6	0.7	0.75	0.8	0.9	1	2
-180	0.020	0.020	0.020	0.020	0.020	0.020	0.020	0.020	0.020	0.020	0.020
-179	0.025	0.025	0.025	0.025	0.025	0.025	0.025	0.025	0.025	0.025	0.025
-175	0.065	0.065	0.065	0.065	0.065	0.065	0.065	0.065	0.065	0.065	0.065
-172	0.110	0.110	0.110	0.110	0.110	0.110	0.110	0.110	0.110	0.110	0.110
-150	0.642	0.642	0.642	0.642	0.642	0.642	0.642	0.642	0.642	0.642	0.642
-115	1.880	1.880	1.880	1.880	1.880	1.880	1.880	1.880	1.880	1.880	1.880
-90	2.080	2.080	2.080	2.080	2.080	2.080	2.080	2.080	2.080	2.080	2.080
-65	1.880	1.880	1.880	1.880	1.880	1.880	1.880	1.880	1.880	1.880	1.880
-30	0.630	0.630	0.630	0.630	0.630	0.630	0.630	0.630	0.630	0.630	0.630
-10	0.210	0.210	0.215	0.015	0.016	0.210	0.185	0.225	0.262	0.297	0.297
-9	0.102	0.102	0.160	0.033	0.026	0.182	0.162	0.193	0.233	0.273	0.273
-8	0.042	0.042	0.104	0.050	0.036	0.153	0.139	0.160	0.203	0.248	0.248
-7	0.018	0.018	0.050	0.035	0.036	0.125	0.117	0.130	0.176	0.225	0.225
-6	0.011	0.011	0.022	0.023	0.036	0.096	0.094	0.100	0.149	0.202	0.202
-5	0.009	0.009	0.012	0.011	0.026	0.068	0.071	0.083	0.132	0.177	0.177
-4	0.009	0.009	0.009	0.009	0.014	0.039	0.048	0.065	0.115	0.152	0.152
-3	0.008	0.008	0.008	0.008	0.011	0.020	0.027	0.042	0.091	0.135	0.135
-1	0.009	0.009	0.008	0.008	0.008	0.009	0.011	0.025	0.060	0.104	0.104
0	0.008	0.008	0.008	0.008	0.008	0.008	0.009	0.017	0.050	0.090	0.090
1	0.009	0.009	0.008	0.008	0.008	0.009	0.011	0.025	0.060	0.104	0.104
2	0.009	0.009	0.008	0.008	0.009	0.010	0.023	0.040	0.080	0.118	0.118
3	0.009	0.009	0.008	0.009	0.010	0.020	0.045	0.065	0.100	0.135	0.135
4	0.010	0.010	0.008	0.009	0.012	0.044	0.068	0.090	0.120	0.153	0.153
5	0.011	0.011	0.009	0.011	0.021	0.068	0.091	0.109	0.144	0.178	0.178
6	0.014	0.014	0.011	0.014	0.040	0.092	0.114	0.128	0.167	0.203	0.203
7	0.019	0.019	0.012	0.020	0.065	0.116	0.137	0.149	0.189	0.226	0.226
8	0.037	0.037	0.014	0.030	0.086	0.140	0.160	0.170	0.210	0.249	0.249
9	0.100	0.100	0.017	0.055	0.106	0.164	0.183	0.198	0.236	0.274	0.274
10	0.210	0.210	0.024	0.090	0.126	0.188	0.206	0.225	0.262	0.298	0.298
15	0.315	0.315	0.222	0.240	0.227	0.308	0.320	0.343	0.374	0.408	0.376
30	0.630	0.630	0.630	0.630	0.630	0.630	0.630	0.630	0.630	0.630	0.630
65	1.880	1.880	1.880	1.880	1.880	1.880	1.880	1.880	1.880	1.880	1.880
90	2.080	2.080	2.080	2.080	2.080	2.080	2.080	2.080	2.080	2.080	2.080
150	0.640	0.640	0.640	0.640	0.640	0.640	0.640	0.640	0.640	0.640	0.640
172	0.110	0.110	0.110	0.110	0.110	0.110	0.110	0.110	0.110	0.110	0.110
175	0.065	0.065	0.065	0.065	0.065	0.065	0.065	0.065	0.065	0.065	0.065
179	0.025	0.025	0.025	0.025	0.025	0.025	0.025	0.025	0.025	0.025	0.025
180	0.020	0.020	0.020	0.020	0.020	0.020	0.020	0.020	0.020	0.020	0.020

D. Hover and Forward Flight Performance Data

The performance data used to validate the rotor model is presented in this section. Rotor moments are defined in Hub Fixed Frame, and thrust is defined in TPP Frame. Pitch-down longitudinal shaft tilt, pitch-up moment, roll-left moment, and thrust-up force are positive directions. The blade pitch angle is assumed as in Equation 3.45.

In Table D.1, hover, and in Table D.2, forward flight performance data are given.

Table D.1. Hover performance data [61]

$\theta_s [deg]$	$V_\infty [kts]$	$\rho [kg/m^3]$	$Speed\ of\ Sound\ [m/s]$	$\Omega [rpm]$	C_T/σ	C_M/σ	C_L/σ	C_P/σ	$\theta_0\ [deg]$	$\theta_{1s}\ [deg]$	$\theta_{1c}\ [deg]$	$\beta_0\ [deg]$
15	1.7	1.2278	339.8	293.2	0.029637	-0.000067	0.000143	0.002197	4.0	0.0	-0.1	2.1
15	1.7	1.2206	340.8	293.6	0.029674	-0.000001	0.000013	0.002208	4.0	-0.1	0.1	2.6
15	0.0	1.2365	338.6	292.0	0.031105	0.000015	0.000017	0.002261	4.1	-0.1	-0.3	2.3
15	0.0	1.2283	339.7	292.1	0.039221	-0.000056	0.000174	0.002832	5.2	0.0	-0.1	2.6
15	0.0	1.2206	340.8	294.1	0.039509	-0.000003	0.000057	0.002838	5.3	0.1	0.0	3.0
15	0.0	1.2370	338.5	292.5	0.040513	0.000082	0.000002	0.002850	5.4	-0.1	-0.4	2.7
15	0.0	1.2206	340.8	293.9	0.049523	0.000059	0.000021	0.003605	6.6	0.0	-0.5	3.7
15	0.0	1.2283	339.7	293.5	0.050263	-0.000026	0.000142	0.003618	6.6	-0.1	-0.2	3.2
15	0.0	1.2370	338.5	292.7	0.051288	0.000028	0.000039	0.003665	6.6	-0.3	-0.4	3.3
15	0.0	1.2206	340.8	296.6	0.056972	0.000023	-0.000040	0.004285	7.7	-0.1	-0.5	4.0
15	0.0	1.2283	339.7	292.9	0.057836	-0.000001	0.000119	0.004306	7.6	-0.1	-0.2	3.6
15	0.0	1.2370	338.5	293.0	0.061310	0.000087	0.000029	0.004553	8.0	-0.2	-0.5	3.8
15	0.0	1.2288	339.7	292.0	0.069125	-0.000125	0.000161	0.005351	8.9	-0.3	-0.2	4.2
15	0.0	1.2206	340.8	293.9	0.070525	0.000056	0.000019	0.005532	9.1	-0.1	-0.7	4.6
15	0.0	1.2365	338.6	292.3	0.070820	0.000088	-0.000004	0.005429	9.0	-0.1	-0.5	4.3
15	0.0	1.2206	340.8	294.5	0.077190	0.000074	0.000050	0.006359	10.1	-0.1	-0.7	5.1
15	0.0	1.2375	338.5	292.5	0.079458	0.000107	0.000020	0.006406	10.1	-0.1	-0.7	4.7
15	0.0	1.2293	339.6	293.8	0.079657	-0.000050	0.000085	0.006515	10.2	-0.1	-0.6	4.6
15	0.0	1.2211	340.7	293.9	0.081048	0.000085	0.000020	0.006647	10.5	-0.4	-0.9	5.2
15	0.0	1.2206	340.8	293.6	0.087186	-0.000034	-0.000012	0.007449	11.2	-0.3	-0.9	5.5
15	0.0	1.2293	339.6	293.6	0.087317	0.000003	0.000109	0.007378	11.0	-0.1	-0.6	5.1
15	0.0	1.2370	338.5	293.3	0.089598	0.000003	-0.000002	0.007525	11.3	-0.5	-0.7	5.2
15	0.0	1.2206	340.8	294.6	0.095925	0.000000	-0.000021	0.008377	12.0	-0.2	-0.8	5.9
15	0.0	1.2298	339.5	294.4	0.098183	-0.000016	0.000006	0.008727	12.4	-0.2	-0.9	5.6
15	0.0	1.2200	340.9	293.7	0.107165	0.000066	0.000004	0.010082	13.6	-0.4	-0.9	6.4
15	0.0	1.2298	339.5	292.4	0.108116	0.000014	0.000015	0.010071	13.5	-0.3	-0.9	6.1
15	0.0	1.2211	340.7	293.7	0.109403	-0.000008	-0.000082	0.010190	13.6	-0.5	-0.9	6.4
10	1.7	1.2489	336.9	292.9	0.018186	-0.000052	0.000076	0.001548	2.2	-0.1	0.1	1.6
10	0.0	1.2427	337.8	291.7	0.018354	-0.000001	0.000065	0.001536	2.2	-0.1	0.1	1.6
10	0.0	1.2442	337.5	290.9	0.018718	-0.000012	0.000088	0.001562	2.3	-0.1	0.3	1.6
10	0.0	1.2437	337.6	291.6	0.021333	0.000073	-0.000108	0.001674	2.7	0.0	0.0	1.7
10	0.0	1.2211	340.7	293.3	0.028619	0.000114	0.000069	0.002143	4.1	0.0	-0.2	2.6
10	0.0	1.2427	337.8	292.4	0.029615	0.000033	0.000020	0.002084	3.8	0.2	0.0	2.2
10	0.0	1.2448	337.5	290.9	0.030052	0.000055	-0.000046	0.002110	3.9	0.0	0.0	2.2
10	0.0	1.2278	339.8	292.9	0.030796	-0.000131	0.000210	0.002231	4.1	-0.2	0.2	2.3
10	0.0	1.2211	340.7	293.9	0.038579	0.000075	0.000023	0.002765	5.2	0.0	-0.4	3.1
10	0.0	1.2437	337.6	290.9	0.038663	0.000012	-0.000062	0.002689	5.1	0.0	-0.6	2.7
10	0.0	1.2442	337.5	290.9	0.040105	0.000021	-0.000036	0.002759	5.3	-0.2	-0.5	2.8
10	0.0	1.2211	340.7	293.8	0.049259	0.000111	-0.000049	0.003561	6.6	0.0	-0.5	3.6
10	0.0	1.2448	337.5	292.0	0.049324	-0.000048	0.000045	0.003481	6.4	-0.4	-0.5	3.2
10	0.0	1.2442	337.5	290.9	0.050259	0.000068	-0.000082	0.003548	6.5	-0.3	-0.6	3.2
10	0.0	1.2442	337.5	290.6	0.058867	0.000023	-0.000041	0.004278	7.6	-0.3	-0.5	3.7
10	0.0	1.2216	340.7	294.0	0.059255	0.000115	-0.000013	0.004465	7.9	0.0	-0.5	4.2
10	0.0	1.2442	337.5	291.0	0.059860	-0.000018	-0.000005	0.004339	7.7	-0.3	-0.6	3.8
10	0.0	1.2216	340.7	293.4	0.068747	0.000123	0.000069	0.005329	8.9	-0.1	-0.5	4.5
10	0.0	1.2278	339.8	293.5	0.069862	-0.000010	0.000086	0.005303	9.0	-0.2	-0.4	4.2

10	0.0	1.2448	337.5	291.1	0.070020	0.000025	-0.000018	0.005339	9.0	-0.5	-0.5	4.4
10	0.0	1.2216	340.7	293.6	0.079650	0.000103	0.000077	0.006475	10.2	-0.1	-0.5	5.0
10	0.0	1.2211	340.7	293.9	0.087431	0.000134	0.000163	0.007385	11.1	-0.1	-0.6	5.5
10	0.0	1.2216	340.7	294.0	0.098079	-0.000007	0.000038	0.008781	12.4	-0.5	-0.8	5.9
10	0.0	1.2216	340.7	294.3	0.108074	-0.000036	0.000050	0.010147	13.7	-0.6	-0.7	6.5
5	0.0	1.2211	340.7	293.9	0.031299	-0.000045	0.000313	0.002213	4.2	-0.2	0.8	1.8
5	0.0	1.2211	340.7	293.9	0.039443	-0.000045	0.000381	0.002775	5.3	-0.2	0.8	3.0
5	0.0	1.2211	340.7	293.9	0.048675	0.000036	0.000044	0.003438	6.5	-0.2	-0.3	3.5
5	0.0	1.2211	340.7	293.5	0.061521	-0.000095	0.000122	0.004453	7.9	-0.2	0.0	3.4
5	0.0	1.2211	340.7	294.4	0.068366	-0.000087	0.000261	0.005145	8.8	-0.2	0.2	3.3
5	0.0	1.2211	340.7	293.5	0.078318	-0.000123	0.000099	0.006198	9.9	-0.5	-0.2	3.4
2	0.0	1.2489	336.9	292.9	0.017751	-0.000128	-0.000038	0.001515	2.2	-0.2	-0.4	1.6
2	0.0	1.2231	340.5	291.6	0.018181	0.000085	-0.000042	0.001524	2.2	0.3	-0.1	1.6
2	0.0	1.2221	340.6	293.1	0.030188	0.000017	0.000001	0.002124	4.0	0.2	0.0	2.3
2	0.0	1.2211	340.7	294.1	0.030755	-0.000231	0.000264	0.002205	4.2	-0.5	1.0	1.6
2	0.0	1.2216	340.7	293.5	0.039488	0.000003	0.000035	0.002741	5.2	0.0	-0.3	2.7
2	0.0	1.2211	340.7	294.2	0.040032	-0.000205	0.000345	0.002805	5.3	-0.5	1.0	2.3
2	0.0	1.2206	340.8	293.9	0.040887	0.000019	-0.000060	0.002928	5.5	-0.1	-0.1	2.7
2	0.0	1.2226	340.5	293.1	0.050501	0.000072	-0.000064	0.003549	6.6	-0.1	-0.7	3.4
2	0.0	1.2211	340.7	293.9	0.051389	-0.000202	0.000306	0.003594	6.6	-0.5	1.0	2.6
2	0.0	1.2211	340.7	295.1	0.057144	-0.000282	0.000386	0.004172	7.6	-0.4	0.9	2.9
2	0.0	1.2231	340.5	291.4	0.060292	-0.000013	-0.000041	0.004346	7.7	0.0	-0.6	3.8
2	0.0	1.2211	340.7	294.0	0.069010	-0.000113	0.000130	0.005263	8.9	-0.3	0.0	4.6
2	0.0	1.2206	340.8	294.0	0.069065	0.000092	-0.000097	0.005432	9.0	0.0	-0.3	4.0
2	0.0	1.2231	340.5	292.0	0.071167	-0.000011	-0.000086	0.005400	9.1	-0.4	-0.7	4.3
2	0.0	1.2236	340.4	293.0	0.078166	-0.000101	-0.000047	0.006104	9.9	-0.2	-0.7	4.6
2	0.0	1.2211	340.7	294.8	0.078325	-0.000080	0.000229	0.006255	10.0	-0.3	0.0	4.3
0	0.0	1.2386	338.3	290.9	0.030505	-0.000050	0.000058	0.002206	4.1	0.0	0.1	2.2
0	0.0	1.2386	338.3	292.1	0.031008	-0.000092	-0.000030	0.002199	4.2	0.0	-0.3	2.3
0	0.0	1.2386	338.3	292.4	0.051005	-0.000155	-0.000024	0.003611	6.7	-0.1	-0.5	3.3
0	0.0	1.2381	338.4	292.9	0.051243	-0.000010	-0.000057	0.003513	6.7	-0.1	-0.2	3.3
0	0.0	1.2345	338.9	292.6	0.061104	0.000029	0.000045	0.004523	8.1	0.1	-0.3	3.9
0	0.0	1.2221	340.6	292.9	0.085743	0.000044	0.000024	0.006738	10.7	0.3	0.0	5.0
0	0.0	1.2133	341.8	293.7	0.088278	-0.000053	-0.000108	0.007419	11.1	-0.3	-0.7	5.1
-5	0.0	1.2360	338.7	292.9	0.030437	0.000015	0.000001	0.002170	4.0	0.1	0.4	2.2
-5	0.0	1.2360	338.7	292.6	0.030505	-0.000017	0.000001	0.002218	4.1	-0.2	0.2	2.2
-5	0.0	1.2360	338.7	292.7	0.039771	-0.000020	0.000007	0.002762	5.2	0.0	0.4	2.7
-5	0.0	1.2365	338.6	292.6	0.049137	0.000053	-0.000018	0.003442	6.4	0.5	0.2	3.2
-5	0.0	1.2370	338.5	292.8	0.060670	0.000007	0.000026	0.004315	7.7	0.1	0.4	3.8
-5	0.0	1.2381	338.4	291.4	0.070371	0.000064	0.000007	0.005295	8.9	0.0	0.1	4.2
-5	0.0	1.2391	338.3	292.4	0.070933	-0.000079	0.000052	0.005233	9.0	-0.1	0.4	4.4
-5	0.0	1.2396	338.2	291.7	0.101581	-0.000008	-0.000130	0.008891	12.6	-0.2	-0.2	5.8
-10	0.0	1.2355	338.7	291.3	0.018930	-0.000121	-0.000133	0.001570	2.3	-0.3	-0.2	1.7
-10	0.0	1.2350	338.8	292.8	0.029621	0.000004	-0.000034	0.002125	3.9	0.1	0.4	2.2
-10	0.0	1.2350	338.8	292.2	0.040486	-0.000042	-0.000045	0.002808	5.3	0.1	0.3	2.8
-10	0.0	1.2360	338.7	292.0	0.051159	-0.000037	-0.000048	0.003589	6.6	0.0	0.3	3.3
-10	0.0	1.2360	338.7	291.2	0.068766	-0.000033	0.000042	0.005254	8.9	-0.2	-0.1	4.2
-10	0.0	1.2355	338.7	291.2	0.100003	-0.000165	0.000053	0.008769	12.5	-0.9	0.3	5.7
-15	0.0	1.2257	340.1	294.8	0.028546	-0.000142	0.000146	0.002139	4.0	0.0	0.2	2.0
-15	0.0	1.2370	338.5	292.3	0.030723	0.000078	-0.000047	0.002185	4.1	0.3	0.3	2.3
-15	0.0	1.2257	340.1	293.8	0.039734	-0.000127	0.000068	0.002807	5.4	0.0	-0.1	2.7
-15	0.0	1.2370	338.5	292.4	0.039795	0.000055	-0.000024	0.002783	5.3	0.2	0.5	2.8
-15	0.0	1.2262	340.0	293.2	0.048005	-0.000112	0.000124	0.003553	6.6	-0.1	-0.3	3.1
-15	0.0	1.2365	338.6	292.3	0.052063	0.000003	-0.000008	0.003634	6.7	0.2	0.5	3.4
-15	0.0	1.2262	340.0	293.9	0.059552	-0.000181	0.000110	0.004401	7.8	-0.2	0.0	3.7
-15	0.0	1.2355	338.7	292.8	0.059655	-0.000020	-0.000016	0.004317	7.7	0.2	0.5	3.8
-15	0.0	1.2267	339.9	293.6	0.068096	-0.000151	0.000184	0.005306	8.9	-0.1	-0.2	4.1
-15	0.0	1.2355	338.7	293.1	0.071014	-0.000061	-0.000010	0.005327	9.0	0.2	0.5	4.2
-15	0.0	1.2267	339.9	293.8	0.080677	-0.000071	0.000100	0.006434	10.2	0.1	-0.2	4.7
-15	0.0	1.2355	338.7	292.7	0.081131	0.000005	-0.000096	0.006435	10.2	0.4	0.6	4.8
-15	0.0	1.2350	338.8	292.8	0.089817	-0.000082	-0.000019	0.007311	11.1	0.2	0.9	5.2
-15	0.0	1.2262	340.0	292.3	0.089912	-0.000220	0.000149	0.007720	11.5	-0.3	-0.5	5.1
-15	0.0	1.2350	338.8	293.0	0.099158	-0.000008	-0.000018	0.008526	12.3	0.4	0.7	5.7
-15	0.0	1.2350	338.8	291.9	0.030181	-0.000050	0.000068	0.002095	3.8	0.0	-0.1	2.2
-15	0.0	1.2355	338.7	291.6	0.035475	-0.000025	0.000044	0.002375	4.4	-0.1	0.2	2.5
-15	0.0	1.2350	338.8	292.7	0.040189	-0.000094	0.000009	0.002662	5.0	-0.2	0.0	2.7
-15	0.0	1.2355	338.7	291.5	0.044833	-0.000166	0.000068	0.002926	5.5	-0.4	0.1	2.9
-15	0.0	1.2350	338.8	292.7	0.049174	-0.000141	0.000003	0.003210	6.1	-0.3	-0.1	3.1
-15	0.0	1.2355	338.7	292.1	0.055419	-0.000030	0.000048	0.003647	6.6	-0.2	0.0	3.4

-15	0.0	1.2350	338.8	292.4	0.061121	-0.000086	0.000024	0.004083	7.3	-0.3	-0.1	3.8
-15	0.0	1.2355	338.7	292.9	0.062845	-0.000065	0.000059	0.004238	7.6	-0.2	0.0	4.0
-15	0.0	1.2355	338.7	292.4	0.070223	-0.000094	0.000052	0.004879	8.4	-0.3	0.0	4.4
-15	0.0	1.2355	338.7	292.6	0.073530	-0.000154	0.000076	0.005076	8.7	-0.6	0.1	4.3
-15	0.0	1.2355	338.7	292.1	0.078979	-0.000091	0.000053	0.005734	9.4	-0.4	0.0	4.6
-15	0.0	1.2355	338.7	292.1	0.083300	-0.000115	0.000082	0.005876	9.6	-0.6	0.4	4.9
-15	0.0	1.2355	338.7	292.5	0.090254	-0.000132	0.000110	0.006714	10.4	-0.4	0.4	5.2
-15	0.0	1.2350	338.8	291.9	0.096104	-0.000135	-0.000051	0.007283	11.0	-0.5	-0.1	5.6
-15	0.0	1.2355	338.7	292.5	0.101000	0.000006	-0.000050	0.007670	11.3	-0.6	0.2	5.6
-15	0.0	1.2350	338.8	293.1	0.103137	-0.000069	0.000049	0.008020	11.8	-0.6	0.5	5.9
-15	0.0	1.2350	338.8	293.0	0.111029	0.000003	0.000027	0.009185	12.7	-0.4	0.1	6.2
-15	0.0	1.2350	338.8	293.4	0.115527	-0.000108	0.000103	0.009765	13.2	-0.5	0.4	6.5
-15	0.0	1.2355	338.7	291.5	0.117498	-0.000043	0.000105	0.010525	13.9	-0.4	0.2	6.8

Table D.2. Forward flight performance data [61]

$\theta_s[deg]$	$V_\infty[kts]$	$\rho[kg/m^3]$	$Speed\ of\ Sound\ [m/s]$	$\Omega[rpm]$	C_T/σ	C_M/σ	C_L/σ	C_P/σ	$\theta_0\ [deg]$	$\theta_{1S}\ [deg]$	$\theta_{1C}\ [deg]$	$\beta_0\ [deg]$
2	20.5	1.2200	340.9	294.2	0.029989	0.000092	0.000003	0.001657	2.3	-0.6	1.9	2.2
2	20.5	1.2200	340.9	293.5	0.040676	0.000097	0.000006	0.002162	3.8	-0.7	2.2	2.8
2	20.4	1.2200	340.9	293.9	0.050599	0.000089	0.000001	0.002751	5.2	-0.9	2.3	3.3
2	20.4	1.2200	340.9	293.8	0.060349	0.000140	0.000022	0.003390	6.4	-0.9	2.4	3.8
2	20.4	1.2200	340.9	293.5	0.071419	0.000121	0.000038	0.004186	7.7	-1.1	2.5	4.4
2	20.5	1.2200	340.9	293.8	0.079811	0.000159	0.000046	0.004890	8.7	-1	2.5	4.8
2	20.4	1.2200	340.9	293.9	0.091121	0.000114	0.000054	0.005971	10	-1.4	2.6	5.4
2	20.4	1.2206	340.8	294.9	0.100996	0.000173	0.000031	0.007018	11.2	-1.3	2.6	5.9
2	20.4	1.2206	340.8	293.8	0.110613	0.000129	0.000063	0.008269	12.4	-1.6	2.8	6.3
2	20.4	1.2211	340.7	293.9	0.119939	0.000133	0.000047	0.009823	13.8	-1.9	2.7	6.8
0	32.4	1.2288	339.7	292.4	0.037936	0.000032	0.000052	0.001677	2.2	-1	1.9	2.7
0	32.4	1.2293	339.6	294	0.050123	0.000053	0.000068	0.002168	3.7	-1.2	2.3	3.4
0	32.5	1.2293	339.6	292.5	0.059503	0.000072	0.000046	0.002642	4.9	-1.5	2.4	3.9
0	32.5	1.2298	339.5	293.3	0.069915	0.000088	0.000054	0.003280	6.1	-1.7	2.6	4.4
0	32.5	1.2298	339.5	292.3	0.074841	0.000082	0.000058	0.003634	6.7	-1.8	2.7	4.7
10	39.8	1.2236	340.4	294.7	0.030156	-0.000032	0.000060	0.001919	2.8	-1.1	0.9	2.2
10	39.8	1.2231	340.5	294	0.039968	-0.000013	0.000059	0.002352	3.9	-1.2	1.2	2.7
10	39.9	1.2231	340.5	293.6	0.050515	0.000033	0.000086	0.002895	5.1	-1.4	1.6	3.3
10	40	1.2236	340.4	292.8	0.060762	0.000051	0.000098	0.003519	6.2	-1.7	1.6	3.8
10	40	1.2236	340.4	292.7	0.070472	0.000048	0.000092	0.004201	7.2	-2	1.8	4.3
10	40	1.2236	340.4	293.1	0.081048	0.000043	0.000135	0.005036	8.5	-2.2	2.1	4.9
10	40	1.2242	340.3	292.6	0.090024	0.000066	0.000109	0.005821	9.5	-2.4	2.2	5.4
10	40	1.2242	340.3	293.2	0.100513	0.000036	0.000155	0.006924	10.7	-2.7	2.6	5.9
10	40	1.2242	340.3	292.9	0.110049	0.000066	0.000164	0.008222	12	-3.1	2.7	6.3
10	40.1	1.2236	340.4	293.3	0.120002	0.000087	0.000196	0.010033	13.6	-3.6	1.8	6.8
2	40.6	1.2195	341.0	292.9	0.037875	0.000055	0.000036	0.001301	2.2	-1	1.5	2.6
2	40.7	1.2195	341.0	293.6	0.040999	0.000063	0.000026	0.001461	2.6	-1.2	1.5	2.8
2	40.6	1.2190	341.0	294.3	0.049910	0.000079	0.000039	0.001924	3.7	-1.3	1.9	3.3
2	40.6	1.2195	341.0	293.5	0.060499	0.000069	0.000050	0.002460	4.8	-1.7	2.1	3.8
2	40.7	1.2195	341.0	293.7	0.070523	0.000104	0.000044	0.003002	5.9	-2	2.3	4.4
2	40.6	1.2195	341.0	293.9	0.080408	0.000083	0.000052	0.003681	7.1	-2.3	2.4	4.9
2	40.7	1.2195	341.0	294.3	0.090072	0.000098	0.000073	0.004437	8.3	-2.5	2.8	5.4
2	40.7	1.2195	341.0	294	0.100010	0.000132	0.000054	0.005294	9.3	-2.7	2.9	5.9
-5	40.1	1.2314	339.3	292.9	0.049816	0.000019	0.000008	0.001439	2.3	-1.4	1.9	3.4
-5	40.2	1.2319	339.2	292.5	0.060181	0.000071	0.000038	0.001743	3.4	-1.5	2.2	4
-5	40.1	1.2319	339.2	292.7	0.069827	0.000051	0.000054	0.002142	4.6	-1.8	2.6	4.5
-5	40	1.2303	339.5	292.7	0.069881	0.000063	0.000041	0.002134	4.6	-1.8	2.5	4.5
-5	40.1	1.2324	339.2	292.2	0.079865	0.000088	0.000050	0.002625	5.7	-2.1	3	5
-5	40	1.2303	339.5	292.7	0.099769	0.000110	0.000084	0.003890	8	-2.5	3.4	6.1
-10	39.9	1.2381	338.4	291.8	0.069544	-0.000020	0.000021	0.001368	3.5	-1.5	2.4	4.6
-10	40	1.2370	338.5	291.1	0.070013	-0.000016	0.000087	0.001331	3.5	-1.4	2.4	4.6
-10	39.9	1.2381	338.4	291.5	0.070314	-0.000037	0.000039	0.001391	3.6	-1.5	2.5	4.6
-10	39.8	1.2381	338.4	291.9	0.079887	0.000031	0.000038	0.001717	4.6	-1.7	2.7	5.2
-10	39.9	1.2375	338.5	291.7	0.080596	-0.000020	0.000089	0.001721	4.7	-1.6	2.7	5.2
-10	39.8	1.2381	338.4	292	0.088993	0.000009	0.000054	0.002149	5.7	-2	3.1	5.7
-10	39.9	1.2381	338.4	291.9	0.090138	0.000029	0.000130	0.002136	5.7	-1.8	3	5.7
-10	39.8	1.2381	338.4	292.4	0.099530	0.000064	0.000060	0.002717	6.8	-2.3	3.4	6.2
-10	39.9	1.2381	338.4	292	0.099873	0.000024	0.000077	0.002746	6.9	-2.3	3.4	6.2
-10	40	1.2370	338.5	292.2	0.101203	0.000011	0.000090	0.002799	7.1	-2.3	3.4	6.3
-10	39.8	1.2381	338.4	292.3	0.109717	0.000079	0.000068	0.003400	8	-2.5	3.6	6.8

-10	39.7	1.2386	338.3	291.9	0.119753	0.000074	0.000034	0.004276	9.2	-2.9	3.9	7.3
-5	49.5	1.2180	341.2	292.2	0.054297	0.000052	0.000058	0.001237	2.2	-1.4	1.8	3.6
-5	49.5	1.2180	341.2	291.9	0.060327	0.000038	-0.000022	0.001378	2.8	-1.7	1.7	4
-5	50.1	1.2242	340.3	293.1	0.060347	0.000015	0.000054	0.001327	2.8	-1.7	1.8	4
-5	49.5	1.2175	341.2	292.2	0.069705	0.000049	0.000025	0.001641	3.9	-1.9	2.1	4.5
-5	50.1	1.2242	340.3	292.4	0.069715	0.000066	0.000639	0.001568	3.8	-1.9	1.9	4.5
-5	50.1	1.2236	340.4	293.6	0.080014	0.000054	0.000079	0.001953	4.9	-2.3	2.4	5.1
-5	49.5	1.2180	341.2	292.2	0.080041	0.000091	0.000000	0.002004	4.9	-2.3	2.3	5
-5	50.1	1.2236	340.4	292.8	0.089774	0.000082	0.000088	0.002358	6	-2.5	2.7	5.6
-5	49.5	1.2211	340.7	291.8	0.090229	0.000088	0.000004	0.002487	6.1	-2.7	2.6	5.6
-5	50	1.2242	340.3	292.7	0.090746	0.000071	0.000061	0.002423	6.1	-2.7	2.8	5.7
-5	50	1.2257	340.1	292.2	0.090904	0.000053	0.000067	0.002455	6.1	-2.7	2.8	5.8
-5	50	1.2247	340.2	292.4	0.091056	0.000055	0.000068	0.002439	6.1	-2.7	2.8	5.7
-5	50.1	1.2242	340.3	293.1	0.099992	0.000047	0.000066	0.002934	7.1	-3	2.9	6.2
-5	49.5	1.2206	340.8	291.7	0.100309	0.000118	0.000005	0.003000	7.1	-2.9	2.8	6.2
-5	49.5	1.2195	341.0	291.7	0.110601	0.000086	0.000022	0.003698	8.3	-3.4	3.2	6.7
-10.01	49.9	1.2164	341.4	293.1	0.064353	-0.000032	0.000027	0.000719	2.2	-1.5	1.6	4.3
-10.01	49.9	1.2164	341.4	293.7	0.070391	-0.000003	0.000049	0.000786	2.8	-1.6	1.8	4.6
-10.01	49.9	1.2164	341.4	292.9	0.080061	0.000031	0.000038	0.000946	3.7	-1.7	2	5.2
-10.01	49.9	1.2164	341.4	293.5	0.090345	0.000077	0.000030	0.001194	4.7	-1.8	2.2	5.7
-10.01	49.9	1.2169	341.3	292.8	0.099661	0.000058	0.000051	0.001506	5.7	-2.2	2.6	6.2
-10.01	49.9	1.2169	341.3	294	0.109770	0.000031	0.000056	0.002004	6.8	-2.6	2.8	6.8
-10.01	49.9	1.2180	341.2	292.6	0.121272	0.000095	0.000031	0.002549	8	-2.9	3	7.4
10.01	60.1	1.2391	338.3	286.3	0.021766	0.000012	0.000003	0.001703	2.3	-1.4	0.3	1.8
9.99	60.4	1.2257	340.1	293.3	0.023013	0.000054	0.000010	0.001746	2.3	-1.4	0.3	1.8
9.99	60.3	1.2257	340.1	292	0.030279	0.000112	0.000006	0.002020	3	-1.5	0.5	2.2
10.01	60.1	1.2381	338.4	291.6	0.030861	0.000077	0.000047	0.002046	3.1	-1.7	0.7	2.3
10.01	60	1.2396	338.2	291.2	0.040117	0.000088	0.000033	0.002471	4.1	-1.9	0.8	2.8
9.99	60.4	1.2257	340.1	293.3	0.040197	0.000099	0.000035	0.002466	4	-1.8	0.7	2.7
9.99	60.4	1.2262	340.0	292.7	0.049579	0.000096	0.000053	0.002946	5	-2.2	1	3.2
10.01	60	1.2406	338.0	291.9	0.050374	0.000090	0.000008	0.003000	5.2	-2.3	1	3.3
10.01	60.1	1.2391	338.3	291.9	0.059195	0.000092	-0.000009	0.003504	6.1	-2.6	1	3.8
9.99	60.4	1.2257	340.1	292.9	0.059949	0.000122	0.000050	0.003537	6.1	-2.6	1.2	3.8
9.99	60.4	1.2262	340.0	293.1	0.068933	0.000101	0.000056	0.004114	7	-2.9	1.3	4.2
10.01	60.1	1.2381	338.4	291	0.071094	0.000143	0.000055	0.004251	7.2	-2.9	1.4	4.4
9.99	60.4	1.2262	340.0	291.9	0.080130	0.000120	0.000074	0.004914	8.2	-3.3	1.7	4.8
10.01	60.1	1.2396	338.2	289.5	0.080148	0.000089	0.000068	0.004950	8.3	-3.3	1.7	4.9
10.01	60.1	1.2386	338.3	290.5	0.089108	0.000107	0.000064	0.005638	9.2	-3.5	1.9	5.4
9.99	60.4	1.2262	340.0	292.2	0.090163	0.000130	0.000103	0.005702	9.2	-3.5	2	5.3
9.99	60.4	1.2262	340.0	292	0.100358	0.000113	0.000071	0.006605	10.3	-3.9	2.3	5.9
9.99	60.4	1.2262	340.0	292.5	0.110253	0.000093	0.000087	0.007648	11.5	-4.3	2.7	6.4
9.99	60.4	1.2262	340.0	292.5	0.119478	0.000147	0.000093	0.008878	12.7	-4.6	3	6.8
1.99	60.2	1.2216	340.7	292.6	0.040740	0.000059	0.000118	0.001614	2.3	-1.5	1.2	2.8
1.99	60.1	1.2206	340.8	292.9	0.060479	0.000038	0.000075	0.002272	4.3	-2.5	1.4	3.9
1.99	60.2	1.2221	340.6	293.3	0.079756	0.000023	0.000060	0.003198	6.4	-3.3	1.8	5
1.99	60.2	1.2221	340.6	292.5	0.089614	0.000135	0.000117	0.003676	7.3	-3.4	2.1	5.5
1.99	60.2	1.2226	340.5	292.5	0.100430	0.000121	0.000100	0.004401	8.5	-3.9	2.4	6.1
1.99	60.2	1.2216	340.7	294.4	0.109572	0.000121	0.000059	0.005135	9.5	-4.2	2.6	6.5
1.99	60.3	1.2216	340.7	292.5	0.119757	0.000165	0.000080	0.006118	10.7	-4.6	3	7
-5	60.2	1.2211	340.7	295.4	0.058629	0.000058	0.000021	0.001005	2.3	-1.7	1.3	3.9
-5	60.2	1.2216	340.7	292.2	0.070249	0.000073	0.000014	0.001202	3.4	-2.1	1.6	4.6
-5	60.2	1.2216	340.7	293.3	0.080313	0.000117	0.000028	0.001439	4.4	-2.3	1.8	5.1
-5	60.2	1.2216	340.7	293.7	0.089612	0.000103	0.000055	0.001748	5.3	-2.7	2	5.7
-5	60.2	1.2221	340.6	292.5	0.100962	0.000110	0.000046	0.002184	6.5	-3.2	2.3	6.3
-5	60.3	1.2221	340.6	292.7	0.109708	0.000132	0.000038	0.002608	7.5	-3.5	2.5	6.8
-5	60.3	1.2221	340.6	293.3	0.110459	0.000104	0.000089	0.002693	7.6	-3.6	2.7	6.8
-5	60.2	1.2216	340.7	292.5	0.119313	0.000109	0.000052	0.003200	8.5	-3.8	2.8	7.3
-10.01	60	1.2175	341.2	292.5	0.070559	0.000067	0.000024	0.000299	2.3	-1.7	1.6	4.7
-10.01	60.1	1.2175	341.2	293	0.080138	0.000079	0.000016	0.000388	3.2	-2.1	1.7	5.3
-10.01	60.1	1.2175	341.2	292.6	0.089748	0.000047	0.000756	0.000538	4.1	-2.3	1.9	5.8
-10.01	60.1	1.2180	341.2	292.3	0.099822	0.000088	0.000035	0.000684	5.1	-2.4	2	6.4
-10.01	60.1	1.2190	341.0	292.8	0.110732	0.000091	0.000039	0.000956	6.1	-2.7	2.2	7
-10.01	59.9	1.2195	341.0	293.1	0.119384	0.000021	0.000029	0.001320	7.1	-3.1	2.4	7.5
9.99	80	1.2236	340.4	291.5	0.014170	0.000056	0.000056	0.001556	2.2	-1.4	0.2	1.3
10	79.9	1.2128	341.9	293.1	0.014705	0.000093	0.000091	0.001566	2.2	-1.3	0.3	1.3
10	80	1.2128	341.9	293.3	0.028391	0.000065	0.000042	0.002161	3.6	-2	0.3	2.1
9.99	80	1.2242	340.3	292.6	0.029925	0.000009	0.000021	0.002243	3.7	-2.2	0.3	2.2
9.99	80.1	1.2242	340.3	292.1	0.039479	0.000034	0.000045	0.002716	4.7	-2.6	0.5	2.7
9.99	80.1	1.2247	340.2	291.7	0.050337	0.000045	0.000042	0.003326	5.7	-3.2	0.7	3.3

10	80.1	1.2118	342.0	293.4	0.050584	0.000063	0.000061	0.003349	5.8	-3.2	0.8	3.2
9.99	80.1	1.2247	340.2	292.5	0.059689	0.000063	0.000100	0.003910	6.7	-3.6	1	3.8
10	80.1	1.2118	342.0	293.6	0.070280	0.000077	0.000047	0.004652	7.8	-4.2	1.3	4.2
10.02	80.1	1.2133	341.8	292.5	0.079573	0.000105	0.000028	0.005334	8.7	-4.4	1.4	4.8
10	80.1	1.2108	342.2	293.4	0.090233	0.000061	0.000068	0.006261	9.9	-5.1	1.9	5.2
10	80.2	1.2118	342.0	294	0.100477	0.000226	0.000017	0.007012	10.8	-5.1	1.9	5.8
10	80.2	1.2123	342.0	294.5	0.109954	0.000148	0.000034	0.008087	12	-5.7	2.5	6.3
10	80.2	1.2123	342.0	292.6	0.115883	0.000076	0.000109	0.008886	12.8	-6.1	3.1	6.5
10	80.2	1.2128	341.9	292.5	0.120308	0.000172	0.000063	0.009582	13.4	-6.3	3.1	6.8
2	79.8	1.2195	341.0	292.4	0.040783	0.000023	0.000079	0.001580	2.3	-2	0.8	2.8
2	79.8	1.2200	340.9	291.6	0.049286	0.000044	0.000082	0.001789	3.1	-2.4	0.8	3.2
2	79.8	1.2206	340.8	290.6	0.059193	-0.000037	0.000123	0.002112	4.1	-3.2	1	3.8
2	79.8	1.2206	340.8	291.7	0.070165	0.000040	0.000134	0.002475	5.2	-3.6	1.2	4.4
2	79.8	1.2200	340.9	291.1	0.079651	0.000030	0.000139	0.002884	6.2	-4	1.5	4.9
2	79.8	1.2190	341.0	291.3	0.090703	0.000041	0.000083	0.003379	7.2	-4.5	1.6	5.5
2	79.9	1.2190	341.0	291.1	0.100619	0.000030	0.000118	0.004013	8.4	-5.1	2	6
2	79.8	1.2180	341.2	291.7	0.110008	0.000091	0.000118	0.004658	9.4	-5.4	2.3	6.6
2	79.9	1.2175	341.2	291.7	0.117770	0.000049	0.000118	0.005513	10.4	-6.1	2.8	6.9
-5	80	1.2190	341.0	292.9	0.063276	0.000072	0.000029	0.000607	2.2	-2.4	1.1	4.3
-5	80	1.2190	341.0	292.6	0.069245	0.000048	0.000030	0.000670	2.9	-2.7	1.2	4.6
-5	79.9	1.2195	341.0	292.1	0.080135	0.000088	0.000024	0.000783	3.9	-3.1	1.3	5.2
-5	80	1.2190	341.0	293.5	0.090119	0.000098	0.000036	0.000967	4.9	-3.4	1.5	5.8
-5	80	1.2185	341.1	292.5	0.100541	0.000080	0.000042	0.001230	5.9	-4	1.7	6.4
-5	80	1.2185	341.1	293.7	0.110004	0.000050	0.000069	0.001594	6.9	-4.4	1.9	6.9
-5	80	1.2180	341.2	292.3	0.120153	0.000058	0.000072	0.002003	8	-4.8	2.2	7.4
10.01	99.9	1.2087	342.5	293.5	0.030310	0.000077	0.000007	0.002510	4.6	-2.9	0.2	2.2
10.01	99.9	1.2087	342.5	294.3	0.037123	-0.000004	0.000006	0.002940	5.4	-3.5	0.3	2.5
10.01	99.9	1.2087	342.5	292.3	0.050367	0.000023	0.000012	0.003792	6.7	-4.2	0.5	3.2
10.01	99.9	1.2097	342.3	293	0.060275	0.000005	0.000029	0.004507	7.7	-4.8	0.8	3.7
10.01	100	1.2092	342.4	291.4	0.068641	0.000007	0.000021	0.005157	8.6	-5.4	1	4.1
10.01	100	1.2092	342.4	295	0.079208	0.000046	0.000082	0.006001	9.8	-5.8	1.5	4.7
10.01	100	1.2097	342.3	293.1	0.090581	0.000046	0.000070	0.007015	10.9	-6.3	1.8	5.2
10.01	100	1.2092	342.4	292.4	0.100551	0.000034	0.000100	0.008048	12	-6.9	2.2	5.7
10.01	100.1	1.2097	342.3	292	0.109185	0.000034	0.000092	0.009178	13.2	-7.5	2.8	6.2
10.01	100	1.2103	342.3	293.5	0.116160	0.000103	0.000075	0.010790	14.5	-8.2	3.6	6.5
2	99.8	1.2144	341.7	292.1	0.037787	0.000400	0.000029	0.001529	2.2	-2.5	0.4	2.7
2	99.7	1.2149	341.6	290.5	0.050663	0.000018	0.000007	0.001868	3.5	-3.4	0.5	3.4
2	99.8	1.2149	341.6	291.3	0.060621	0.000032	0.000027	0.002161	4.5	-3.9	0.7	3.9
2	99.8	1.2128	341.9	290.5	0.069973	0.000015	0.000036	0.002498	5.5	-4.5	0.9	4.4
2	99.8	1.2123	342.0	291.4	0.080155	0.000050	0.000079	0.002909	6.6	-5	1.3	5
2	99.9	1.2133	341.8	292.1	0.089475	0.000010	0.000029	0.003408	7.7	-5.7	1.4	5.5
2	99.8	1.2139	341.7	290.8	0.100379	0.000042	0.000083	0.003999	8.7	-6.2	1.7	6.1
2	99.8	1.2133	341.8	291	0.104838	0.000036	0.000037	0.004300	9.2	-6.5	1.7	6.3
-5	99.5	1.2211	340.7	291.9	0.070069	0.000032	0.000012	0.000289	2.8	-3.5	0.9	4.7
-5	99.7	1.2216	340.7	291.6	0.079867	0.000082	0.000013	0.000330	3.8	-3.9	1	5.3
-5	99.7	1.2200	340.9	292.4	0.090516	0.000088	-0.000017	0.000459	4.8	-4.5	1.1	5.9
-5	99.7	1.2206	340.8	292	0.099872	0.000073	0.000002	0.000672	5.8	-5.1	1.3	6.4
-5	99.7	1.2206	340.8	292.3	0.110759	0.000099	0.000047	0.000973	6.9	-5.6	1.5	7
-5	99.7	1.2211	340.7	290.8	0.119931	0.000077	-0.000004	0.001494	8.1	-6.4	1.8	7.5
-5	99.7	1.2211	340.7	290.8	0.120031	0.000074	-0.000006	0.001491	8.1	-6.4	1.8	7.5

E. NACA0012 Airfoil Data

The aerodynamic characteristics of NACA0012 airfoil obtained by using the JavaFoil program are presented in Table E.1, Figure E.1, and Figure E.2

Table E.1. 2D lift and drag coefficient table of the NACA0012

	Cl	Cd
Mach / AoA	0	0
-180	0.000	0.01691
-172	-0.938	0.01933
-160	-1.512	0.05403
-150	-1.013	0.17363
-30	-0.643	0.27088
-15	-1.108	0.05044
-10	-1.131	0.01835
-8	-0.935	0.01947
-6	-0.714	0.01809
-5	-0.598	0.01924
-3	-0.36	0.01788
0	0	0.01691
2	0.241	0.01758
4	0.48	0.01847
6	0.714	0.01809
8	0.935	0.01933
9	1.038	0.01928
10	1.131	0.01832
12	1.261	0.02256
15	1.111	0.04996
30	0.643	0.27122
150	1.013	0.17329
156	1.343	0.08945
158	1.44	0.07
160	1.512	0.05386
172	0.938	0.01947
180	0	0.01691

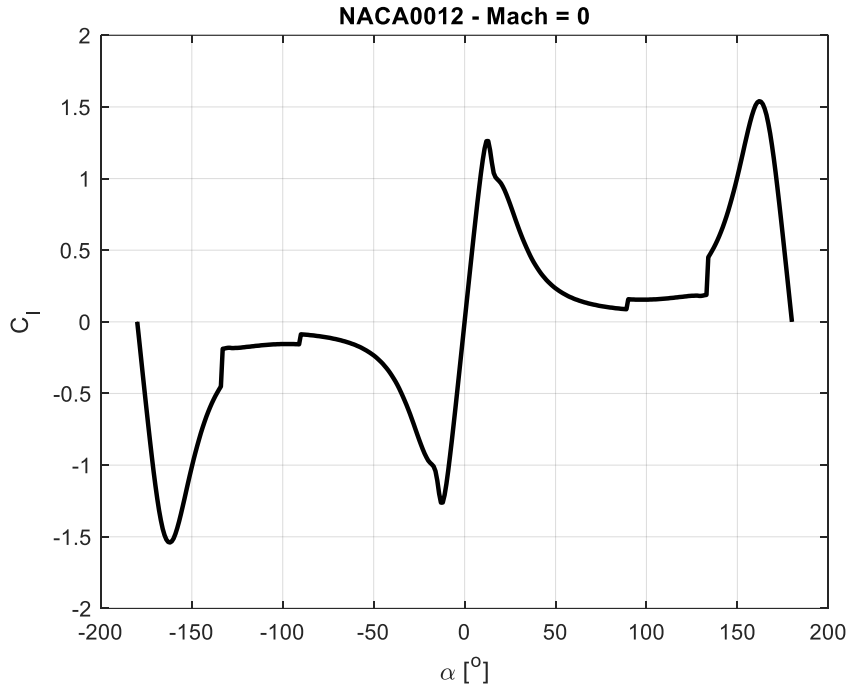

Figure E.1. Cl data of NACA0012

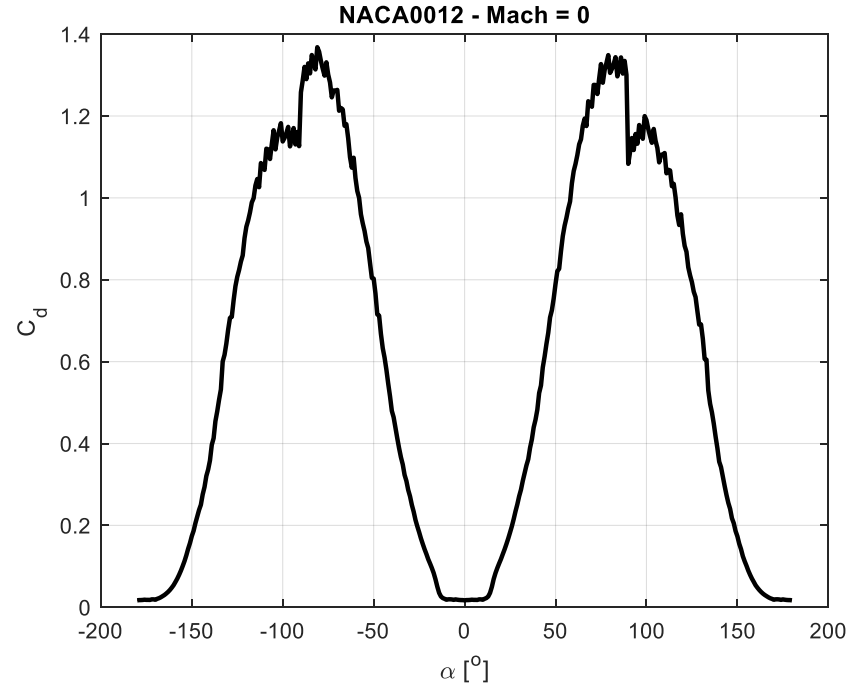

Figure E.2. Cd data of NACA0012